TRANSFORMATION TEXTURES IN HOT ROLLED STEELS

by

Martha Patricia Butrón Guillén

A Thesis Submitted to the Faculty of Graduate Studies and Research in Partial Fulfillment of the Requirements for the Degree of Doctor of Philosophy

Department of Mining and Metallurgical Engineering

McGill University

Montreal, Canada

January 1995

ABSTRACT

The way in which texture development is affected by hot rolling, intercritical rolling, and warm rolling was studied in a plain carbon, a niobium microalloyed and an interstitial free steel. Three processing parameters were varied: the austenitizing temperature (1250°C or 1150°C), amount of reduction (90% or 75%) and finish rolling temperature (1020°C, 870°C, 770°C, 730°C and 630°C for the first two materials, and 1020°C, 920°C, 870°C, 820°C, 720°C and 620°C for the IF steel). It was found that lower reheating temperatures and larger deformations lead to more intense textures. The effect of finish rolling temperature was different for each steel. In the plain carbon, only warm rolling produced a strong texture. In the interstitial free steel, the strongest textures were again produced by rolling in the ferrite range. In the niobium microalloyed steel, the retardation of austenite recrystallization intensifies the fcc deformation texture components; thus, a fairly strong texture is inherited by the ferrite, which is in turn enhanced by further deformation. The experimental textures were compared with the transformation textures predicted by using the Kurdjumov-Sachs relationship. It was found that when most of the reduction was applied in the austenite recrystallization range, the cube texture appeared to form, which transformed preferentially into the rotated cube $\{001\}<110>$. When the austenite remained in the pancaked state, the expected transformation products of the fcc rolling texture, i.e. the copper $\{112\}<111>$, brass $\{110\}<112>$, S $\{123\}<634>$ and Goss $\{110\}<001>$, again appeared, with clear preferences for particular variants. The calculations indicate that the final ferrite texture formed from either recrystallized or deformed austenite is significantly modified by both variant selection and selective growth.

RÉSUMÉ

L'effet du laminage à chaud (laminage austénitique, laminage intercritique et laminage ferritique) sur le développement de la texture a été étudié pour un acier au carbone, un acier microallié au niobium et un acier IF. On a fait varier trois paramètres opératoires: la température d'austénitisation (1250°C ou 1150°C), le taux de réduction (90% ou 75%) et la température finale de laminage (1020°C, 870°C, 770°C, 730°C et 630°C pour les deux premiers matériaux et 1020°C, 920°C, 870°C, 820°C, 720°C et 620°C pour l'acier IF). Les températures de réchauffage plus réduites et les déformations plus élevées mènent à des textures plus intenses. L'effet de la température de finition est différent pour chaque acier. Dans les aciers au carbone, seul le laminage ferritique produit une texture forte. Dans les aciers IF, les textures les plus fortes sont également produites par laminage ferritique. Dans les aciers microalliés au niobium, le retard de la recristallisation de l'austénite a renforce les composantes de textures de déformation c.f.c.; une texture assez forte est donc heritée par la ferrite, qui est à son tour amplifiée par la déformation ultérieure. Les textures expérimentales ont été comparées avec les textures prédites en employant la relation de Kurdjumov-Sachs. Il a été observé que lorsque la plus grande partie de la déformation est effectuée dans le domaine de recristallisation de l'austénite, la texture cubique apparaît, et se transforme de préférence en l'orientation cubique tournée $\{001\}<110>$. Quand l'austénite reste à l'état écroui, les composantes de transformation attendues de la texture de laminage c.f.c., i.e. cuivre $\{112\}<111>$, laiton $\{110\}<112>$, S $\{123\}<634>$ et Goss $\{110\}<001>$, apparaissent de nouveau, avec une préférence prononcée pour des variantes particulières. Les calculs indiquent que la texture finale ferritique, formée à partir de l'austénite recristallisée ou déformée, est modifiée de manière significative, à la fois par sélection des variantes et croissance sélective.

RESUMEN

En este trabajo se estudia el desarrollo de la textura despues de laminación en caliente, intercrítica y laminación en fase ferrítica en tres tipos de aceros: al carbono, microaleado con niobio y libre de elementos intersticiales ("IF"). Se variaron tres parámetros de procesamiento: temperatura de austenización (1250°C ó 1150°C), porcentaje de reducción (90% ó 75%) y temperatura final de laminación (1020°C, 870°C, 770°C, 730°C y 630°C para los dos primeros materiales, y 1020°C, 920°C, 870°C, 820°C, 720°C y 620°C en el acero "IF"). Se encontró que con temperaturas más bajas de austenizacion y mayor deformación se obtienen las texturas más intensas. El efecto de la temperatura final de laminación fue diferente para cada acero. En el acero al carbono, solamente se obtuvo una textura bien definida en el caso de laminación en fase ferritica; este mismo tipo de laminación produjo las texturas más intensas en el acero "IF". En el acero microaleado, la presencia de niobio retarda la recristalización de la austenita, reforzando los componentes de textura de deformación en dicha fase; la ferrita hereda una textura bien definida, que es reforzada al continuar la deformación. Los resultados experimentales se compararon con texturas de transformación teóricas obtenidas usando la relación de Kurdjumov-Sachs. Se encontró que cuando la deformación se aplica en la región de recristalización de la austenita, se forma la textura de cubo $\{100\}<001>$, y ésta se transforma preferencialmente en la orientación $\{001\}<110>$. Cuando la austenita conserva una estructura deformada, se obtienen las orientaciones típicas de deformación en dicha fase, las cuales se transforman con preferencia por ciertas variantes en cada caso. Los resultados teóricos indican que la textura final de la ferrita, transformada ya sea de austenita recristalizada ó deformada, es modificada de manera importante tanto por selección preferencial de variantes como por crecimiento selectivo de ciertas orientaciones.

ACKNOWLEDGEMENTS

I want to express my most sincere thankfulness to Professor John J. Jonas, supervisor of this thesis, for his continuous guidance, motivation and infinite patience. The long scientific discussions we had over the subject of this work were always fruitful, and very helpful. It has been a privilege to work with him at McGill University.

Thanks are also due to Professor Ranjit K. Ray, from the Indian Institute of Technology, who initiated this project and with whom I had the opportunity to collaborate during his many visits to McGill University. I am also indebted to Dr. George E. Ruddle for his assistance in the hot rolling experiments at the Metals Technology Laboratories of CANMET, in Ottawa, and to Prof. Jerzy A. Szpunar, who kindly gave me access to the texture laboratory at McGill University.

I am grateful to Dr. Jose Gerardo Cabañas Moreno, professor at the E.S.I.Q.I.E., National Polytechnic Institute in Mexico City, for suggesting that I should undertake my doctoral studies at McGill, for his confidence in me and his constant encouragement.

My sojourn at McGill University was in part possible thanks to a scholarship granted by the National Council of Science and Technology of Mexico; to all the people who supported my application and to the government of Mexico, I offer my sincere gratitude.

I am indebted to my fellow graduate students and research associates from all around the world, for their friendship and the good times we shared in Montreal. Here I must mention Dominique Daniel, Christine Roucoules, Toshiaki Urabe, Jerzy Baczynski, Leo Kestens, Jean Savoie, Youdong Zhou, and especially Mr. Peter Blandford, with whom I enjoyed talking not only about texture, but also about the English language, literature, politics, Canadian traditions, etc. Also, my gratitude to my Mexican friends in Montreal, and particularly to Eduardo Turcott, for all their support.

The immense help in all sorts of administrative matters of Lorraine Mello, Jeanne Gould and Carol Rousseau, and in technical matters of Edwin Fernandez was greatly appreciated.

Last, but not least, I want to thank my parents, Ernesto Butrón Peralta and Lesvia Elvira Guillén de Butrón, and my brothers Marco Antonio and Jorge Alejandro, for their love and understanding.

TABLE OF CONTENTS

LIST OF FIGURES

LIST OF TABLES

Chapter I

INTRODUCTION

The term *texture* has been extensively used in science, although with many different connotations. As early as the seventeenth century, Robert Boyle (1626-1691) employed it when describing the properties of matter: after motion, size and figure, he considered order and situation as important properties of matter, and jointly denoted the latter two as "texture" [1]. Nowadays, texture is used in the field of geology with a variety of meanings. It can merely denote grain size; it can refer to particular kinds of grain-to-grain relations or intergrowth; or it can combine three aspects of microstructure: crystallinity, granularity, and the shape and spatial distribution of grains [2]. In metallurgy, and in this work, texture implies preferred crystallographic orientation in a polycrystalline aggregate; that is, it involves the statistical tendency for the constituent crystal grains to be oriented in particular ways.

The importance of the study of the formation and nature of textures in metals emanates from the effect of texture on properties. Such effects apply especially to sheet materials, and include:

(i) modification of the strength and ductility;

(ii) changes in the ratio of width strain to thickness strain during deformation (in particular, during deep drawing), denoted as the strain ratio or r-value;

(iii) anisotropy of the r-ratio; the latter involves inhomogeneous deformation along different directions during deep drawing, leading to the formation of *ears* around the periphery of drawn cups.

Textures are formed and modified by processes such as deformation, recrystallization and transformation. The latter is particularly important when steels are employed in the normalized or as-hot rolled condition. In this case, a parent texture is formed and inherited by the product phase according to certain orientation relationships. There have been numerous studies of texture formation during cold rolling and recrystallization; by contrast, little research has been carried out on the texture of hot rolled sheet steels.

The objective of this work was to determine how transformation textures develop in three different classes of hot rolled steels: a plain carbon, a niobium microalloyed, and an interstitial free steel. For this purpose, the investigation was divided into 3 main parts: hot rolling (including warm rolling), texture determination of the rolled materials, and the analytic prediction of product components from individual parent orientations.

First, extensive rolling experiments were conducted in which the following processing parameters were controlled: austenitizing temperature, amount of reduction, and finish rolling temperature. Then, texture measurements were carried out on each

rolled sample. The texture results are presented here in the form of (200) and (110) pole figures, $\varphi_2 = 45°$ sections of the ODF, and the intensities along the RD, TD and ND fibres. These representations are complementary in nature, and are included here in order to provide as complete a picture as possible. They are useful because they can be readily compared with other data. The anaiytical work consisted of the prediction of the transformation products from a number of recrystallization and deformation parent orientations; the results are presented in detail below and compared with the experimental data obtained from the rolling experiments.

In Chapter II, the various forms of texture representation are introduced, and in Chapter III the relations between parent and transformation product orientations are described. The mechanisms which account for them are also summarized. Hot rolling textures are reviewed in Chapter IV. Next, in Chapter V, the experimental procedure concerning the hot rolling trials and texture measurements carried out for this work are explained. The complete set of microstructure and texture results is the subject of Chapter VI. Chapter VII deals with the simulation work; the basis of the calculations is presented, as well as the detailed sets of results for both recrystallization and deformation parent components. The experimental and calculation results are compared and discussed in Chapter VIII, and finally, the conclusions reached in this work are presented in Chapter IX.

Chapter II

TEXTURE REPRESENTATION

Most technologically important materials have a polycrystalline structure. Generally speaking, the individual crystallites are anisotropic, and this gives rise to macroscopic anisotropy if they have a non-random orientation distribution, i.e. a *texture*. The directional properties may also be due to internal stresses, the anisotropic shape and arrangement of phases, anisotropic dislocation substructures, and many other factors. The anisotropic structural parameters may influence the mechanical, physical and chemical properties of the materials, such as elastic modulus, yield strength, electrical and thermal conductivity, etc. In some cases, outstanding material properties are only needed along a particular direction: for example, high formability in a deep drawing sheet is required in the sheet plane but not in the normal direction. Therefore, materials with specific properties can be produced, by controlling the texture, without the need to improve the overall properties. This can be attained, for instance, through plastic deformation, recrystallization, or phase transformation.

The most important anisotropy parameter, the texture, can be described in terms of individual grain orientations, or as the average over a certain volume. The most frequently used method of measurement is by x-ray diffraction followed by "pole figure inversion", a mathematical method by which the orientation distribution function (ODF) of the crystallites is obtained.

If the crystallographic orientation of the crystallites is designated by g (to be defined in the next section), then the orientation distribution function of the crystallites is given by either the relative volume or the relative number of crystallites that have the orientation g within a certain infinitesimal orientation element dg. This is shown schematically in Figure II.1. The ODF is then defined by:

$$\frac{dV}{V} = f(g) \cdot dg, \quad \text{(texture by volume)}, \tag{II.1}$$

or

$$\frac{dN}{N} = f^n(g) \cdot dg, \quad \text{(texture by number)}, \tag{II.2}$$

where V is the total volume of the sample and N the total number of crystallites in the sample.

f(g) is the usual symbol for the orientation distribution function that describes the crystallographic texture. It is generally assumed that the number of crystallites is infinite, and that f(g) is a non-negative continuous function. It is customary to normalize the function f(g) as follows:

$$\int f(g) \cdot dg = 1 \tag{II.3}$$

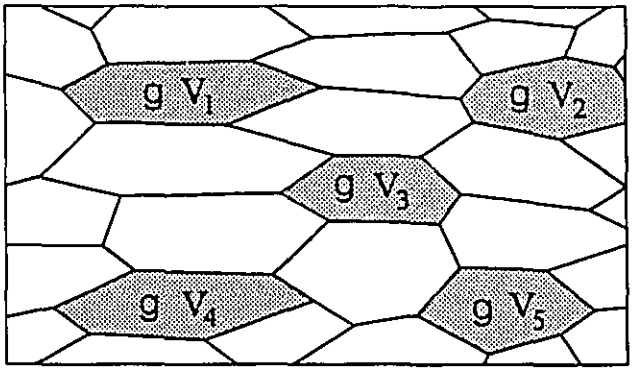

Figure II.1 The volume fraction of crystallites of orientation g within the sample.

II.1 Sample and Crystal Orientations

In order to relate the crystallite orientation to the sample, it is necessary to define two different coordinate systems. The reference frame K_A, a right-handed cartesian coordinate system, is attached to the sample. The choice of this system is arbitrary, but it is generally convenient to relate it with some geometric characteristics of the sample. For example, in rolled metals, the three obvious orthogonal vectors $\vec{s}_1$, $\vec{s}_2$ and $\vec{s}_3$ of K_A are the rolling direction RD, the transverse direction TD and the normal direction ND. A second coordinate system is associated with *each* crystal in the sample. This is the K_B system, and it is also cartesian and right-handed. Again, the choice for this reference frame is arbitrary, but in a cubic crystal it is advantageous to use the [100], [010] and [001] directions to define the vectors $\vec{c}_1$, $\vec{c}_2$ and $\vec{c}_3$ of K_B.

The orientation of a crystallite in the sample is then defined by the orientation of the crystal coordinate system K_B with respect to the sample coordinate system K_A. The

orientation can thus be represented as the rotation g which brings a movable coordinate system K_A into coincidence with K_B. Symbolically, this is expressed as:

$$K_B = g \cdot K_A \tag{II.4}$$

The rotation g can also be expressed in matrix form. Since the three axes $\vec{s}_1$, $\vec{s}_2$ and $\vec{s}_3$ of the sample coordinate system and the three axes $\vec{c}_1$, $\vec{c}_2$ and $\vec{c}_3$ of the crystal coordinate system form nine angles, their cosines can be arranged in a matrix as follows:

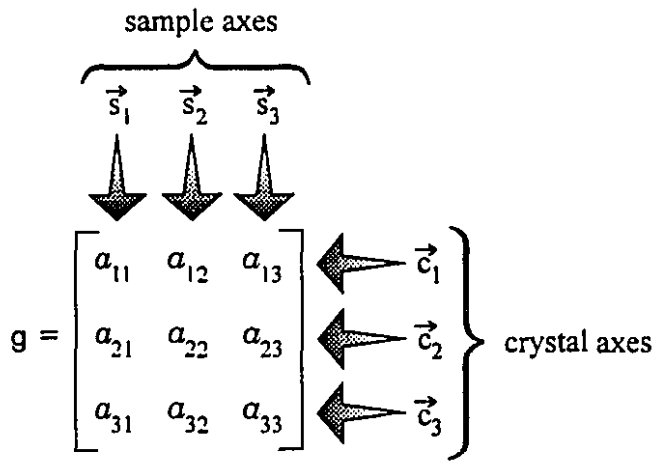

(II.5)

Here, the components of the first column a_{11} a_{21} a_{31} are the direction cosines of the sample $\vec{s}_1$ axis with respect to the crystal coordinate system. Therefore, they describe the crystal direction that corresponds to the rolling direction. The components a_{13} a_{23} a_{33} of the last column describe the crystal direction that is parallel to the sample $\vec{s}_3$ axis, or sheet normal in a rolled material. If the rolling and normal directions are designated by the Miller indices *u'v'w'* and *h'k'l'*, respectively, then by multiplying them by an appropriate factor the integer numbers *uvw* and *hkl* can be obtained:

$$g = \begin{bmatrix} u' & v' & h' \\ v' & \bullet & k' \\ w' & \bullet & l' \end{bmatrix} \quad , \quad g = (hkl)[uvw] \qquad \text{(II.6)}$$

This description of a rotation (and thus, of an ideal orientation) is widely used for cubic metals, (*hkl*) being the Miller indices of the crystallographic plane parallel to the rolling plane. Figure II.2 shows the sample and crystal coordinate systems, as well as the [*hkl*] and [*uvw*] directions for a crystallite.

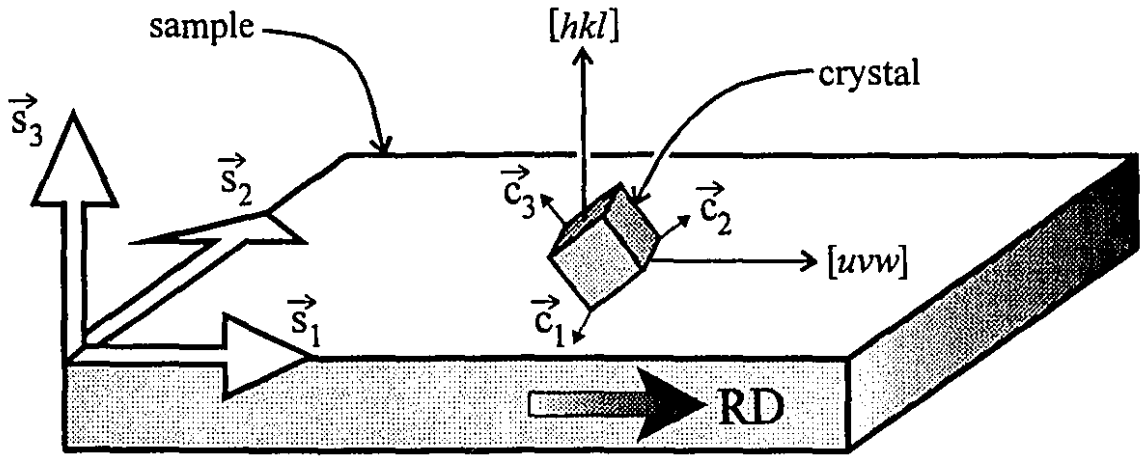

Fig. II.2 The sample coordinate system K_A and the crystal coordinate system K_B.

II.2 Euler Space

A crystallite orientation is often described by means of three Euler angles φ_1, Φ, φ_2 [3]. Figure II.3 illustrates the way these are defined. The sample system ($\vec{s}_1$ $\vec{s}_2$ $\vec{s}_3$) is first rotated by an angle φ_1 around $\vec{s}_3$. The rotated axes are in turn rotated by an

angle Φ around the new position of the $\vec{s}_1$ axis. By now, $\vec{s}_3$ has already become $\vec{c}_3$, around which a third rotation by an angle φ_2 is carried out. These three successive rotations bring the sample reference system into coincidence with the crystal reference system.

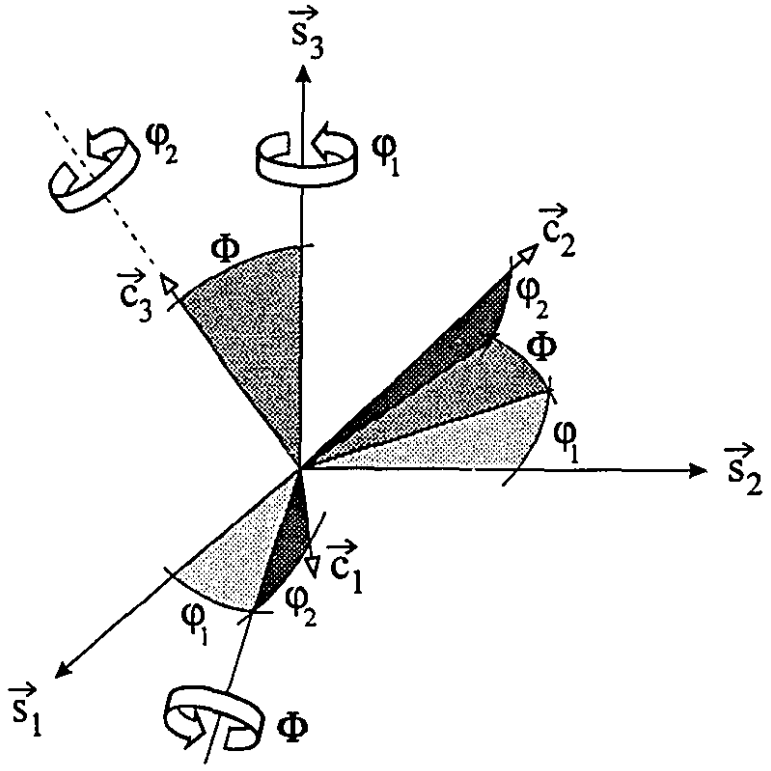

Figure II.3 The Euler angles φ_1, Φ, φ_2 that relate the crystal system $(\vec{c}_1\ \vec{c}_2\ \vec{c}_3)$ to the sample system $(\vec{s}_1\ \vec{s}_2\ \vec{s}_3)$.

In matrix representation, these three rotations may be expressed as:

$$g_{\varphi_1}^{\vec{s}_3} = \begin{bmatrix} \cos\varphi_1 & \sin\varphi_1 & 0 \\ -\sin\varphi_1 & \cos\varphi_1 & 0 \\ 0 & 0 & 1 \end{bmatrix} \qquad \text{(II.7)}$$

$$g_{\Phi}^{\bar{s}_1} = \begin{bmatrix} 1 & 0 & 0 \\ 0 & \cos\Phi & \sin\Phi \\ 0 & -\sin\Phi & \cos\Phi \end{bmatrix} \tag{II.8}$$

$$g_{\varphi_2}^{\bar{s}_3} = \begin{bmatrix} \cos\varphi_2 & \sin\varphi_2 & 0 \\ -\sin\varphi_2 & \cos\varphi_2 & 0 \\ 0 & 0 & 1 \end{bmatrix} \tag{II.9}$$

The following matrix, which represents the orientation of a crystallite in terms of Euler angles, is obtained by matrix multiplication:

$$g(\varphi_1, \Phi, \varphi_2) =$$

$$\begin{bmatrix} \cos\varphi_1\cos\varphi_2 - \sin\varphi_1\sin\varphi_2\cos\Phi & \sin\varphi_1\cos\varphi_2 + \cos\varphi_1\sin\varphi_2\cos\Phi & \sin\varphi_2\sin\Phi \\ -\cos\varphi_1\sin\varphi_2 - \sin\varphi_1\cos\varphi_2\cos\Phi & -\sin\varphi_1\sin\varphi_2 + \cos\varphi_1\cos\varphi_2\cos\Phi & \cos\varphi_2\sin\Phi \\ \sin\varphi_1\sin\Phi & -\cos\varphi_1\sin\Phi & \cos\Phi \end{bmatrix}$$

(II.10)

All possible orientations can be obtained within the following ranges of the Euler angles:

$$0 \le \varphi_1 \le 2\pi, \qquad 0 \le \Phi \le \pi, \qquad 0 \le \varphi_2 \le 2\pi. \tag{II.11}$$

This is the so-called asymmetric unit; it can be further divided into the subspaces H' and H°, whose ranges are defined as follows:

$$\text{for H',} \qquad 0 \le \varphi_1 \le 2\pi, \qquad 0 \le \Phi \le \pi/2, \qquad 0 \le \varphi_2 \le \pi/2, \tag{II.12}$$

and for H°, all three Euler angles have values between 0° and 90°, inclusive.

The three Euler angles are often employed as cartesian coordinates in a three-dimensional space, called the orientation or Euler space. In general, each crystal

orientation is represented by a point in Euler space, and each point in Euler space represents a crystal orientation. This is the space in which the orientation distribution function f(g) is presented. The totality of all crystals in the material is represented by a cloud of points, from which a continuous distribution function can be constructed. Figure II.4 illustrates these representations [4]. Moreover, instead of a three-dimensional picture of Euler space, it is customary to represent a texture by means of a series of two-dimensional sections, with either φ_1 or φ_2 constant.

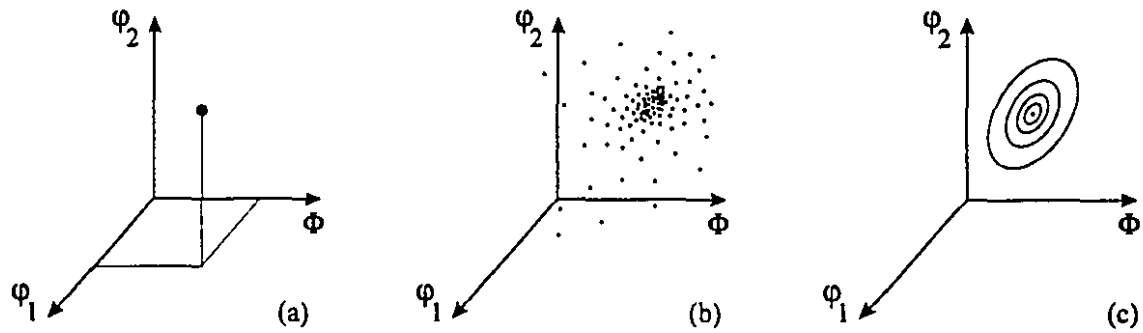

Figure II.4 Representation of the Euler angles by cartesian coordinates for (a) one crystallite, (b) all crystallites of the sample and (c) equidensity lines of the orientation distribution [4].

Unfortunately, Euler space is a distorted space. For instance, in the $\Phi=0°$ plane, a peculiar degeneracy occurs. While, in general, an orientation is represented in Euler space by a point, in the case of $\Phi=0°$, it is represented by a line. This follows from the definition of the Euler angles in equation II.10, which simplifies to the following for $\Phi=0°$:

$$g(\varphi_1,\Phi,\varphi_2)_{\Phi=0°} = \begin{bmatrix} \cos(\varphi_1+\varphi_2) & \sin(\varphi_1+\varphi_2) & 0 \\ -\sin(\varphi_1+\varphi_2) & \cos(\varphi_1+\varphi_2) & 0 \\ 0 & 0 & 1 \end{bmatrix} \qquad \text{(II.13)}$$

Hence all points in the $\Phi=0°$ plane with the same value of $\varphi_1 + \varphi_2$ represent one and the same orientation.

When symmetry is taken into consideration, it is possible to work in one of the subspaces, for instance H° in the case of deformed or recrystallized cubic metals. However, even within this reduced range, each crystallite has at least 3 equivalent Euler angle representations due to a three-fold axis in the symmetry of the crystal [5].

II.3 Pole Figure Measurement and Inversion

Experimental texture data are usually obtained in the form of pole figures. The most frequently used method of pole figure measurement is by x-ray diffraction [6]. Using monochromatic radiation, the deflection angle $2\Theta_{hkl}$ of the beam reflected by the (*hkl*) lattice planes is defined, according to Bragg's law, by the following expression:

$$n \cdot \lambda = 2 \cdot d_{hkl} \cdot \sin \Theta_{hkl} \qquad \text{(II.14)}$$

where n is an integer, λ is the wavelength of the radiation, and d_{hkl} is the interplanar distance. A second necessary condition is the "mirror condition", which states that the normal direction of the reflecting lattice plane must coincide with the bisectrix **k** of the incident and reflected beams. This is shown schematically in Figure II.5:

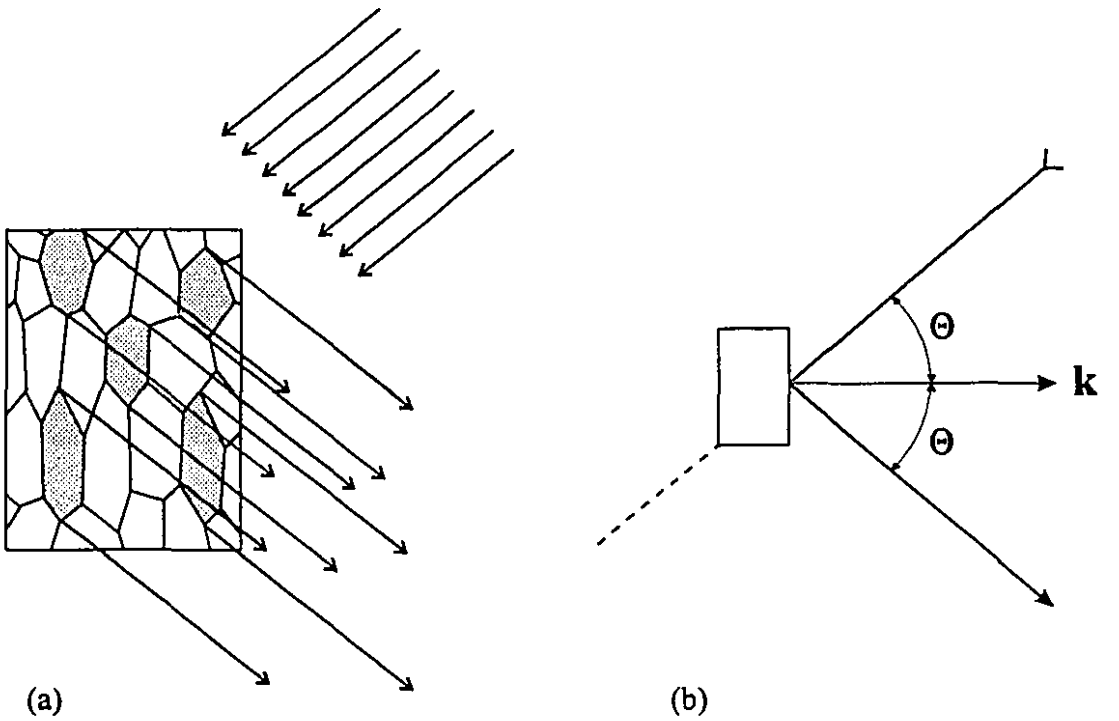

Figure II.5 The principles of polycrystal diffraction: (a) the incident beam is reflected in the appropriately oriented crystals; (b) the geometry of reflection [7].

A detector measures the intensity of the reflected beam; this is proportional to the total volume of the crystallites in the sample which fulfill the above two conditions. This can be expressed as the following volume fraction:

$$\frac{dV}{V} = \frac{1}{4\pi} \cdot P_{hkl}(y) \cdot dy \quad ; \quad y = \{\alpha, \beta\}, \quad dy = \sin\alpha \cdot d\alpha \cdot d\beta \qquad (II.15)$$

Here the normal direction to the reflecting lattice plane (*hkl*) is parallel to a specific sample direction *y* which, in turn, is parallel to the bisectrix direction **k**. The specimen directions *y* can then be sampled by rotating it through angles α and β. The distribution function $P_{hkl}(y)$ of [*hkl*]-normal directions obtained in this way is called the (*hkl*)-pole figure.

For presentation, the pole figure is normalized, and the pole densities are expressed as multiples of the random density:

$$P_{hkl}(y)_{\text{random}} \equiv 1 \qquad \text{(II.16)}$$

and therefore,

$$\int P_{hkl}(y)\, dy = 4\pi \qquad \text{(II.17)}$$

The above definition of the pole figure (Equation II.15) is based on an *individual crystal direction* [*hkl*] and not on a set of symmetrically equivalent directions, <*hkl*>. Consequently, experimental pole figures are superposed pole figures corresponding to both the directions [*hkl*] and $[\bar{h}\,\bar{k}\,\bar{l}]$ (i.e. it includes reflections from 'positive' and 'negative' planes).

The relation between pole figures and the orientation distribution function f(g) is the following: the pole density at a point *y* results from all the crystals whose [*hkl*] directions coincide with the sample direction *y*, independently of any rotations about this direction, since such a rotation does not change the position of the reflecting lattice plane. The pole density at *y* is therefore an integral of the orientation distribution function f(g) taken over the path in Euler space over which the condition *hkl* || *y* is fulfilled:

$$P_{hkl}(y) = \frac{1}{2\pi} \int_{hkl \parallel y} f(g) \cdot d\chi \; ; \quad y = \{\alpha, \beta\}, \; g = \{\varphi_1, \Phi, \varphi_2\} \qquad \text{(II.18)}$$

where χ describes a rotation of the crystal about the common *hkl*, i.e. *y* direction. This equation has been called the *fundamental relation of texture analysis*.

The pole figure is thus a two-dimensional orientation distribution function. As a result, in general, the ODF f(g) cannot be determined from a single pole figure. However, by combining several different pole figures, which are also integrals over the ODF but along different paths, the missing information can be obtained.

The solution to equation II.18 is called *pole figure inversion*, which allows the three-dimensional function to be constructed from several of its two-dimensional projections. The problem of pole figure inversion has a unique solution only if an infinite set of pole figures is available. If the texture is not too sharp, then the calculation resulting from a finite number of pole figures is nearly unique. Four different methods have been proposed for the inversion of pole figures:

1. the discretization method [8, 9],
2. the series expansion method [10, 11],
3. the probabilistic method [12, 13], and
4. the integral transformation method [14].

The first three methods have been used for numerical calculations of f(g); the fourth method provides the most straightforward solution to the problem, but has not yet been applied.

The series expansion method, also called the harmonic method, was proposed independently by Roe [10] and by Bunge [11] in 1965. This is the method employed in this work, and is presented in the next section.

II.4 The Harmonic Method

In this method, an analytical solution to Equation II.18 is found by using certain specific distribution functions, the generalized harmonic functions.

Both the pole figures and the unknown texture function are developed into the appropriate series,

$$P_{hkl}(\alpha,\beta)=\sum_{\lambda=0}^{L}\sum_{\nu=1}^{N(\lambda)}F_{\lambda}^{\nu}(hkl)\cdot K_{\lambda}^{\nu}(\alpha,\beta) \qquad \text{(II.19)}$$

$$f(\varphi_1,\Phi,\varphi_2)=\sum_{\lambda=0}^{L}\sum_{\mu=1}^{M(\lambda)}\sum_{\nu=1}^{N(\lambda)}C_{\lambda}^{\mu\nu}\cdot T_{\lambda}^{\mu\nu}(\varphi_1,\Phi,\varphi_2) \qquad \text{(II.20)}$$

In this way, Equation II.18 can be transformed into a system of linear equations between the corresponding coefficients,

$$F_{\lambda}^{\nu}(hkl)=\frac{4\pi}{2\lambda+1}\sum_{\mu=1}^{M(\lambda)}C_{\lambda}^{\mu\nu}\cdot K_{\lambda}^{\mu}(\Theta_{hkl},\gamma_{hkl}) \qquad \text{(II.21)}$$

where Θ_{hkl} and γ_{hkl} are the polar coordinates of the normal **k** to the reflecting lattice plane (hkl).

Finally, the coefficients $F_{\lambda}^{\nu}(hkl)$ are obtained from the measured pole figure values, using the inversion of Equation II.19,

$$F_{\lambda}^{\nu}(hkl) = \oint P_{hkl}(\alpha,\beta) \cdot K_{\lambda}^{*\nu}(\alpha,\beta) \cdot \sin\alpha \cdot d\alpha \cdot d\beta \qquad \text{(II.22)}$$

A detailed description of this method can be found elsewhere [3]. The method has been implemented in some modern texture measurement equipment, which automatically calculates the orientation distribution function after measurement of a series of pole figures. This is followed by a plotting of the results. Such an apparatus was used in this work.

Chapter III

TRANSFORMATION TEXTURES

There are several transformations that are crystallographic in nature, for instance, twinning and the shear transformation from austenite to martensite. In such cases, if a texture has already developed in the initial material, the parent texture can be inherited after transformation, resulting in a product texture. Under such conditions, the crystallographic relationship defining the transformation can be used to relate the parent and product textures. This is of particular importance in the case of rolled steels, for which a large amount of processing is carried out within the austenite region. The phenomena occurring at this stage will influence the properties of the material after it has transformed and cooled down to room temperature. They will also affect the properties following any further production stages, such as annealing and cold rolling. However, the direct study of the development of texture within the austenite range is hindered because of the high temperatures at which this occurs. This problem can be overcome to some extent by determining the final (product) texture experimentally and then *untransforming* it to its parent components, by following the crystallographic

relationships governing the transformation. It is then possible to establish the parent processing parameters required to produce the desired final texture.

A particular parent orientation does not transform into a single component but rather into a fixed number of product orientations, called variants. Furthermore, the variants often appear with different probabilities. Variant selection is the result of the presence of physical fields, such as stress or temperature gradients, and must be taken into account when studying transformation textures.

The most important relationships describing the transformation of a cubic parent orientation into its cubic product components are reviewed here. The problem of variant selection is also discussed.

III.1 Orientation Relationships between Parent and Product Components

The crystallographic link between the parent and product components has been described in different forms. Frequently, the parallelism between the planes and directions which coincide before and after transformation is used. For cubic lattices, this can be represented either as parallelism between two sets of planes and two sets of directions (generally contained in the planes employed),

$$\{h_1k_1l_1\} \,||\, \{h_2k_2l_2\}; \qquad <u_1v_1w_1> \,||\, <u_2v_2w_2> \quad \text{(III.1)}$$

or as parallelism between two sets of planes and a further two sets of planes,

$$\{h_1k_1l_1\} \,||\, \{h_2k_2l_2\}; \qquad \{h'_1k'_1l'_1\} \,||\, \{h'_2k'_2l'_2\}; \quad \text{(III.2)}$$

where the subscripts 1 and 2 refer to the parent and product structures, respectively.

A second description employs the invariant axis. For any specific orientation relationship there exists an axis that does not change during transformation. The transformation can then be described as a rotation about this axis, defined as g ($\hat{d}$. ω). Furthermore, the rotation can be expressed in terms of three Euler angles, g (φ_1, Φ, φ_2).

III.2 The Austenite to Martensite Transformation

In steels, the transformation of austenite to martensite takes place by a shear mechanism without the formation and growth of nuclei. This distinguishes it from the transformation to polygonal ferrite or pearlite, which occurs by means of a diffusion mechanism. Thus, even though the crystal structure changes from face-centered cubic in the austenite to tetragonal in the martensite, the atoms undergo only small local displacements from their average positions in the crystal lattice.

The most important mechanisms which describe these atomic movements are those developed by Bain [15], Kurdjumov and Sachs [16], Nishiyama [17, 18] and Wassermann [19], and Greninger and Troiano [20, 21]. They consider factors such as the orientation of the product crystal with respect to the lattice of the original phase, and the habit plane or plane in the matrix on which the martensite crystals form. All four are described in the following sections.

III.2.1 The Bain Mechanism

This is the simplest mechanism describing the austenite to martensite transformation [15]. The face-centered cubic structure of the austenite can also be considered as a body-centered tetragonal lattice, with an axial ratio c:a of $\sqrt{2}$:1. As shown in Figure III.1, there are three directions along which the tetragonal axis can be accommodated within the original fcc structure. In this figure, only the iron atoms are depicted. The carbon atoms occupy the octahedral sites common to both structures and do not move. The transformation is then interpreted as a change in the axial ratio c:a of the superimposed tetragonal cell to a value somewhere between 1.00 and 1.08, depending on the carbon content of the steel [22], resulting in the tetragonal martensite α' lattice.

In the Bain mechanism, the transformation can be expressed alternatively as a 45° rotation about a $<100>$ axis common to each crystal. The lattice correspondence relation is therefore:

$$\{001\}_\gamma \parallel \{001\}_\alpha ; \qquad \langle 100\rangle_\gamma \parallel \langle 110\rangle_\alpha \tag{III.3}$$

There are three alternatives for the plane parallelism condition, and in each case only one alternative can simultaneously satisfy the direction parallelism requirement. This gives three variants for each parent orientation, according to this mechanism.

In terms of Euler angles, the Bain mechanism can be expressed as the rotation:

$$g = (45°, 0°, 0°). \tag{III.4}$$

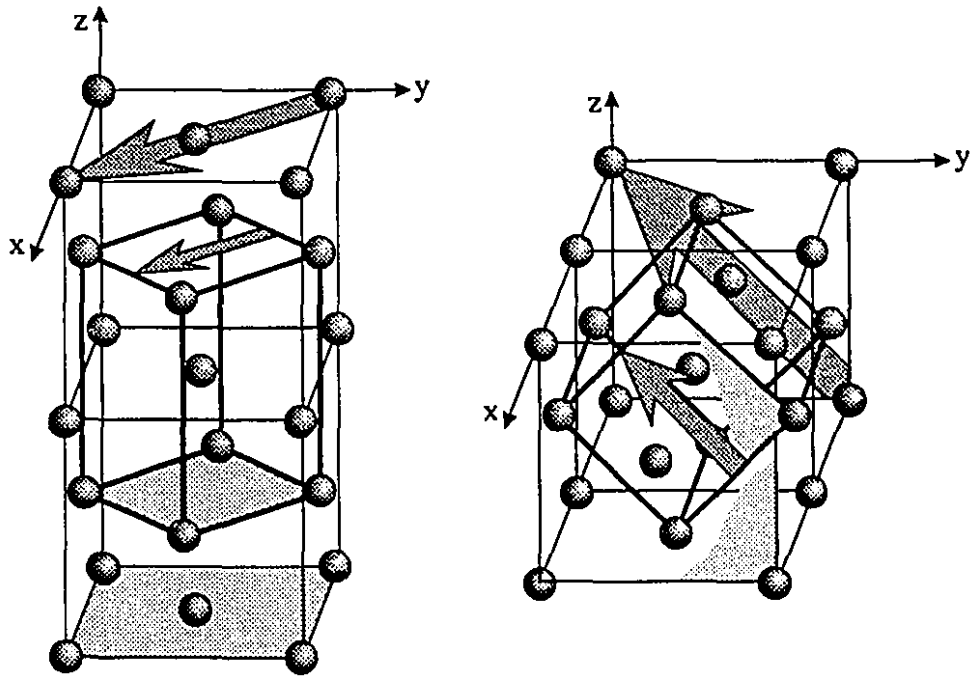

(a) $(001)_\gamma \parallel (001)_\alpha$
$[100]_\gamma \parallel [1\bar{1}0]_\alpha$

(b) $(001)_\gamma \parallel (100)_\alpha$
$[100]_\gamma \parallel [0\bar{1}1]_\alpha$

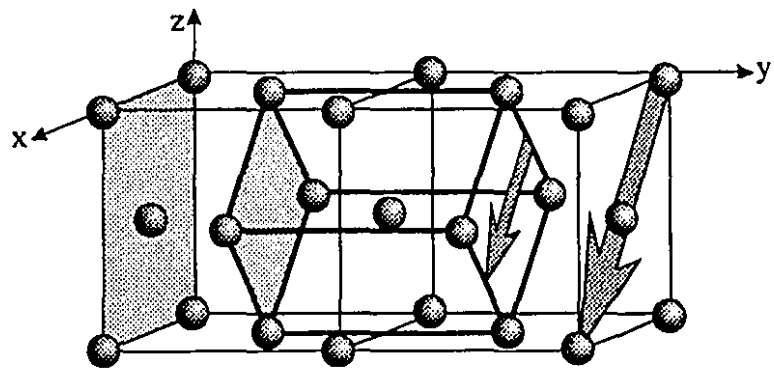

(c) $(001)_\gamma \parallel (010)_\alpha$
$[100]_\gamma \parallel [10\bar{1}]_\alpha$

Figure III.1 The Bain mechanism for the transformation of austenite to martensite. (a), (b) and (c) represent the three directions along which the tetragonal axis can be accommodated within the original fcc structure. Only the iron atoms are shown.

III.2.2 The Kurdjumov-Sachs Relation

Working with a cylindrical rod of a 1.4% C steel, which formed a single crystal after being austenitized, Kurdjumov and Sachs found that martensite crystals formed within the austenite matrix on quenching. Then, the orientations of the martensite crystals with respect to the lattice of the retained austenite were determined by means of x-ray diffraction. Finally, the samples were tempered and the orientations of the cubic ferrite were obtained.

They found that the closest-packed planes of the tetragonal martensite, (011), lay almost parallel to the close-packed (111) planes of the austenite matrix, with a [011] martensite lattice direction lying almost parallel to a [111] direction of the austenite. On the tempered ferrite, the same relations held, with minor deviations. Table III.1 shows the relationships for martensite and ferrite with respect to the parent austenite.

Table III.1 K-S Relationships Between Austenite and Martensite/Ferrite

Tetragonal Martensite α' with Respect to Austenite γ	α-Iron with Respect to Retained Austenite γ
$(011)_{\alpha'}$ plane parallel to $(111)_{\gamma}$	$(011)_{\alpha}$ plane parallel to $(111)_{\gamma}$
$[1\bar{1}1]_{\alpha'}$ direction parallel to $[10\bar{1}]_{\gamma}$	$[1\bar{1}1]_{\alpha}$ direction parallel to $[10\bar{1}]_{\gamma}$
$(001)_{\alpha'}$ 9° from $\{100\}_{\gamma}$	$(001)_{\alpha}$ 10.5° from $\{100\}_{\gamma}$
$(100)_{\alpha'}$ 4.5° from $\{110\}_{\gamma}$	$(100)_{\alpha}$ 5.5° from $\{110\}_{\gamma}$
$(010)_{\alpha'}$ 8° from $\{110\}_{\gamma}$	$(010)_{\alpha}$ 10° from $\{110\}_{\gamma}$

Kurdjumov and Sachs described the transformation of austenite into either α' martensite or α-iron as a simple shearing of the austenite lattice. Only small atomic movements and minor dimensional readjustments are necessary to allow for the parameter changes that take place in such a transformation.

The transformation mechanism can be visualized by considering certain planes and directions in the lattices of the austenite, martensite and ferrite, as shown in Figure III.2. First, in Figure III.2(a), the fcc austenite is referred to a new set of axes where the close-packed (111) plane, defined by the directions $[10\bar{1}]$ and $[\bar{1}10]$, is chosen as the base of the cell. The third edge is defined by the cube direction [111] normal to the base. This new unit may then be considered as trigonal, with three iron atoms in the cell having the coordinates $000, \frac{2}{3}\frac{1}{3}\frac{1}{3}, \frac{1}{3}\frac{2}{3}\frac{2}{3}$, due to the three-fold symmetry of the $[111]_\gamma$ direction. Consider now the bcc α-ferrite phase in Figure III.2(c). It can be described as a monoclinic unit with the (011) close-packed plane as the base of the true body-centered cubic cell, with edges defined by the cube directions $[1\bar{1}1]$ and $[11\bar{1}]$. Then, the third axis defining this monoclinic cell corresponds to the cubic lattice direction [011], the normal to the (011) plane. Finally, in Figure III.2(b), the tetragonal martensite structure is regarded as a new triclinic cell with an axial ratio c/a = 1.06, the planes and directions being the same as in the previous case and with only slight changes in the angular relationships and cell dimensions. Then, by projecting the iron atoms in the three unit cells onto their respective basal planes, the Kurdjumov-Sachs mechanism can be described in terms of the atomic processes that occur. This is shown in Figure III.3, where the open and shaded circles correspond to the various height levels of the iron atoms in the structures. The positions of the interstitial carbon atoms are not shown.

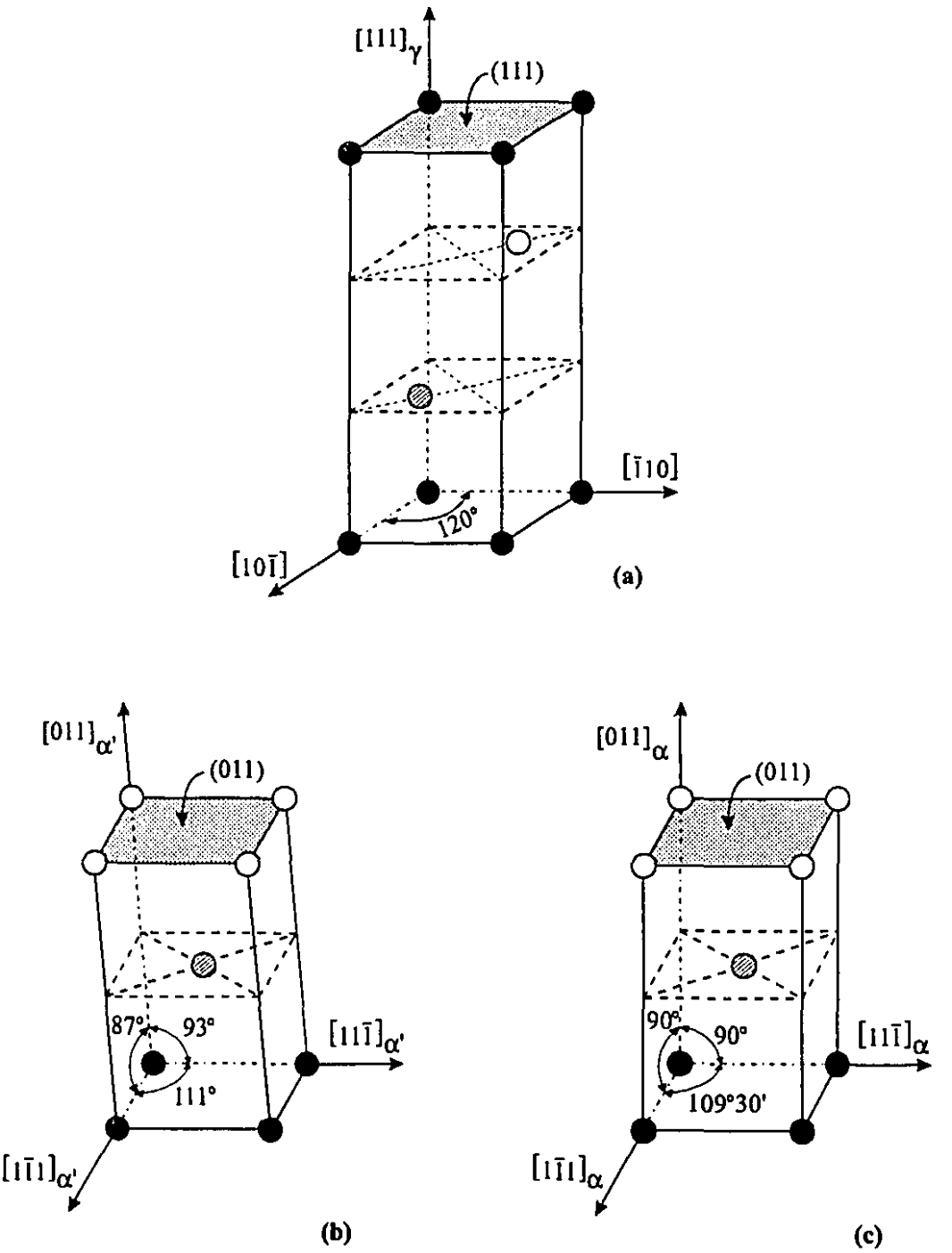

Figure III.2 The crystal lattices of (a) austenite, (b) martensite and (c) ferrite, referred to a trigonal, triclinic and monoclinic cell, respectively [23].

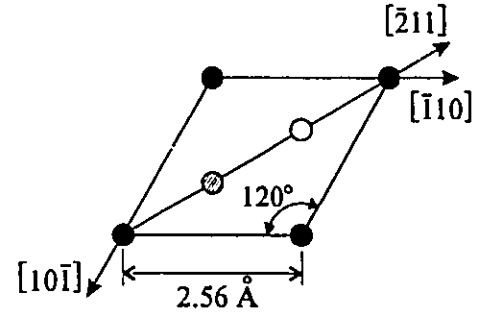

(a)

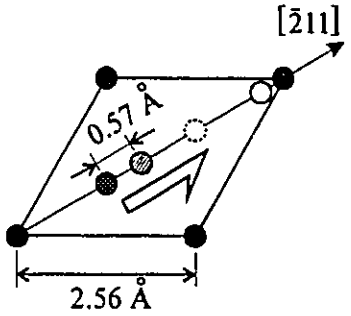

(b)

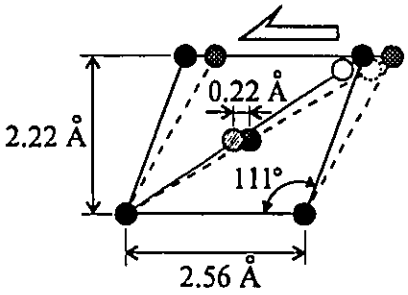

(c)

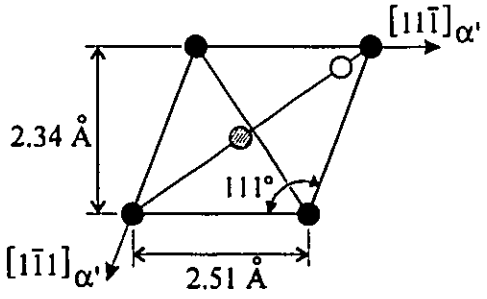

(d)

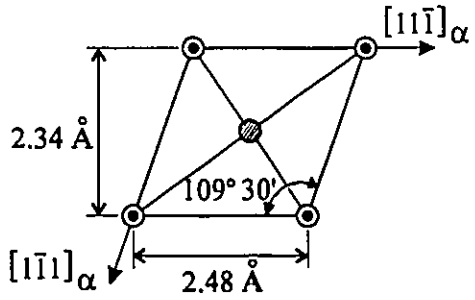

(e)

Figure III.3 The atomic processes involved in the Kurdjumov-Sachs mechanism [23]:

(a) the initial austenite structure,

(b) shearing the $(111)_\gamma$ planes,

(c) second shear along $[\bar{1}10]_\gamma$,

(d,e) final minor length changes.

Figure III.3 (a) represents the projection of the original austenite lattice. The first step in the transformation is the shearing of the close-packed $(111)_\gamma$ planes over each other along the $[\bar{2}11]_\gamma$ direction, as indicated in (b). Then a second shear applied along the $[\bar{1}10]_\gamma$ axis reduces the basal angle from 120° to 111°, as depicted in (c). Finally, some small length changes are necessary to produce the martensite cell, as given in (d). In this way, the (111) planes and [111] directions in the austenite are converted into (011) planes and [011] directions in the martensite, respectively. In order to produce bcc ferrite, as represented in Figure III.3 (e), the first shear must be large enough to move the atom in the second austenite layer at $\left(\frac{2}{3}\frac{1}{3}\frac{1}{3}\right)$ to the centre of the base, and the second shear must reduce the base angle to 109°30'.

Summarizing, the Kurdjumov-Sachs relationship is commonly expressed as the following parallelism condition:

$$(111)_\gamma \,||\, (110)_\alpha \,; \qquad [1\bar{1}0]_\gamma \,||\, [1\bar{1}1]_\alpha \qquad \text{(III.5)}$$

or, alternatively, as:

$$(111)_\gamma \,||\, (110)_\alpha \,; \qquad [11\bar{2}]_\gamma \,||\, [1\bar{1}2]_\alpha \qquad \text{(III.6)}$$

In terms of invariant axes, the Kurdjumov-Sachs relationship can be described as a 90° rotation about <112> axes common to each crystal. There are 12 equivalent <112> axes and two senses of rotation for each, resulting in 24 variants for this orientation relationship.

When expressed as a rotation in terms of Euler angles, this relation is given as:

$$g = (84.23°, 48.19°, 84.23°) \qquad \text{(III.7)}$$

III.2.3 The Nishiyama-Wassermann Transformation

This relationship was proposed independently by Nishiyama [17, 18] and by Wassermann [19]. It describes the diffusionless martensitic transformation observed in an iron alloy containing up to about 30% Ni. After quenching, an austenitic alloy with less than 33% Ni partly transforms into the bcc α form; tetragonality is not possible due to the absence of interstitial carbon.

This transformation can be described by the following mechanisms:

1. A simple shear of 19°28' in the $[\bar{2}11]_\gamma$ direction of the close-packed $(111)_\gamma$ plane, as in the Kurdjumov-Sachs mechanism. This ensures that the orientations of the planes of greatest atomic density are the same for the initial and final structures.
2. An expansion of 13.3% along the $[01\bar{1}]_\gamma$ direction, a contraction of 7.5% along the $[\bar{2}11]_\gamma$, and a contraction of 1.9% normal to these two directions.

In terms of parallel planes and directions, the Nishiyama-Wassermann relation is expressed as follows:

$$(111)_\gamma \,||\, (110)_\alpha \,; \qquad [1\bar{1}0]_\gamma \,||\, [001]_\alpha \tag{III.8}$$

or equivalently,

$$(111)_\gamma \,||\, (110)_\alpha \,; \qquad [11\bar{2}]_\gamma \,||\, [1\bar{1}0]_\alpha \tag{III.9}$$

From energy considerations, the Nishiyama-Wassermann relationship is claimed to be more plausible than the others, because it better preserves the packing density in corresponding planes in the parent and product structures. For instance, from the second parallelism condition, the relation $[1\,1\,\bar{2}]_\gamma \;||\; [1\,\bar{1}\,0]_\alpha$ implies the planar relationship $(0\,1\,\bar{1})_\gamma \;||\; (100)_\alpha$; these planes are second in order of reticular density. By contrast, the K-S condition given as equation III.5 is equivalent to the planar relationship $(1\,\bar{3}\,1)_\gamma \;||\; (2\,1\,\bar{1})_\alpha$; these are planes which, in their respective lattices, stand third in order of greatest reticular density.

According to the planar condition $(111)_\gamma \;||\; (110)_\alpha$, there are four alternatives for the austenite and six for the bcc phase; similarly, according to the direction condition $[1\,\bar{1}\,0]_\gamma \;||\; [001]_\alpha$, three and two alternatives are available, respectively, for the parent and product phases. The Nishiyama-Wassermann relation therefore results in 12 variants after transformation.

This relationship does not have a rotation axis with rational indices. However, the transformation can be expressed analytically as a 95.27° rotation around the axis $[h,k,l]=\left[\left(-1+\sqrt{2}+\sqrt{3}\right),\left(1+\sqrt{2}+\sqrt{3}\right),\left(\sqrt{2}\right)\right]$.

If expressed as a rotation in terms of Euler angles, the Nishiyama-Wassermann relationship is the following:

$$g = (80.26°, 48.19°, 45°) \qquad \text{(III.10)}$$

III.2.4 The Mechanism of Greninger and Troiano

Greninger and Troiano found [20] that the needle-shaped martensite crystals in a 0.35%C steel aggregate to form a plate-like array, which indeed delineates the (111) planes of austenite, as predicted by the mechanisms of both Kurdjumov-Sachs and Nishiyama-Wassermann. However, with higher carbon contents the transformation mechanism seems to become much more complex, and in none of the alloy steels they examined did martensite form on a low-index plane of the decomposing austenite. For a steel with 0.8%C and 0.22% Ni [21], they described the transformation as a state intermediate between the predictions of Kurdjumov-Sachs and Nishiyama-Wassermann, with the following relations for the two phases:

$$\langle 110\rangle_\gamma : [11\bar{1}]_\alpha \cong 2.5° \quad \text{and} \quad \langle 112\rangle_\gamma : [10\bar{1}]_\alpha \cong 2° \qquad \text{(III.11)}$$

III.2.5 Comparison of the Bain, Kurdjumov-Sachs and Nishiyama-Wassermann Mechanisms

Several mechanisms have been proposed to describe the transformation of a cubic fcc phase into a cubic bcc one. However, it is difficult to account satisfactorily with a single model for all the observed characteristics of such transformations. Some of the problems encountered may be related to the orientation of the product crystal with respect to the lattice of the parent phase, or to the occasional irrational indices of the habit plane. In practice, the mechanisms proposed by Bain, Kurdjumov-Sachs and Nishiyama-Wassermann have been used with reasonable success. Compared to each other, the differences are minor: to obtain the Kurdjumov-Sachs result from the

orientation predicted by Nishiyama-Wasserman, a further rotation of -5°16' about $[011]_\alpha$ is necessary; this is illustrated in Figure III.4. Furthermore, the Nishiyama-Wassermann mechanism is equivalent to the one proposed by Bain with the addition of a rotation of -9°44' about the $[100]_\alpha$ direction.

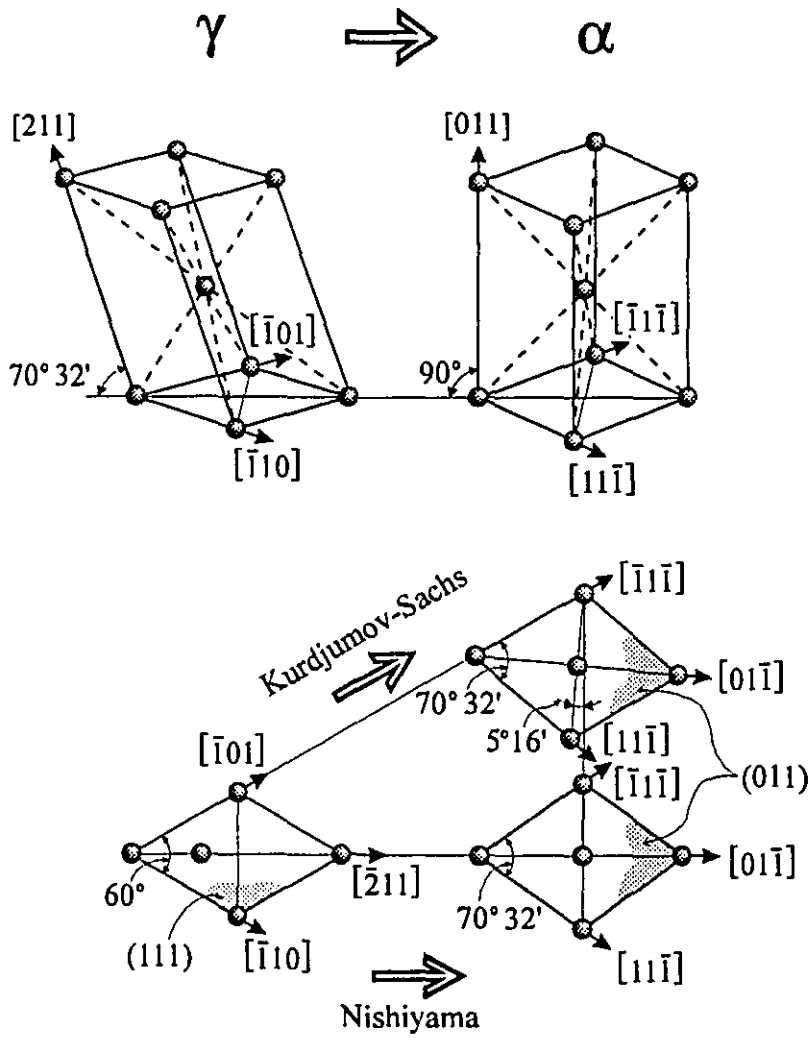

Figure III.4 Comparison of the Kurdjumov-Sachs mechanism with that of Nishiyama-Wassermann [23].

Another way of comparing these three mechanisms is by plotting some of the (100), (110) and (111) poles in a single stereographic projection, for both an austenite crystal of orientation $\{111\}<110>$ and a ferrite crystal of orientation $\{110\}<001>$, as shown in Figure III.5 [3]. The diagrams themselves represent the Nishiyama-Wassermann relationship. From these, two rotations are necessary to produce the Bain relation : a 54.7° rotation of the γ to move the (100) pole to the normal direction, and a 45° rotation of the α to again rotate the (100) pole into the normal direction. Thus, the Bain condition is represented here as $[110]_\gamma \,||\, [100]_\alpha$ (as in Nishiyama-Wassermann) and $(100)_\gamma \,||\, (100)_\alpha$. Combining both rotations with respect to the rolling direction RD leads to the relative variation $\Delta\beta_{RD}$:

$$\Delta\beta_{RD} = (54.7° - 45°) = 9.7° \qquad \text{(III.12)}$$

Similarly, the Kurdjumov-Sachs relationship can be obtained by means of two rotations: one, of 60°, to rotate the (110) pole into the rolling direction, another, of 54.7° in the α to align the (111) pole again with RD. Now, combining these rotations about ND, the relative variation $\Delta\beta_{ND}$ is obtained:

$$\Delta\beta_{ND} = (60° - 54.7°) = 5.3° \qquad \text{(III.13)}$$

The relative distance in Euler space between the Bain and Kurdjumov-Sachs relations is therefore:

$$\Delta\beta_{B\text{-}KS} = \sqrt{(9.7)^2 + (5.3)^2} = 11.1° \qquad \text{(III.14)}$$

These relations are presented schematically in Figure III.6 [3].

Unfortunately, a definite choice between the various relationships is not possible when their respective predictions are being compared with experimental data because the ideal orientations that are measured are never exact.

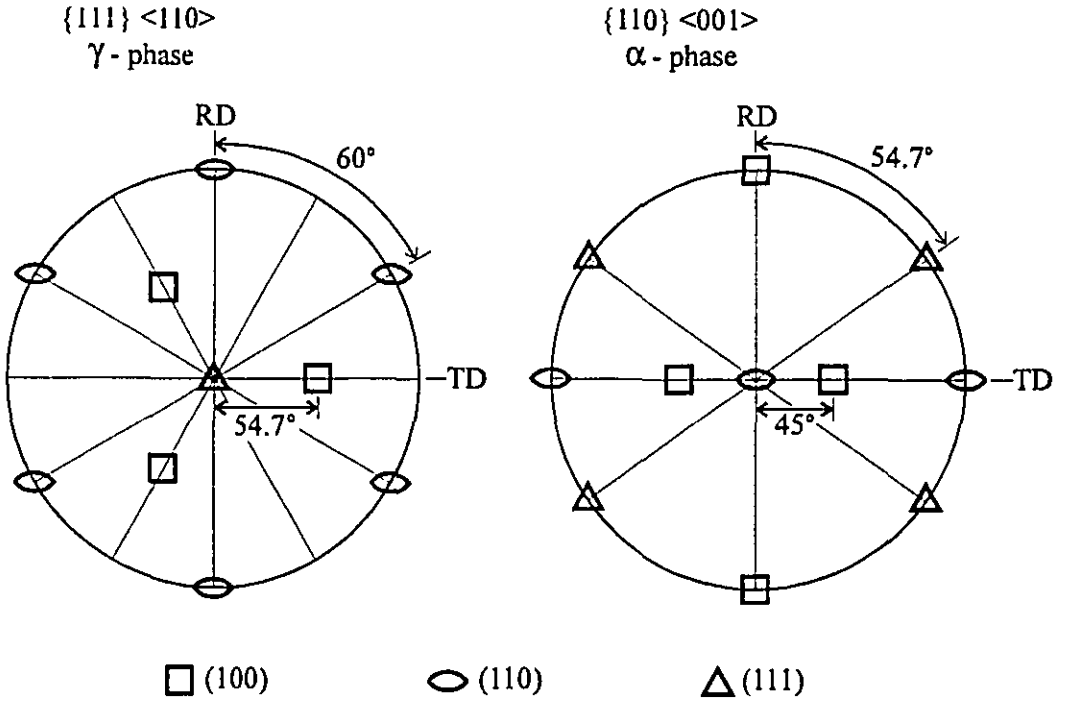

Figure III.5 Illustration of the orientation relations according to Bain, Kurdjumov-Sachs and Nishiyama-Wassermann [3].

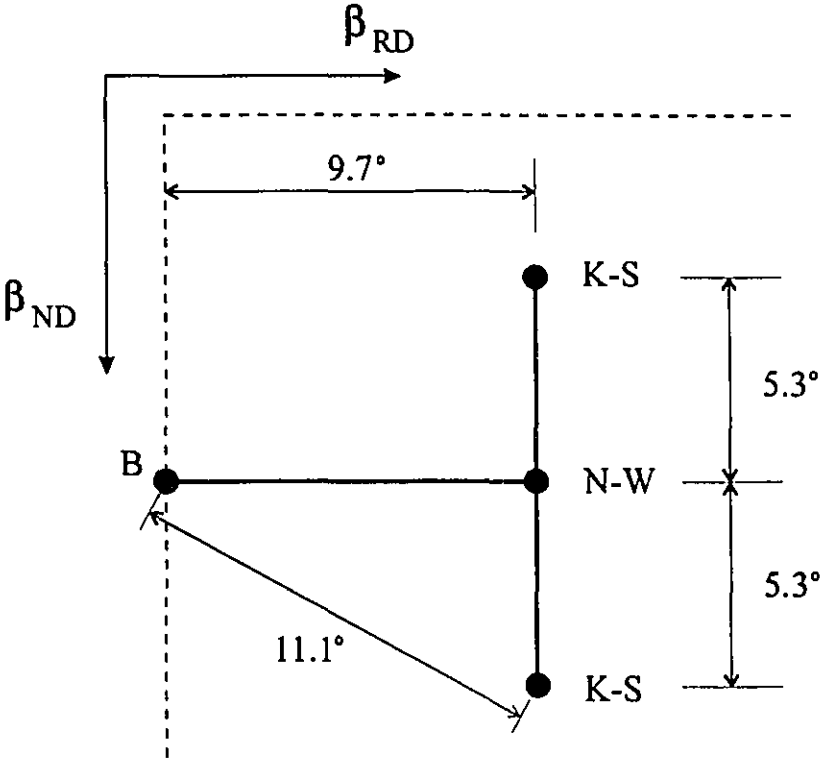

Figure III.6 Relative positions of the Bain (B), Kurdjumov-Sachs (KS) and Nishiyama-Wassermann (NW) relations in Euler space [3].

III.3 Variants and Variant Selection

Texture inheritance after phase transformation has been studied both experimentally and by modelling. However, when comparing experimental and predicted transformation textures, it is often the case that the former are sharper than the latter if all the variants are taken into consideration. Under these conditions, the product orientations that are present are nevertheless among those expected from the parent orientations. Thus, a certain degree of variant selection appears to be necessary if the theoretical predictions are to agree with the experimental results. Transformation *without* variant selection seems to be common when the parent material is comparatively strain-free and the transformation does not lead to significant lattice strains [24]. Several examples of texture transformation without variant selection have been reported in the literature [25, 26].

The occurrence of variant selection has been noted in a number of studies, especially when a shear transformation, such as martensite formation, is involved. The characteristics of variant selection depend on the materials, types of transformation and also on the conditions under which the transformation takes place. The prediction of product textures, when variant selection is taken into consideration, requires the incorporation of a weight for each variant. Then, the volume fraction taken up by each of the variants is no longer equal.

Several selection rules have been proposed, the most important ones being the following [27, 28]:

(i) the "shape deformation" (SD) model,

(ii) the "Bokros-Parker" (BP) model,

(iii) the "active slip system" (AS) model,

(iv) the "twinning shear" (TS) model,

(v) the "Bain strain" (BS) model, and

(vi) the "geometrical parameters" (GP) model,

Here the nomenclature for the first five models is the one proposed by Furubayashi et al. [29].

In the SD model, the shear deformation associated with the formation of martensite (observable as an external shape change) was considered as the influential factor in variant selection. However, the analysis of experimental data for steels and iron base alloys has not confirmed the validity of such predictions.

The BP model was proposed after a study of martensite formation in a deformed monocrystal of an Fe30Ni alloy [30]. According to this model, the favoured variants are the ones whose corresponding habit planes are nearly perpendicular to activated glide planes in the austenite. This behaviour was considered to be a consequence of the anisotropic substructure introduced during the deformation. Nevertheless, this model is considered by some authors to be only partially successful for the prediction of variant selection during the martensite transformation.

The third model, labeled "AS", again considers the active slip systems in the austenite, especially those subjected to the largest shear stresses during deformation and before transformation. The variants favoured according to this model are the ones

containing the slip systems with the maximum resolved shear stress during rolling. The textures predicted by this model are weaker than those observed experimentally.

In the "TS" model, the first shear associated with the fcc to bcc transformation is regarded as the deformation effected by the applied stress. Then, the critical atomic movement required to initiate martensite formation is the shear that first takes place along the $\{111\}_\gamma<211>_\gamma$ direction, followed by the second shear necessary to complete the transformation. The frequencies of several martensite variants observed experimentally after such stress induced martensite formation can be predicted with this model.

The "BS" model relates the applied strain during deformation with the Bain strain, characteristic of the martensite transformation. Since the compression axis associated with the Bain strain is parallel to $<100>_\gamma$, when an external compressive stress is applied, the variant that will be favoured is the one with a $[100]_\gamma$ axis parallel to such a stress. Reasonable agreement with experiment has been obtained with this model.

Finally, the "GP" model proposes that the variants selected during martensite formation are those which produce the least deformation in the plane of the sheet. This conclusion was reached after finding that the rolling reduction and residual stresses had no preponderant effect on selection, and that the active glide system rules were also inapplicable. Thus, the dimensional parameters of the sample were themselves considered to induce variant selection, because of the volume increases and shape changes occurring during transformation.

The simulation of transformation textures by methods that take variant selection into consideration involves mechanisms that depend on the material and on the transformation conditions. Because of the large number of parameters involved, a general model has not yet been proposed or accepted.

Chapter IV

HOT ROLLING TEXTURES IN STEELS

IV.1 Thermomechanical Treatment

In the processing of metals, hot deformation is applied not only to attain a desired shape but also to improve the properties of the material. The manufacturing practice which incorporates thermal and mechanical effects is known as thermomechanical processing; in particular, controlled rolling has been employed for about forty years for the production of structural plate steels. In such steels, the aim is the refinement of the microstructure to improve both strength and toughness. This is done, in conventional controlled rolling, by deformation at lower than normal finish rolling temperatures. The resulting mechanical properties are superior to those of normalized steels of the same chemical composition and are obtained less expensively.

The chemical composition of the steel is another important factor affecting the improvement of its final properties. In the late 1950's, it was found that small additions of niobium are effective in increasing the strength of steel, and so it has been used, alone or in combination with vanadium (or titanium), in the production of high

strength steels. The main effect of such microalloying elements is the retardation of austenite recrystallization. Therefore, the ferrite grain size is reduced not only by refinement of the austenite by recrystallization, but also by deforming the austenite below its recrystallization temperature. The latter additional step produces a large increase in the number of ferrite nuclei during the γ to α transformation.

Accelerated cooling after controlled rolling has been successfully applied since the 1980's. This process enables a high strength product to be manufactured in alloys with a leaner alloy content or a lower carbon equivalent. Such treatments are currently employed not only for the production of plate, but also of hot strip, bars and sections.

Rolling is not limited to the austenite region; sometimes, it is continued down into the (γ + α) region (intercritical rolling), or even into the α region (warm rolling). In such cases, additional strengthening is achieved in the ferrite due to the formation of dislocation substructures.

The development of texture is another important factor which influences the strength and toughness, as well as their anisotropy, in steel. When hot rolling is finished in the range of deformed austenite in steels containing molybdenum, niobium or titanium, a fairly strong γ texture is formed, consisting mainly of copper $\{112\}<111>$ and brass $\{110\}<112>$ components. Such texture is inherited by the ferrite, with the $\{332\}<113>$ and $\{311\}<011>$ as the most important orientations. When finishing temperatures in the ($\alpha+\gamma$) two-phase region are employed, the orientations found in the ferrite include $\{332\}<113>$-$\{554\}<225>$ and $\{211\}<011>$-$\{311\}<011>$. Also, the $\{001\}<110>$ component is strongly

developed by deformation of the ferrite. This is described in more detail in the next sections.

IV.2 Development of Hot Rolling Textures

The texture of hot rolled steel has a strong influence on later texture development during cold rolling and annealing in the conventional production of sheets. Cold rolled steel sheet is widely used, in part because of its good formability, whereas the drawability of hot rolled steel sheet is not generally as good. Recently, however, the use of hot rolled sheet has increased due to energy saving considerations and the demand for lower cost products.

Some factors affecting the texture of hot rolled sheets are:

1. chemical composition,
2. the conditions of hot rolling, mainly reduction and finishing temperature,
3. friction between the material and the rolls, i.e., lubrication,
4. subsequent annealing of the hot rolled sheets.

Friction between the material and the rolls is the main cause of strain inhomogeneity through the thickness, and therefore in the texture [31, 32]. Decreasing the friction by means of lubrication is now regarded as one of the methods of improving the deep drawability of hot rolled sheets. Another way of improving the drawability is the application of an annealing treatment after hot rolling, as a means of increasing the strength of the {111} type texture, and reducing the amount of the {100}<001>

component [33, 34]. The first two factors are considered as the most critical, and are reviewed next.

IV.3 Effect of Chemical Composition

The alloying elements in steel have considerable influence on the recrystallization behaviour of austenite. When such recrystallization is retarded due to the presence of precipitates (for instance, Nb(C,N)), the rolling deformation is accumulated before transformation. This results in the formation of a product texture. Niobium, vanadium and titanium have all been used as microalloying elements. Their behaviours in terms of precipitation and grain refinement are different and depend on other factors, such as the level of nitrogen or the thermomechanical process itself [35, 36]; in practice they are used in various combinations to maximize the positive contributions of each.

In niobium microalloyed steels, the main texture components are the $\{332\}<113>_{\alpha}$ and $\{311\}<011>_{\alpha}$ [37], their parent orientations being $\{110\}<112>_{\gamma}$ and $\{112\}<111>_{\gamma}$, respectively. The $\{332\}<113>_{\alpha}$ component was found to be more sensitive to the amount of alloying elements and to the cooling rate after deformation. From the recrystallization behaviour of copper single crystals rolled to a reduction of 95%, the strain energy in $\{112\}<111>_{\gamma}$ grains seems to be greater than in $\{110\}<112>_{\gamma}$ grains [38]; thus, the nucleation of ferrite is expected to occur more frequently in the former. However, the nucleation of ferrite also occurs on the austenite grain boundaries; such nuclei were found to grow more rapidly into neighbouring austenite grains with which no lattice relationship existed [39]. The

growth of such incoherent nuclei can be extensive, for instance, with slow cooling, resulting in a more random texture, and this effect would be more pronounced in $\{110\}<112>_\gamma$ grains, in which little nucleation is found on deformation bands. Thus, to obtain a strong $\{332\}<113>_\alpha$ texture, which is favourable to strength and toughness, the addition of alloying elements (such as Mn, Ni, Cr and Mo) and rapid cooling are desirable, as experimental results have corroborated [40, 41].

Manganese is still used as an economical solid solution strengthener, but at a reduced level. When the content of manganese is increased from 1.28% to 2.48% in a 0.1%C-0.4%Si-0.05%Nb steel, the main texture components are still $\{311\}<011>_\alpha$ and $\{332\}<113>_\alpha$, but the intensity of the latter increases considerably [37]. This increase seems to correspond to a change in the microstructure, from polygonal ferrite-pearlite to fine acicular ferrite. The effect of Ni, Cr and Mo is similar to that of Mn, both in terms of texture and microstructure [37].

Reduced carbon content has been employed as a means of improving a variety of properties, from plate weldability to formability in sheet steels. The most dramatic example can be seen in the development of interstitial-free sheet steels, now a vital material in the automobile industry, where excellent deep drawability and a decrease in thickness are required [42]. The elimination of carbon in solution has been reported to be an essential condition for obtaining high r-value in hot bands [43]. In particular, if virtually no carbon in solution is present during warm rolling (a condition that can only be met in IF steels), a {111} recrystallization texture conductive to deep drawability is formed at the midplane of the sheet, as long as the reduction is greater than 75% [44].

IV.4 Effect of Finish Rolling Temperature

The controlled rolling of steels involves finishing in one of the following temperature ranges:

1. the recrystallized austenite region,
2. the unrecrystallized austenite region,
3. the intercritical ($\gamma+\alpha$) region, or
4. the ferrite region.

In the first case, the transformation texture is quite weak. If the deformation is applied in the unrecrystallized austenite region, a fairly sharp rolling texture develops when sufficient strain has accumulated in the γ, and this texture is later inherited by the ferrite. Such a transformation texture is further sharpened and modified by lowering the finish rolling temperature, so that the transformed α phase is also deformed.

The only systematic study of the development of transformation textures is the one due to Inagaki [37, 45-49]. Figures IV.1 and IV.2 illustrate some of his experimental results [46], obtained on a Nb-V and a Nb-V-free steel, respectively, and finish rolled at various temperatures.

The characteristics of the transformation textures produced by finish rolling in each of the regions mentioned above are described in the sections that follow.

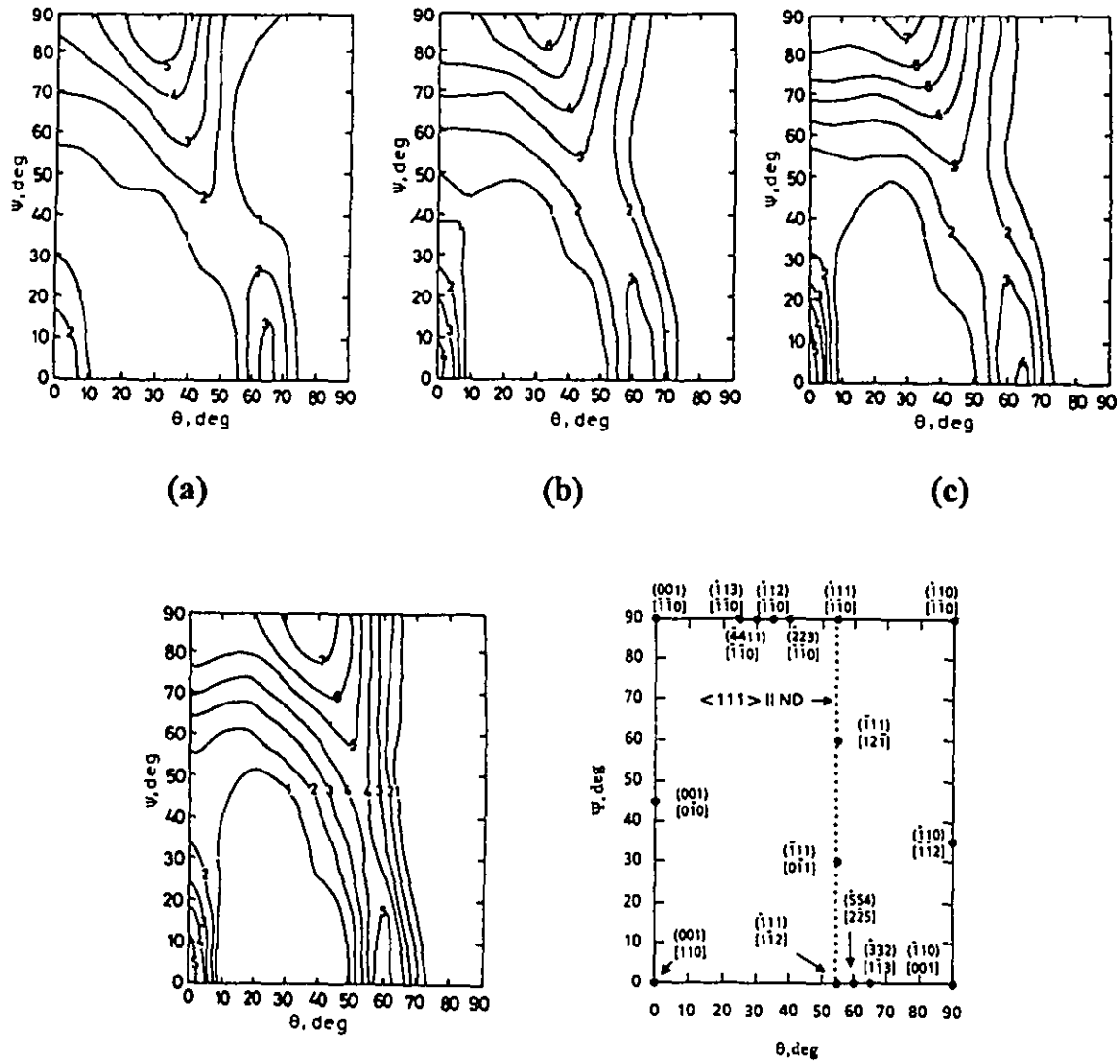

Figure IV.1 Transformation textures in a Nb-V steel finish rolled at (a) 850°C, (b) 800°C, (c) 750°C and (d) 650°C; (e) the key to the most important components (Φ=45° section in Roe notation).

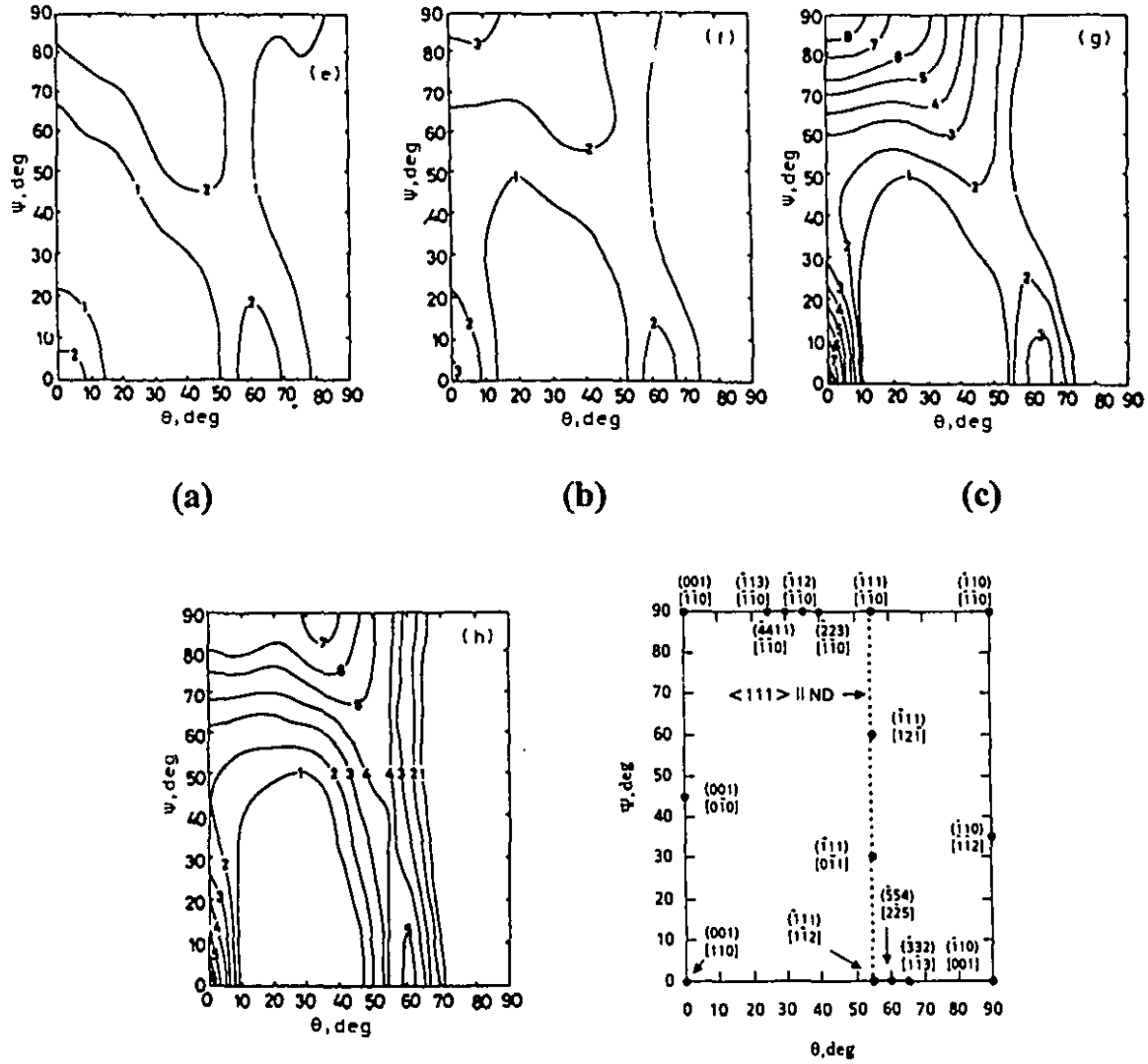

Figure IV.2 Transformation textures in a Nb-V-free steel finish rolled at (a) 840°C, (b) 800°C, (c) 750°C and (d) 650°C; (e) the key to the most important components (Φ=45° section in Roe notation).

IV.4.1 Deformation in the Recrystallized Austenite Region

In this region, grain refinement is accomplished by means of static recrystallization of the austenite [50]. However, finishing above the T_{nr} (the temperature of no-recrystallization) generally results in a weak transformation texture [25, 26, 45, 46, 51-55]. In plain carbon steels, the main components are located along $\{100\}$-$\{111\}<011>$, and have very low intensities; in microalloyed steels, the texture is again quite weak, although more of it is concentrated around the rotated cube, $\{100\}<011>$ [52].

Such differences in the behaviour of plain carbon and microalloyed steels are a consequence of the amount of deformation required to produce recrystallization within the time available; it is greater than at room temperature and its temperature dependence is higher in the microalloyed steel [56], due to strain induced precipitation [57].

IV.4.2 Deformation in the Unrecrystallized Austenite Region

In this region, the surface area of the austenite grain boundaries is increased, and a high density of deformation bands is created in the matrix. Thus, ferrite nucleation occurs in the interiors of the grains as well as at the boundaries, resulting in refinement of the ferrite grain size. Another consequence of the retardation of austenite recrystallization is the development of a strong parent texture, later inherited by the product phase.

The main components of the texture after finish rolling in the unrecrystallized austenite region have been identified as {332}<113> and {113}<110>, as well as the neighboring orientations {554}<225> and {112}<110> or {4 4 11}<110>, respectively [26, 37, 45, 46, 51-53, 58]. The rotated cube, {001}<110>, produced by rolling in the recrystallized region may still be present [51]. In plain carbon steels, a broad peak centred around {332}<113> together with some {001}<110> are evident [46]. In the case of Nb-V steels, lowering the finishing temperature in this range results in the rotation of the {332}<113> towards {554}<225>, and of the {4 4 11}<110> towards {223}<110>, together with an increase in their intensities [46]. When a fixed finishing temperature is employed, smaller reductions result in weaker textures, and the strength of the {332}<113> component decreases compared to that of the {113}<110> orientation [51].

IV.4.3 Deformation in the ($\gamma+\alpha$) Two-Phase Region

It has been found that finish rolling in the ($\gamma+\alpha$) region results not only in further ferrite grain refinement, but also in increases in the yield and ultimate tensile strengths [28, 59-61].

The texture of steels hot rolled in the ($\gamma+\alpha$) region is sharper than that of steels finish rolled in the austenite range [52, 56, 60-64]. The texture begins to develop during deformation of the austenite. The continuation of deformation after the phase transformation starts results in increased austenite pancaking and, if the conditions are suitable, in pancaking and then recrystallization of the ferrite. Thus, at the end of deformation, the texture includes components produced by the $\gamma\rightarrow\alpha$ transformation as

well as others resulting from warm rolling of the ferrite. The composition (and presence of precipitates), temperature, amount of reduction in each rolling pass, and finishing temperature are the most important process parameters. Furthermore, the amount of ferrite formed is significant, and is thus responsible for the distinction between finishing in the upper and lower ($\gamma+\alpha$) ranges [46]. In the first case, since the amount of ferrite formed is relatively small, the contribution to the texture from crystal rotations in the α phase is not particularly significant. In the case of finishing in the lower ($\gamma+\alpha$) range, most of the austenite has already transformed into ferrite; the ferrite grains continue to be deformed in the final rolling passes, thus sharpening the texture inherited from the γ.

The major texture components in steels finish rolled below the Ar_3 but above the Ar_1 have been identified as a partial <110> fibre running from {001}<110> to {111}<110>, and the {111}<*uvw*> fibre [45, 52, 56, 60-63, 65]. In Nb microalloyed steels, the two main components of the texture inherited from deformed austenite are progressively modified with further rolling in the ($\gamma+\alpha$) range, with {332}<113> rotating into {554}<225> and then into {111}<112>, and {113}<110> first changing into {112}<110> and finally into {223}<110> [46]. It has been shown by means of crystal plasticity calculations [66] that further deformation of the ferrite at this stage will gradually convert the {111}<112> component into the {111}<110>. Since these last two orientations both belong to the ND fibre, which is identified with favorable deep drawing characteristics of the steel, it is clear that it is important to enhance the formation of the {332}<113> component during transformation.

In the case of plain carbon steels, a strong {001}<110> component has also been observed; this has been attributed to the low rate of grain rotation in this vicinity during rolling of the α phase [46, 66].

IV.4.4 Deformation in the Ferrite Region

The texture formed by rolling in the lower (γ+α) region is already near the stable end texture for ferrite rolling [46]. Therefore, the texture changes induced by finish rolling in the ferrite range are not expected to be particularly significant. Sometimes, however, this type of rolling is used to further improve the mechanical properties of the steel [61]. This is especially the case for extra low carbon steels [31-34, 67]. These materials can attain high R values after finish rolling in the α region, with or without a suitable annealing treatment after deformation. This is brought about by the strengthening of the {111} orientations. The processing conditions that favour the production of hot or warm rolled steels with high R values are then:

i) finish rolling in the ferrite *no-recrystallization* region,
ii) addition of Ti or Nb to extra low carbon Al-killed steels, to raise the ferrite T_{nr},
iii) minimal content of solute carbon during rolling, attained by precipitating it as TiC or NbC,
iv) good lubrication during hot rolling, to avoid inhomogeneities of the texture through the thickness.

Chapter V

EXPERIMENTAL PROCEDURE

V.1 Materials

Three different commercial materials were studied, a plain carbon, a niobium microalloyed and an interstitial-free (IF) steel. Table V.1 gives their actual compositions. The first two steels were received as 50 mm thick transfer bars, while the third one was originally 25 mm thick. The dimensions of the specimens prepared for rolling as well as the rolling direction (RD) are shown in Figure V.1.

Table V.1 Chemical Compositions of the Steels

STEEL	C	Mn	P	S	Si	V	Nb	Ti	ASA*	N
Plain C	.20	1.24	.011	.004	.186	.004	.002	-	.044	.0065
Nb	.18	1.35	.005	.008	.244	.003	.034	-	.048	.0074
IF	.0038	0.17	.006	.006	.008	-	.019	.018	.043	.0030

* Acid Soluble Aluminium

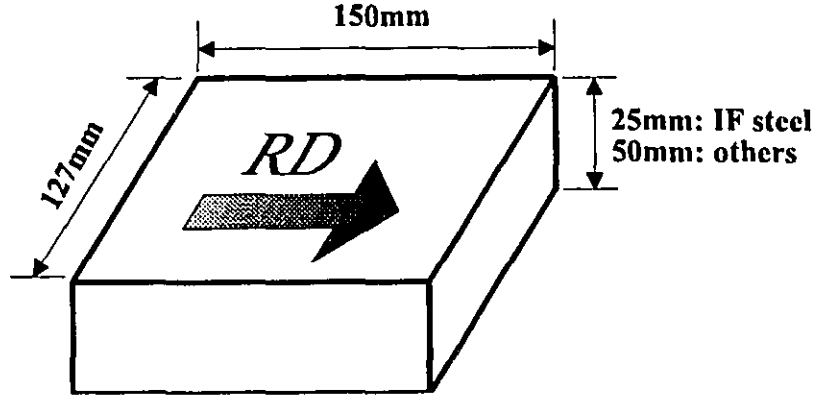

Fig. V.1 Dimensions of the hot rolling specimens.

V.2 Hot Rolling Trials

Hot rolling was carried out without lubrication on the instrumented reversible rolling mill of the Metals Technology Laboratories of EMR-CANMET in Ottawa, Canada. The variables that were controlled are the austenitizing temperature, amount of reduction, and finish rolling temperature.

In the plain carbon and niobium microalloyed steels, the finishing temperatures were defined as 1020°C, 870°C, 770°C, 730°C and 630°C. Such temperatures correspond to the following structural ranges: recrystallized austenite, unrecrystallized austenite, austenite plus ferrite (at the beginning of transformation), austenite plus ferrite (with a larger proportion of ferrite), and single phase ferrite. However, some microstructural differences between the plain carbon and microalloyed steels are expected to be present for the two higher finishing temperatures, since their temperatures of no-recrystallization (T_{nr}) have been estimated to be 900°C and 990°C,

respectively [68]. For these two materials, the specimen temperature during deformation was monitored with optical pyrometers, which were calibrated by inserting thermocouples into holes drilled into the central parts of some samples deformed during preliminary rolling tests. After hot rolling, two different cooling conditions were employed: air cooling for samples of every finishing temperature, and water quenching from the austenite range for specimens with the two higher finish rolling temperatures. The sample identifications, and corresponding processing parameters, are shown in Table V.2 for both the plain carbon and niobium microalloyed steels. The austenitizing temperatures employed were 1250°C and 1150°C, with a soaking time of two hours in both cases. The nominal reductions initially selected were 75% and 90%; however, some variation occurred during the actual tests. The detailed rolling schedules, including the temperature of each deformation step and the equivalent strain accumulated after each rolling pass, are given in Table V.3.

For the IF steel, all samples were austenitized for two hours at either 1250°C or 1150°C, and then hot rolled to 75% or 90% of reduction. Table V.4 shows the sample designations, as well as the nominal deformation conditions that applied. The finishing temperatures employed for the interstitial free steel were 1020°C, 920°C, 870°C, 820°C, 720°C and 620°C. With the two higher temperatures, the material was expected to be fully austenitic during all the stages of deformation. With finishing temperatures of 870°C and 820°C, the last rolling pass was given when the steel had already started the transformation to ferrite. Finally, for the two lower temperatures, the material was expected to be in the ferritic state when the last step of deformation was applied. The temperature was always registered by embedded thermocouples during the actual rolling experiments. Only air cooling after rolling was employed in this set of

Table V.2 Sample Identifications and Corresponding Processing Parameters for the Plain Carbon and Niobium Microalloyed Steels

SAMPLE		T_γ[a]		%RED		T_f[b]					COOLING	
Plain C	Niobium	1250	1150	90	75	1020	870	770	730	630	A[c]	W[d]
C1	N1											
C2	N2											
C3	N3											
C4	N4											
C5	N5											
C6	N6											
C7	N7											
C8	N8											
C9	N9											
C10	N10											
C11	N11											
C12	N12											
C13	N13											
C14	N14											
C15	N15											
C16	N16											
C17	N17											
C18	N18											
C19	N19											
C20	N20											
C21	N21											

[a] Austenitizing temperature, [°C]
[b] Finish rolling temperature, [°C]
[c] Air cooling
[d] Water cooling

Table V.3 Detailed Rolling Schedules for the Plain Carbon and Niobium Microalloyed Steels

No. of Passes	% Reduction	Austenitizing Temperature [°C]	Finishing Temperature [°C]	Temperature at the beginning of each rolling pass [°C]						
				ε_{eq} accumulated after each rolling pass [mm/mm]						
				Pass No.1	Pass No.2	Pass No.3	Pass No.4	Pass No.5	Pass No.6	Pass No.7
3	75	1250	1020	1220	1120	1020				
				0.45	0.98	1.49				
4	90	1150	1020	1150	1120	1090	1020			
				0.54	1.21	2.00	3.24			
4	75	1250	870	1200	1025	930	870			
				0.37	0.75	1.16	1.80			
4	75	1250	770	1200	1050	865	770			
				0.37	0.75	1.19	1.80			
4	75	1250	730	1200	1050	865	730			
				0.37	0.75	1.19	1.80			
5	90	1250	1020	1230	1200	1150	1090	1020		
				0.45	0.98	1.59	2.39	3.24		
5	75	1250	630	1200	1050	930	730	630		
				0.37	0.75	1.16	1.46	1.85		
6	90	1250	870	1200	1025	930	920	900	870	
				0.37	0.75	1.16	1.80	2.59	3.45	
6	90	1150	870	1150	1050	930	915	900	870	
				0.37	0.75	1.16	1.80	2.59	3.45	
6	90	1250	770	1200	1050	925	860	830	770	
				0.37	0.75	1.19	1.80	2.59	3.45	
6	90	1150	770	1150	1050	930	860	820	770	
				0.37	0.75	1.19	1.80	2.59	3.45	
6	90	1250	730	1200	1050	925	860	820	730	
				0.37	0.75	1.19	1.80	2.59	3.45	
6	90	1150	730	1150	1050	925	860	820	730	
				0.37	0.75	1.19	1.80	2.59	3.45	
7	90	1250	630	1200	1050	930	830	730	680	630
				0.37	0.75	1.16	1.46	1.85	2.59	3.45
7	90	1150	630	1150	1050	930	830	730	680	630
				0.37	0.75	1.16	1.46	1.85	2.59	3.45

experiments. Two rolling schedules were designed, with either two or three steps of deformation. The details of these schedules are shown in Tables V.5 and V.6, for every condition studied.

Table V.4 Sample Designations and Nominal Deformation Conditions Applied to the IF Steel

SAMPLE	T_γ		%RED		T_f					
NAME	1250	1150	90	75	1020	920	870	820	720	620
IF1	■		■		■					
IF2		■	■		■					
IF3		■		■	■					
IF4	■		■			■				
IF5		■	■			■				
IF6		■		■		■				
IF7	■		■				■			
IF8		■	■				■			
IF9	■		■					■		
IF10		■	■					■		
IF11	■			■				■		
IF12		■		■				■		
IF13	■		■						■	
IF14		■	■						■	
IF15	■			■					■	
IF16		■		■					■	
IF17	■		■							■
IF18		■	■							■

Table V.5 Equivalent Strains Accumulated after each Rolling Pass for the Two Schedules Employed in the Deformation of the IF Steel

No. of Passes	% Reduction	ε_{eq} accumulated after each rolling pass [mm/mm]		
		Pass No.1	Pass No.2	Pass No.3
2	75	0.93	1.93	—
3	90	0.95	2.11	5.22

Table V.6 Processing Parameters and Temperatures at each Rolling Pass for the IF Steel

No. of Passes	% Reduction	Austenitizing Temperature [°C]	Finishing Temperature [°C]	Temperature at the beginning of each rolling pass [°C]		
				Pass No.1	Pass No.2	Pass No.3
2	75	1150	1020	1100	1060	
2	75	1150	920	1100	930	
2	75	1250	820	930	840	
2	75	1150	820	930	840	
2	75	1250	720	840	730	
2	75	1150	720	840	730	
3	90	1250	1020	1200	1150	1020
3	90	1150	1020	1100	1070	990
3	90	1250	920	1200	1100	930
3	90	1150	920	1100	1070	930
3	90	1250	870	1100	930	875
3	90	1150	870	1100	930	875
3	90	1250	820	1100	930	840
3	90	1150	820	1100	930	840
3	90	1250	720	1100	840	730
3	90	1150	720	1100	840	730
3	90	1250	620	1100	840	630
3	90	1150	620	1100	840	630

V.3 Metallographic Analysis

Optical metallography was carried out on samples taken from every hot rolling experiment. The area analyzed was located on the plane of longitudinal section running through the centre of each plate. The microstructures were examined through the entire thickness, but only the regions closest to the mid-thickness planes were used for comparison of the results of different experiments.

The samples were prepared according to standard procedures. First, the samples were cut. Then, they were ground using silicon carbide paper numbers 120, 280, 400 and 600. The next procedure was final polishing using an alumina slurry containing approximately one part abrasive to ten parts distilled water. Finally, the samples were etched using 2% nital for the plain carbon and niobium microalloyed steels, and 4% nital for the interstitial free steel. The microstructures were then photographed using a light microscope in bright-field illumination.

V.4 Texture Analysis

V.4.1 Preparation of Texture Samples

Texture measurements were carried out on the central mid-thickness planes of the rolled steels. Figure V.2 shows schematically the position of the texture samples cut from the hot-rolled pieces. Great care was taken in sample preparation to avoid any change in texture due to grinding deformation. The surfaces of interest, 15 mm × 25 mm in

area, were prepared by machining, paper grinding, diamond polishing and electropolishing. A numerically controlled surface-grinder with a magnetic clamp, automatic feed table and flooding coolant flow was used for machining. A coarse (60 grit) grinding wheel was used, and the operation was carefully monitored to avoid any heating of the specimen. Also, parallelism of the original (rolling) and final (texture measurement) planes was maintained in all cases. The initial thickness of each specimen was recorded, and the final one after this first preparation step was equal to ½(initial thickness) + 0.2 mm. This extra material was removed by the following operations. For paper grinding, the 120, 280, 400 and 600 silicon carbide grinding papers were used, in that order. Diamond polishing was carried out using first a 6 μm and then a 1 μm diamond paste.

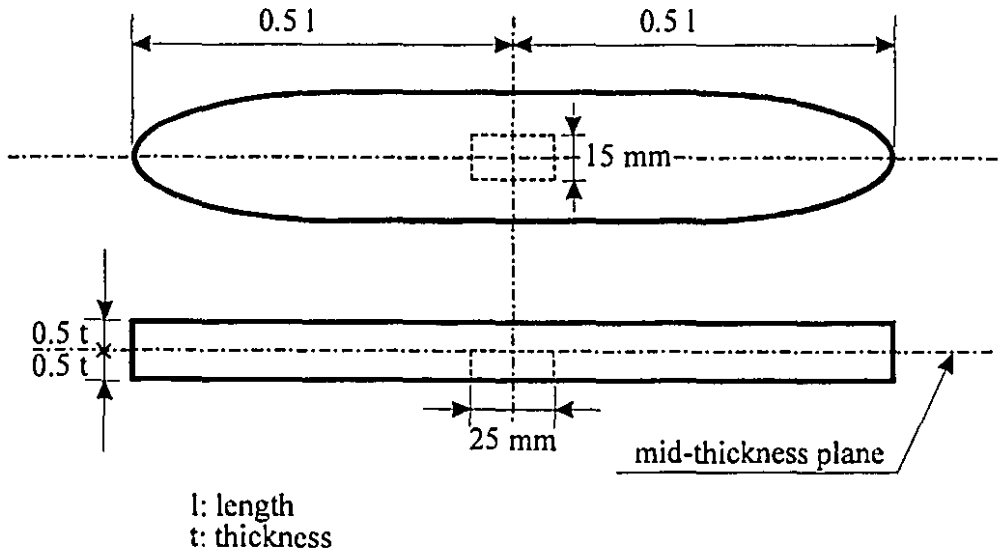

Figure V.2 Schematic representation of a hot rolled slab, showing the position from which the texture samples were taken.

The final step in the preparation of samples for texture measurement was electropolishing. This operation removes any remaining deformed material attributable to the previous procedures. The electrolyte employed was a solution of perchloric and glacial acetic acid, water-cooled to keep it at room temperature, and a stainless steel cathode was used. To ensure homogeneous distribution of the electrical current, the sample was held with an alumel wire with a diameter of 0.254 mm. This wire was held in place by passing it through slits cut in the corners of the sample, as shown in Figure V.3. The average operating conditions for electropolishing were: current - 3 amperes, voltage - 20 volts, and time - 45 seconds. Immediately afterwards, the samples were thoroughly washed with alcohol and dried.

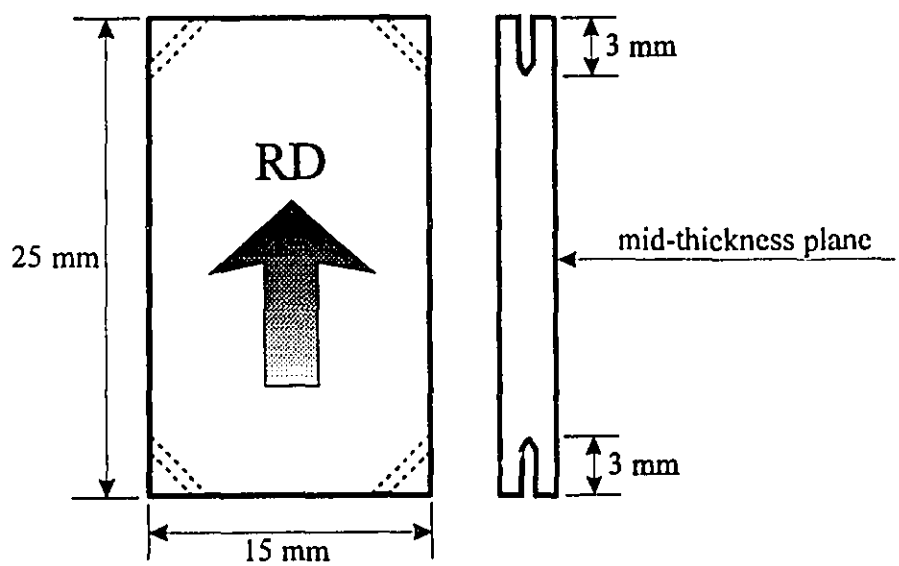

Figure V.3 Dimensions of a typical sample for texture measurement.

V.4.2 Pole Figure Measurement Equipment

The texture of the hot rolled samples was determined using the pole figure inversion method. This requires direct measurement of a number of pole figures followed by calculation of the ODF.

The pole figure measurements were performed on a fully automatic Siemens texture goniometer, model D-500 (Eulerian cradle type), using cobalt K_α radiation. For each sample, three incomplete pole figures ({110}, {200} and {112}) were measured, using the Schulz reflection method [23]. Figures V.4 and V.5 illustrate two views of the apparatus employed; a schematic representation is given in Figure V.6.

As shown in the schematic view of the goniometer, both the x-ray source and the counter are fixed, while the specimen is subjected to three different movements: a simple translation along the rolling direction, which improves the statistics of the measurement by increasing the scanned area; a rotation (β) about an axis perpendicular to the specimen surface, and a rotation (α) about an orthogonal axis. By means of these two rotations, it is possible to scan most of the pole figure, along the path shown in Figure V.7. The angle α is varied from 0° to 80° inclusive, at intervals of 5°. The rotation with respect to β runs from 0° to 360°, with continuous scanning.

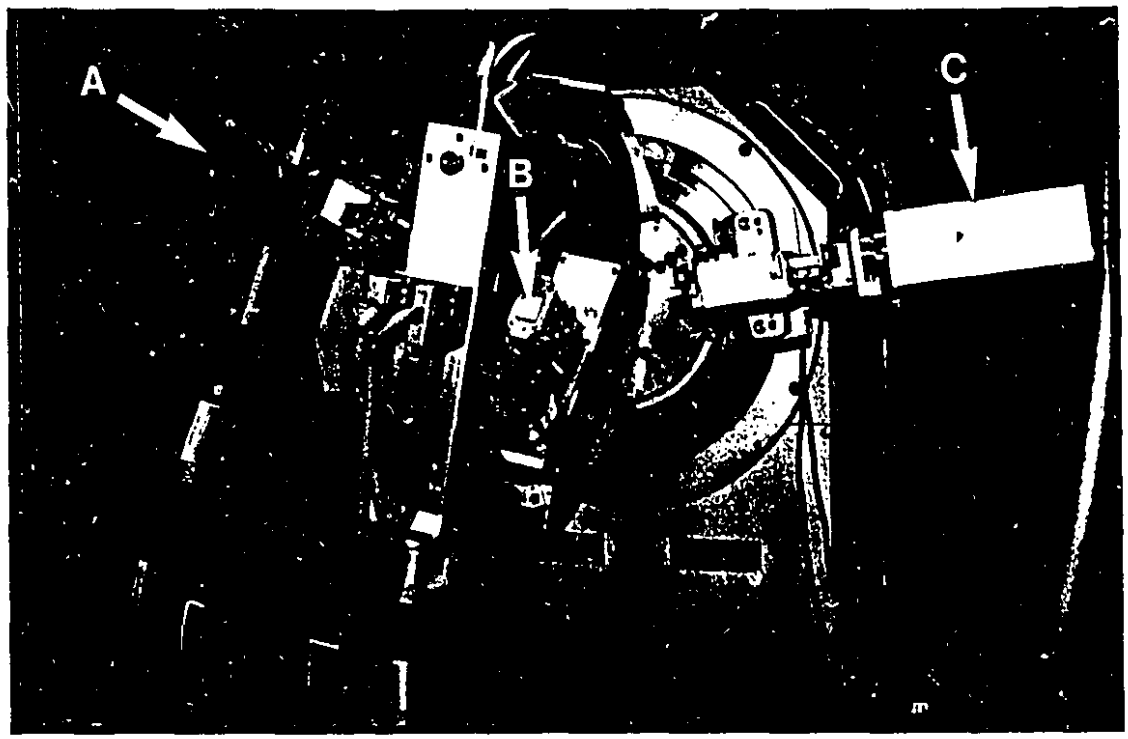

Figure V.4 Siemens texture goniometer.

A: X-ray source

B: Sample

C: X-ray counter

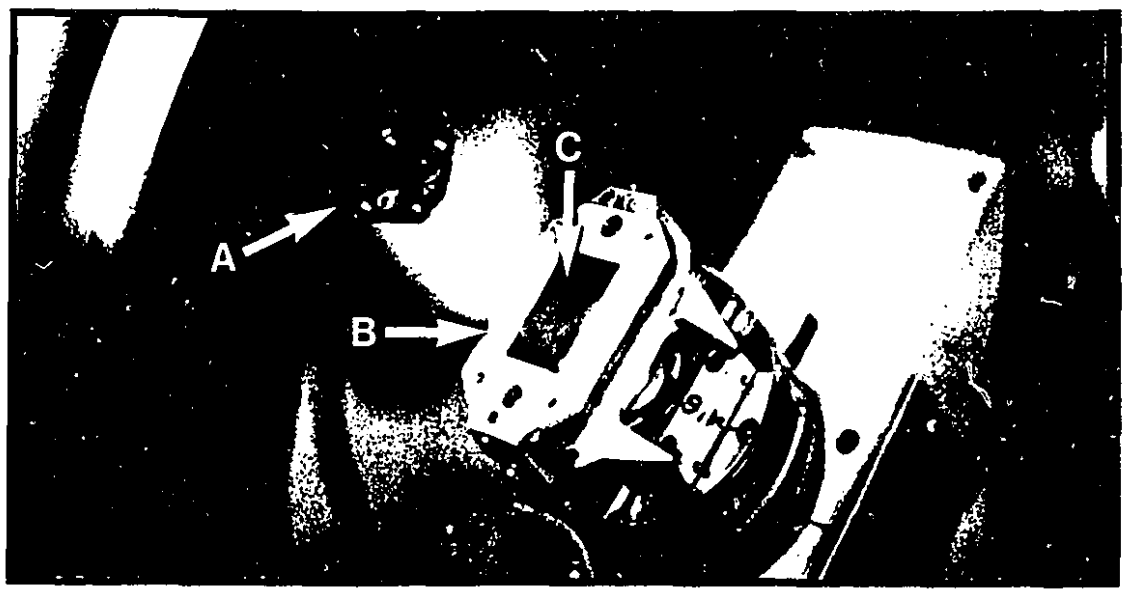

Figure V.5 Detail of the Siemens texture goniometer.

A: Nose of the X-ray source

B: Sample holder

C: Sample

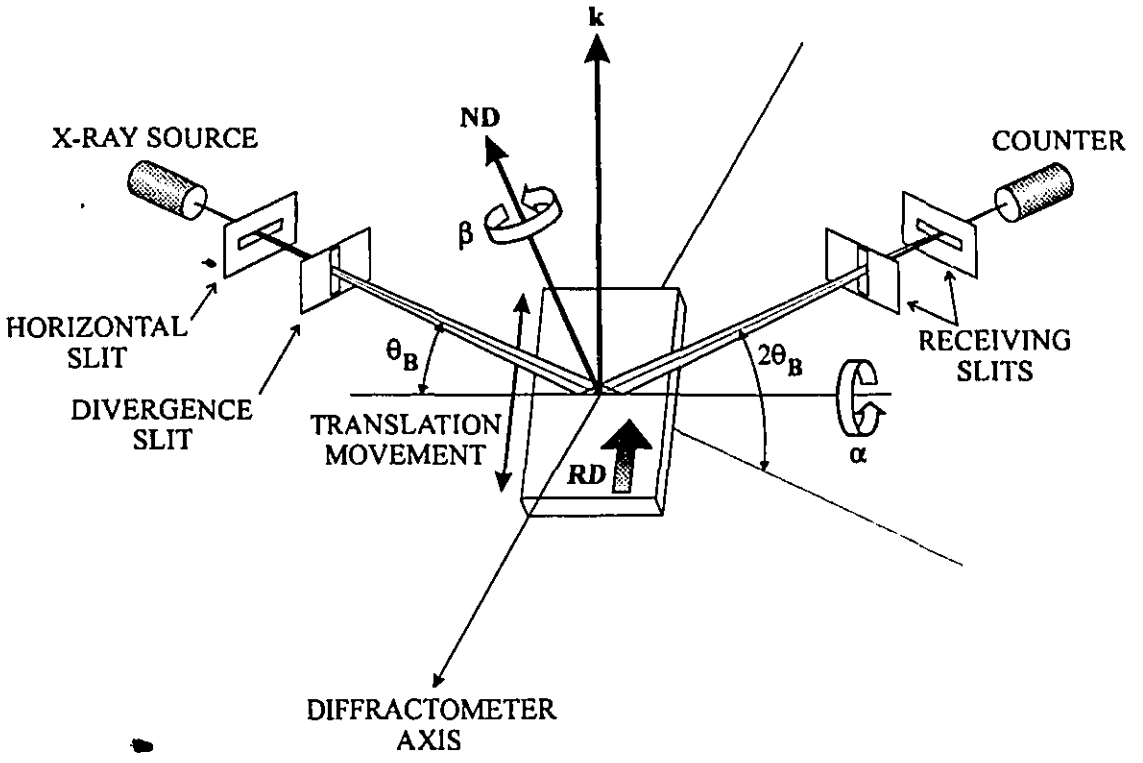

Figure V.6 Schematic diagram showing the geometrical arrangement of the texture goniometer employed.

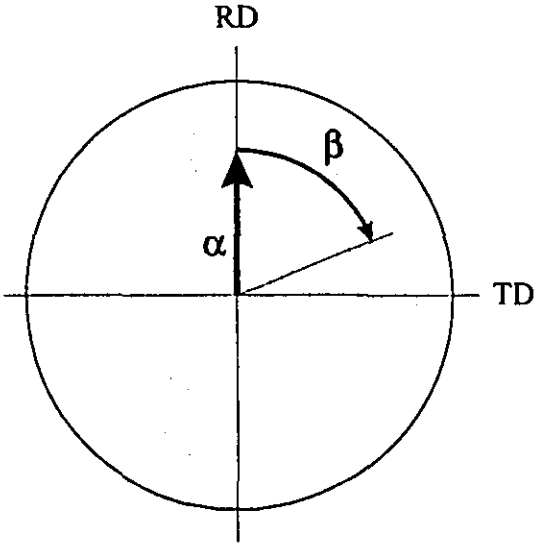

Figure V.7 Scanning path used to generate a pole figure.

The radiation beam satisfies the Bragg condition for a single set of reflecting planes. The normal (**k**) to the diffracting planes {hkl} remains fixed in space; when the specimen is rotated about the two perpendicular axes, many different directions in the sample are brought into coincidence with this diffracting normal. A diffraction intensity is detected whenever a grain arrives at a position such that a set of the prescribed {hkl} planes coincides with the fixed normal **k**, and the total diffracted intensity at any time is proportional to the volume of crystals with such an orientation. Some corrections are necessary; for instance, the use of slits as a means of minimizing the defocussing errors.

In order to determine the proportionality between the diffracted intensity and the pole density, it is necessary to define a "random intensity". This is the intensity of a textureless specimen measured under the same experimental conditions. The textureless sample employed in this work was a sintered high purity carbonyl iron. In an actual measurement, the regions in the pole figure which display lower intensities than the random level may be considered depleted in poles, whereas the regions with higher intensities can be described using contours of 2 times random, 3 times random, etc.

Orientation distribution functions were calculated from the pole figure data. The three fibres which are the most significant for steels were obtained from the ODF data and plotted. Finally, complete pole figures were recalculated, also from the ODF data.

Chapter VI

EXPERIMENTAL RESULTS

VI.1 Optical Metallography

Optical metallography was performed after the hot rolling experiments. The resulting photomicrographs are shown in Figures VI.1 to VI.3 for the plain carbon steel, Figures VI.4 to VI.6 for the niobium microalloyed steel and Figures VI.7 and VI.8 for the interstitial free steel.

VI.1.1 Plain Carbon Steel

In the plain carbon steel austenitized at 1250°C and hot rolled to 90% reduction, the microstructure changes from large, nearly equiaxed ferrite grains to flat and elongated ones as the finish rolling temperature is lowered (see Figure VI.1). The relatively coarse microstructure of the sample finish rolled at 1020°C was produced by transformation from austenite grains formed by static recrystallization after deformation at such a high temperature. In the deformed austenite range ($T_f = 870°C$), the

resulting microstructure is finer than in the previous case, but the ferrite grains are still nearly equiaxed. The shape of the pearlite grains indicates that some pancaking of the untransformed austenite occurred, as the temperature of no-recrystallization (T_{nr}) was estimated to be 900°C for this steel (section V.2). Rolling in the intercritical range (finish rolling temperatures of 770°C and 730°C) produced a finer structure; more pearlite pancaking is present, indicating that rolling was carried out well below the T_{nr} of the austenite. After warm rolling at 630°C, the ferrite grains appear flat and elongated; thus, deformation of the transformed ferrite was not followed by recrystallization.

When the austenitization temperature is 1150°C, Figure VI.2, the resulting microstructures are similar to the previous ones for corresponding finishing temperatures. Again, finish rolling in the austenite recrystallization range results in large, equiaxed grains, and as the finish rolling temperature is decreased, the microstructure becomes finer, but is still mostly undeformed, until finally the grains are elongated after finish rolling in the ferrite range.

A different behaviour results when the reduction applied is 75%, as shown in Figure VI.3. The grains are much larger, compared to the previous two cases, especially for the finish rolling temperature of 1020°C. When deformation is applied within the austenite recrystallization range, it is possible to refine the high temperature structure by repeated static recrystallization; the recrystallized austenite grain size is a function of the amount of rolling reduction. It is clear that a reduction of 75% is not enough to produce a fine microstructure, and this will deteriorate both the strength and the toughness of the steel. Even when the finish rolling temperature is decreased down

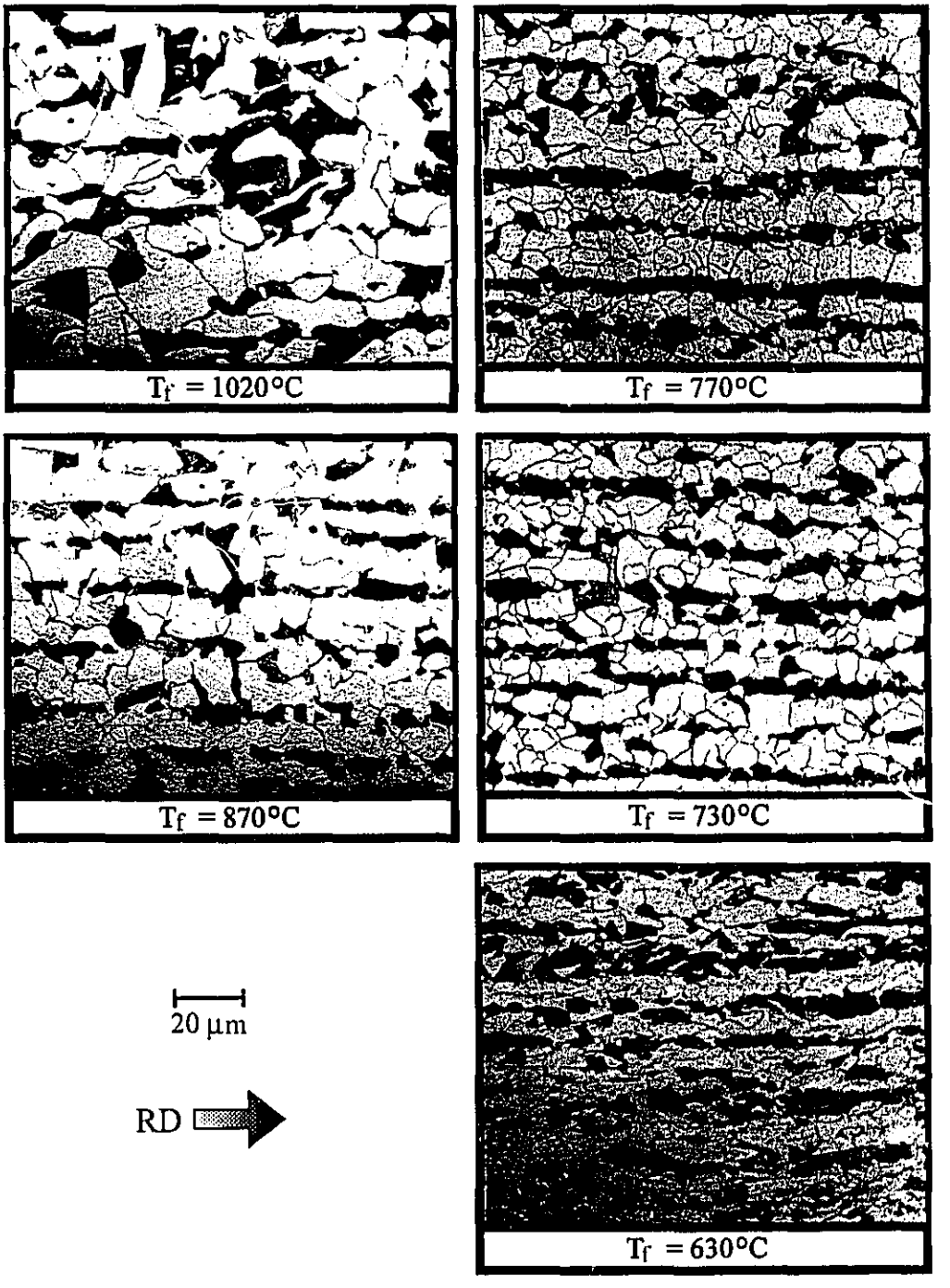

Figure VI.1 Optical micrographs of the plain carbon steel, austenitized at 1250°C and hot rolled to 90% reduction at several finish rolling temperatures. 2% nital etch.

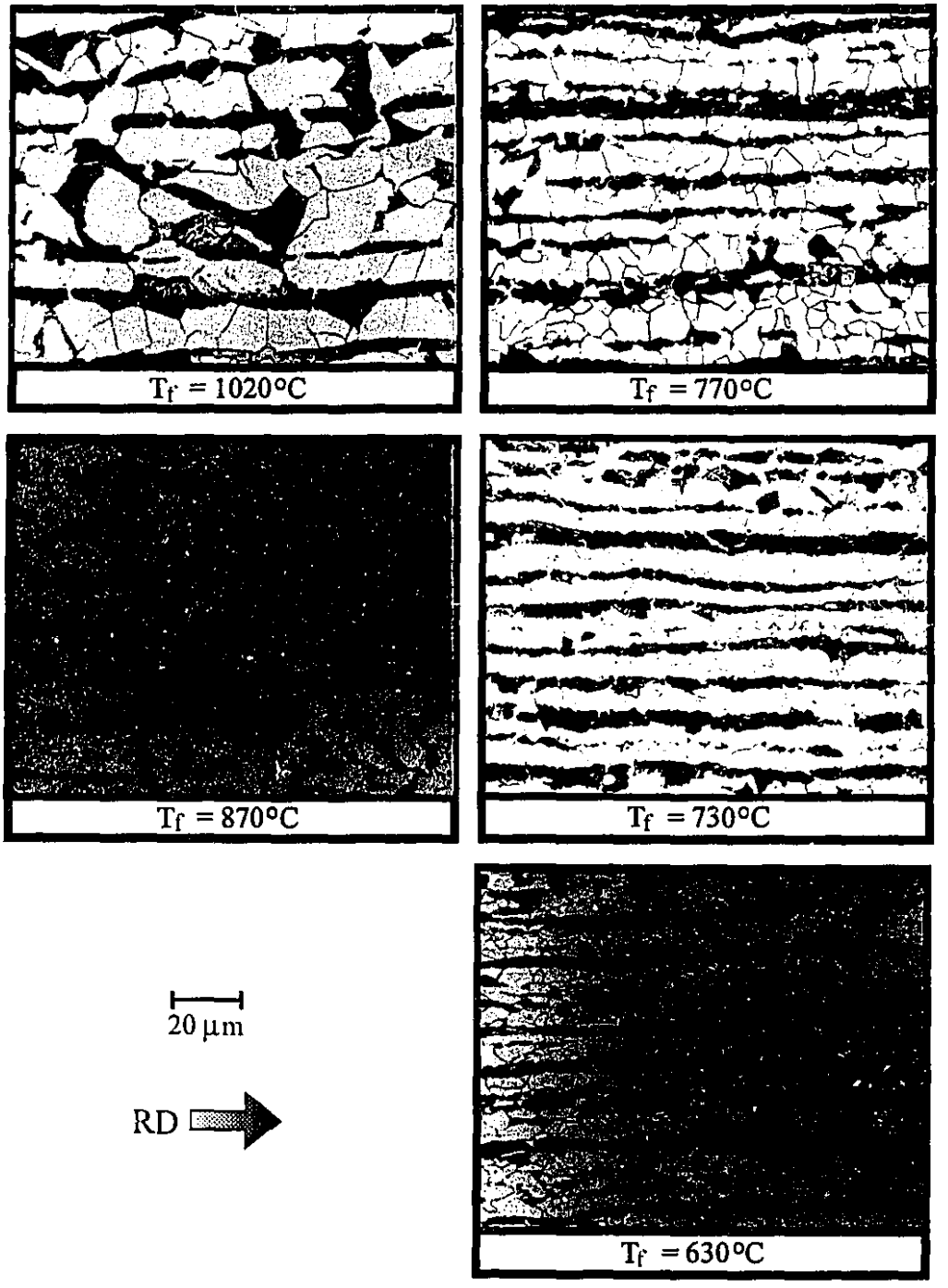

Figure VI.2 Optical micrographs of the plain carbon steel, austenitized at 1150°C and hot rolled to 90% reduction at several finish rolling temperatures. 2% nital etch.

Figure VI.3 Optical micrographs of the plain carbon steel, austenitized at 1250°C and hot rolled to 75% reduction at several finish rolling temperatures. 2% nital etch.

into the ferrite range, the final microstructure consists of large and fairly equiaxed grains.

VI.1.2 Niobium Microalloyed Steel

In the austenite recrystallization range, the niobium microalloyed steel is expected to display a microstructure similar to that of the plain carbon steel, consisting of somewhat smaller equiaxed grains because of the solute drag effect of Nb addition. In addition, the presence of niobium is expected to increase the temperature of no-recrystallization to an estimated 990°C. This is because, in reversing mills where large interpass times prevail, carbonitride precipitation occurs and prevents static recrystallization. This is due to the suppression of grain boundary migration by the pinning effect of the fine precipitates. Therefore, pancaking takes place, and still further refinement of the microstructure is possible.

The micrographs corresponding to an austenitization temperature of 1250°C, 90% reduction and various finish rolling temperatures are displayed in Figure VI.4. Indeed, the microstructure of the sample with a T_f of 1020°C is similar to the analogous one of the plain carbon steel. Then, when rolling is finished in the austenite no-recrystallization region and in the two intercritical ranges, a progressively finer ferrite grain size is obtained. Finally, when the last steps of deformation are applied to the transformed ferrite, elongated grains are observed.

Lowering the austenitization temperature to 1150°C does not bring about any substantial changes to the final microstructure, see Figure VI.5, compared to the

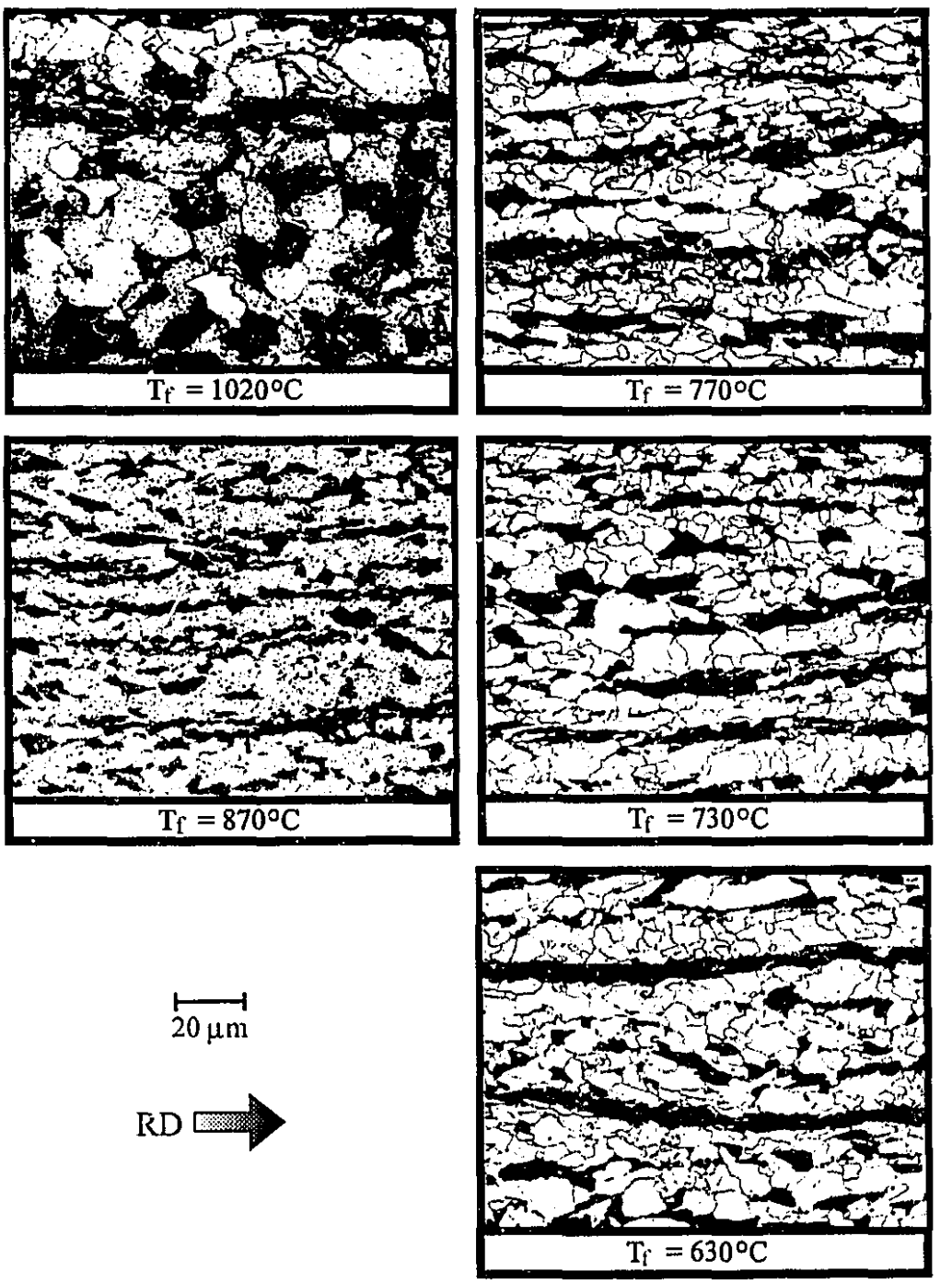

Figure VI.4 Optical micrographs of the Nb microalloyed steel, austenitized at 1250°C and hot rolled to 90% reduction at several finish rolling temperatures. 2% nital etch.

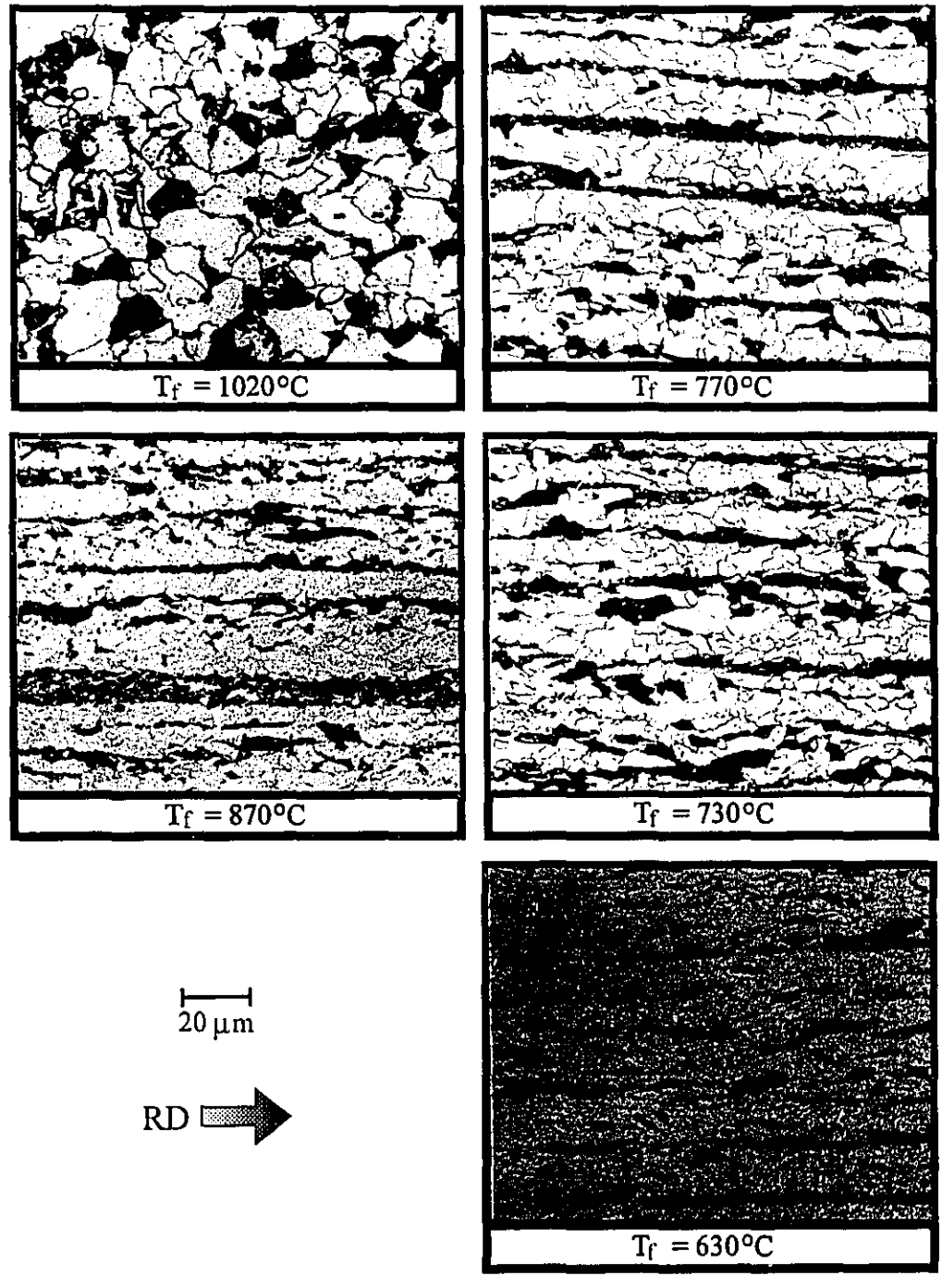

Figure VI.5 Optical micrographs of the Nb microalloyed steel, austenitized at 1150°C and hot rolled to 90% reduction at several finish rolling temperatures. 2% nital etch.

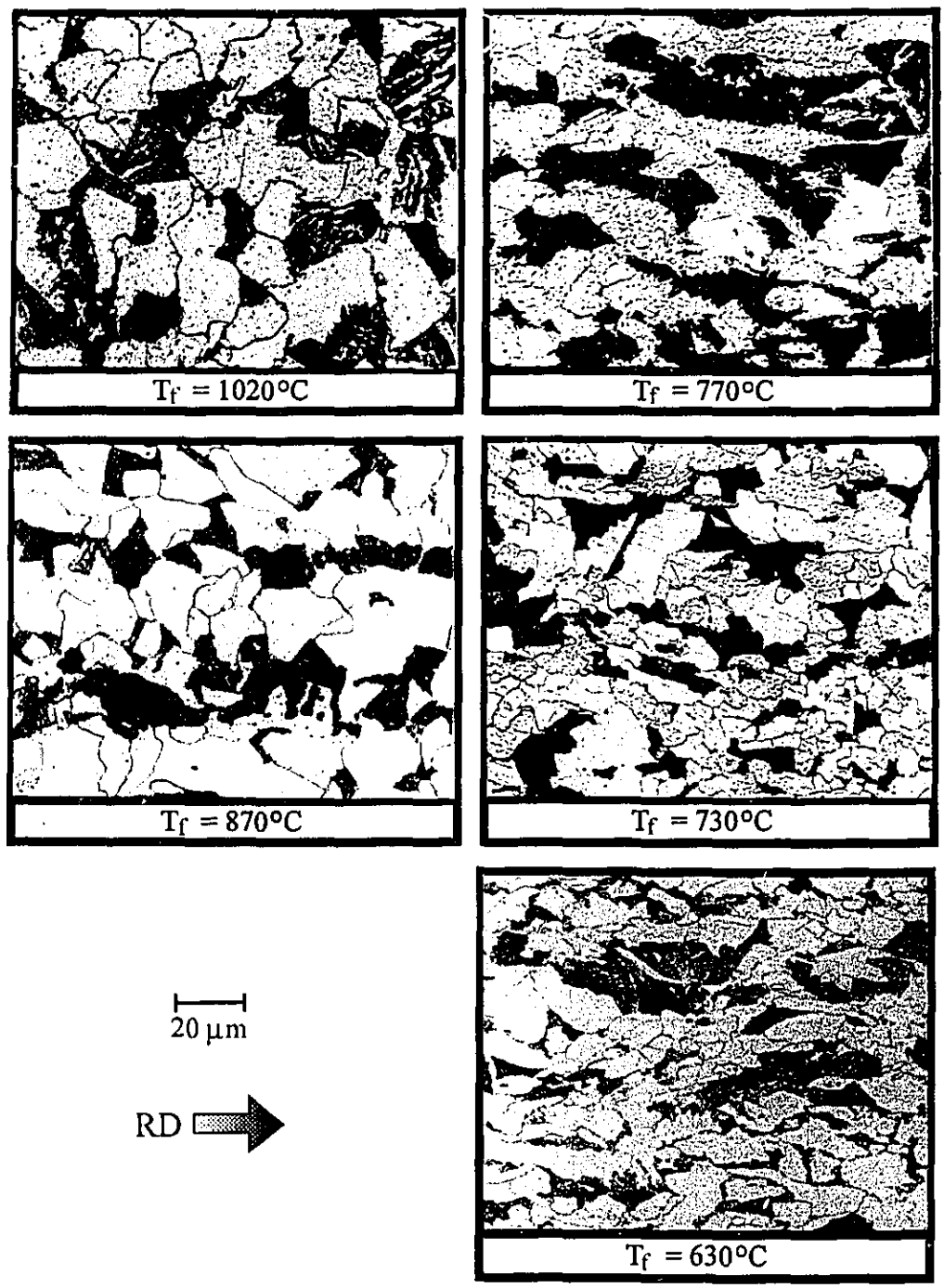

Figure VI.6 Optical micrographs of the Nb microalloyed steel, austenitized at 1250°C and hot rolled to 75% reduction at several finish rolling temperatures. 2% nital etch.

previous case. On the other hand, when the reduction is lowered to 75%, Figure VI.6, larger equiaxed grains are again produced, as for the plain carbon steel. Likewise, finish rolling in the ferrite region still yields elongated grains.

VI.1.3 Interstitial Free Steel

In the interstitial free steels, virtually all the carbon and nitrogen are tied up as carbides and nitrides of the niobium, titanium and aluminum. The morphology of these precipitates has a strong influence on the recrystallization and grain growth behaviour of the steel; coarse TiC and NbC precipitates and a fine hot band grain size result in high ductilities and r-values [69].

Optical micrographs of the IF steel austenitized at 1250°C and deformed to 90% reduction are presented in Figure VI.7, for six finishing temperatures. For the samples deformed within the austenite region, T_f=1020°C and 920°C, the microstructure consists of fairly large, equiaxed grains. When finish rolling is completed in the intercritical range, T_f=870°C, the grains are still equiaxed but display a mixture of sizes. Finally, finish rolling in the ferrite region results in a mixture of small, recrystallized grains and pancaked (i.e. deformed) ones (T_f=820°C), and in a completely deformed microstructure at the two lower finishing temperatures. Austenitizing at a temperature of 1150°C (also with a rolling reduction of 90%) leads to similar trends in terms of the ferrite microstructure, see Figure VI.8. The ferrite grains of the samples deformed in the austenite region are equiaxed, although slightly larger than in the previous case. For the rest of the samples, there are no differences with respect to the material austenitized at the higher temperature.

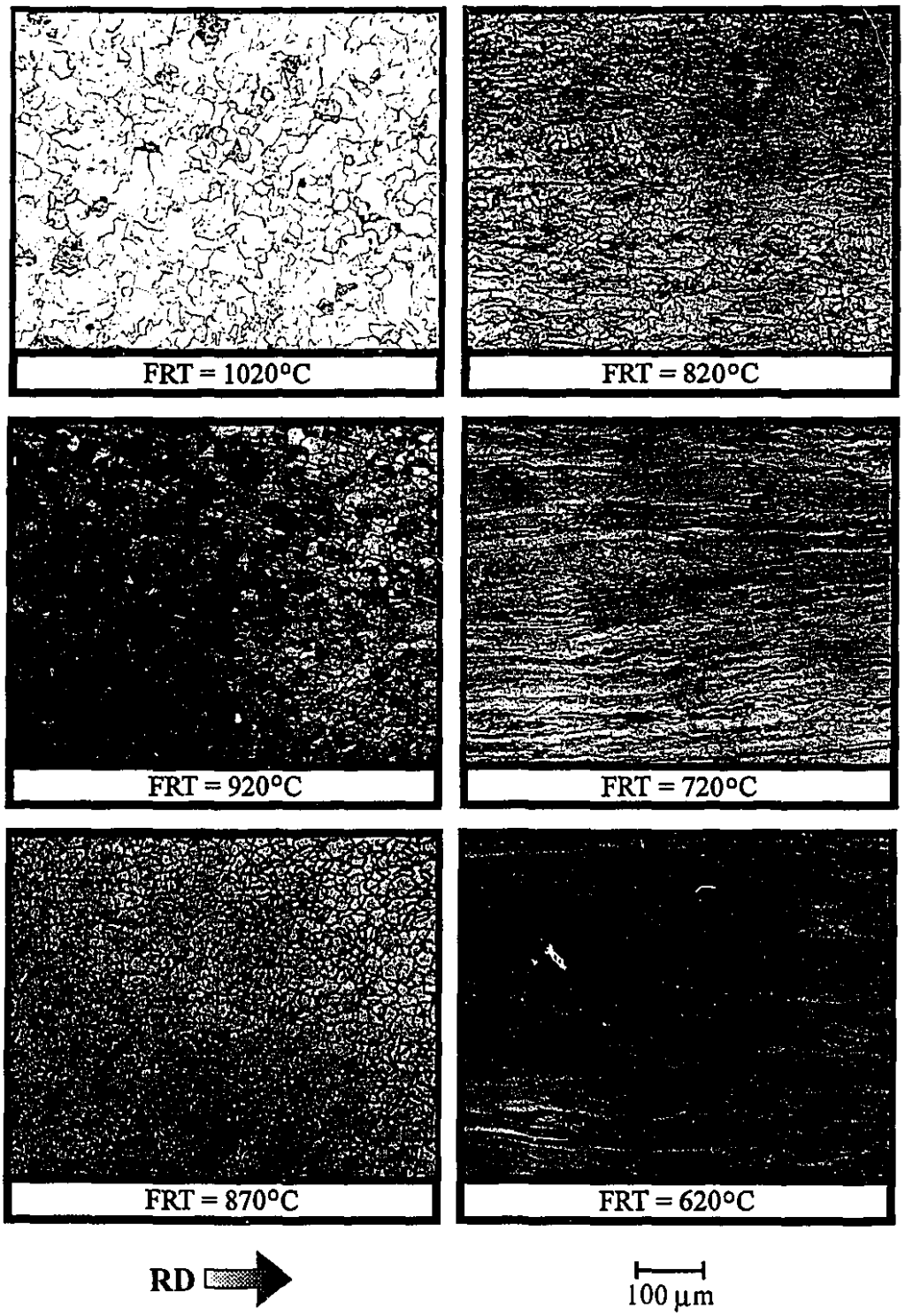

Figure VI.7 Optical micrographs of IF steel hot bands, austenitized at 1250°C, hot rolled to 90% reduction and finish rolled at the temperatures indicated. 4% nital etch.

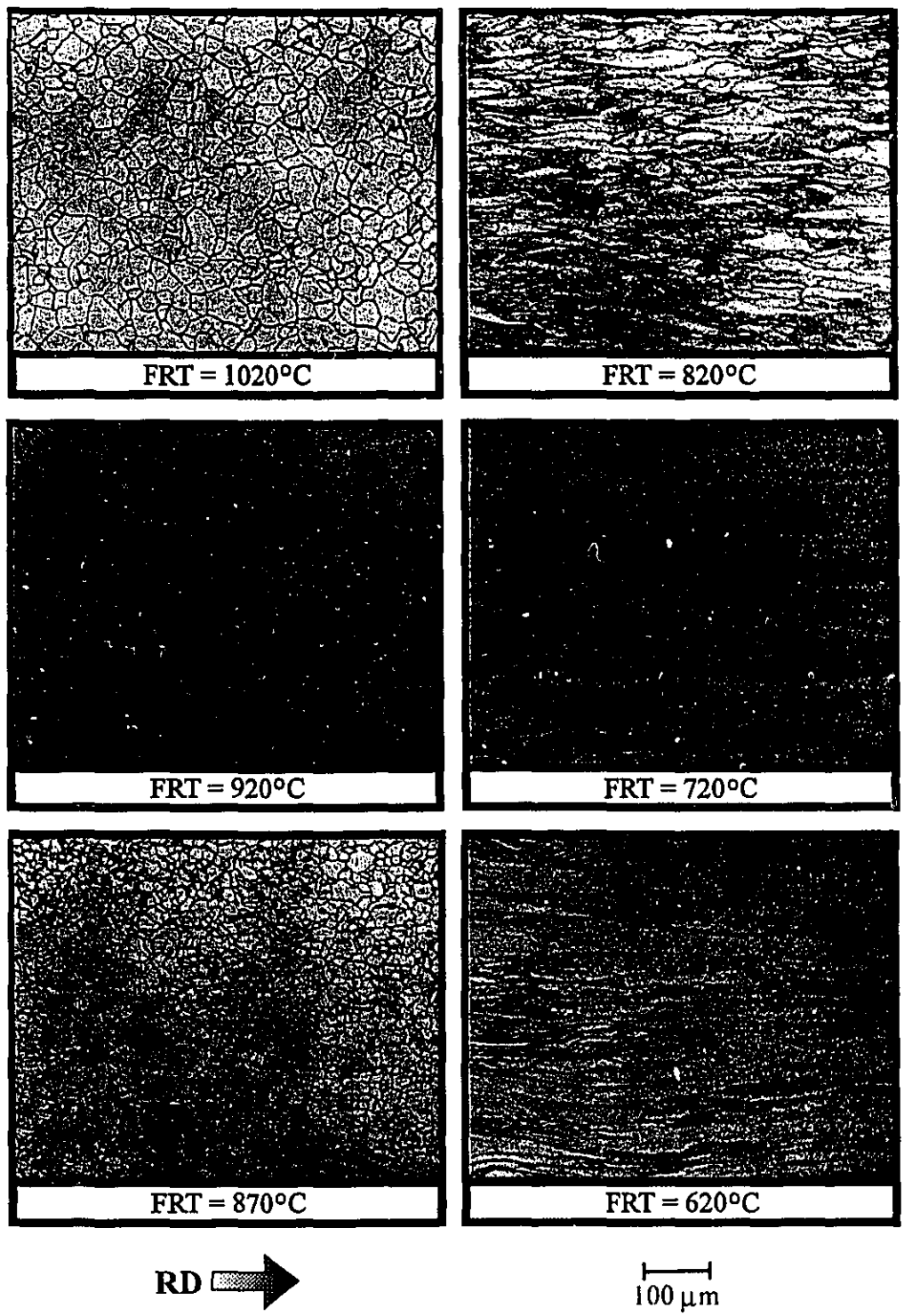

Figure VI.8 Optical micrographs of IF steel hot bands, austenitized at 1150°C, hot rolled to 90% reduction and finish rolled at the temperatures indicated. 4% nital etch.

VI.2 Textures

The experimental textures determined after hot rolling of the samples described in Tables V.2 and V.4 above are presented in the following three sections. Each section covers the results for a particular steel; furthermore, various groups were formed within which all the processing conditions were kept constant, except for the finishing temperature. Such results are given in three complementary forms: as pole figures, ODF's and fibres. Of the three pole figures measured, two are presented here, the complete (200) and (110) ones, recalculated from the corresponding ODF's. Only the $\varphi_2=45°$ section of the ODF is shown, since this is the one that contains the most relevant orientations in steels. The three fibres selected are the ones contained in this section of the ODF, namely the RD, TD and ND fibres. The RD fibre lies along $\varphi_1=0°$, and includes orientations related by rotations along the RD || <110> axis. The TD fibre contains orientations with a common <110> || TD, and runs along $\varphi_1=90°$. Orientations on the ND fibre have a common <111> || ND, and it is located at $\Phi=55°$ in the $\varphi_2=45°$ section.

The locations of some of the most important ideal texture components are given in Figure VI.9 for the (200) pole figure, and in Figure VI.10 for the (110) pole figure. Also, for the $\varphi_2=45°$ section of the ODF, the positions in Euler space of the most important ideal orientations are presented in Figure VI.11.

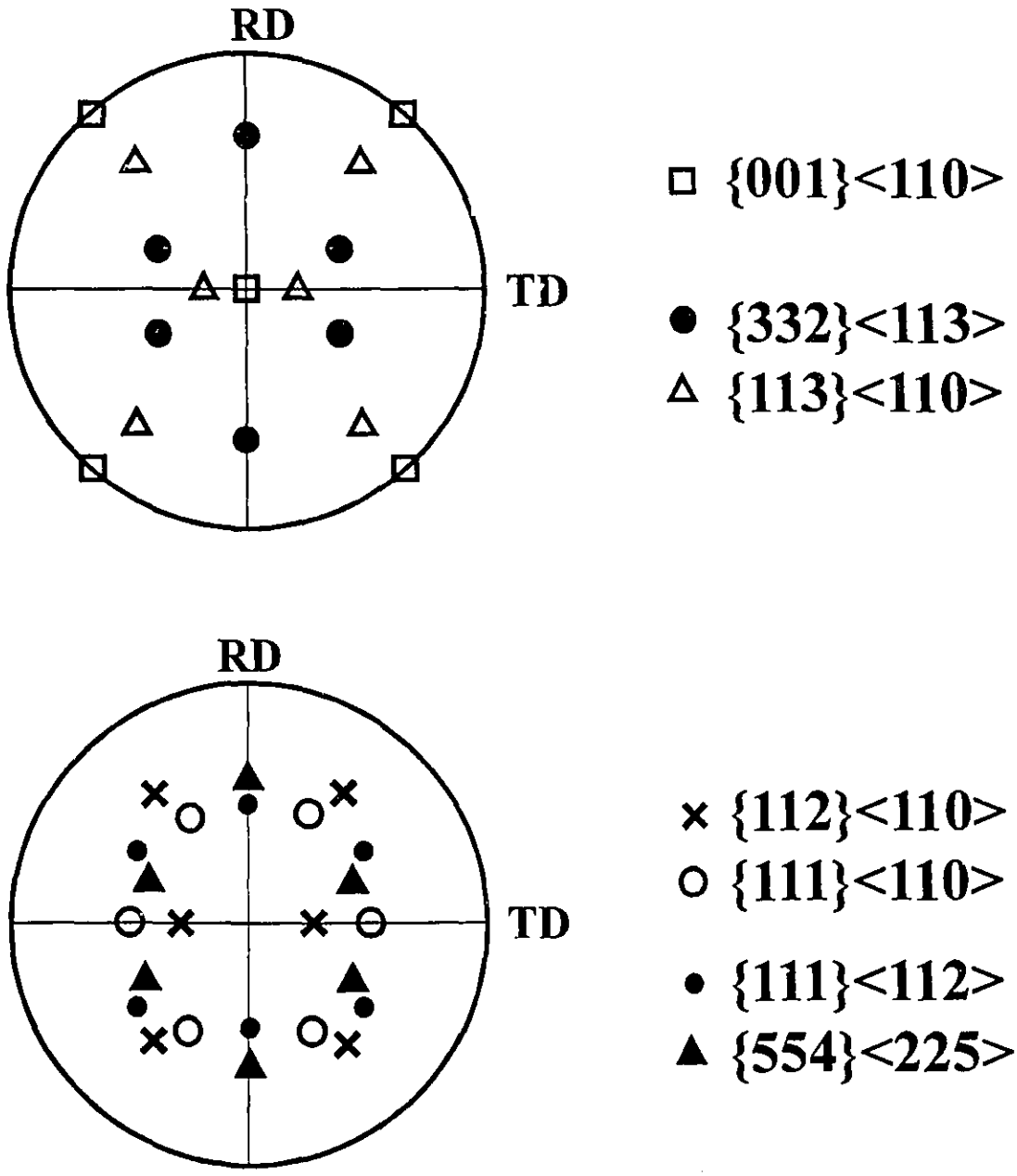

Figure VI.9 (200) pole figures showing the ideal positions of some important orientations in ferrite.

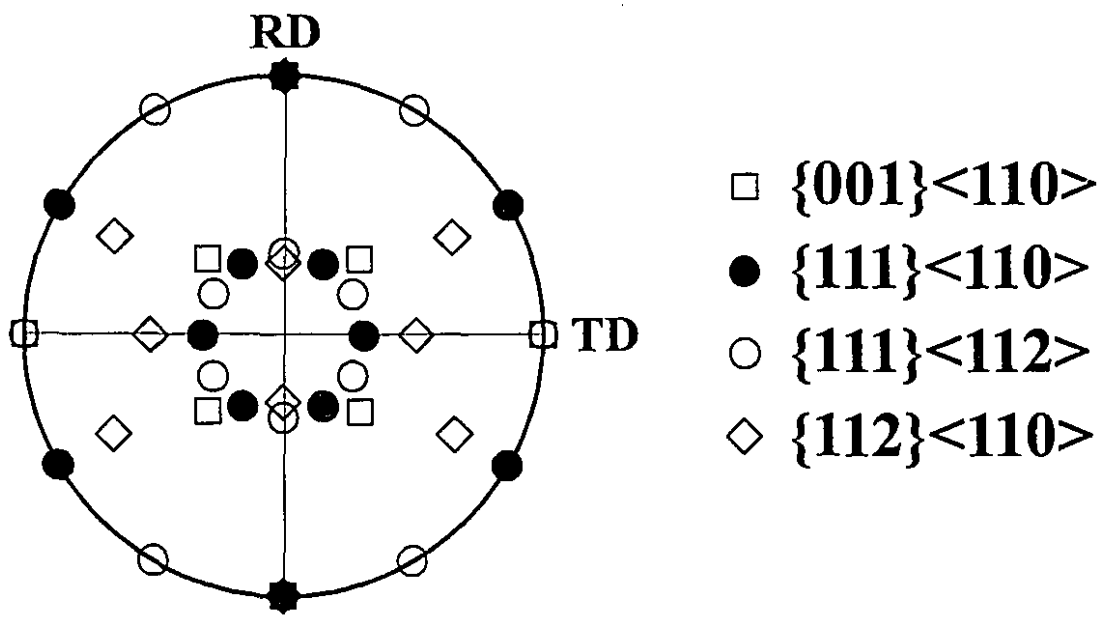

Figure VI.10 (110) pole figure showing the ideal positions of some important orientations in ferrite.

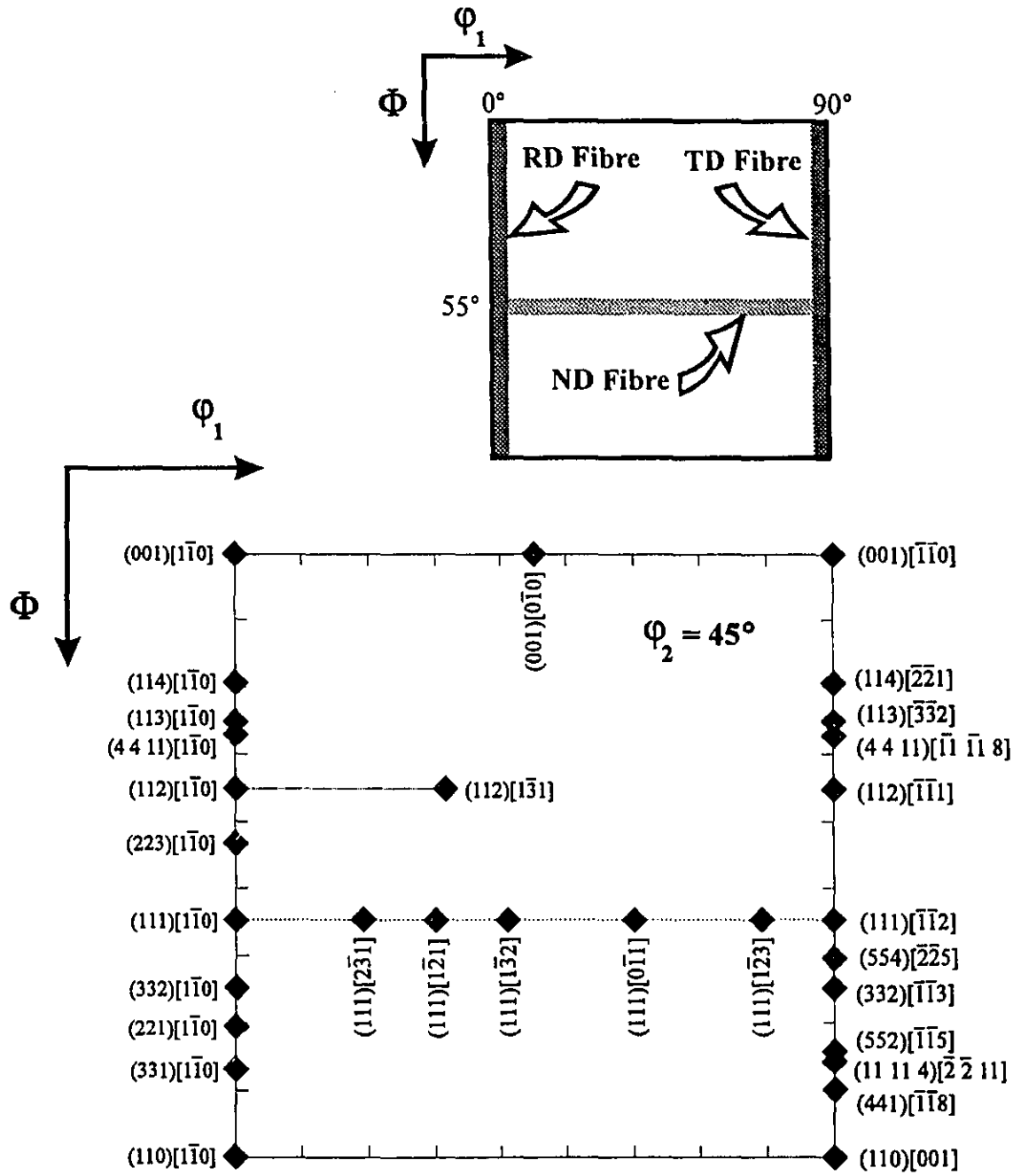

Figure VI.11 The φ_2 = 45° section of the ODF showing the ideal positions of some important orientations in ferrite, and the location of the RD, TD and ND fibres.

VI.2.1 Plain Carbon Steel

The texture results for the plain carbon steel austenitized at 1250°C and deformed to 90% reduction are shown in Figures VI.12 to VI.15. For the four higher finish rolling temperatures, the intensities of both the pole figures and the ODF's are fairly low. The main component is the {001}<110>; some other orientations are found, such as {113}-{112}<110>, {110}<110>, and even orientations close to {332}<113>, but none of them shows any predominance. It is interesting to note that, although the {001}<110> component is known to transform from the cube parent orientation, which corresponds to recrystallized austenite, its intensity is not the highest for the sample finish rolled at 1020°C. On the contrary, it has the lowest intensity with respect to the other samples in this group, and furthermore it is quite strong after ferrite rolling.

When rolling is finished in the ferrite region, corresponding to the 630°C finishing temperature, a sharper texture is developed. Again, the {001}<110> orientation is present, but the strongest component is found between the {112}<110> and {223}<110>. Furthermore, the ND fibre is clearly observed, with a steady intensity of 4 all along the fibre. For this finish rolling temperature, the {110}<110> has disappeared completely.

A reduction of only 75% leads to very random textures; the data obtained under these conditions, after austenitizing at 1250°C, are presented in Figures VI.16 to VI.19. The intensities in both the (200) and (110) pole figures are below 3 for all finishing temperatures, and from the ODF's it can be seen that there is a wide spread of

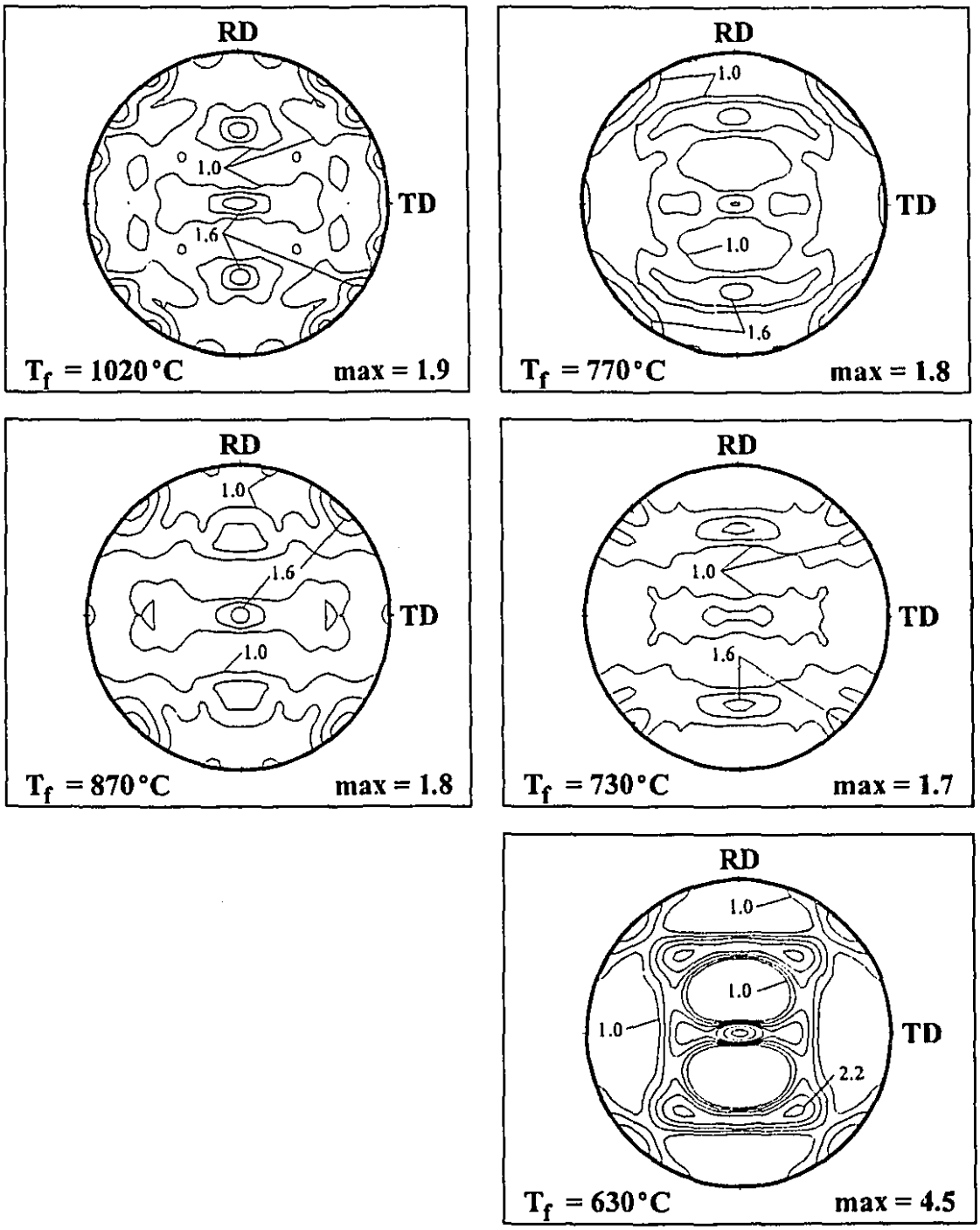

Figure VI.12 (200) pole figures for the plain carbon steel, austenitized at 1250°C and hot rolled to 90% reduction, for several finish rolling temperatures.

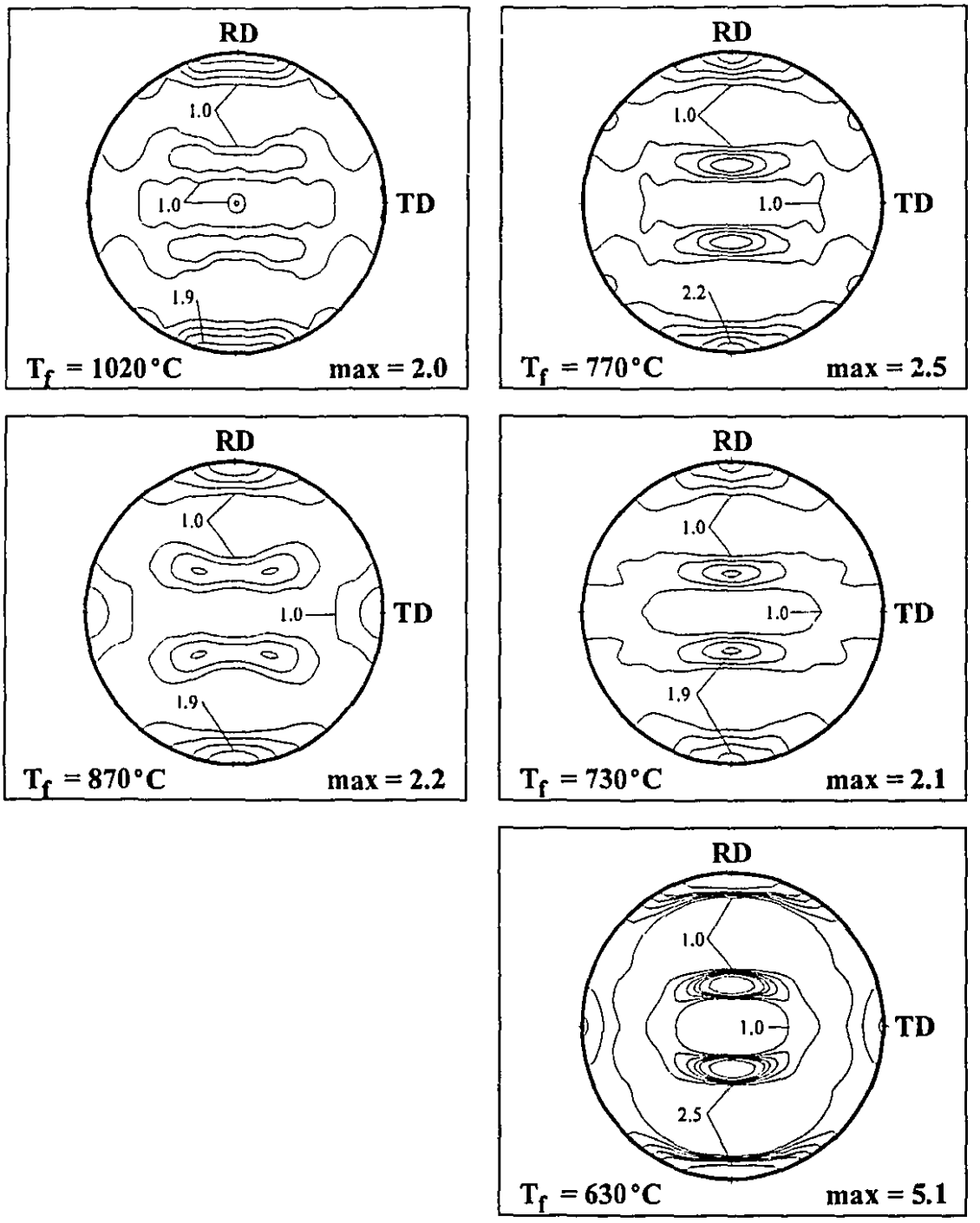

Figure VI.13 (110) pole figures for the plain carbon steel, austenitized at 1250°C and hot rolled to 90% reduction, for several finish rolling temperatures.

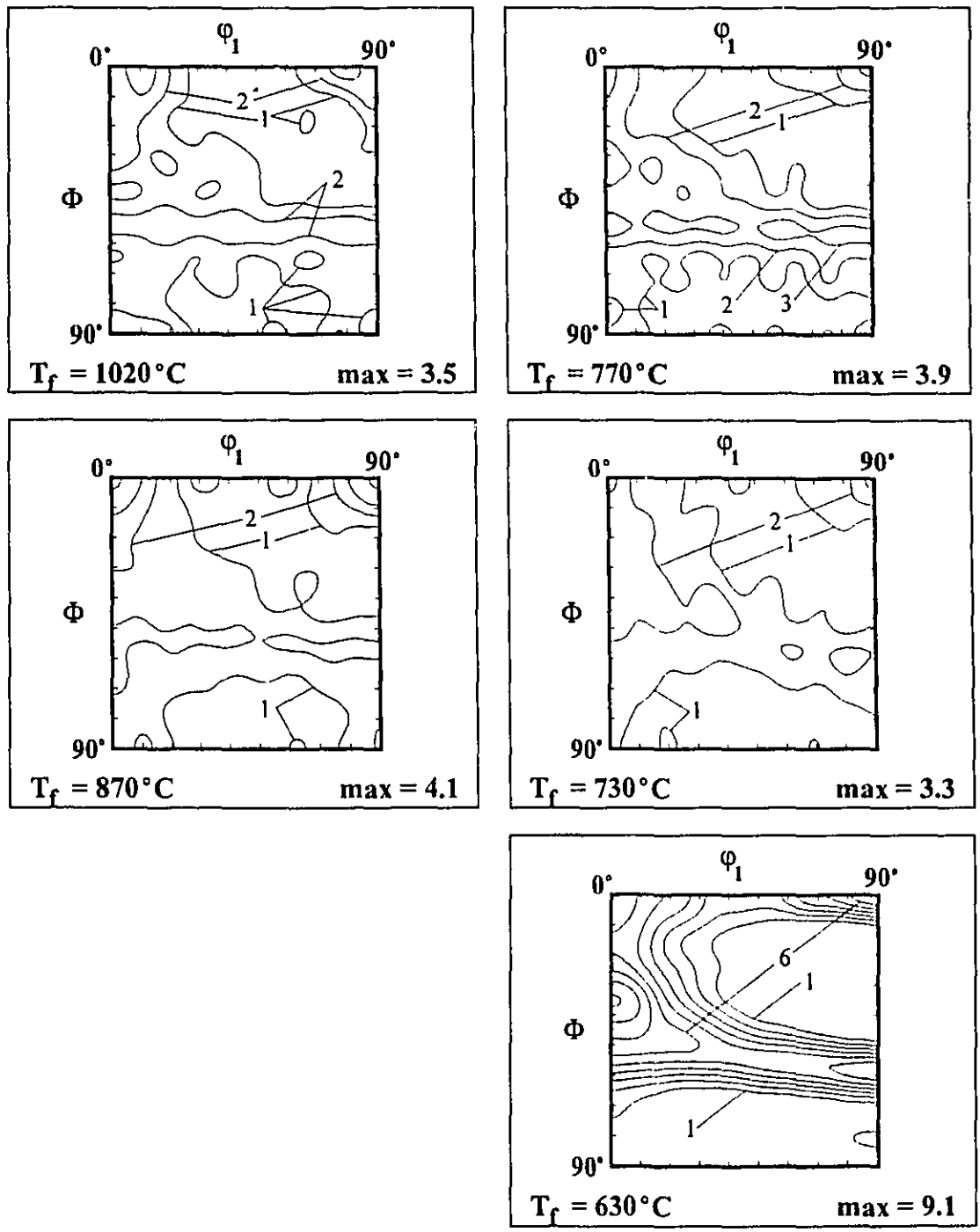

Figure VI.14 φ_2=45° sections of the ODF's for the plain carbon steel, austenitized at 1250°C and hot rolled to 90% reduction, for several finish rolling temperatures.

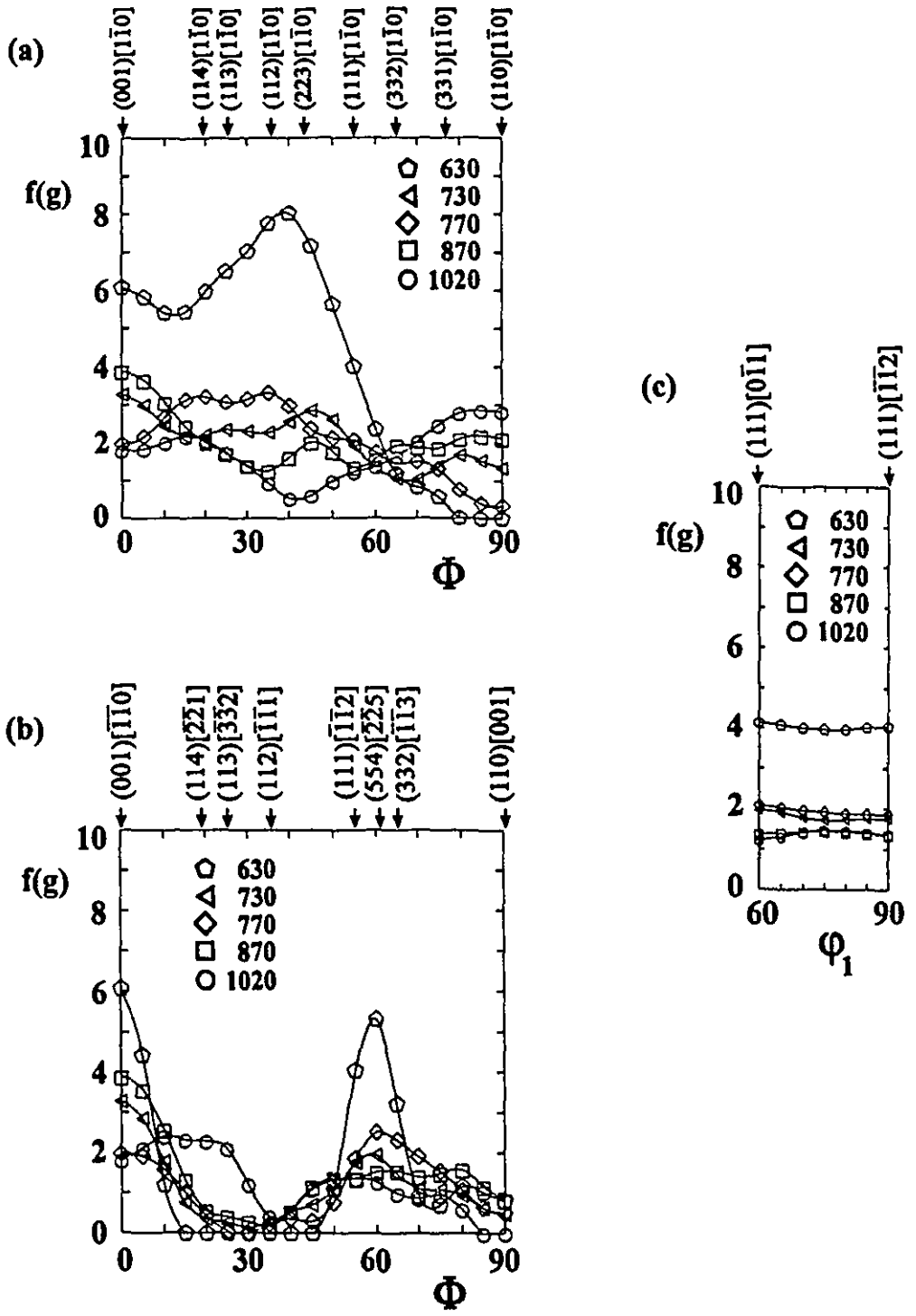

Figure VI.15 (a) RD, (b) TD and (c) ND fibres for the plain carbon steel, austenitized at 1250°C and hot rolled to 90% reduction, for several finish rolling temperatures.

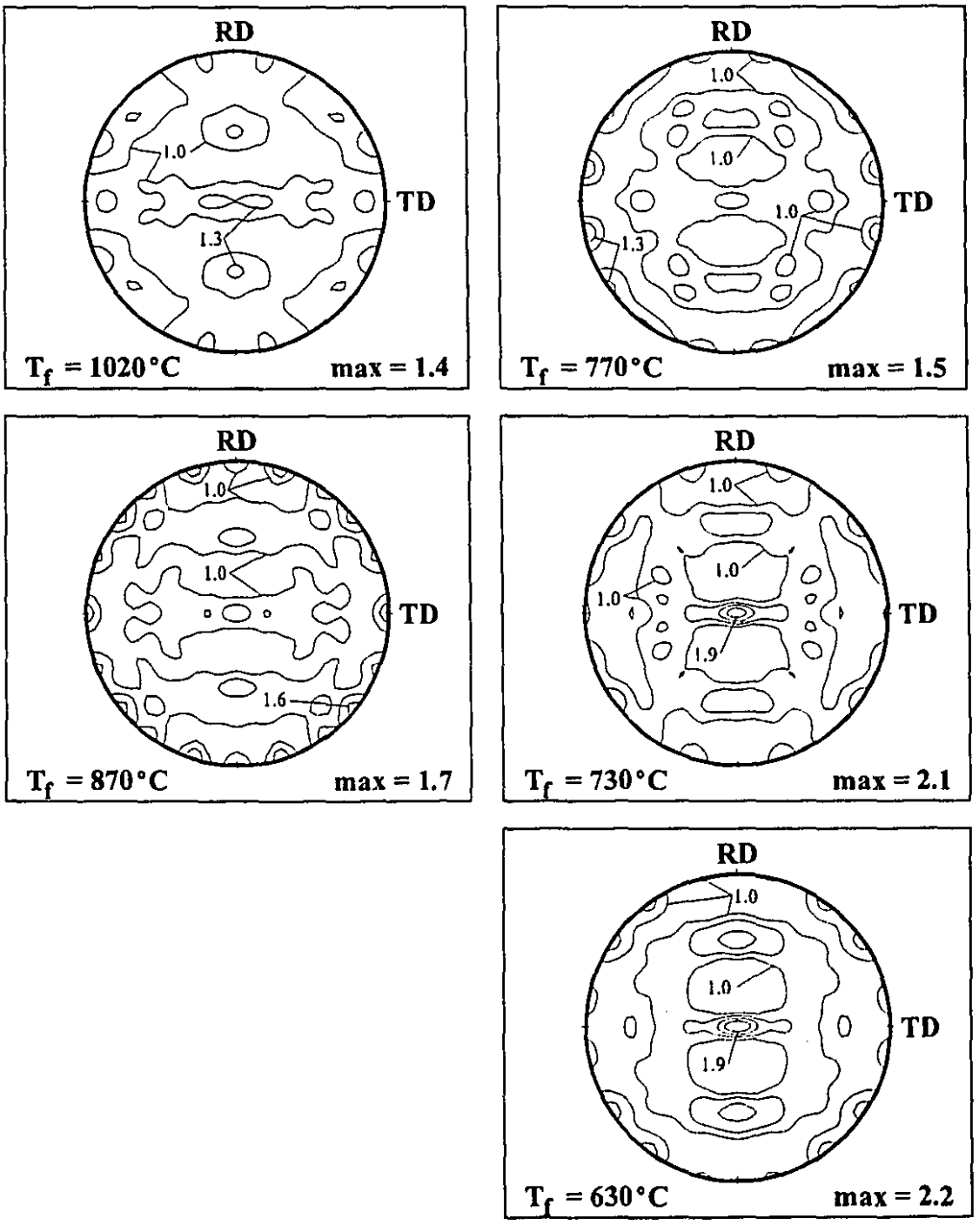

Figure VI.16 (200) pole figures for the plain carbon steel, austenitized at 1250°C and hot rolled to 75% reduction, for several finish rolling temperatures.

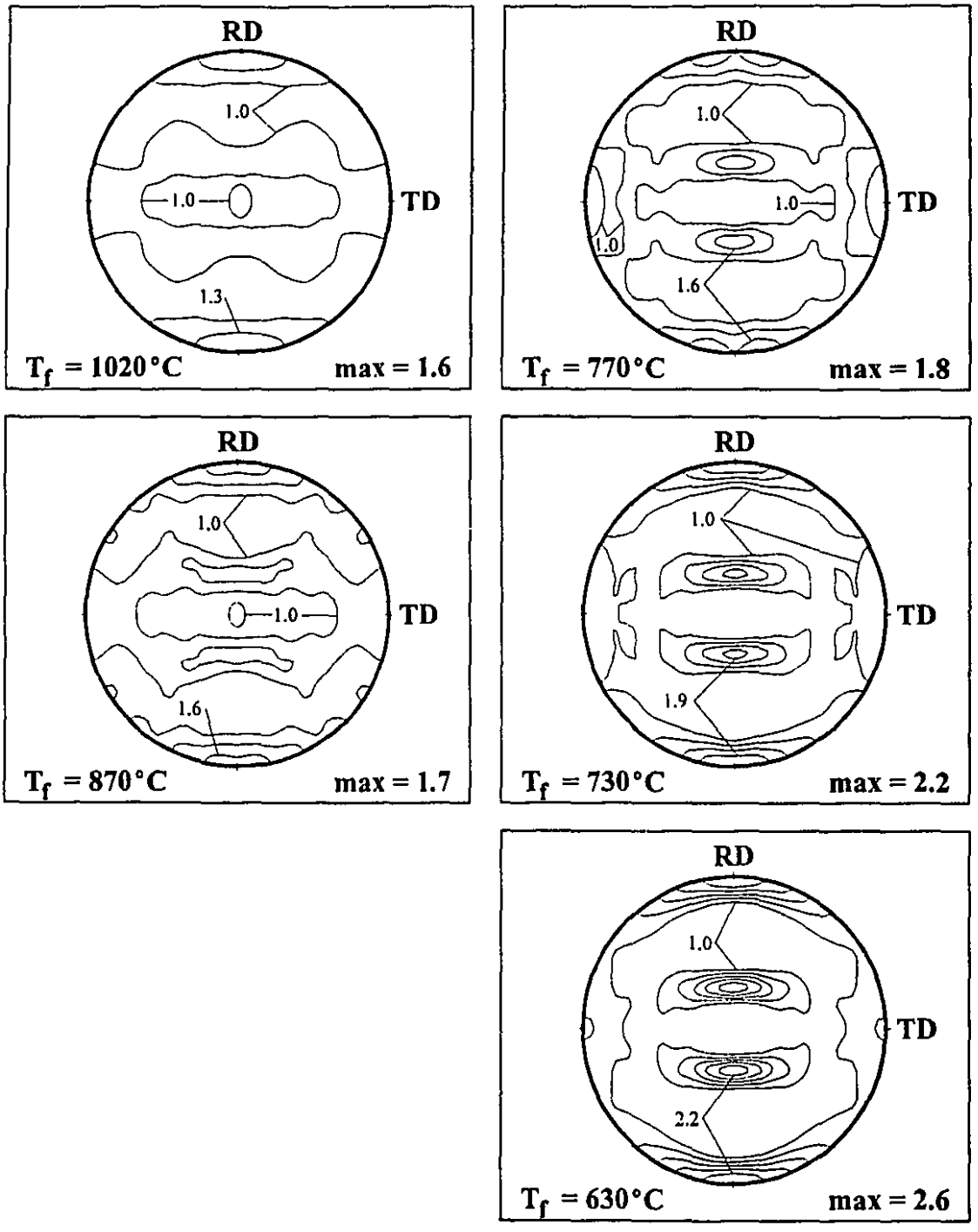

Figure VI.17 (110) pole figures for the plain carbon steel, austenitized at 1250°C and hot rolled to 75% reduction, for several finish rolling temperatures.

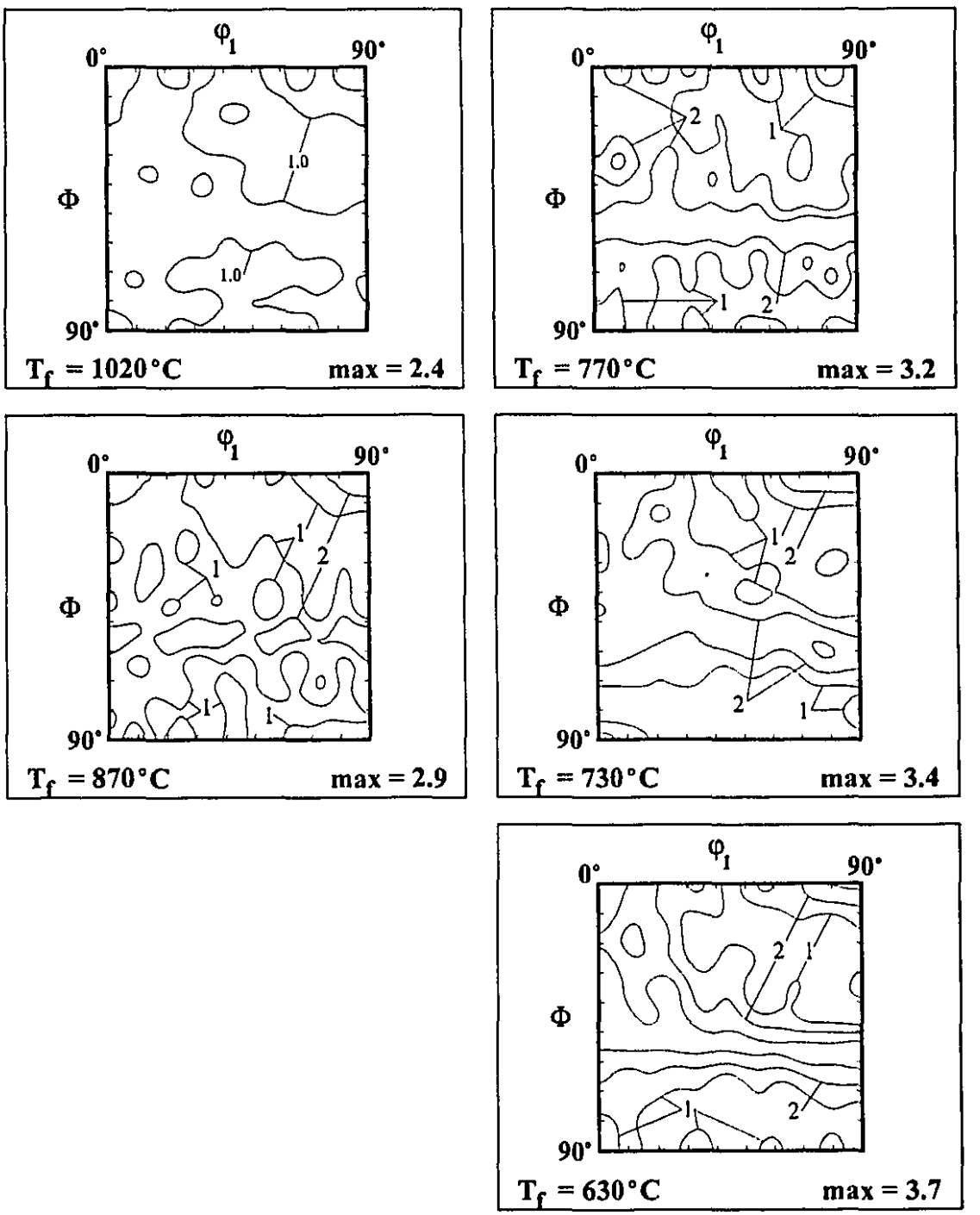

Figure VI.18 φ_2=45° sections of the ODF's for the plain carbon steel, austenitized at 1250°C and hot rolled to 75% reduction, for several finish rolling temperatures.

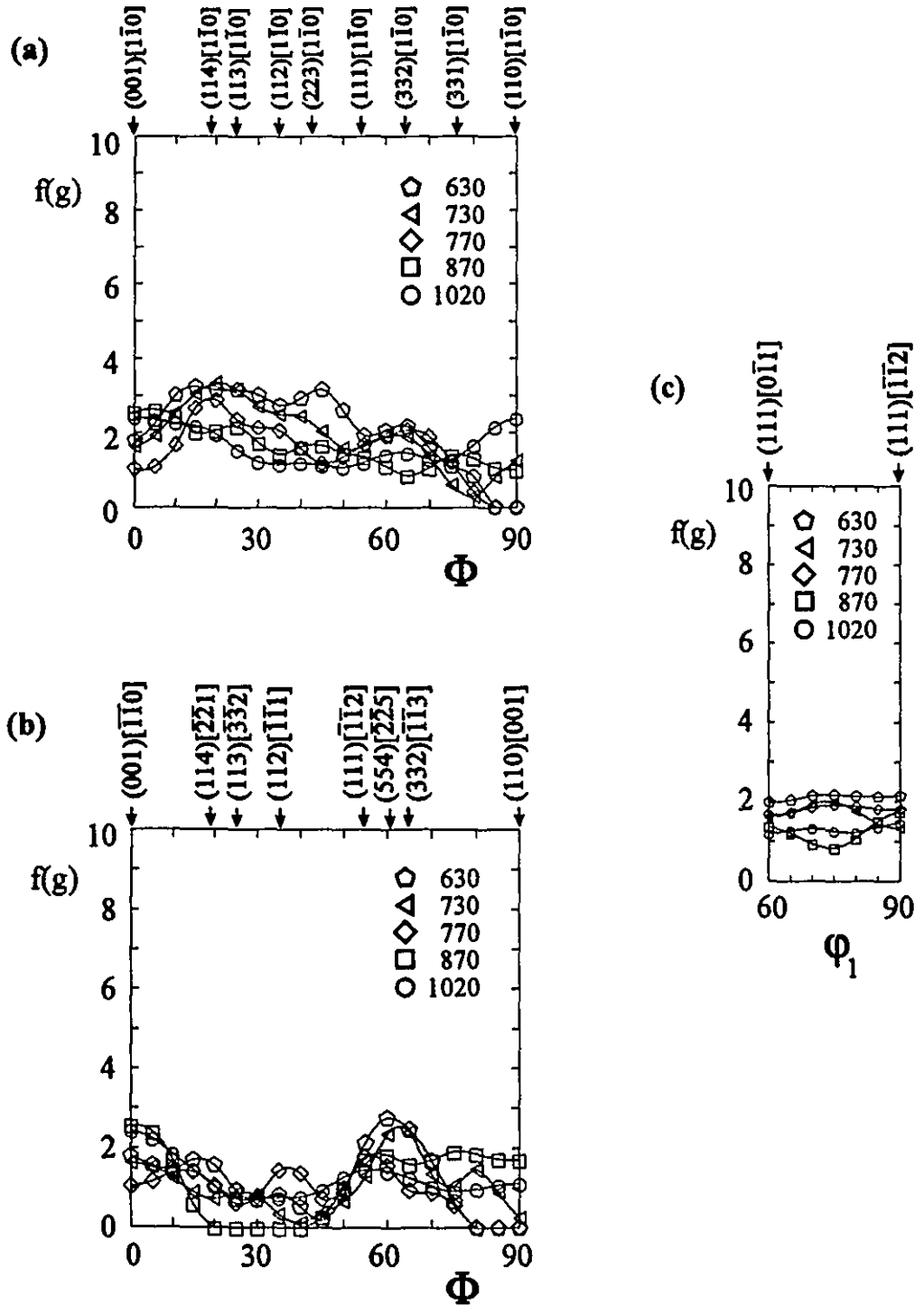

Figure VI.19 (a) RD, (b) TD and (c) ND fibres for the plain carbon steel, austenitized at 1250°C and hot rolled to 75% reduction, for several finish rolling temperatures.

weak texture components. This can be observed more clearly in Figure VI.19, where the fibres are plotted. There is not a single predominant component in all the samples in this group, only a dispersion of orientations with <110> || RD stretching from {001}<110> to {332}<110>, a minor peak around {554}<225>, and a weak ND fibre.

The third set of experiments for the plain carbon steel corresponds to an austenitization temperature of 1150°C, hot rolled to 90% reduction. The results are presented in Figures VI.20 to VI.23. Both the pole figures and ODF's are well defined, with the strongest texture corresponding to the sample finish rolled in the ferrite range. The {001}<110> component is present with intermediate intensity for the T_f of 1020°C, decreasing in strength for the temperatures of 870°C and 770°C, and becoming the major orientation in the sample finish rolled at the lowest temperature. The gradual strengthening of the {554}<225> orientation with the decrease in the T_f is evident, as is the small but steady strengthening of the ND fibre. The rotated Goss, {110}<110>, is present with moderate intensity after rolling in the austenite no-recrystallization region, but gradually vanishes at the lowest finish rolling temperature. Comparing this set of textures with the corresponding set austenitized at 1250°C, it should be noted that the maxima are less intense and more scattered for the lower soaking temperature, and also that the differences in texture have been reduced between pairs of finish rolling temperatures. The transition from one T_f to the next is somewhat more gradual, and in particular, the sample finish rolled in the lower intercritical range is at some points closer to the warm rolled specimen.

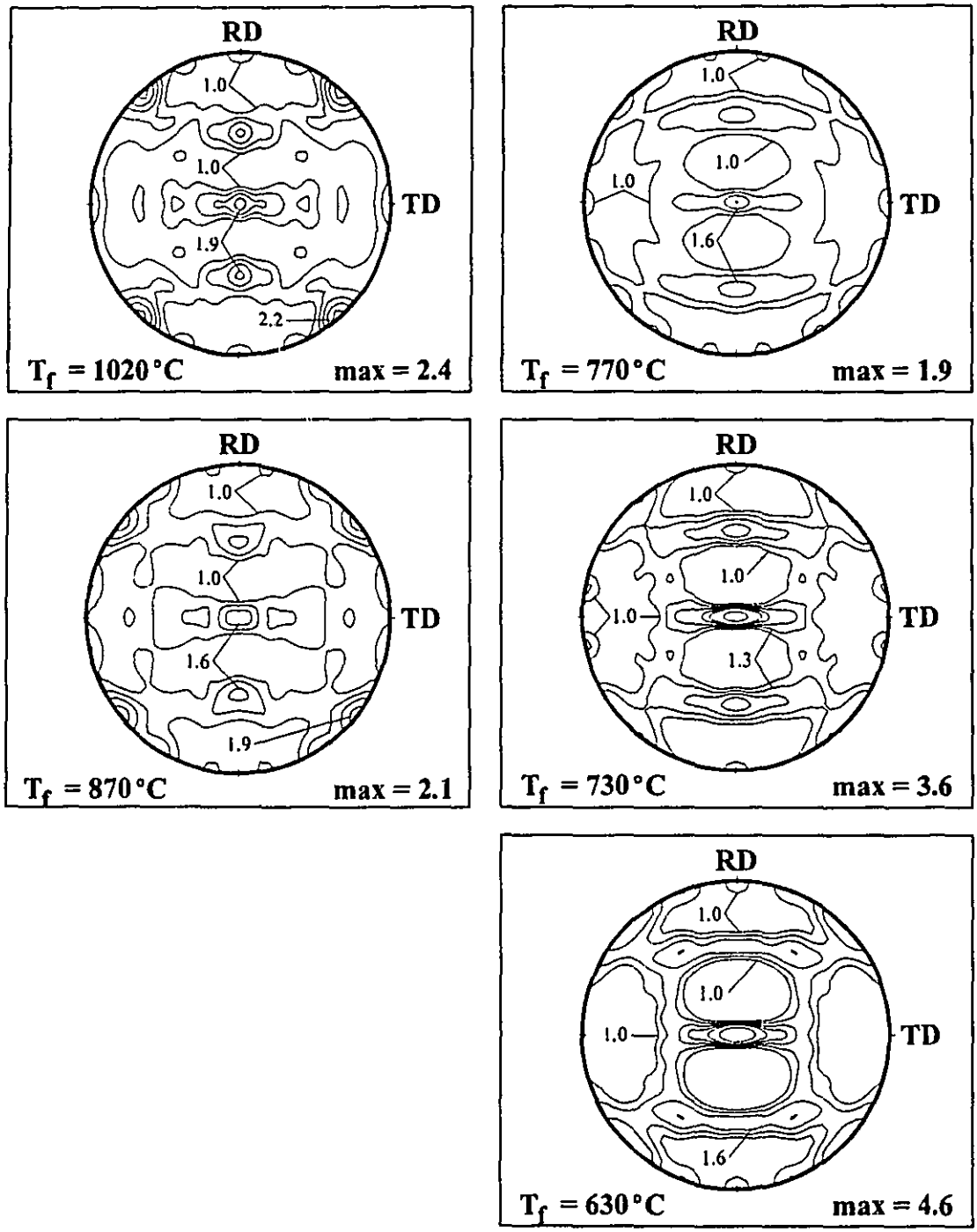

Figure VI.20 (200) pole figures for the plain carbon steel, austenitized at 1150°C and hot rolled to 90% reduction, for several finish rolling temperatures.

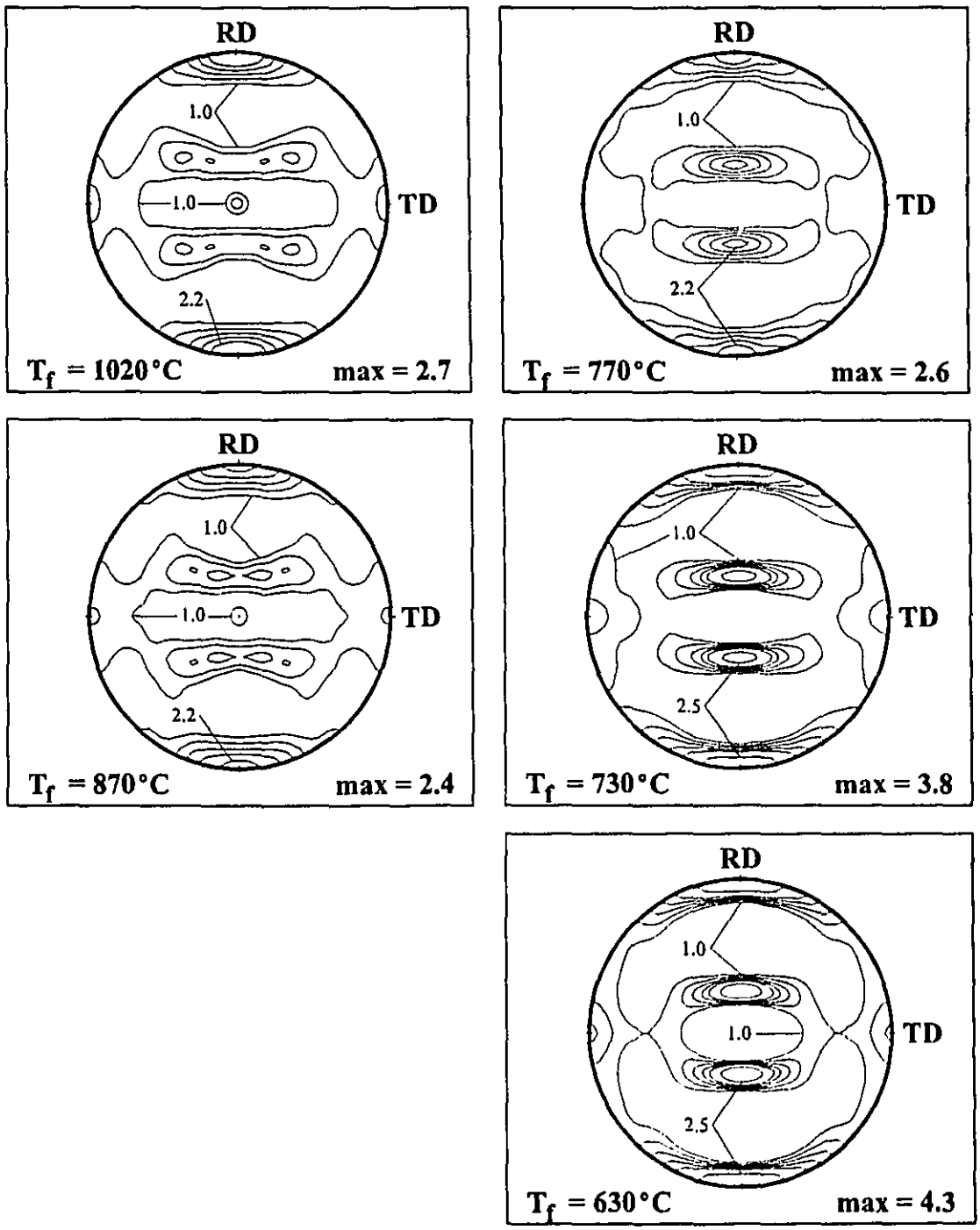

Figure VI.21 (110) pole figures for the plain carbon steel, austenitized at 1150°C and hot rolled to 90% reduction, for several finish rolling temperatures.

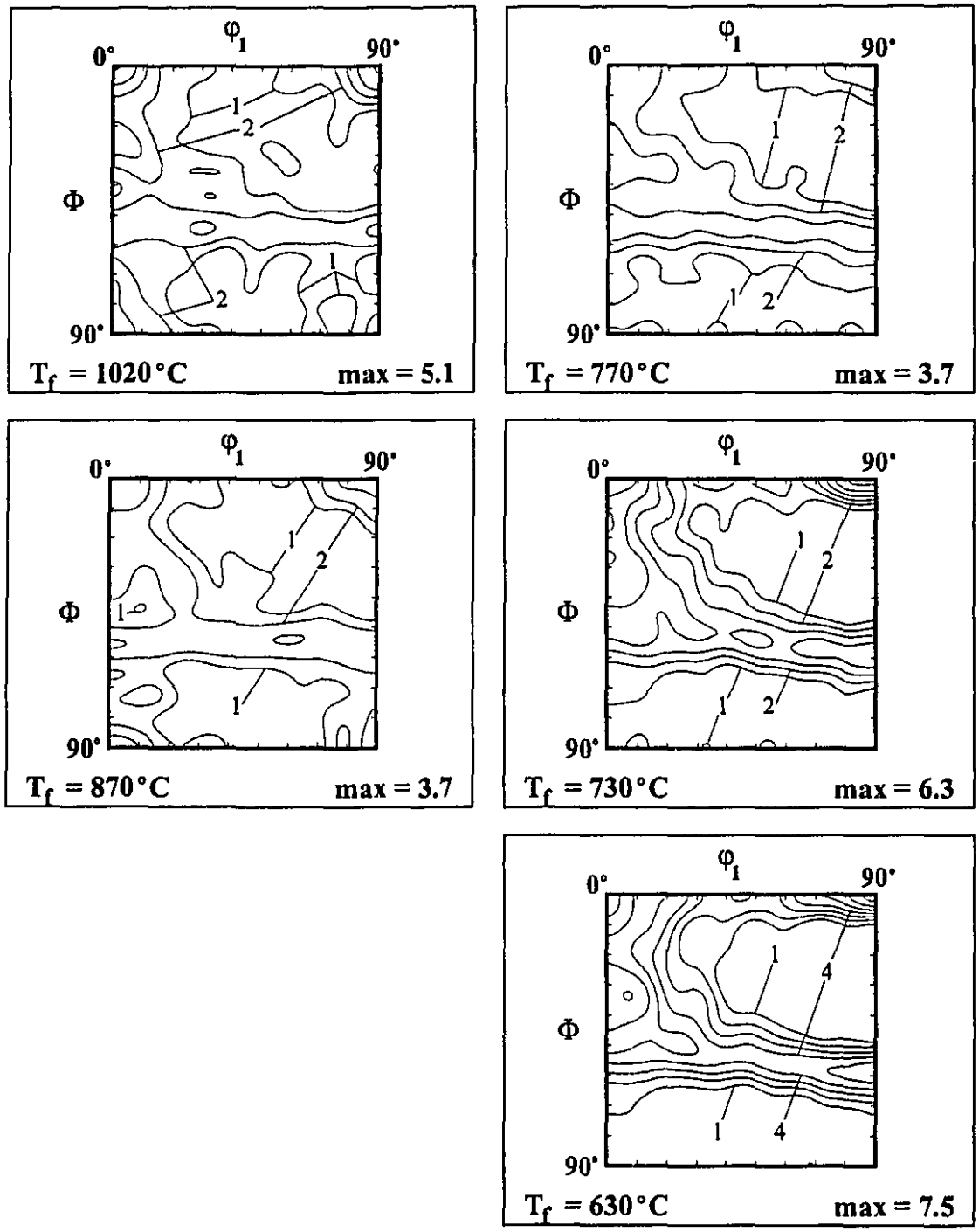

Figure VI.22 φ_2=45° sections of the ODF's for the plain carbon steel, austenitized at 1150°C and hot rolled to 90% reduction, for several finish rolling temperatures.

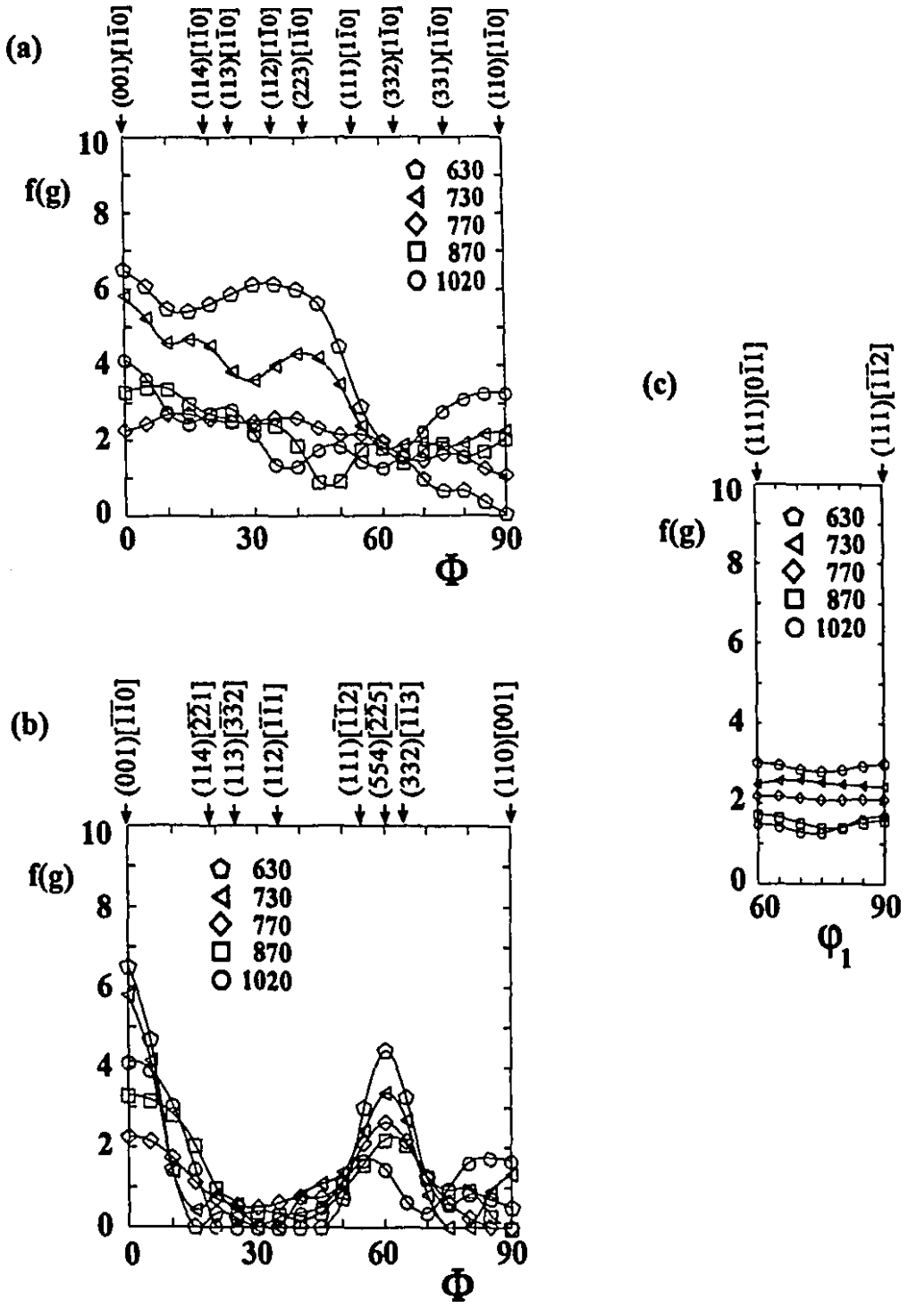

Figure VI.23 (a) RD, (b) TD and (c) ND fibres for the plain carbon steel, austenitized at 1150°C and hot rolled to 90% reduction, for several finish rolling temperatures.

VI.2.1.1 Quenched Samples

Six plain carbon samples were quenched after hot rolling, in order to assess the influence of the cooling rate during transformation on texture development. Only the two finish rolling temperatures within the austenite range were used, thus avoiding the deformation of material already transformed. Austenitizing temperatures of 1250°C and 1150°C, as well as reductions of both 75% and 90% were selected, resulting in three pairs of samples, with the same experimental conditions but for two finish rolling temperatures. The corresponding texture results are shown in Figures VI.24 to VI.29. In general, the textures are weak and flat, with only a few significant characteristics. Both the {001}<110> and {110}<110> orientations were more evident at the higher T_f, while they appeared with either a weaker intensity or were absent at a finishing temperature of 870°C. The ND fibre is not particularly strong, as in the case of the air cooled material, but displays both maxima and minima at intermediate positions within the range $60° < \varphi_1 < 90°$.

Austenitizing at 1250°C and deforming to 90% reduction results in a very low density RD fibre, with only the rotated cube and rotated Goss components mentioned above displaying slightly higher intensities. The TD fibre is characterized by some other small maxima, but all with intensities under 3. After rolling to 75% reduction, some components grow stronger along the RD and TD fibres, in several places in the former case and mainly around {554}<225> in the latter. This last orientation was better defined when the austenitizing temperature was 1150°C; it is stronger for the 870°C finish rolling temperature but is also evident at T_f=1020°C.

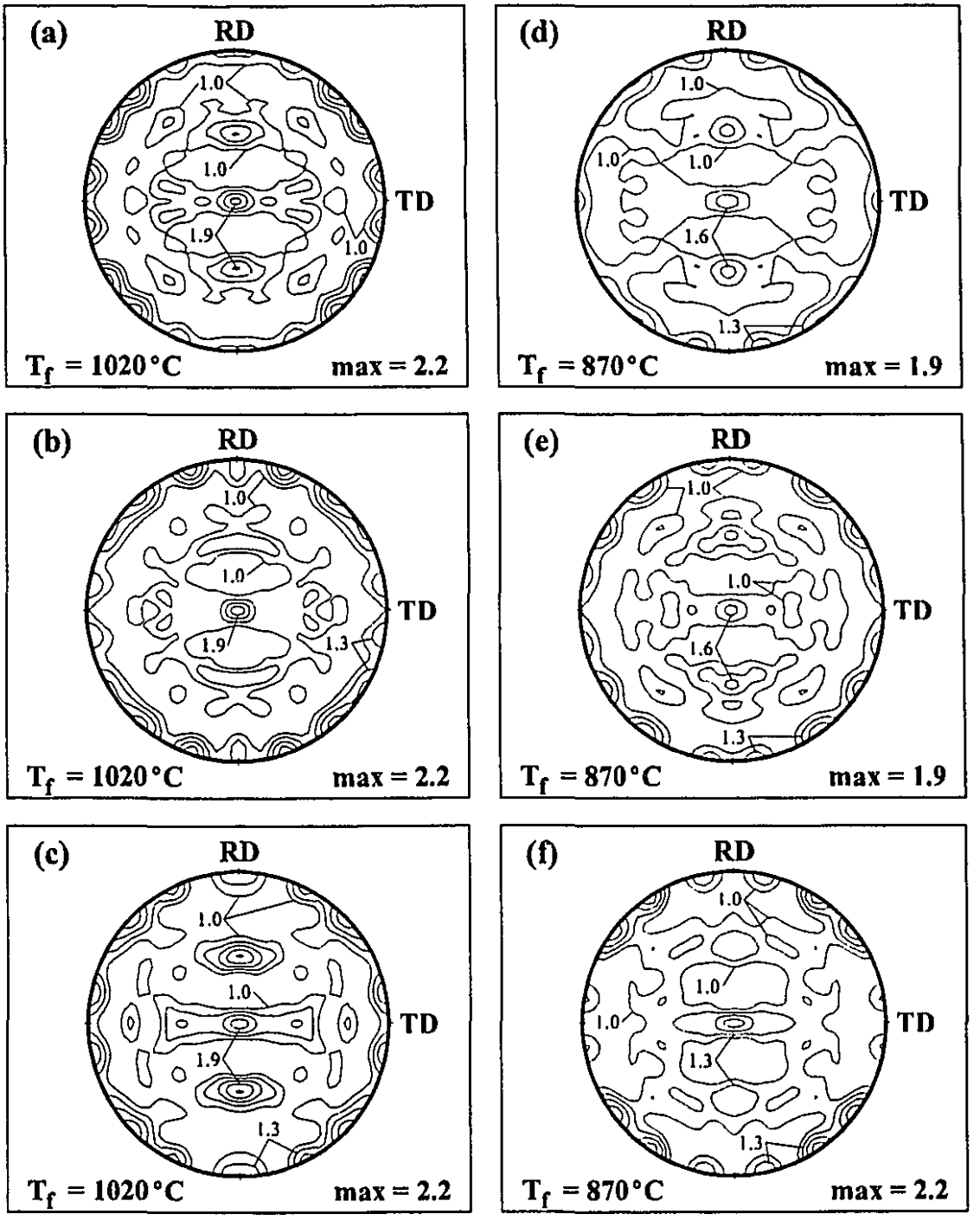

Figure VI.24 (200) pole figures for the plain carbon steel, quenched samples, for two finish rolling temperatures. Other parameters as follows: (a) and (d), T_γ = 1250°C, 90% reduction; (b) and (e), T_γ = 1250°C, 75% reduction; (c) and (f), T_γ = 1150°C, 90% reduction.

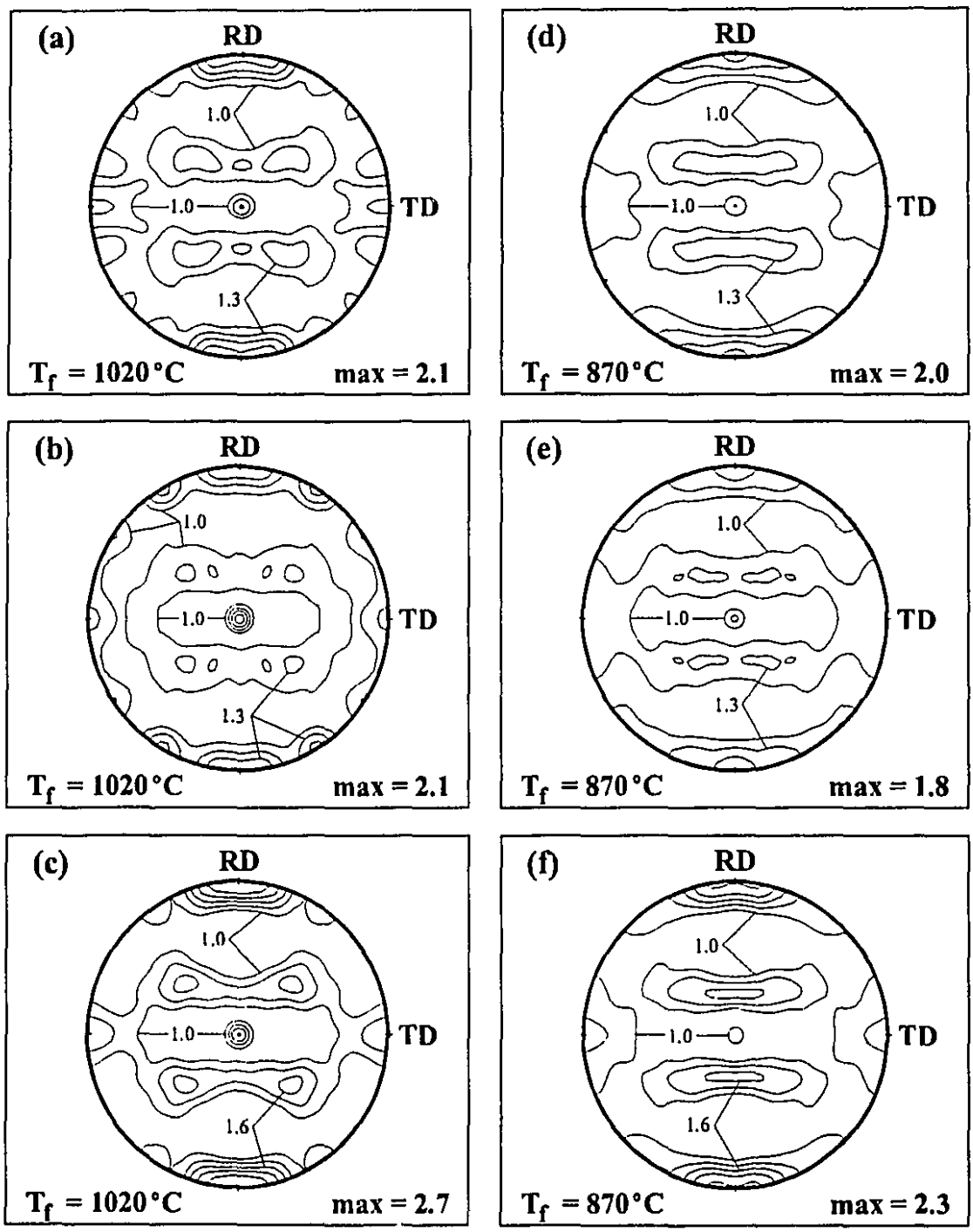

Figure VI.25 (110) pole figures for the plain carbon steel, quenched samples, for two finish rolling temperatures. Other parameters as follows: (a) and (d), T_γ = 1250°C, 90% reduction; (b) and (e), T_γ = 1250°C, 75% reduction; (c) and (f), T_γ = 1150°C, 90% reduction.

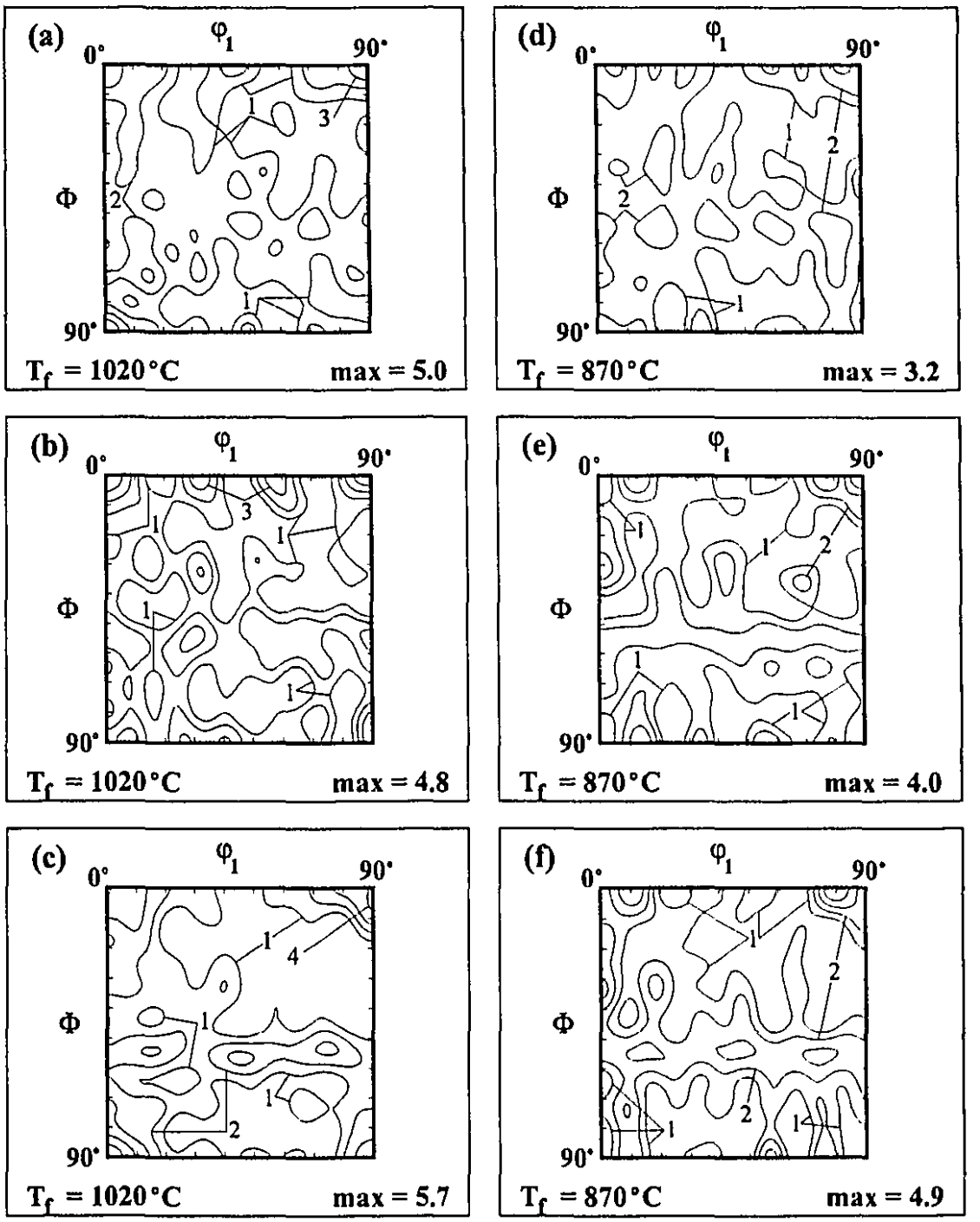

Figure VI.26 φ_2=45° sections of the ODF's for the plain carbon steel, quenched samples, for two finish rolling temperatures. Other parameters as follows: (a) and (d), T_γ = 1250°C, 90% reduction; (b) and (e), T_γ = 1250°C, 75% reduction; (c) and (f), T_γ = 1150°C, 90% reduction.

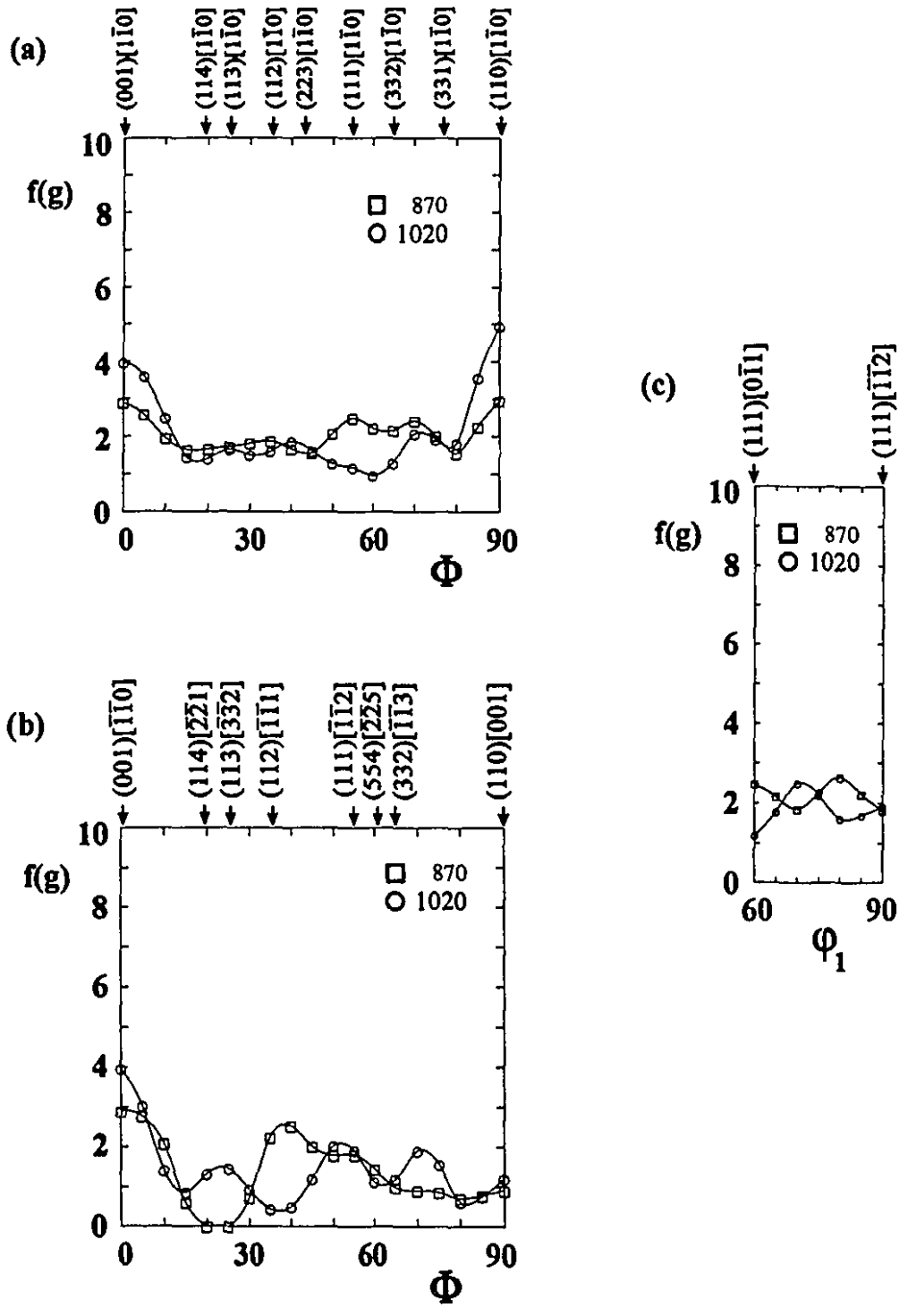

Figure VI.27 (a) RD, (b) TD and (c) ND fibres for the plain carbon steel, quenched samples, austenitized at 1250°C and hot rolled to 90% reduction, for two finish rolling temperatures.

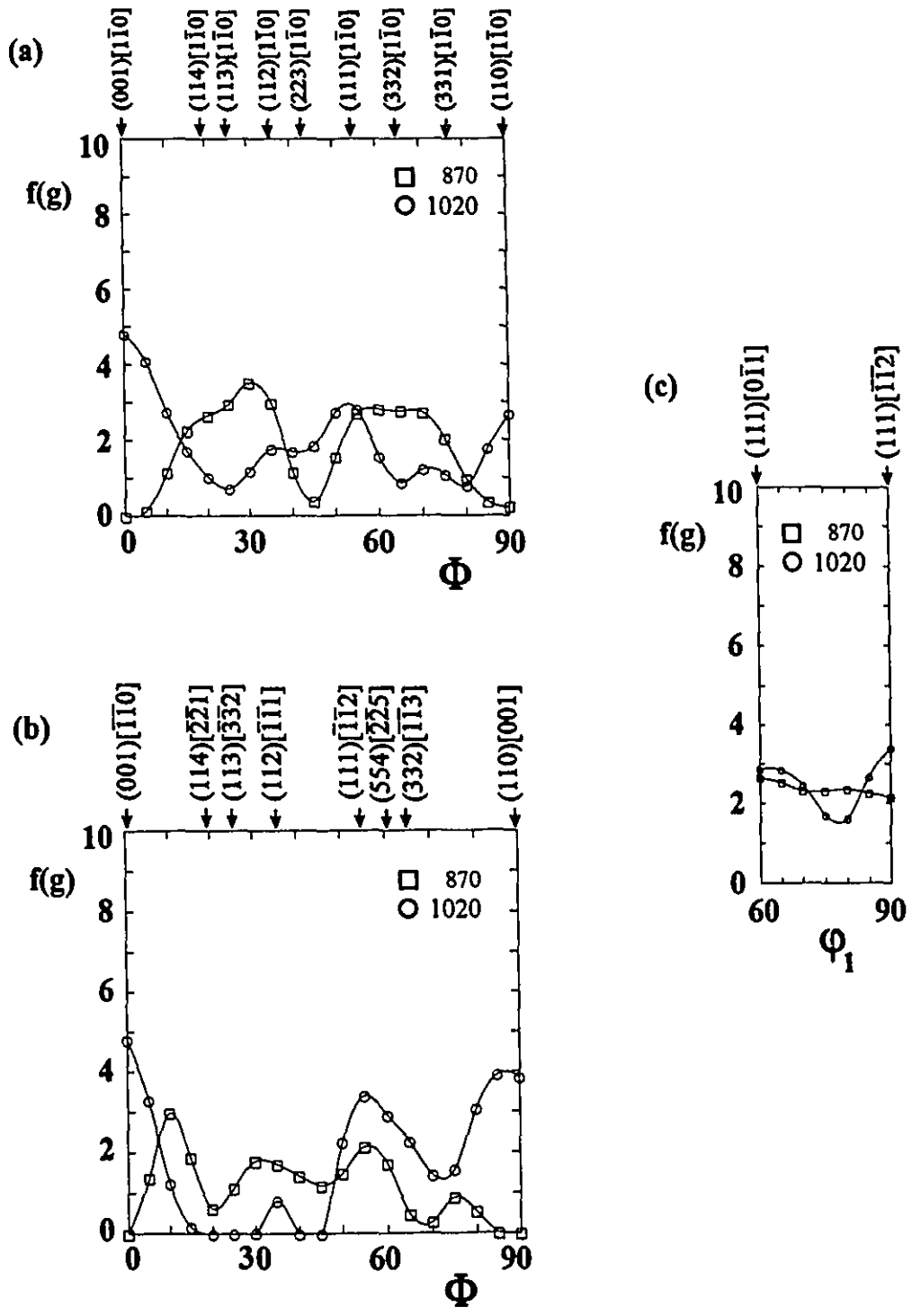

Figure VI.28 (a) RD, (b) TD and (c) ND fibres for the plain carbon steel, quenched samples, austenitized at 1250°C and hot rolled to 75% reduction, for two finish rolling temperatures.

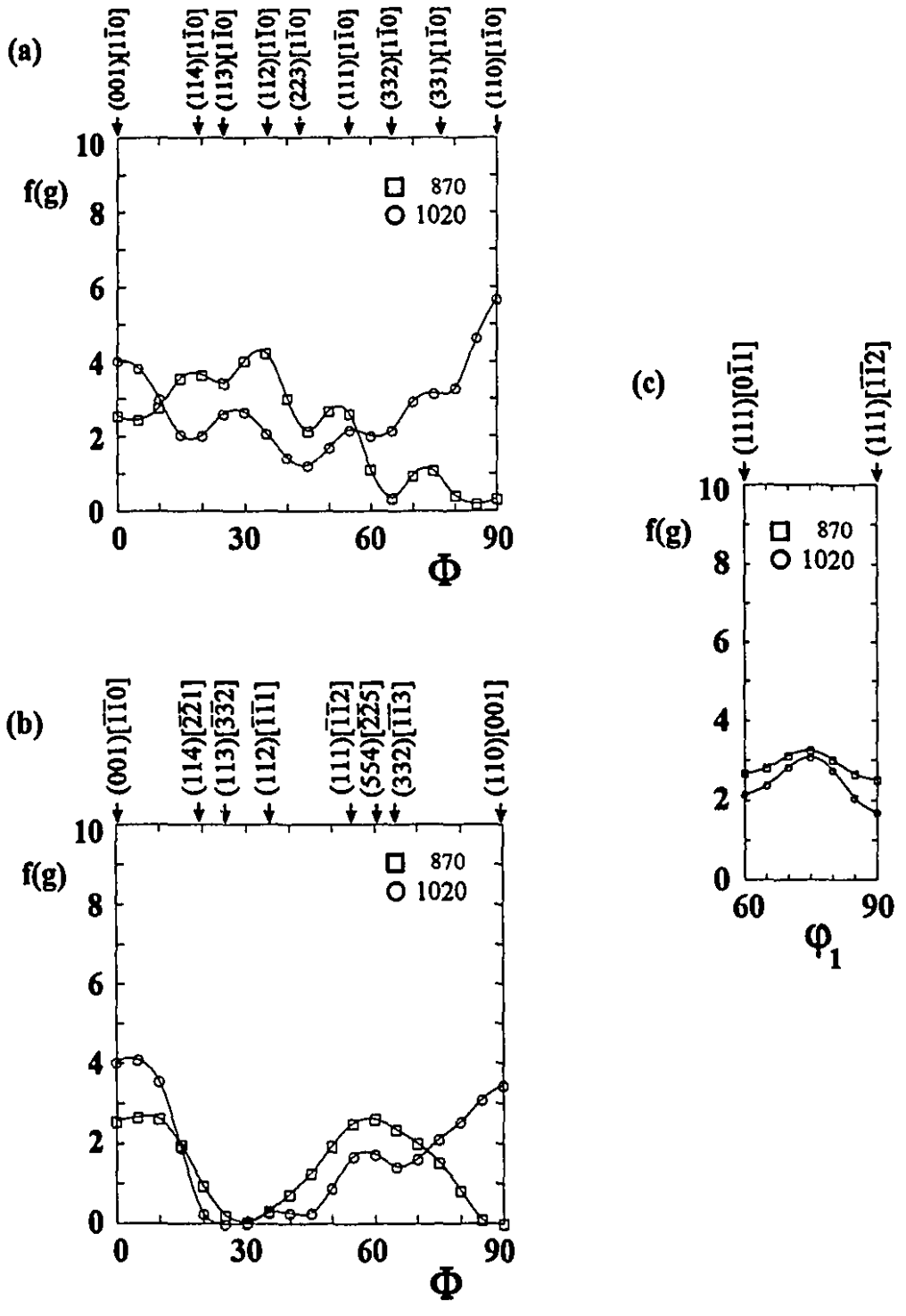

Figure VI.29 (a) RD, (b) TD and (c) ND fibres for the plain carbon steel, quenched samples, austenitized at 1150°C and hot rolled to 90% reduction, for two finish rolling temperatures.

VI.2.2 Niobium Microalloyed Steel

The first group of texture results for the niobium microalloyed steel is presented in Figures VI.30 to VI.33; these correspond to an austenitizing temperature of 1250°C and a reduction of 90%. The pole figures for each finish rolling temperature are all well defined, Figures VI.30 and VI.31, the ones of the sample finish rolled at 1020°C having the lowest intensities; in the latter case, the maxima are located around the {001}<110> orientation. For finishing temperatures of 870°C down to 630°C, the pole distribution is similar, and, as before, the highest intensities are attained after ferrite rolling. All the φ_2=45° sections display the presence of ND and RD fibre components, including a strong {001}<110> orientation, Figure VI.32. Additionally, the ND fibre appears shifted towards the {211}<113> component, which is also located on this section of the ODF (see Figure VI.11). From the description in terms of fibres, Figure VI.33, it is clear that the texture is quite strong around the {113}-{112}<110> section of the RD fibre for all samples except the one rolled within the austenite recrystallization range. The rotated cube remains strong for all finish rolling temperatures, and the rotated Goss decreases in intensity as the temperature is decreased. The sample finish rolled at 630°C displays a strong peak close to {554}<225>, and is the only one with a relatively strong and stable ND fibre.

In the second group of tests for this steel, Figures VI.34 to VI.37, austenitized at 1250°C and rolled to 75% reduction, the textures are roughly half as intense as in the previous case. The behaviour is similar, regardless of the finish rolling temperature, and there are no particular peaks in the fibres. Still present are the {001}<110> and {110}<110> components, and there is also a spread around the

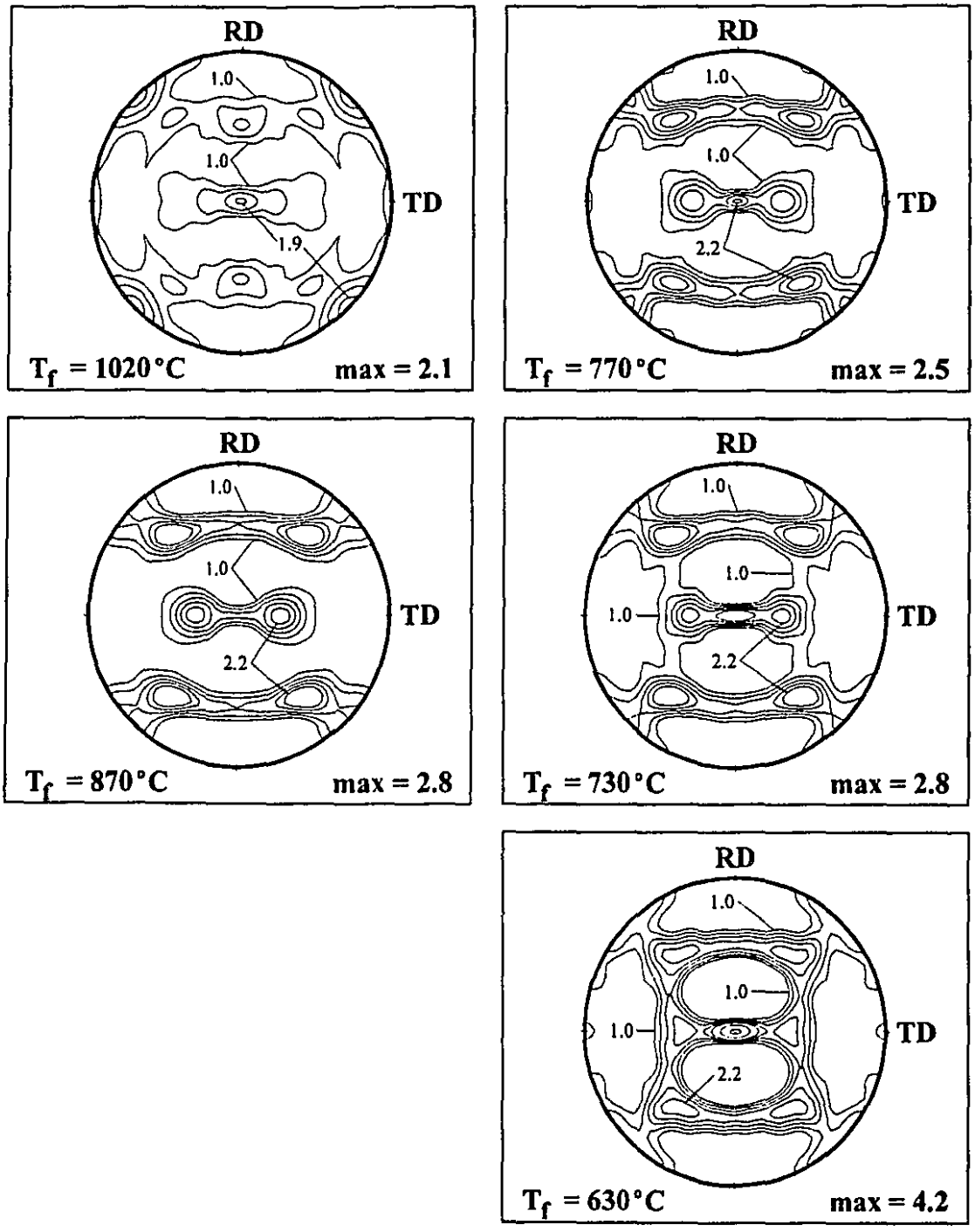

Figure VI.30 (200) pole figures for the niobium microalloyed steel, austenitized at 1250°C and hot rolled to 90% reduction, for several finish rolling temperatures.

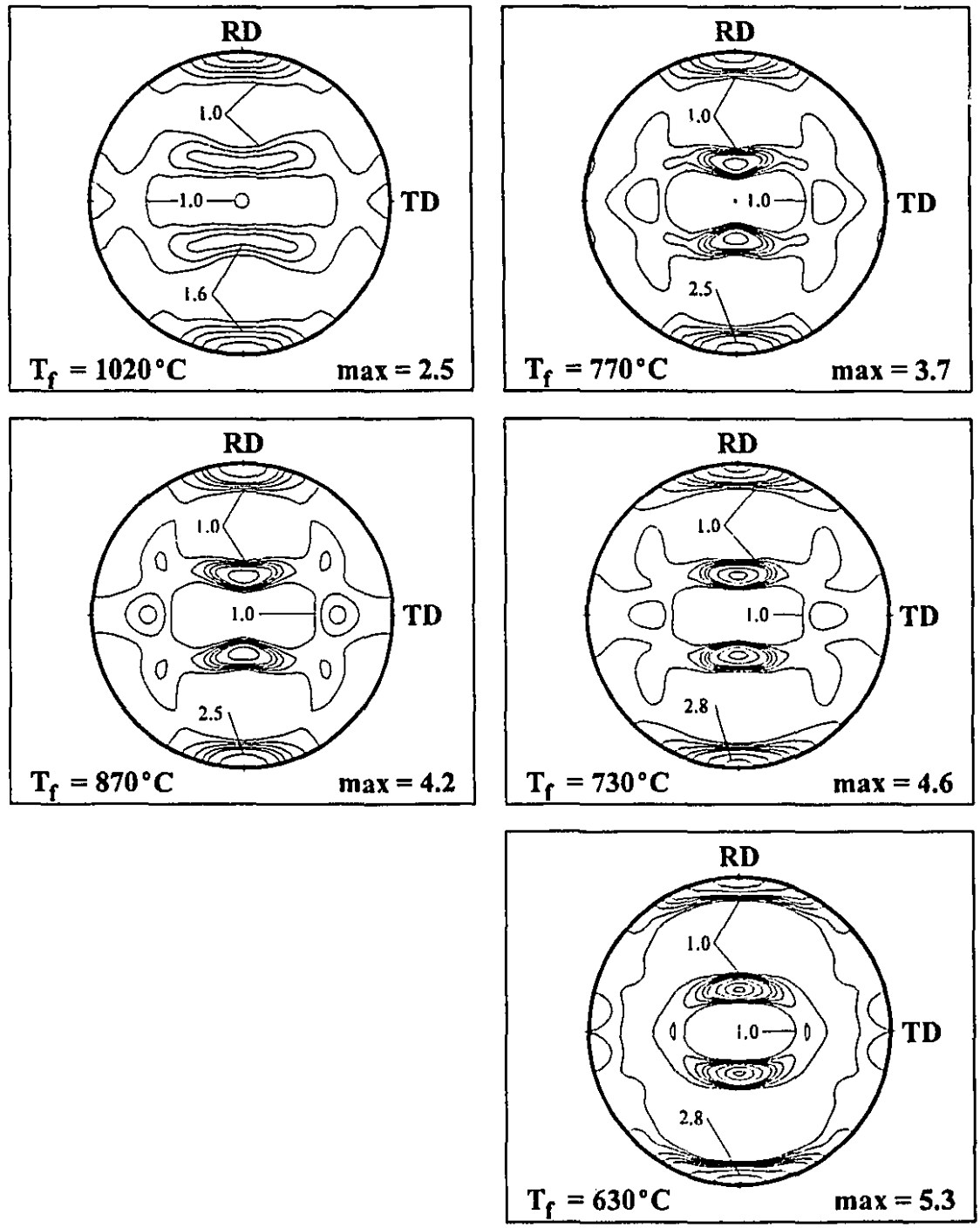

Figure VI.31 (110) pole figures for the niobium microalloyed steel, austenitized at 1250°C and hot rolled to 90% reduction, for several finish rolling temperatures.

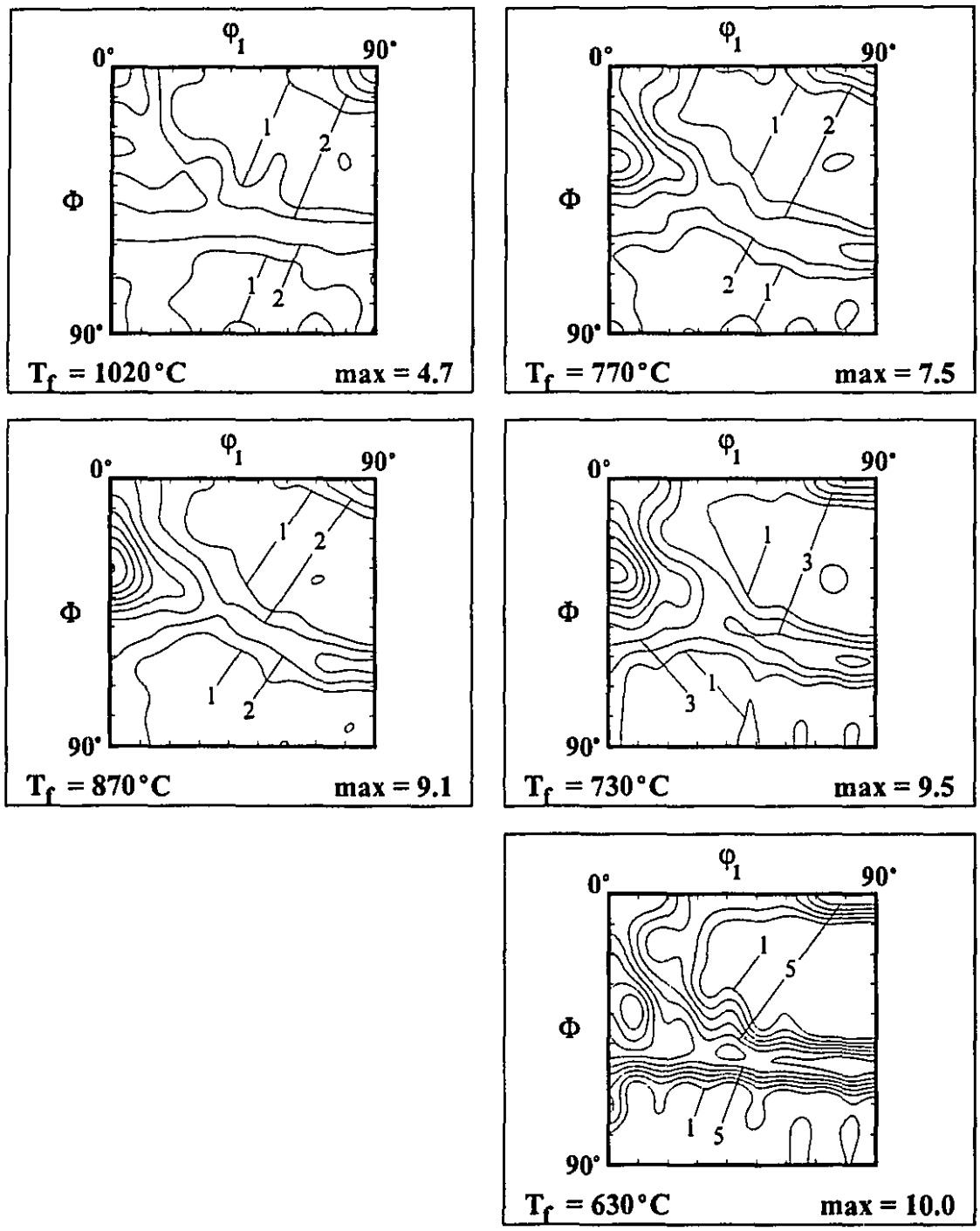

Figure VI.32 φ_2=45° sections of the ODF's for the niobium microalloyed steel, austenitized at 1250°C and hot rolled to 90% reduction, for several finish rolling temperatures.

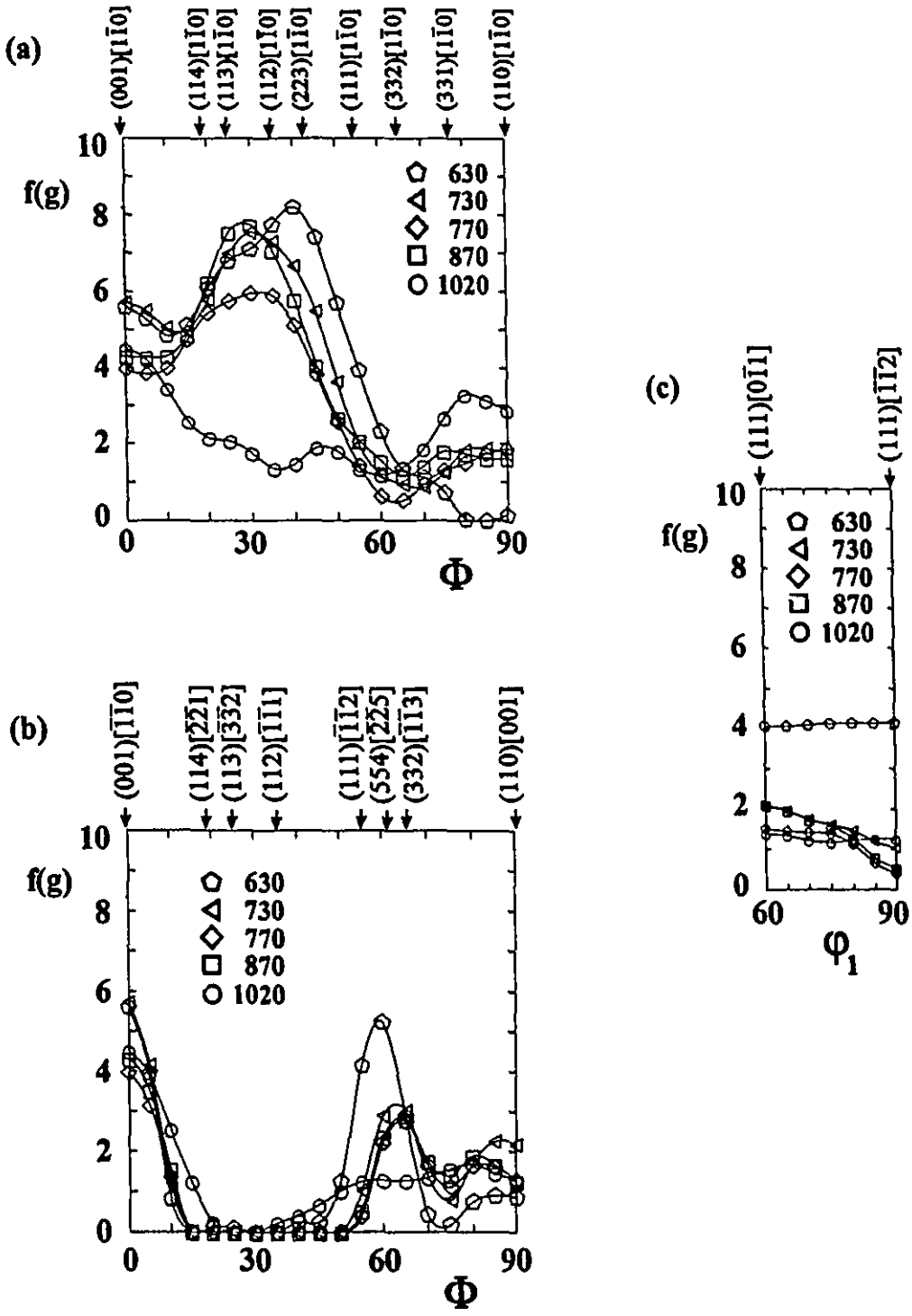

Figure VI.33 (a) RD, (b) TD and (c) ND fibres for the niobium microalloyed steel, austenitized at 1250°C and hot rolled to 90% reduction, for several finish rolling temperatures.

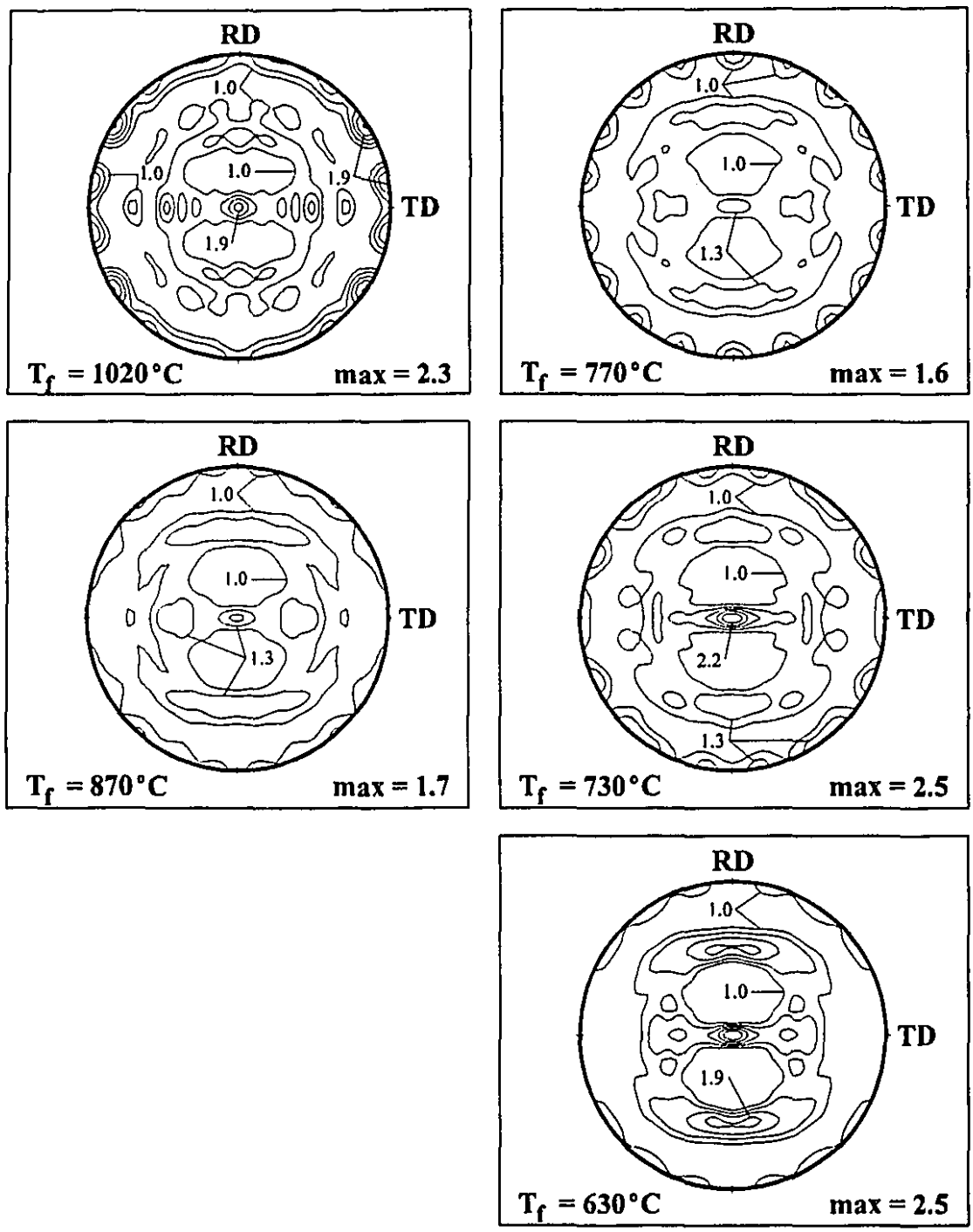

Figure VI.34 (200) pole figures for the niobium microalloyed steel, austenitized at 1250°C and hot rolled to 75% reduction, for several finish rolling temperatures.

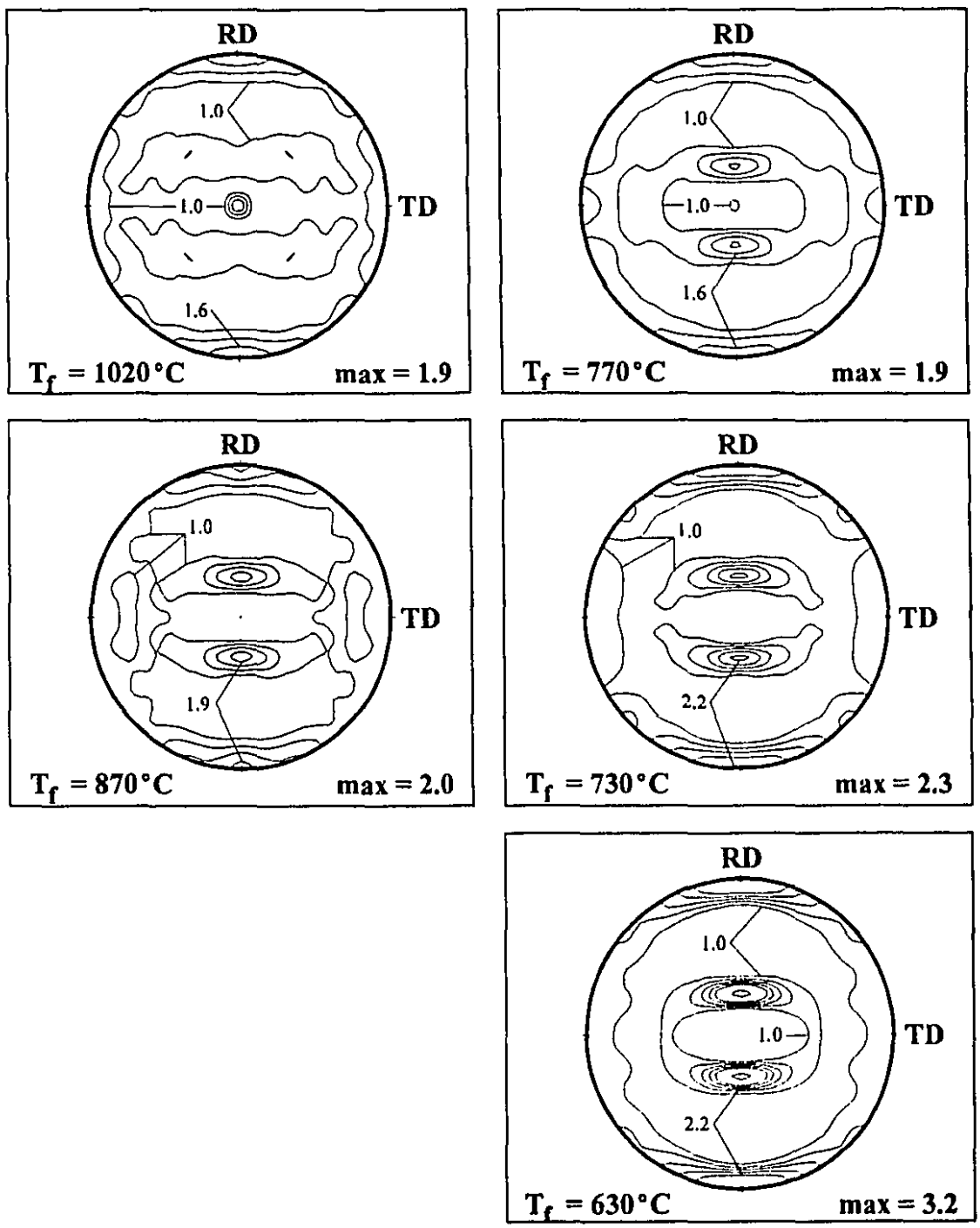

Figure VI.35 (110) pole figures for the niobium microalloyed steel, austenitized at 1250°C and hot rolled to 75% reduction, for several finish rolling temperatures.

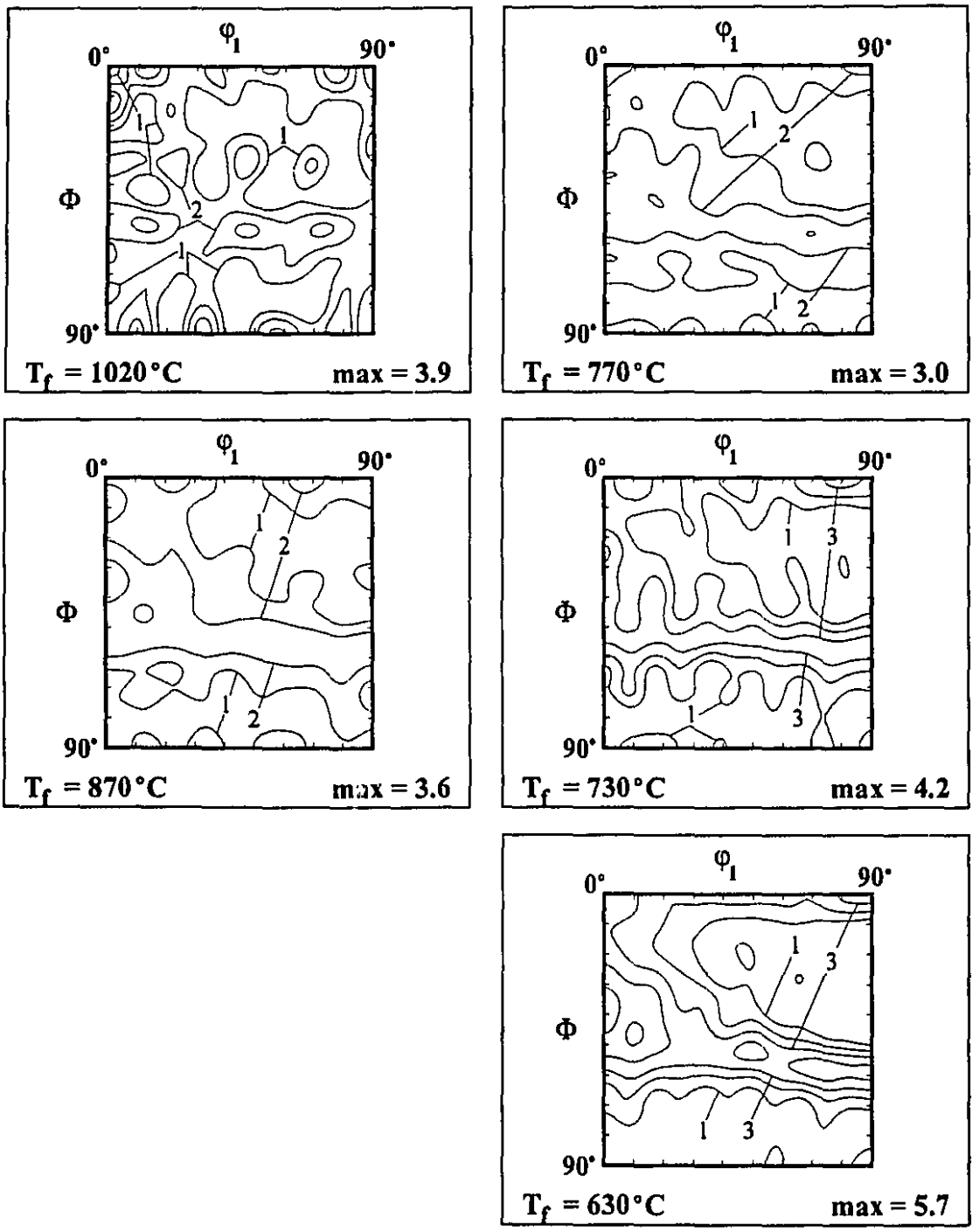

Figure VI.36 φ_2=45° sections of the ODF's for the niobium microalloyed steel, austenitized at 1250°C and hot rolled to 75% reduction, for several finish rolling temperatures.

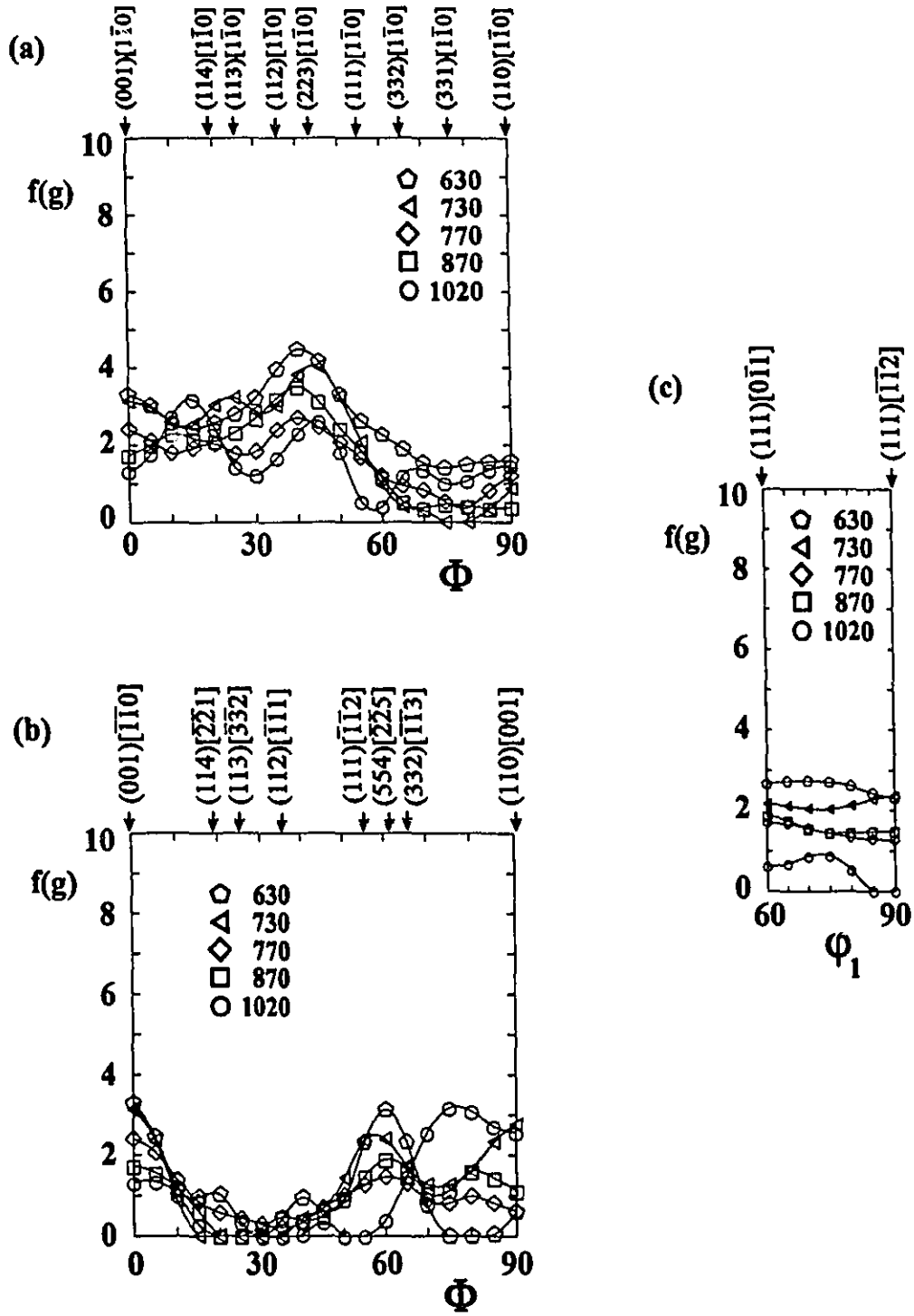

Figure VI.37 (a) RD, (b) TD and (c) ND fibres for the niobium microalloyed steel, austenitized at 1250°C and hot rolled to 75% reduction, for several finish rolling temperatures.

{112}<110> orientation. Finally, the ND fibre remains with intensities always lower than 3.

Controlled rolling with a deformation of 90%, after austenitizing at 1150°C, produced the strongest textures in the ferrite rolling sample, with an intensity of f(g)=9.3 for the {112}<110> component, Figures VI.38 to VI.41. The next most important texture components in this sample are the {001}<110> and {554}<225> orientations. The ND fibre is the strongest in this group, although it remains below f(g)=4. As can be seen in Figure VI.41, the texture evolved gradually as the finish rolling temperature was decreased.

VI.2.2.1 Quenched Samples

A group of six niobium microalloyed steel samples were quenched immediately after deformation, using the same processing parameters as described for the plain carbon steel in section VI.2.1.1. Figures VI.42 to VI.47 display the texture results obtained. Contrary to the observations reported above for the plain carbon steel, fairly strong textures were obtained for the samples finish rolled at 870°C, in the three cases studied. As the T_f is decreased, there is a clear enhancement of the {113}-{112}<110> and {554}<225> components. This is accompanied by a slight increase in the strength of the {001}<110> component when the reduction is 90%, and other minor changes which are readily evident in the RD, TD and ND fibres of Figures VI.45 to VI.47.

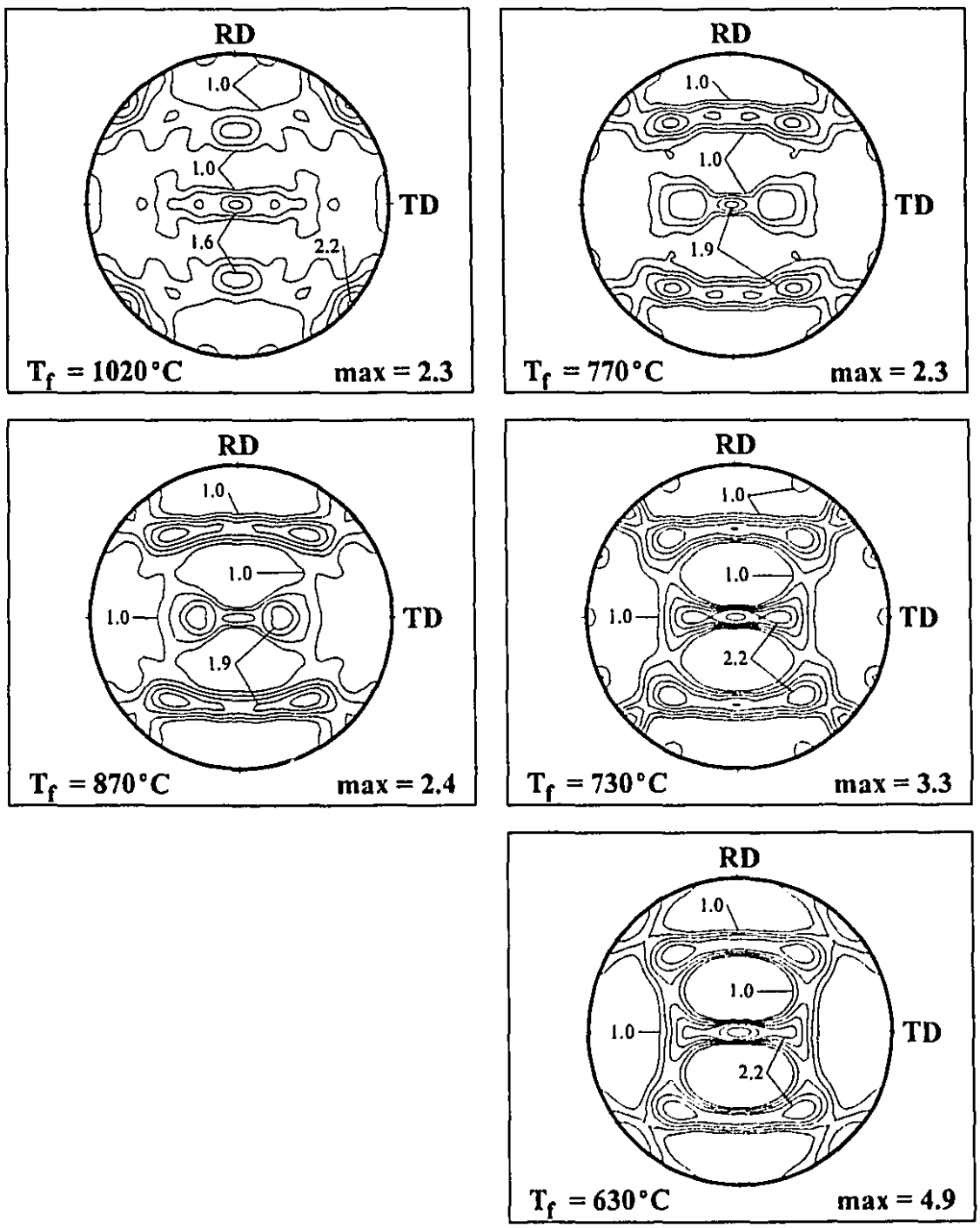

Figure VI.38 (200) pole figures for the niobium microalloyed steel, austenitized at 1150°C and hot rolled to 90% reduction, for several finish rolling temperatures.

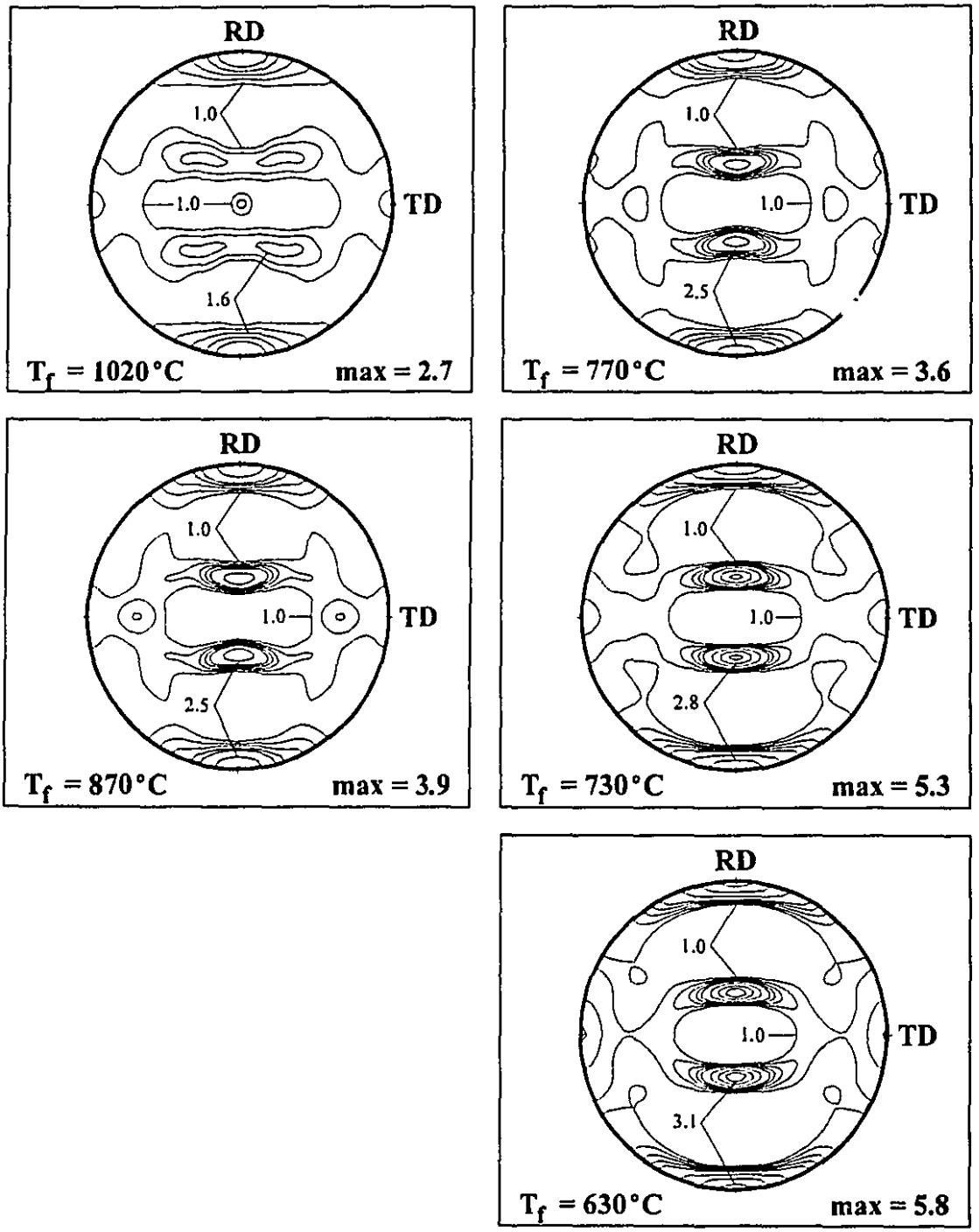

Figure VI.39 (110) pole figures for the niobium microalloyed steel, austenitized at 1150°C and hot rolled to 90% reduction, for several finish rolling temperatures.

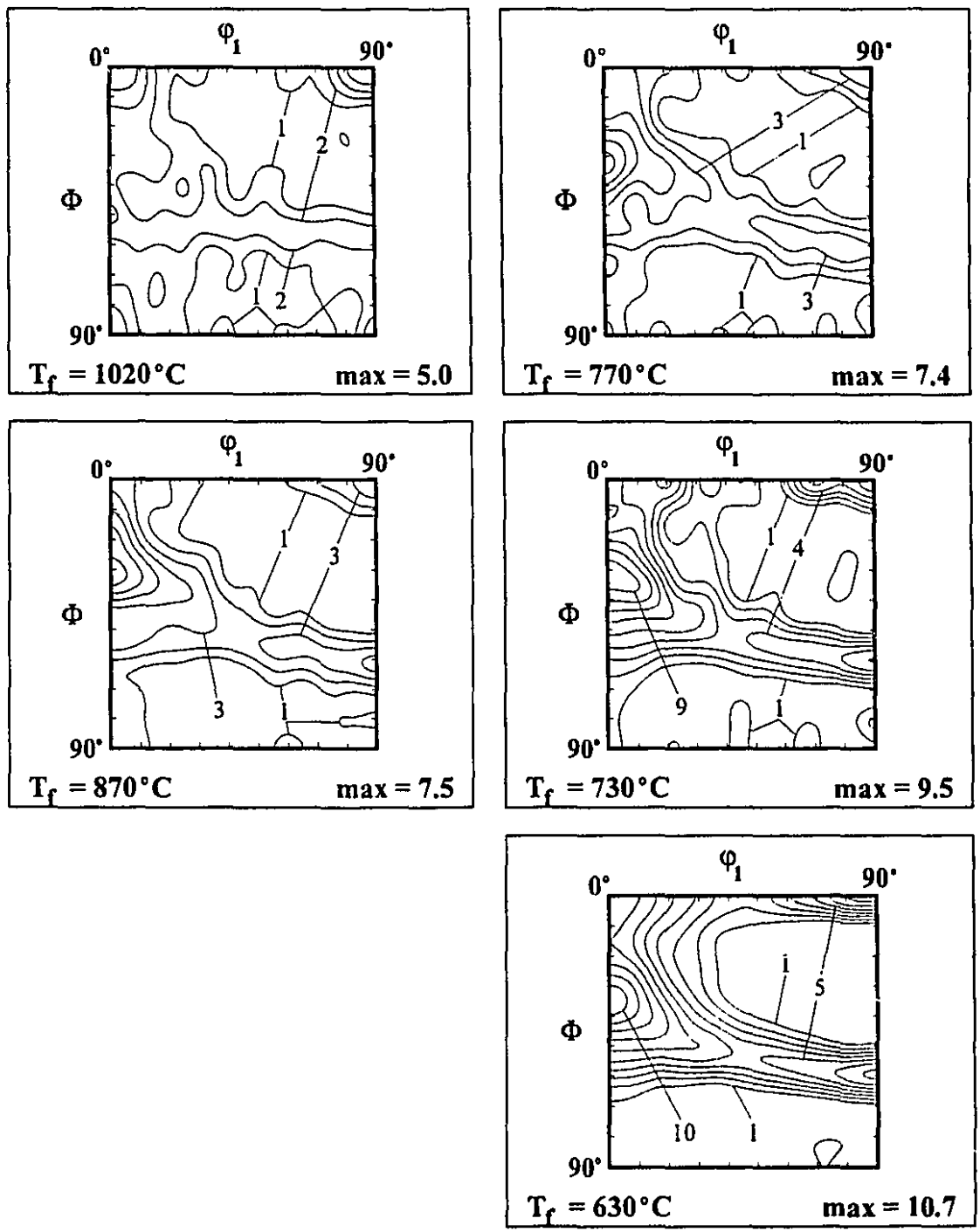

Figure VI.40 φ_2=45° sections of the ODF's for the niobium microalloyed steel, austenitized at 1150°C and hot rolled to 90% reduction, for several finish rolling temperatures.

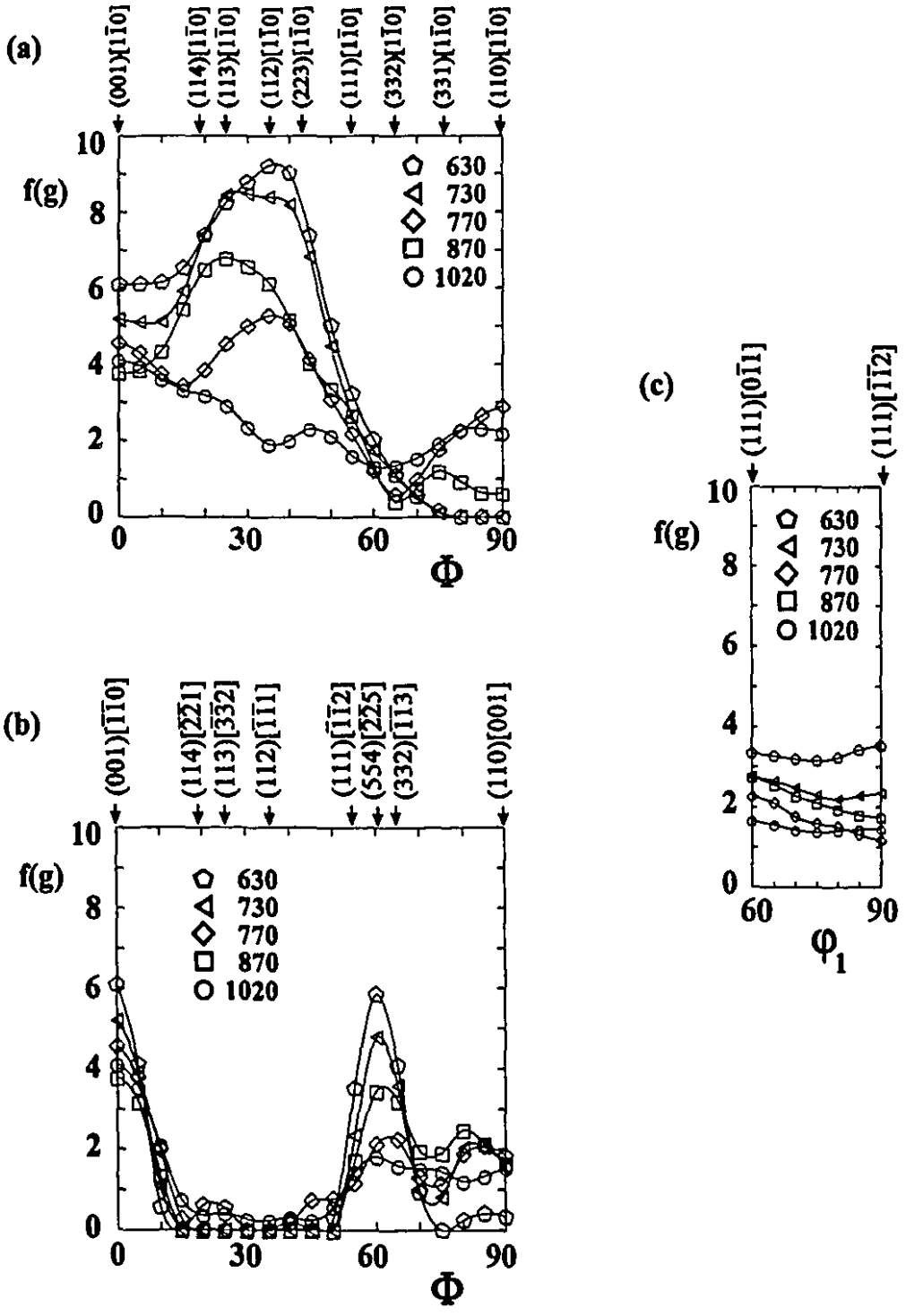

Figure VI.41 (a) RD, (b) TD and (c) ND fibres for the niobium microalloyed steel, austenitized at 1150°C and hot rolled to 90% reduction, for several finish rolling temperatures.

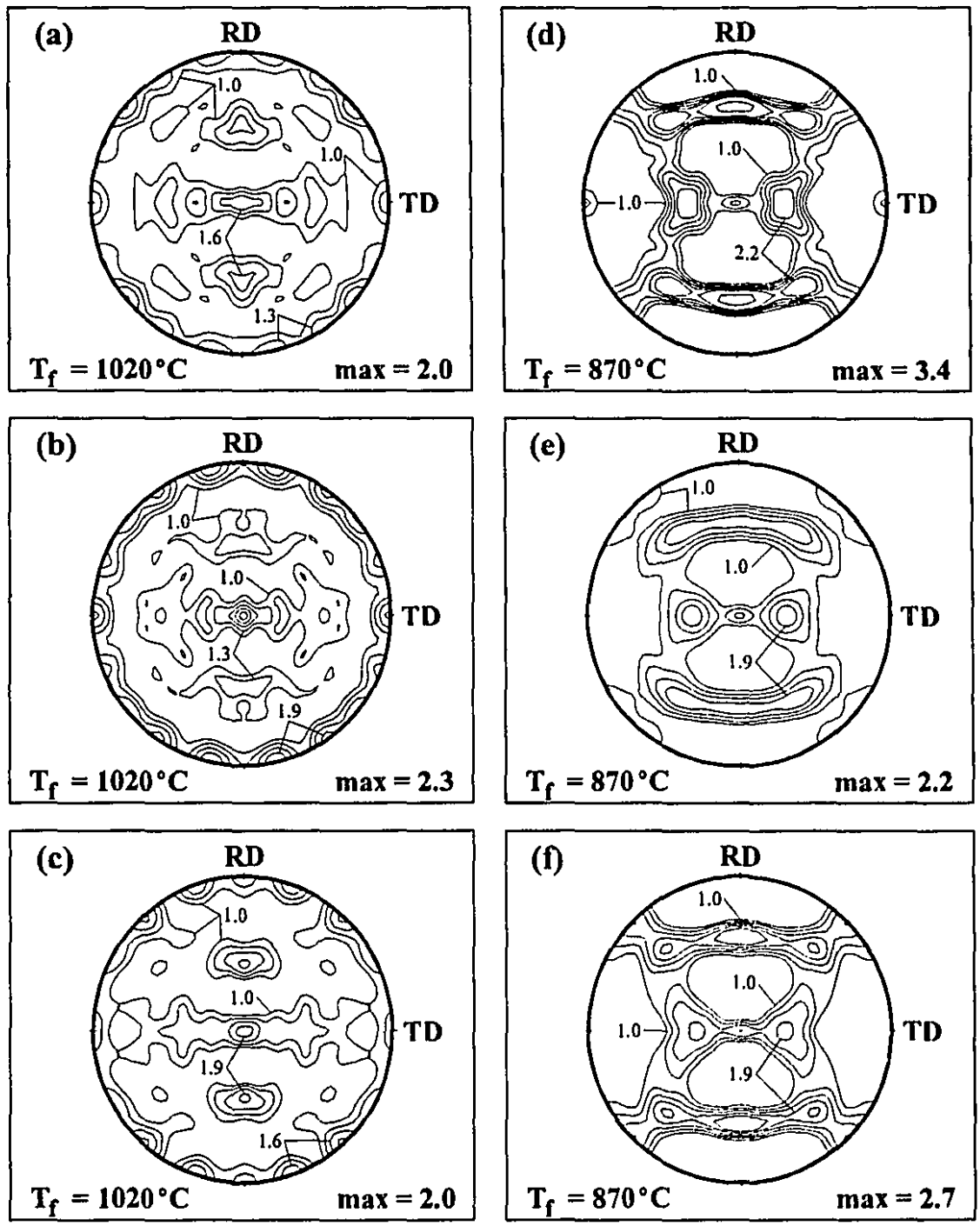

Figure VI.42 (200) pole figures for the niobium microalloyed steel, quenched samples, for two finish rolling temperatures. Other parameters as follows: (a) and (d), T_γ = 1250°C, 90% reduction; (b) and (e), T_γ = 1250°C, 75% reduction; (c) and (f), T_γ = 1150°C, 90% reduction.

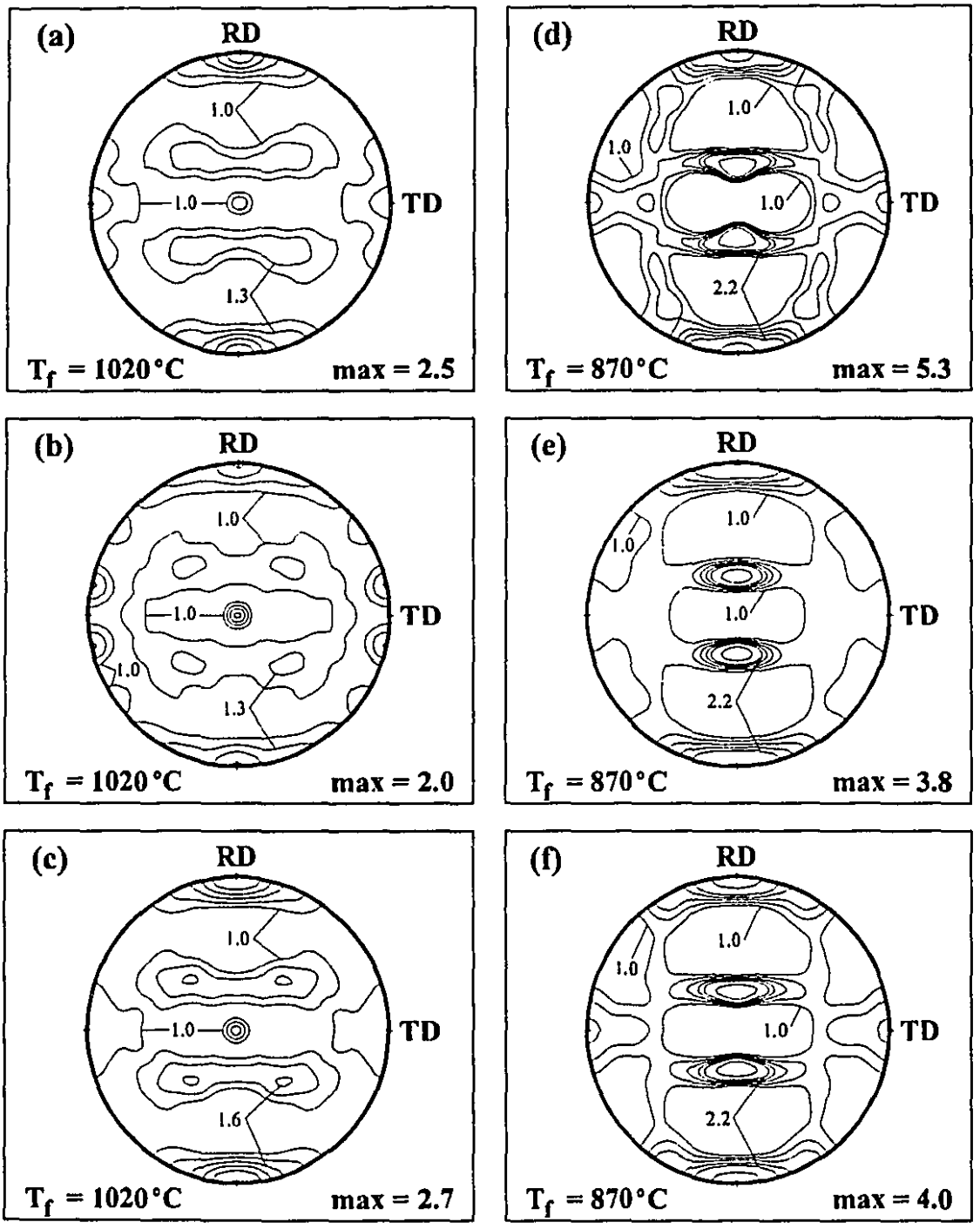

Figure VI.43 (110) pole figures for the niobium microalloyed steel, quenched samples, for two finish rolling temperatures. Other parameters as follows: (a) and (d), T_γ = 1250°C, 90% reduction; (b) and (e), T_γ = 1250°C, 75% reduction; (c) and (f), T_γ = 1150°C, 90% reduction.

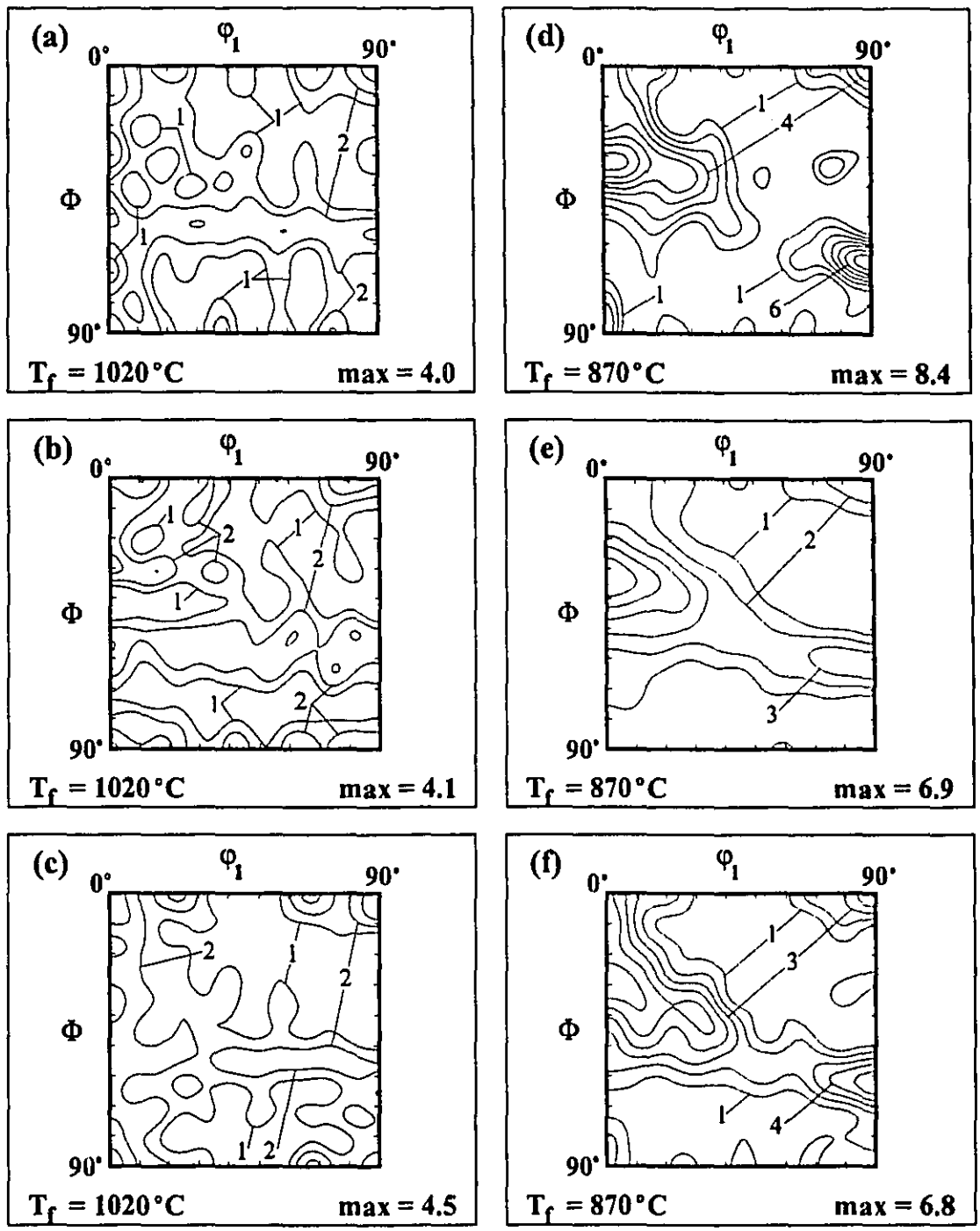

Figure VI.44 φ_2=45° sections of the ODF's of the niobium microalloyed steel, quenched samples, for two finish rolling temperatures. Other parameters as follows: (a) and (d), T_γ = 1250°C, 90% reduction; (b) and (e), T_γ = 1250°C, 75% reduction; (c) and (f), T_γ = 1150°C, 90% reduction.

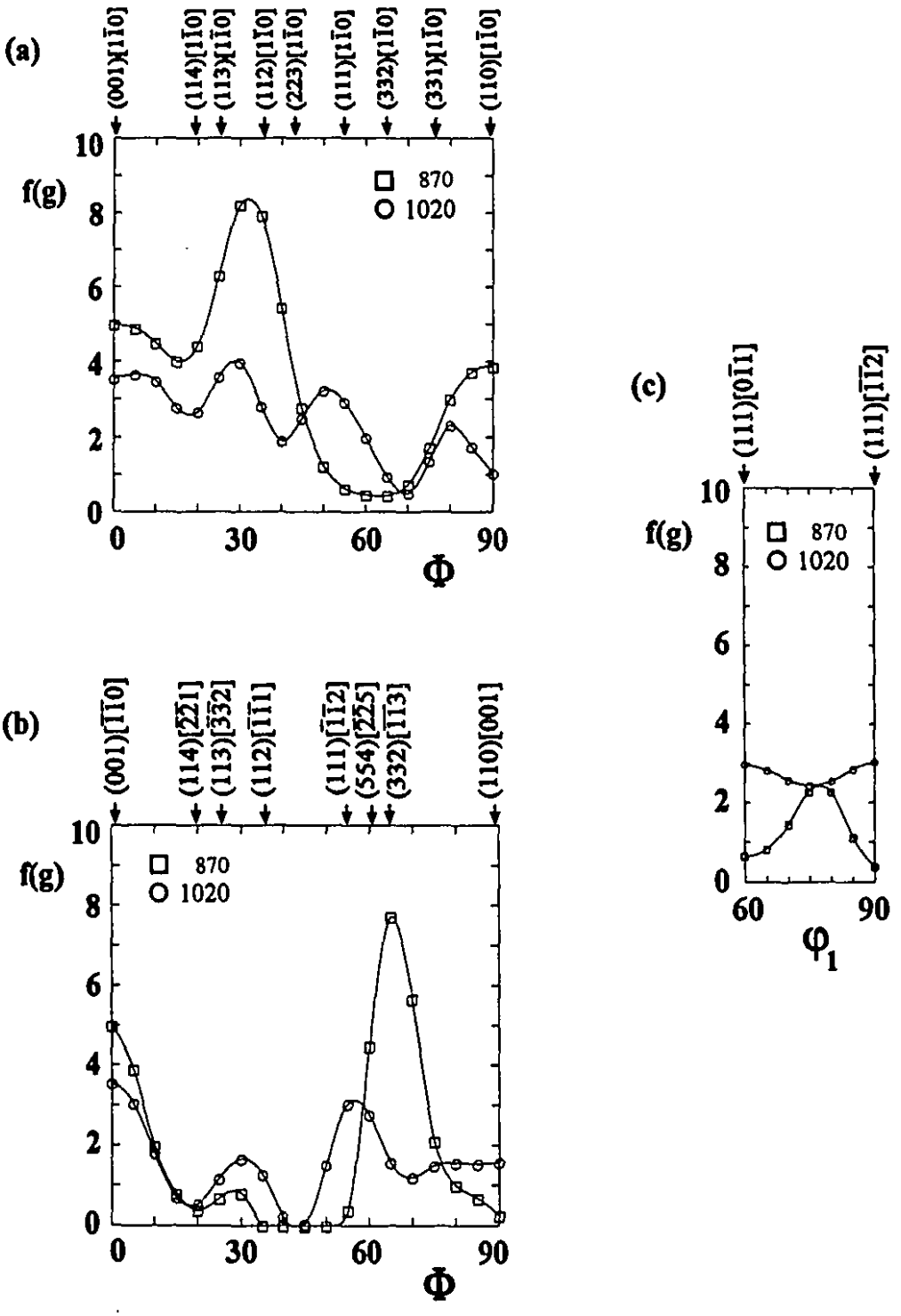

Figure VI.45 (a) RD, (b) TD and (c) ND fibres for the niobium microalloyed steel, quenched samples, austenitized at 1250°C and hot rolled to 90% reduction, for two finish rolling temperatures.

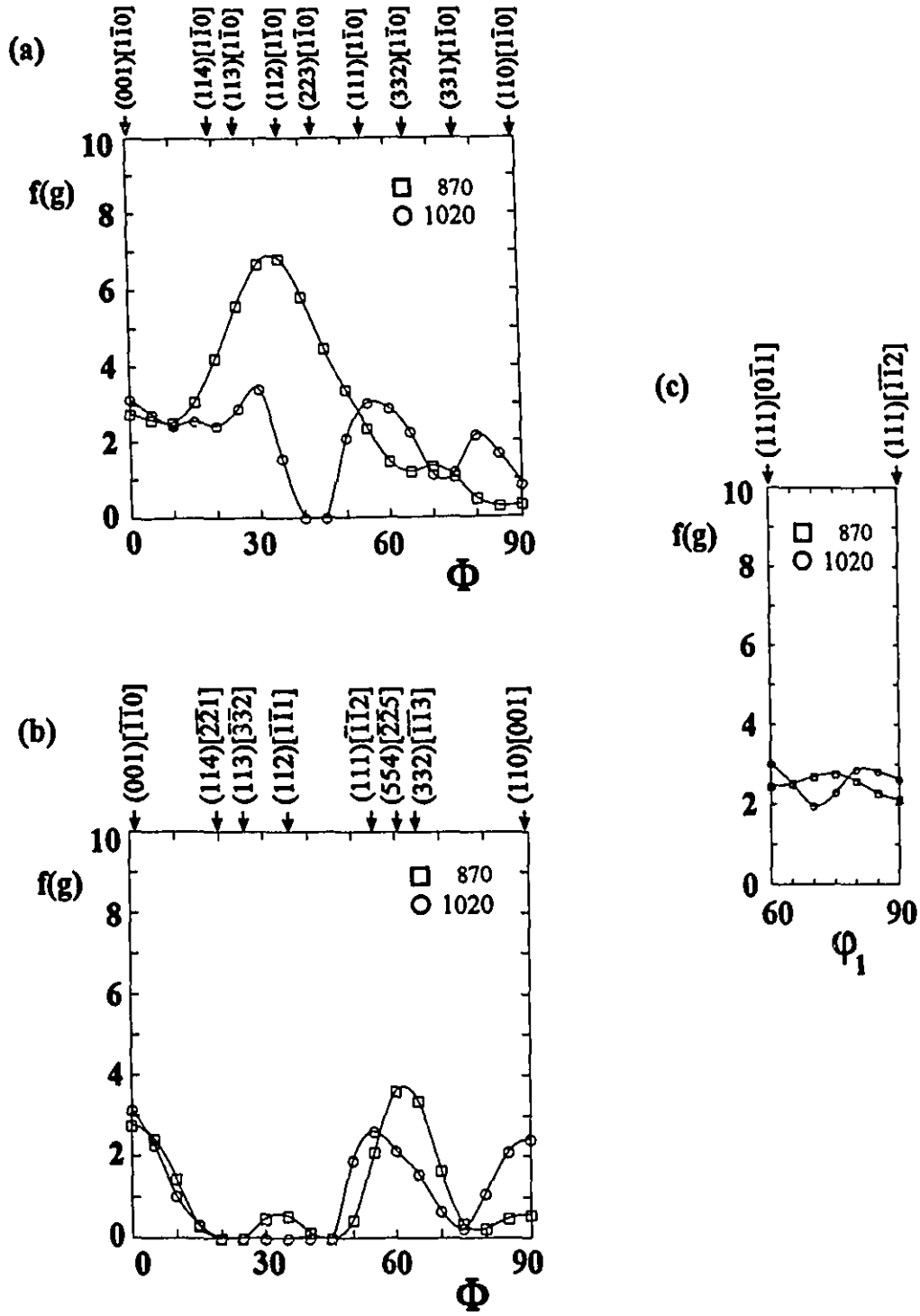

Figure VI.46 (a) RD, (b) TD and (c) ND fibres for the niobium microalloyed steel, quenched samples, austenitized at 1250°C and hot rolled to 75% reduction, for two finish rolling temperatures.

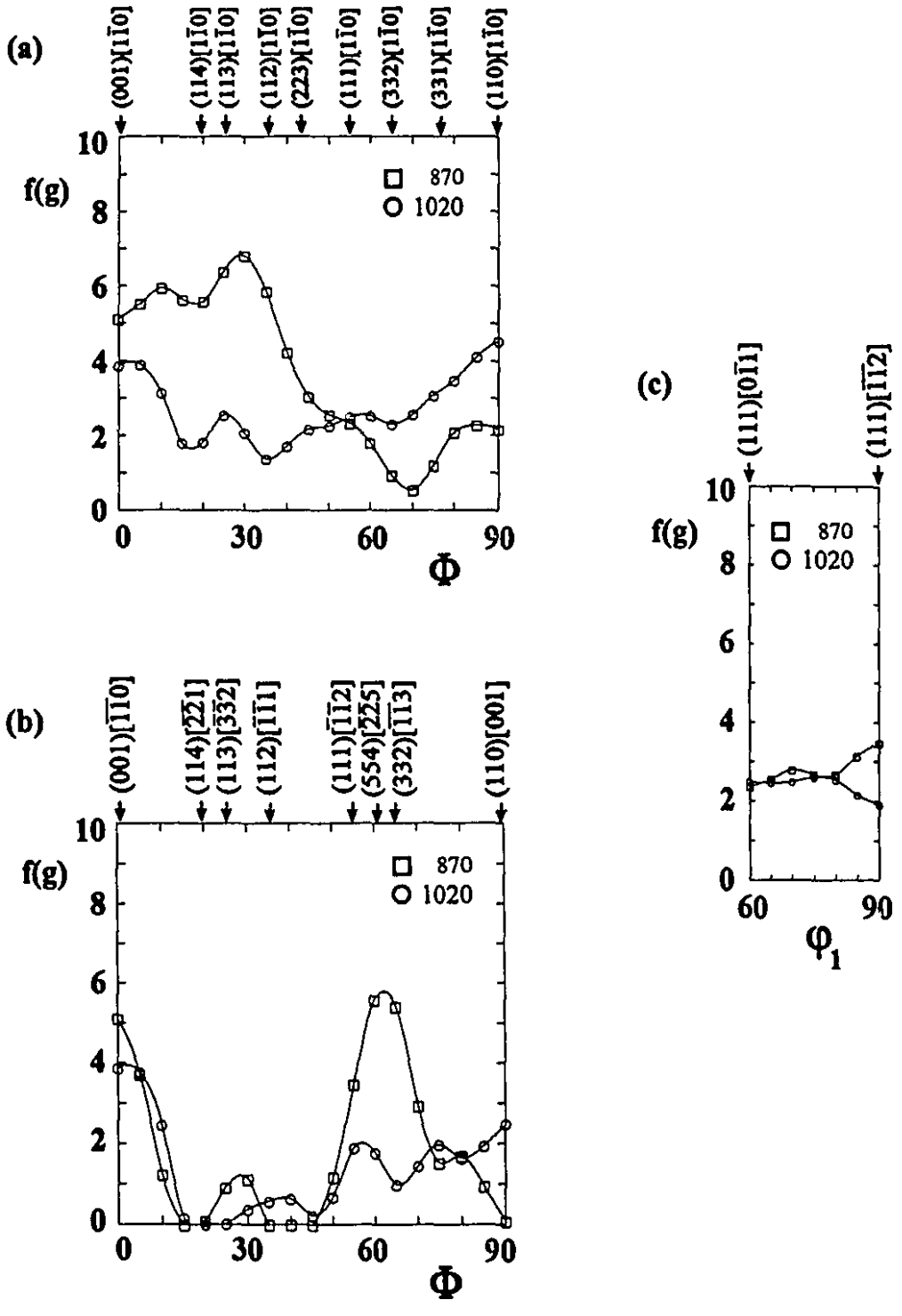

Figure VI.47 (a) RD, (b) TD and (c) ND fibres for the niobium microalloyed steel, quenched samples, austenitized at 1150°C and hot rolled to 90% reduction, for two finish rolling temperatures.

VI.2.3 Interstitial Free Steel

The rolling experiments concerning the interstitial free steel were divided into 4 groups. The first included the results for the six samples given 90% reductions at the various finish rolling temperatures, after austenitizing at 1250°C. These are presented in Figures VI.48 to VI.51. In the second group, for which the principal processing parameters were austenitization at 1250°C and 75% reduction, only two samples are presented, corresponding to finish rolling temperatures of 820°C and 720°C (see Figures VI.52 to VI.55). The third group again covers all six finishing temperatures, with 90% reduction after soaking at 1150°C, Figures VI.56 to VI.59. Finally, a fourth set of results is shown in Figures VI.60 to VI.63, with samples austenitized at 1150°C, deformed to 75% reduction, and with finish rolling temperatures of 1020°C, 920°C, 820°C and 720°C.

The textures developed in the interstitial free steel are well defined, with the preferred orientations showing two contrasting behaviours, which are a function of finish rolling temperature and somewhat independent of the other processing parameters. For finishing temperatures of 1020°C, 920°C and 870°C, the textures are relatively flat, with the rotated cube $\{001\}<110>$ being the most important component. Some $\{110\}<110>$ is also present, especially at the highest temperature. In the samples finish rolled at the lower temperatures (820°C, 720°C and 620°C), sharper textures are observed. The section of the RD fibre that includes orientations between $\{001\}<110>$ and $\{111\}<110>$ is enhanced, and the ND fibre is also strengthened as the finish temperature is lowered. Finally, the TD fibre texture components located around $\{554\}<225>$ are clearly more intense at the three lower finishing temperatures.

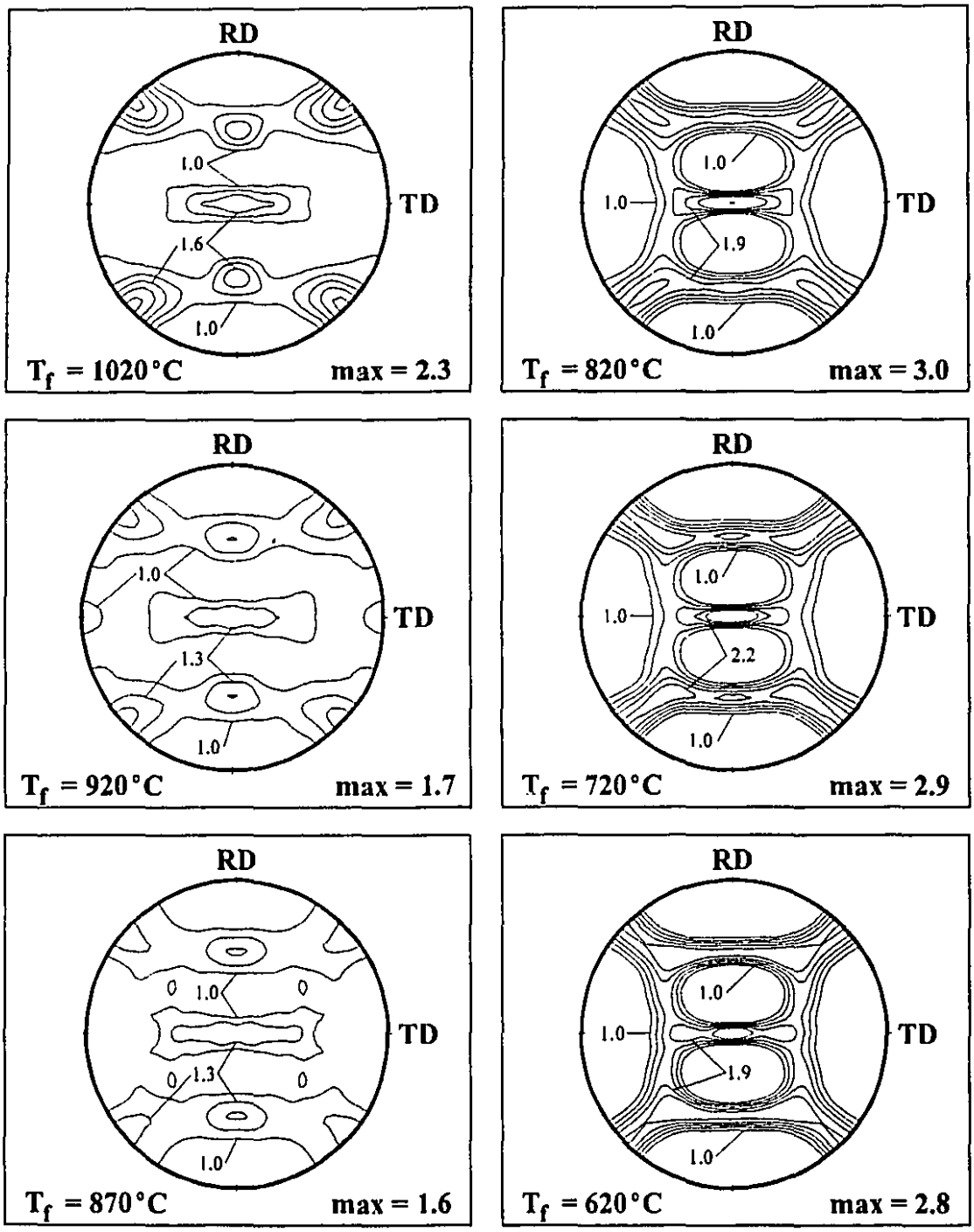

Figure VI.48 (200) pole figures for the interstitial free steel, austenitized at 1250°C and hot rolled to 90% reduction, for several finish rolling temperatures.

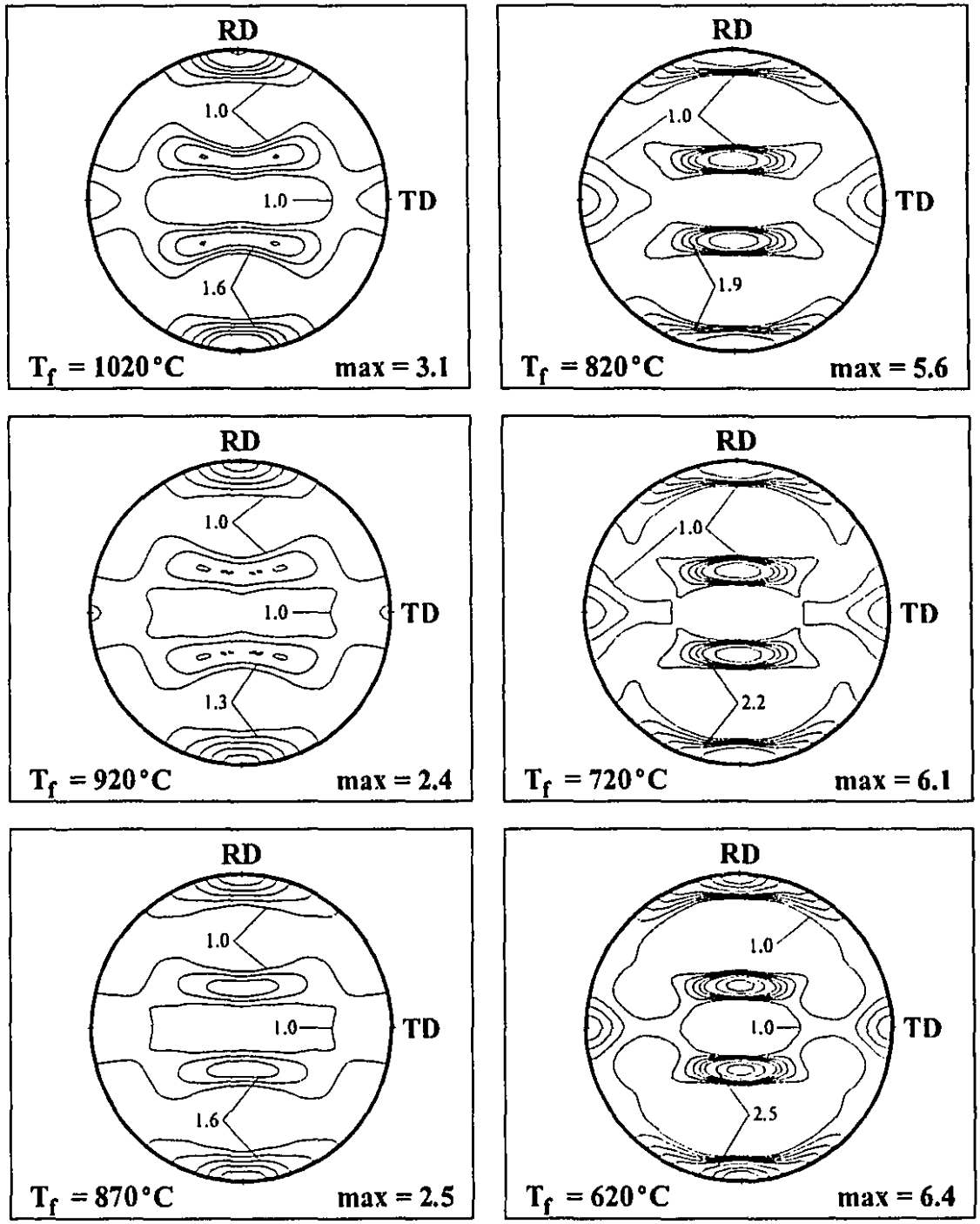

Figure VI.49 (110) pole figures for the interstitial free steel, austenitized at 1250°C and hot rolled to 90% reduction, for several finish rolling temperatures.

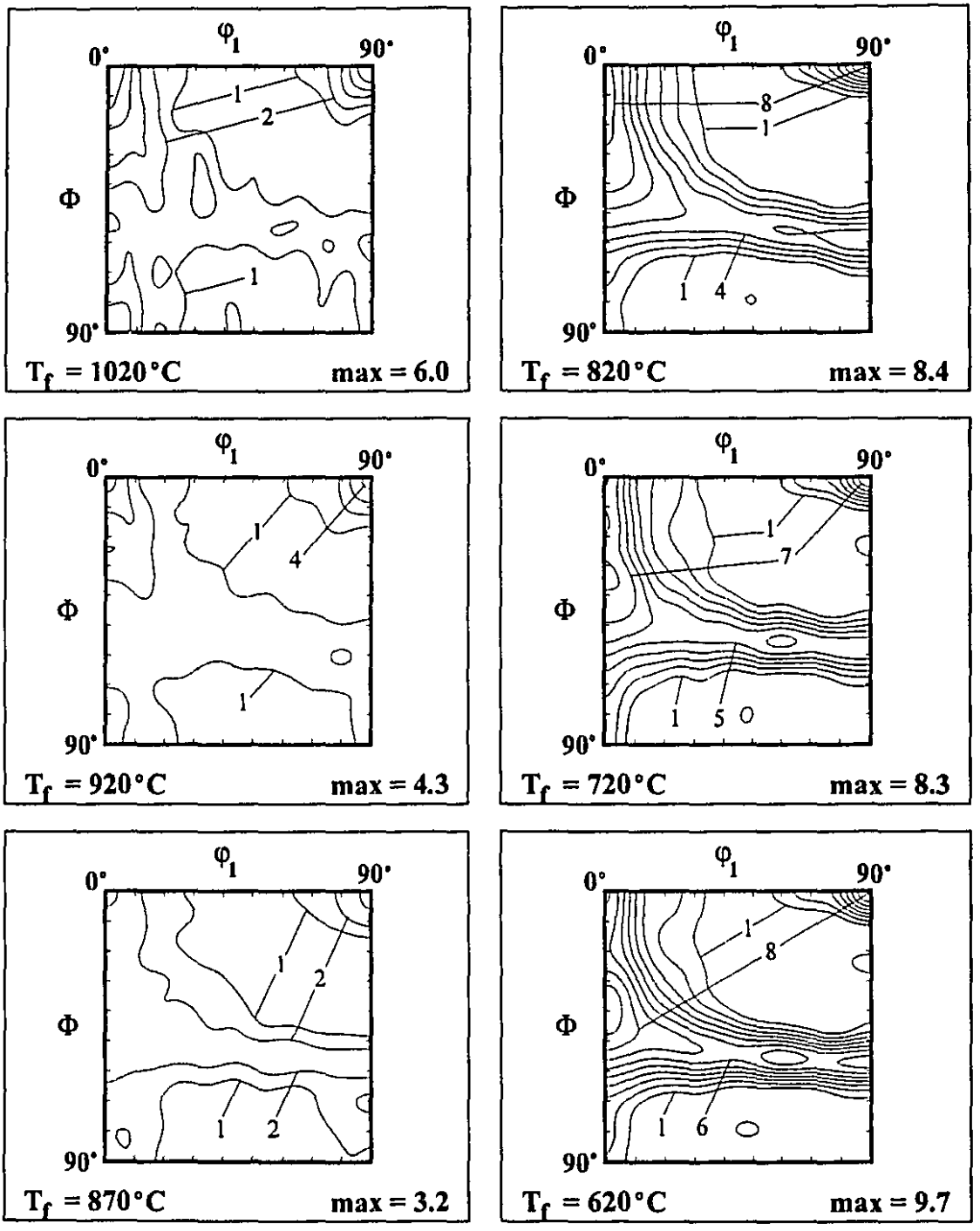

Figure VI.50 φ_2=45° sections of the ODF's for the interstitial free steel, austenitized at 1250°C and hot rolled to 90% reduction, for several finish rolling temperatures.

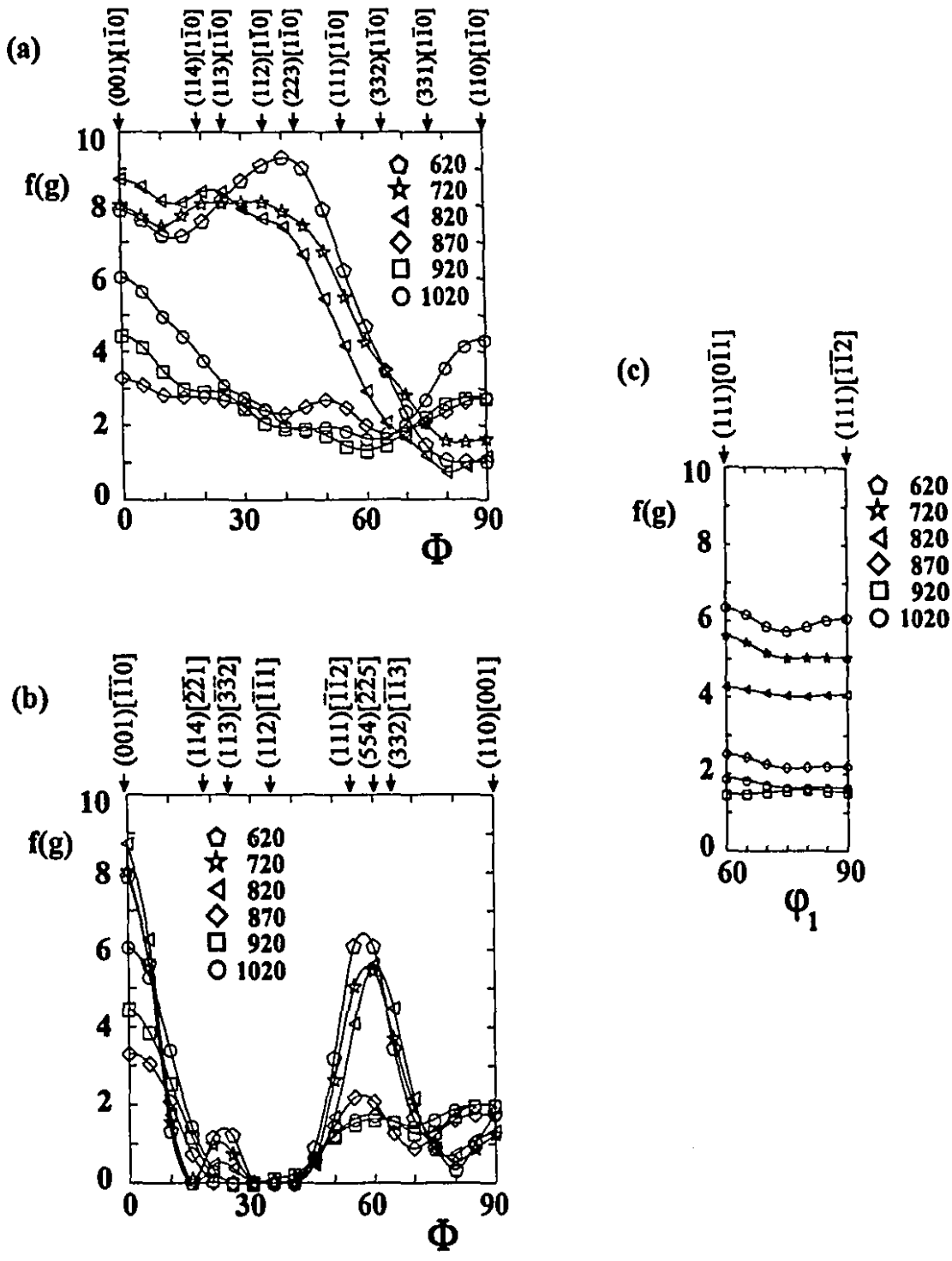

Figure VI.51 (a) RD, (b) TD and (c) ND fibres for the interstitial free steel, austenitized at 1250°C and hot rolled to 90% reduction, for several finish rolling temperatures.

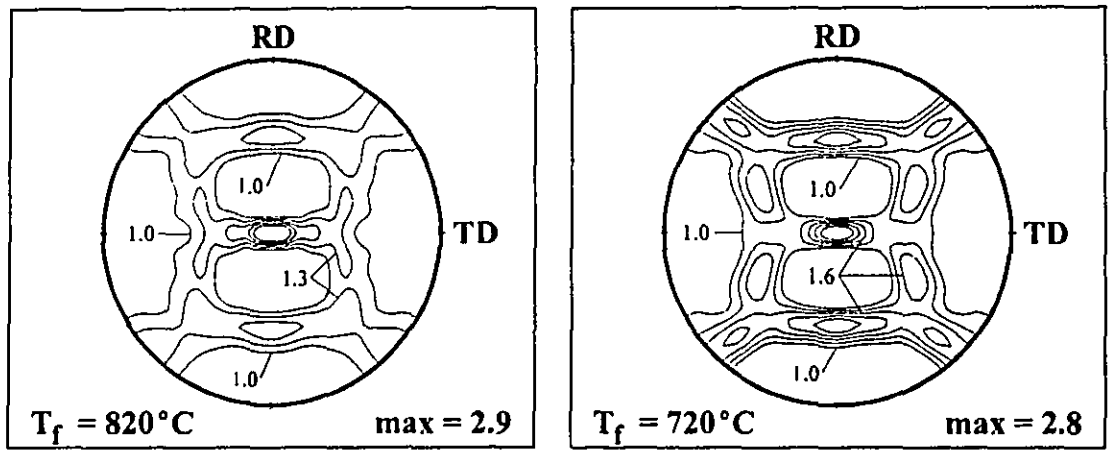

Figure VI.52 (200) pole figures for the interstitial free steel, austenitized at 1250°C and hot rolled to 75% reduction, for finish rolling temperatures of 820°C and 720°C.

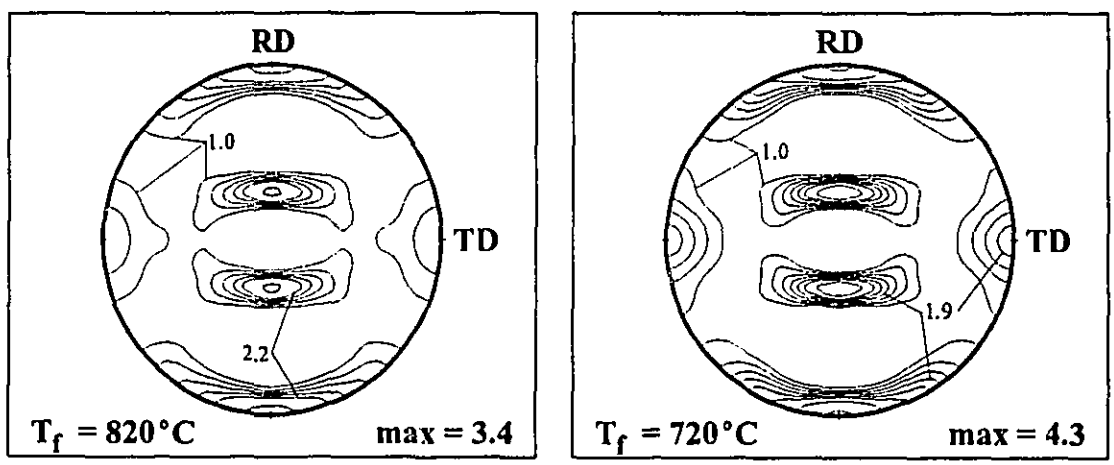

Figure VI.53 (110) pole figures for the interstitial free steel, austenitized at 1250°C and hot rolled to 75% reduction, for finish rolling temperatures of 820°C and 720°C.

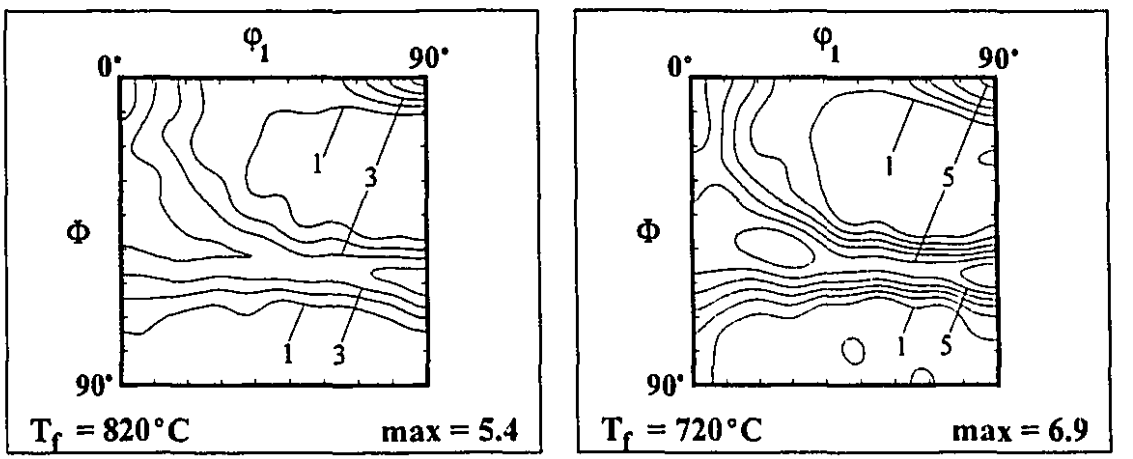

Figure VI.54 φ_2=45° sections of the ODF's for the interstitial free steel, austenitized at 1250°C and hot rolled to 75% reduction, for finish rolling temperatures of 820°C and 720°C.

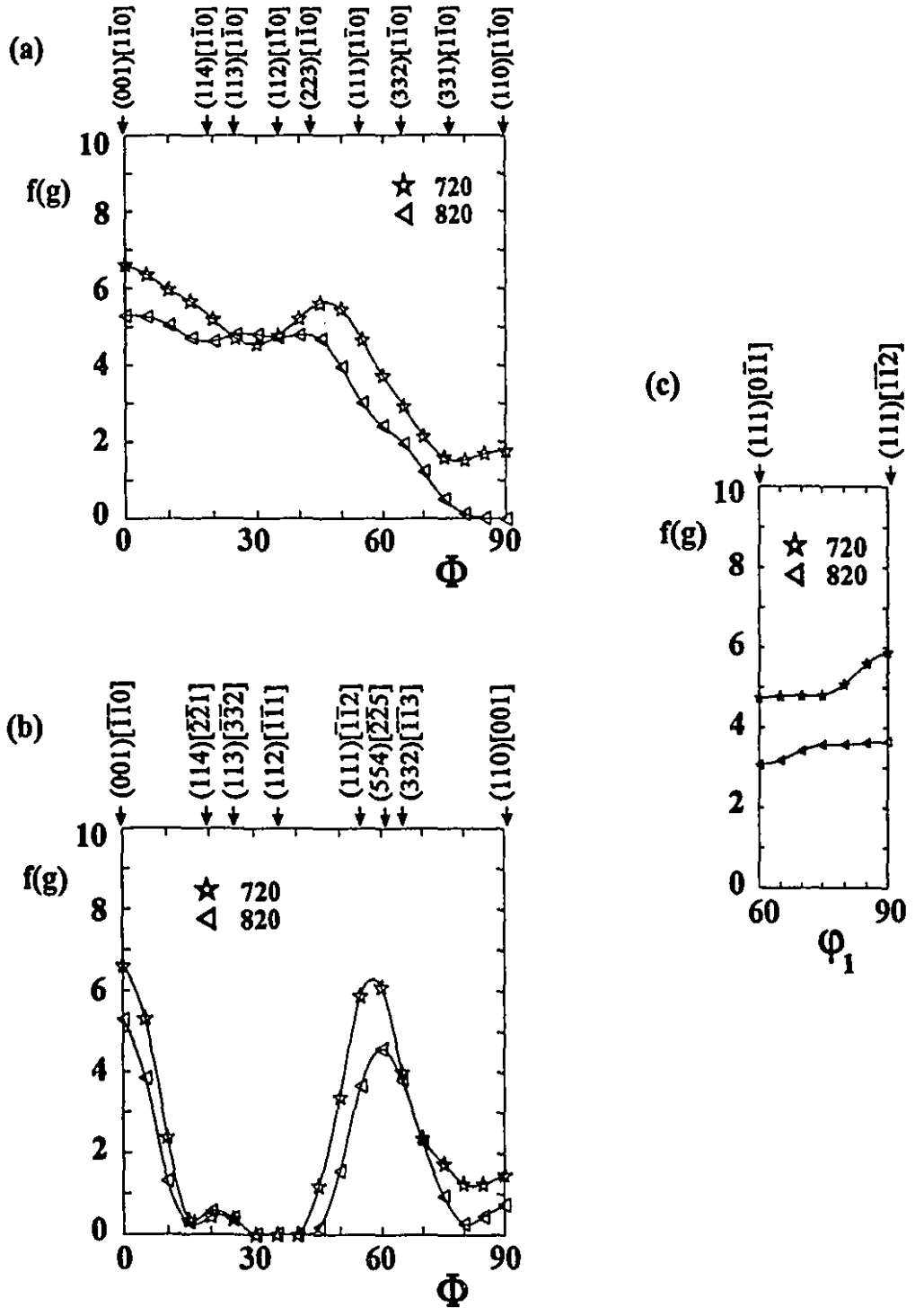

Figure VI.55 (a) RD, (b) TD and (c) ND fibres for the interstitial free steel, austenitized at 1250°C and hot rolled to 75% reduction, for finish rolling temperatures of 820°C and 720°C.

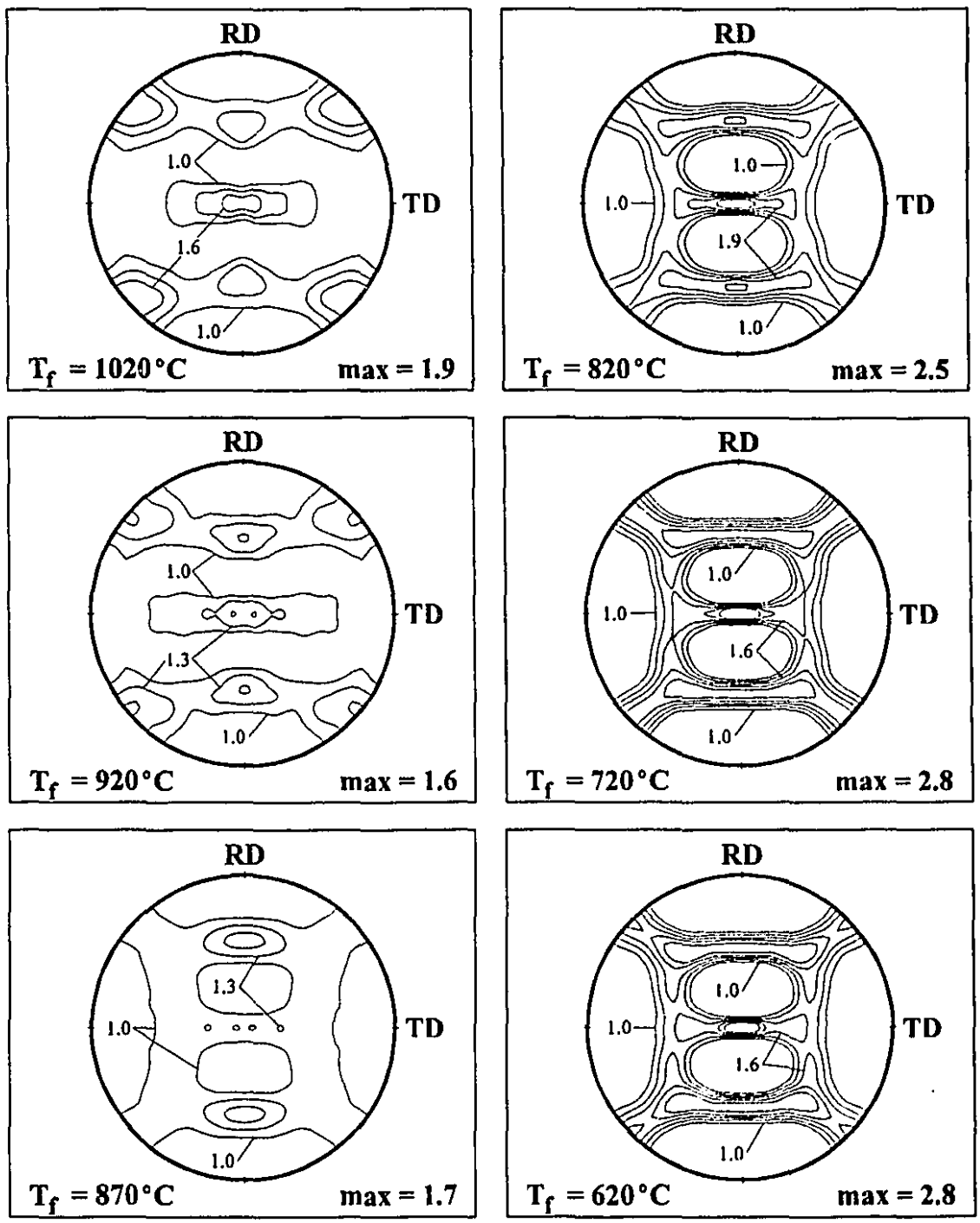

Figure VI.56 (200) pole figures for the interstitial free steel, austenitized at 1150°C and hot rolled to 90% reduction, for several finish rolling temperatures.

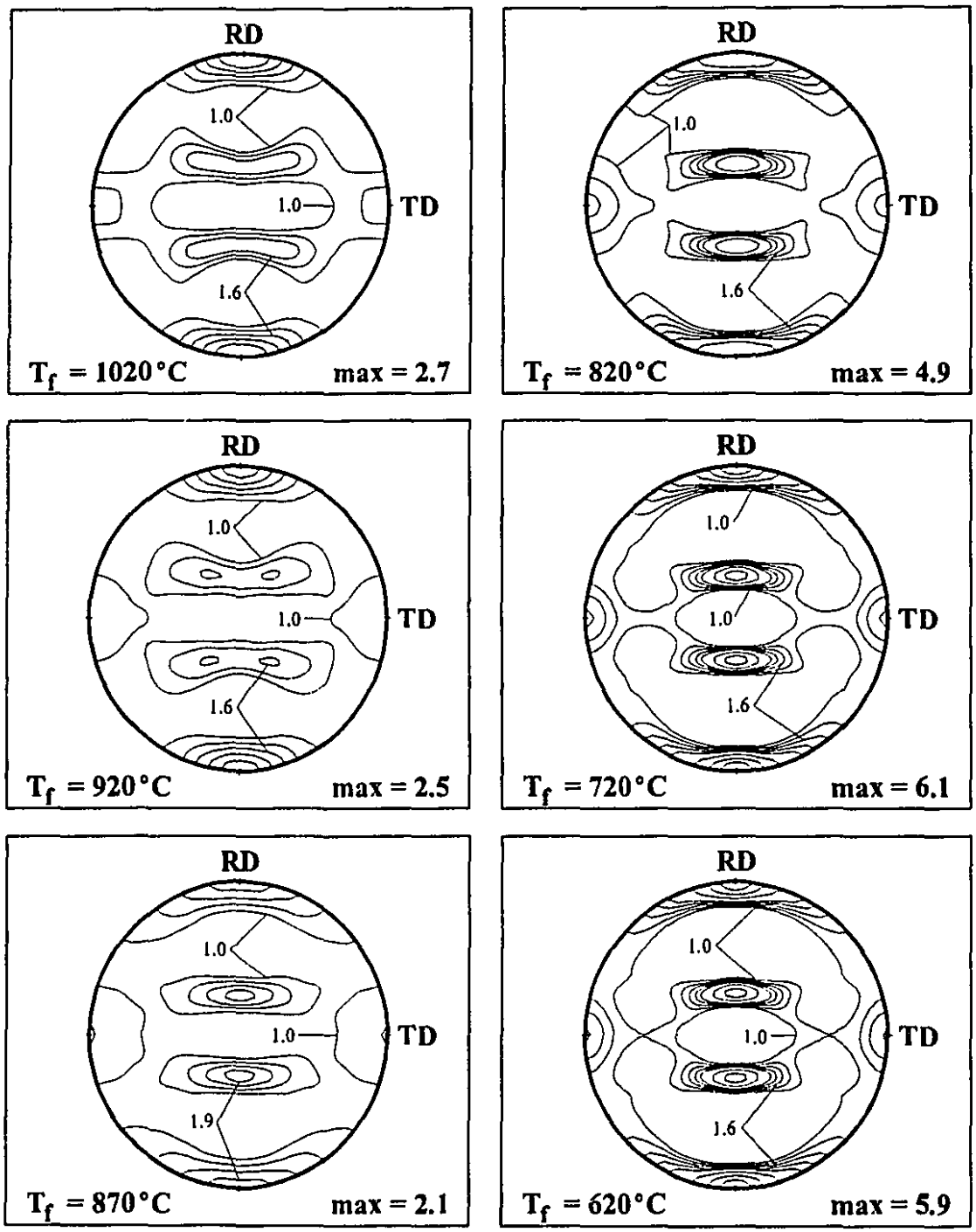

Figure VI.57 (110) pole figures for the interstitial free steel, austenitized at 1150°C and hot rolled to 90% reduction, for several finish rolling temperatures.

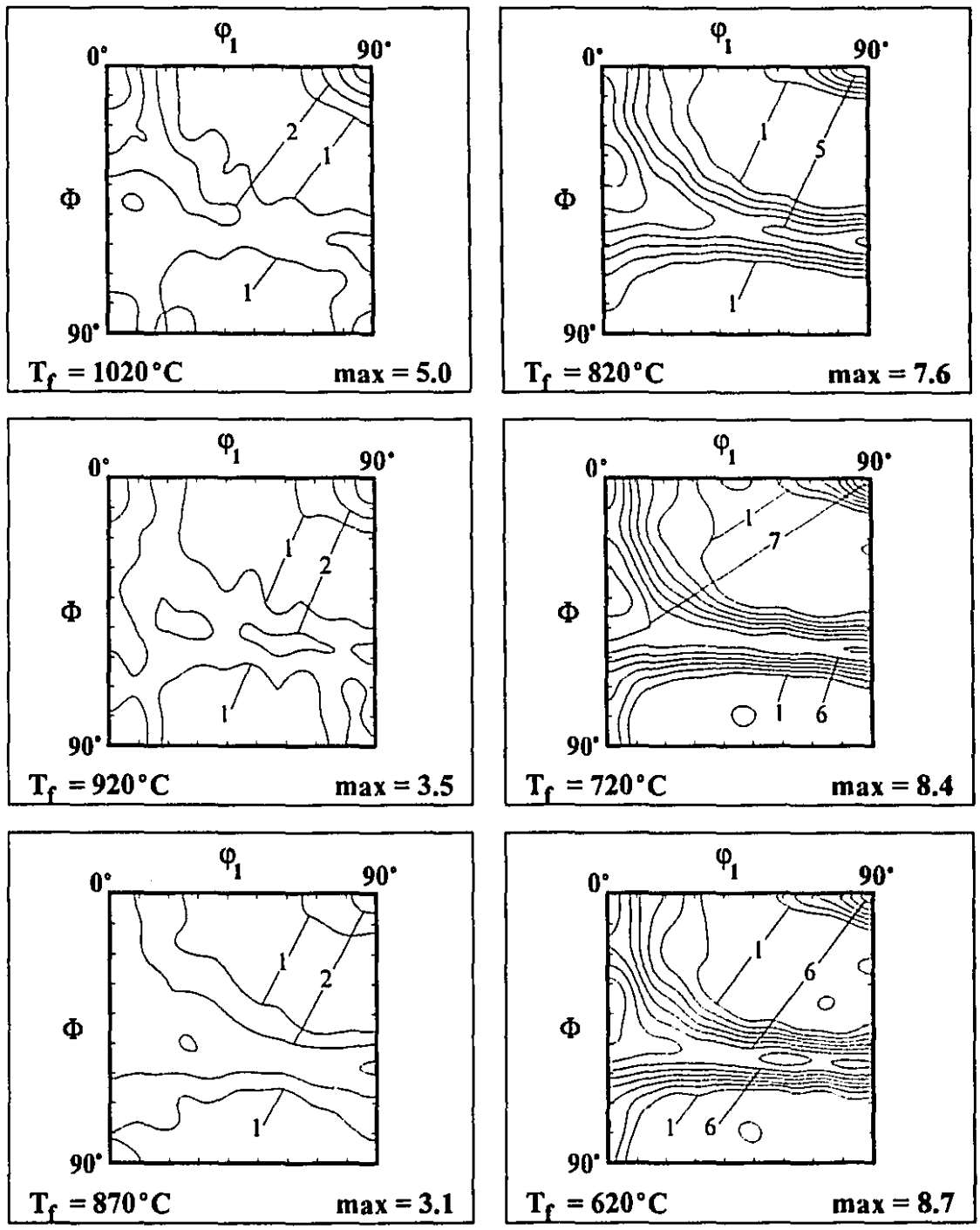

Figure VI.58 φ_2=45° sections of the ODF's for the interstitial free steel, austenitized at 1150°C and hot rolled to 90% reduction, for several finish rolling temperatures.

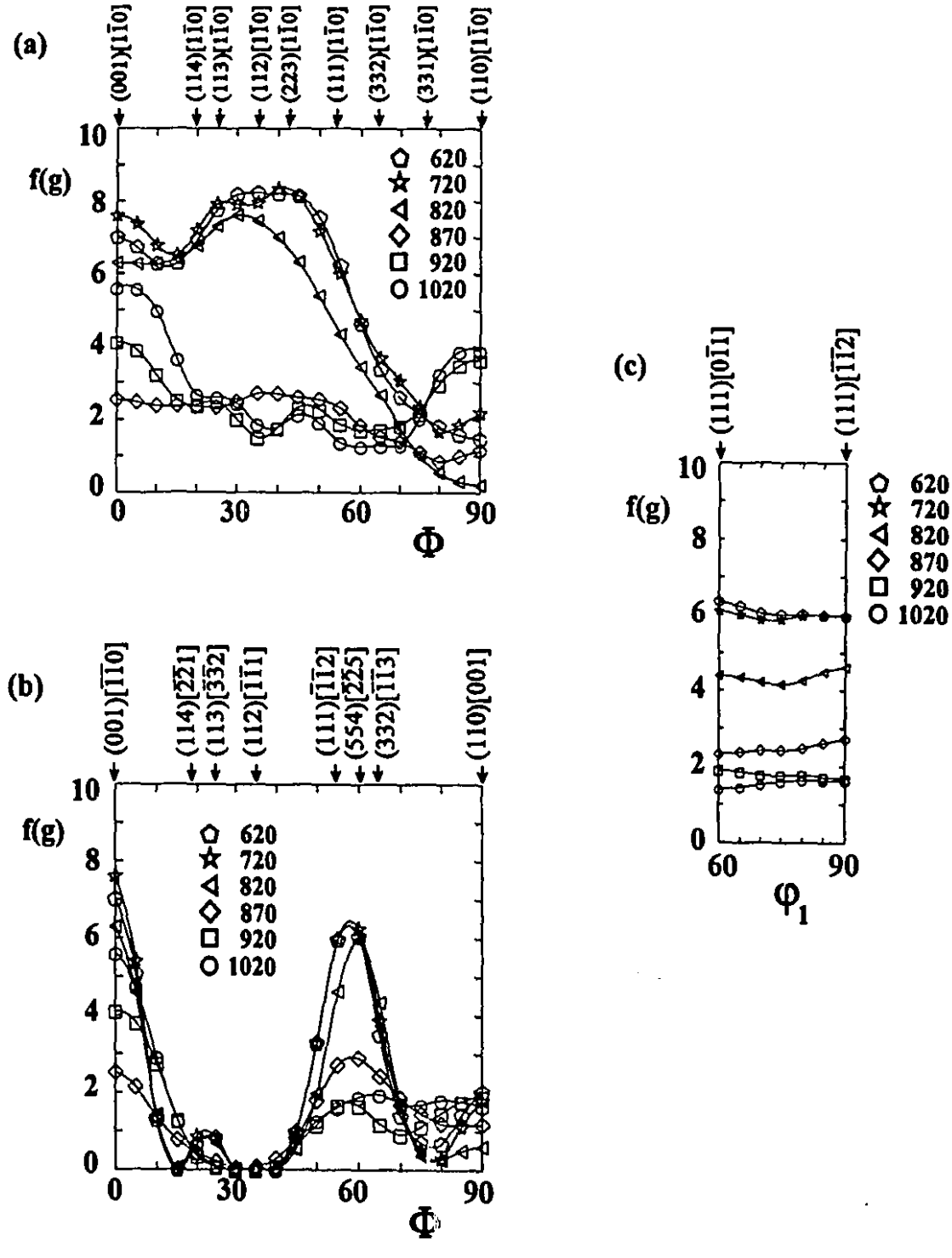

Figure VI.59 (a) RD, (b) TD and (c) ND fibres for the interstitial free steel, austenitized at 1150°C and hot rolled to 90% reduction, for several finish rolling temperatures.

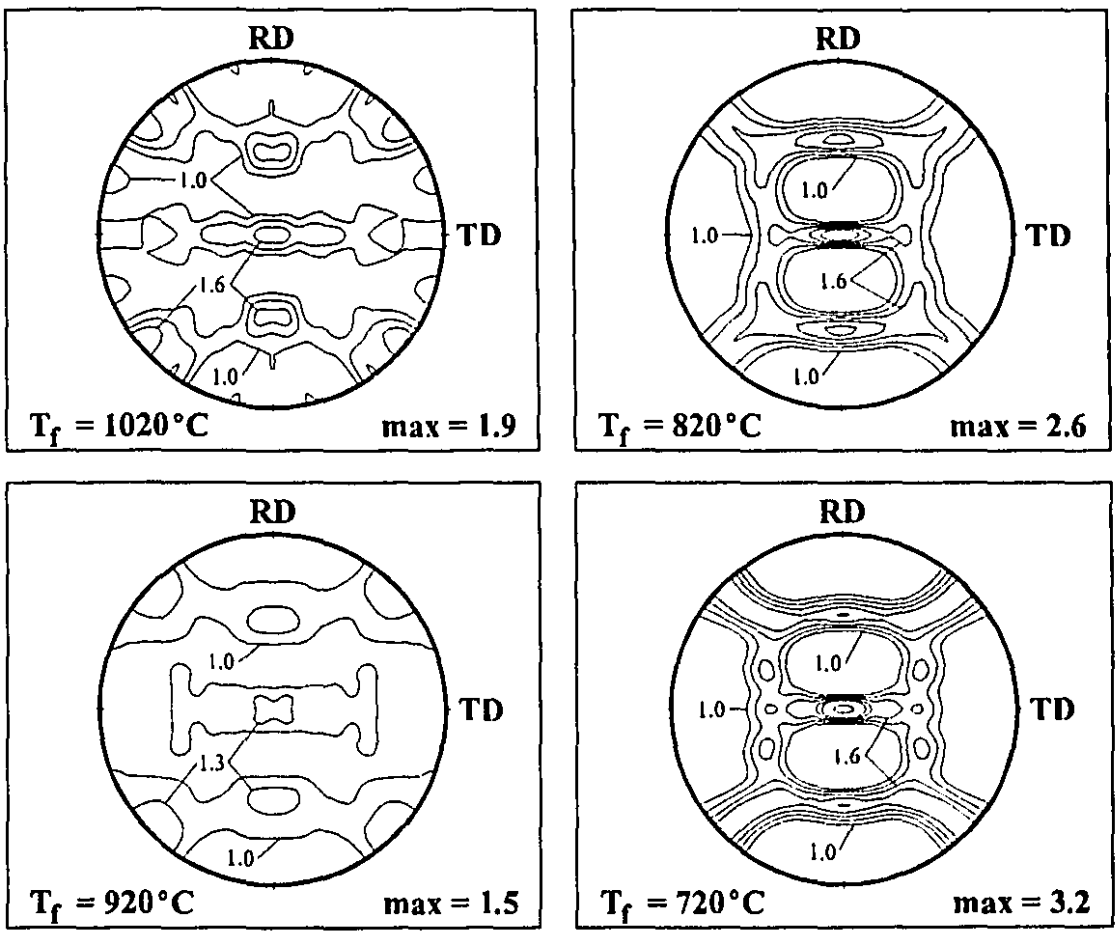

Figure VI.60 (200) pole figures for the interstitial free steel, austenitized at 1150°C and hot rolled to 75% reduction, for several finish rolling temperatures.

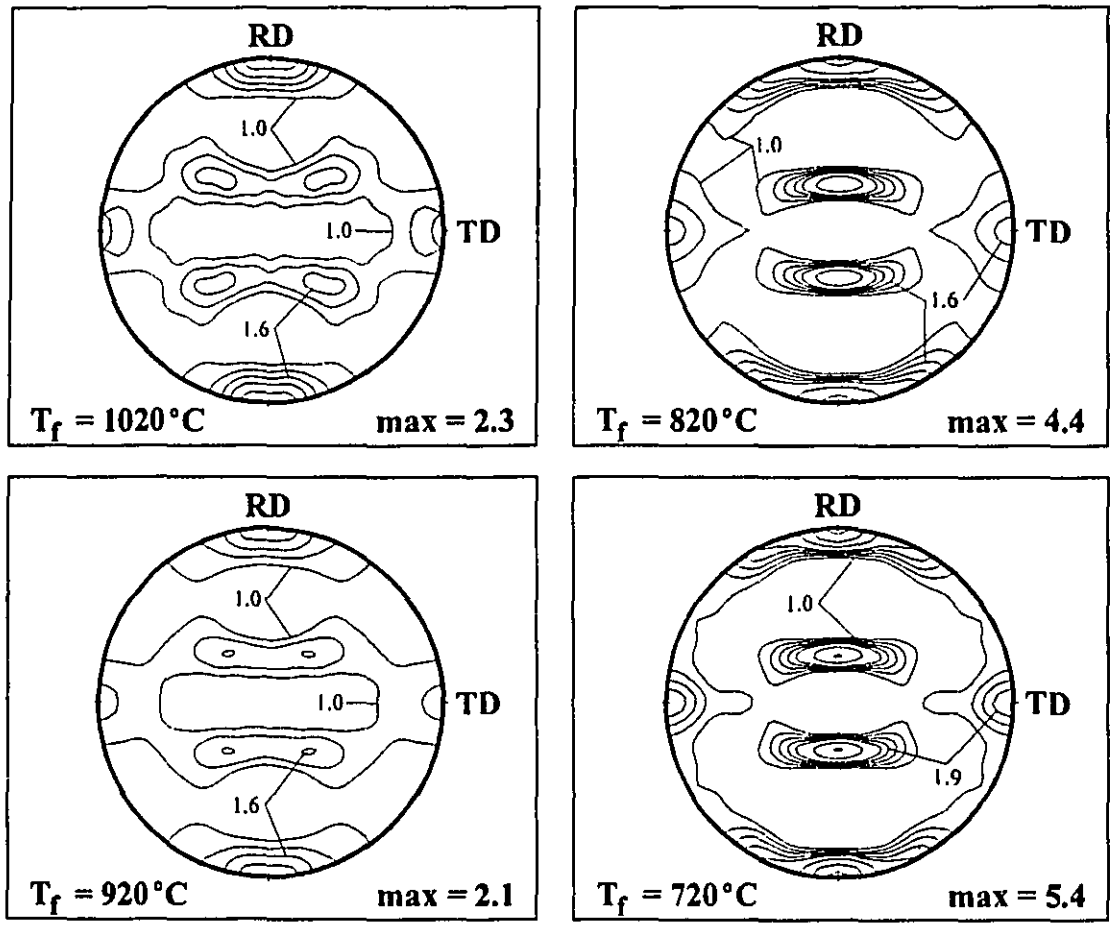

Figure VI.61 (110) pole figures for the interstitial free steel, austenitized at 1150°C and hot rolled to 75% reduction, for several finish rolling temperatures.

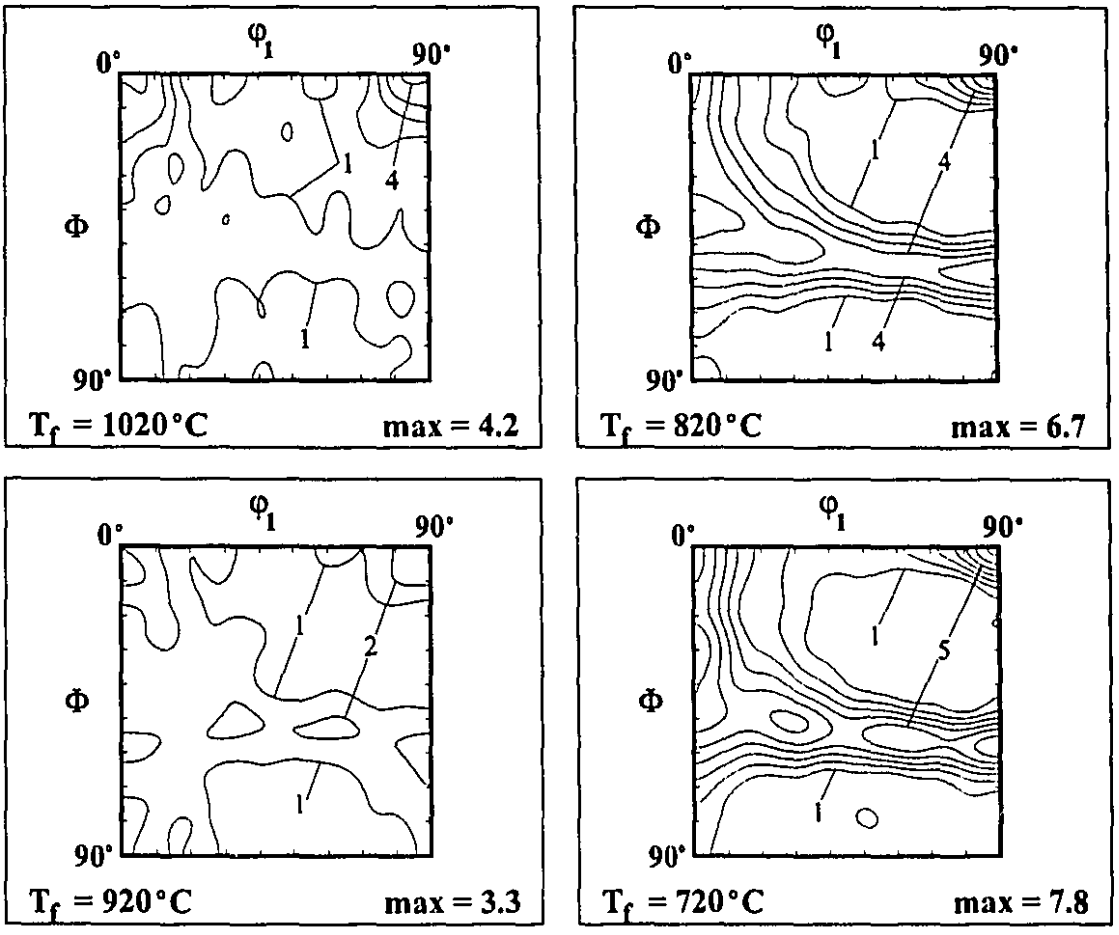

Figure VI.62 φ_2=45° sections of the ODF's for the interstitial free steel, austenitized at 1150°C and hot rolled to 75% reduction, for several finish rolling temperatures.

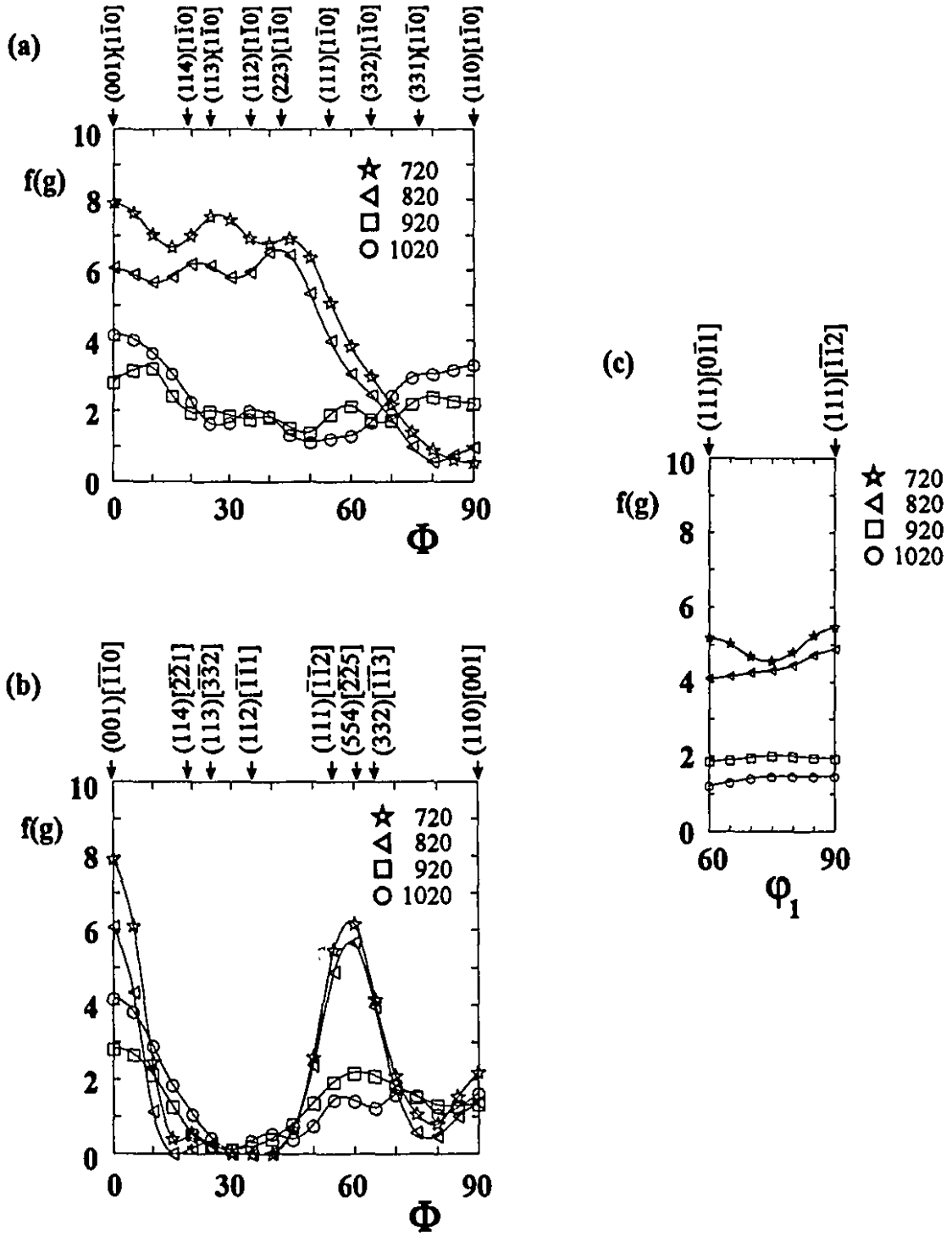

Figure VI.63 (a) RD, (b) TD and (c) ND fibres for the interstitial free steel, austenitized at 1150°C and hot rolled to 75% reduction, for several finish rolling temperatures.

Chapter VII

TRANSFORMATION CALCULATION RESULTS: DERIVATION OF THE PRINCIPAL PRODUCT COMPONENTS

VII.1 The Kurdjumov-Sachs Relation

The transformation of a number of selected parent orientations, which have been experimentally observed and reported in the literature, was carried out analytically and in a discrete manner. The transformation relationship employed was that of Kurdjumov-Sachs, since it has been shown [70] that this is the one which best describes the transformation of austenite to ferrite in controlled rolled steels. Each of the 24 rotation axes was clearly identified; these are listed in Table VII.1. All 24 variants were recorded in terms of both Euler angles and Miller indices. No variant selection was applied.

Table VII.1 The 24 Axes of Rotation of the Kurdjumov-Sachs Relationship

No.	Axis	No.	Axis	No.	Axis
1	$[\bar{1}2\bar{1}]$	9	$[12\bar{1}]$	17	$[\bar{1}12]$
2	$[1\bar{2}1]$	10	$[\bar{1}\bar{2}1]$	18	$[1\bar{1}\bar{2}]$
3	$[\bar{1}\bar{1}2]$	11	$[\bar{2}\bar{1}\bar{1}]$	19	$[2\bar{1}1]$
4	$[11\bar{2}]$	12	$[211]$	20	$[\bar{2}1\bar{1}]$
5	$[2\bar{1}\bar{1}]$	13	$[\bar{1}\bar{2}\bar{1}]$	21	$[\bar{1}\bar{1}\bar{2}]$
6	$[\bar{2}11]$	14	$[121]$	22	$[112]$
7	$[1\bar{1}2]$	15	$[21\bar{1}]$	23	$[\bar{1}21]$
8	$[\bar{1}1\bar{2}]$	16	$[\bar{2}\bar{1}1]$	24	$[1\bar{2}\bar{1}]$

VII.2 Selection of Initial Parent Orientations

A number of experimentally observed parent orientations were selected to represent the texture of austenite. These orientations included both the most important ones, as well as some minor texture components reported in the literature. The data used include textures in austenitic stainless steels [51, 71, 72], deformed copper and brass [73], iron-nickel alloys [74] and nickel-cobalt alloys [70].

VII.2.1 Recrystallization Parent Components

The selected recrystallization parent orientations are the following:

1. {100}<001>,
2. {110}<111>,
3. {100}<012>,

4. {221}<212>,

5. {113}<332>,

6. {112}<534>.

Of these, the strongest one in recrystallized fcc textures is the cube, {100}<001>. The other five orientations have been observed to occur but with less strength.

VII.2.2 Deformation Parent Components

The four most important deformation parent orientations included in the transformation calculations are the following:

1. Copper, {112}<111>,

2. Brass, {110}<112>,

3. S, {123}<634>,

4. Goss, {110}<001>.

The additional deformation parent orientations analyzed are the seven listed below:

1. {123}<121>,

2. {123}<412>,

3. {123}<856>,

4. {146}<211>,

5. {332}<113>,

6. {168}<211>,

7. {135}<712>.

Finally, three other parent orientations were considered, corresponding to the following intermediate positions: Goss-brass ({011}<511>), brass-S ({168}<211>) and S-copper ({236}<322>).

VII.3 Transformation Calculations

The calculation of the product components for each of the parent orientations was carried out following the procedure described in this section. The actual program, written in FORTRAN, is given in Appendix A.

The initial input is the parent orientation to be transformed, expressed in Miller index form (*hkl*)[*uvw*]. Here, (*hkl*) and [*uvw*] correspond to the rolling plane and rolling direction, respectively. Consider the sample coordinate system K_A and the crystal coordinate system K_B, shown in Figure II.2. The crystal orientation can be represented by the rotation g ((*hkl*)[*uvw*]), which brings these two coordinate systems into coincidence. In terms of the sample reference frame, (*hkl*) is assigned to the normal direction $\vec{s}_3$ of the sheet plane and [*uvw*] represents the rolling direction $\vec{s}_1$. The transverse direction, $\vec{s}_2$, can be readily calculated by the vector product ($\vec{s}_3 \times \vec{s}_1$), and after normalizing these three vectors, the [SC] (sample-crystal) matrix is built. This is actually the rotation matrix defined by the Miller indices (*hkl*)[*uvw*], and is given by:

$$[SC] = g((hkl)[uvw]) = \begin{pmatrix} \frac{u}{n} & \frac{kw-lv}{mn} & \frac{h}{m} \\ \frac{v}{n} & \frac{lu-hw}{mn} & \frac{k}{m} \\ \frac{w}{n} & \frac{hv-ku}{mn} & \frac{l}{m} \end{pmatrix} \qquad \text{(VII.1)}$$

where $m = \sqrt{h^2+k^2+l^2}$ and $n = \sqrt{u^2+v^2+w^2}$ are the normalizing factors.

The transformation from austenite to ferrite is characterized by the Kurdjumov-Sachs relationship. As already mentioned, this is defined as a rotation of $\pm 90°$ around each of the twelve possible $<112>$ axes; therefore, 24 rotations are necessary to

obtain the 24 variants. Each rotation is most conveniently represented in matrix notation, which is described as follows: The direction of the rotation is represented by the vector $\vec{d}$ = (dd1,dd2,dd3), which is normalized into $\hat{d}$ = (d1,d2,d3) with:

$$di = \frac{ddi}{\sqrt{dd1^2 + dd2^2 + dd3^2}} \qquad i = 1,2,3 \qquad \text{(VII.2)}$$

The angle of rotation is called ω. A first rotation is necessary to bring the [001] direction of the crystal (the vector $\vec{c}_3$) into coincidence with the direction $\hat{d}$, the rotation axis. Then, the $\vec{c}_3$ axis is rotated through the angle ω. Finally, the first rotation is inverted. This is expressed as:

$$g(\hat{d}, \omega) = g^{-1}(\vec{c}_3 \rightarrow \hat{d}) \cdot g(\vec{c}_3, \omega) \cdot g(\vec{c}_3 \rightarrow \hat{d}) \qquad \text{(VII.3)}$$

and explicitly the matrix g ($\hat{d}$, ω) is given as [75]:

$$g(\hat{d}, \omega) =$$

$$= \begin{bmatrix} (1-d1^2)\cdot\cos\omega + d1^2 & d1\cdot d2\cdot(1-\cos\omega) + d3\cdot\sin\omega & d1\cdot d3\cdot(1-\cos\omega) - d2\cdot\sin\omega \\ d1\cdot d2\cdot(1-\cos\omega) - d3\cdot\sin\omega & (1-d2^2)\cdot\cos\omega + d2^2 & d2\cdot d3\cdot(1-\cos\omega) + d1\cdot\sin\omega \\ d1\cdot d3\cdot(1-\cos\omega) + d2\cdot\sin\omega & d2\cdot d3\cdot(1-\cos\omega) - d1\cdot\sin\omega & (1-d3^2)\cdot\cos\omega + d3^2 \end{bmatrix}$$

(VII.4)

Finally, the rotation of the given parent orientation (defined as the matrix "RES") is performed by multiplying the two matrices g ($\hat{d}$, ω) and [SC]:

$$[RES] = g(\hat{d}, \omega) \cdot g((hkl)[uvw]) \qquad \text{(VII.5)}$$

Obviously, this operation (and all the considerations that follow) must be carried out for each of the 24 variants defined by the Kurdjumov-Sachs relationship.

This matrix represents the product component, and its orientation is uniquely characterized by the rotation g ($\hat{d}$, ω). However, the definition of such a matrix is a function of the orientation of the initial coordinate system. If the crystal possesses some kind of symmetry, there may be different ways to position the axis and angle of rotation, physically indistinguishable between themselves. Additionally, the symmetries in the fixed sample coordinate system (orthogonal in the case of rolled sheet) will also produce equivalent orientations.

It is therefore necessary to take into consideration both the crystal and sample symmetries. Table VII.2 gives explicitly the 24 possible symmetry elements of the cubic crystal system, in matrix representation [5]; these are called the [Sym] matrices. In Table VII.3, the four symmetric cases of a rolled polycrystalline sheet are described, also as matrices [76] and are denominated [Tb]. Hence the application of these symmetries consists of the following two matrix multiplications, resulting, respectively, in the matrices named [Tab] and [SB]:

$$[Tab] = [RES] \cdot [Tb] \qquad (VII.6)$$

$$[SB] = [Sym] \cdot [Tab] \qquad (VII.7)$$

Table VII.2 The 24 Symmetry Elements of the Cubic Crystal System

1.	$\begin{bmatrix} 1 & 0 & 0 \\ 0 & 1 & 0 \\ 0 & 0 & 1 \end{bmatrix}$	2.	$\begin{bmatrix} -1 & 0 & 0 \\ 0 & 1 & 0 \\ 0 & 0 & -1 \end{bmatrix}$	3.	$\begin{bmatrix} -1 & 0 & 0 \\ 0 & -1 & 0 \\ 0 & 0 & 1 \end{bmatrix}$	4.	$\begin{bmatrix} 1 & 0 & 0 \\ 0 & -1 & 0 \\ 0 & 0 & -1 \end{bmatrix}$
5.	$\begin{bmatrix} 0 & 1 & 0 \\ 0 & 0 & 1 \\ 1 & 0 & 0 \end{bmatrix}$	6.	$\begin{bmatrix} 0 & -1 & 0 \\ 0 & 0 & 1 \\ -1 & 0 & 0 \end{bmatrix}$	7.	$\begin{bmatrix} 0 & -1 & 0 \\ 0 & 0 & -1 \\ 1 & 0 & 0 \end{bmatrix}$	8.	$\begin{bmatrix} 0 & 1 & 0 \\ 0 & 0 & -1 \\ -1 & 0 & 0 \end{bmatrix}$
9.	$\begin{bmatrix} 0 & 0 & 1 \\ 1 & 0 & 0 \\ 0 & 1 & 0 \end{bmatrix}$	10.	$\begin{bmatrix} 0 & 0 & -1 \\ 1 & 0 & 0 \\ 0 & -1 & 0 \end{bmatrix}$	11.	$\begin{bmatrix} 0 & 0 & -1 \\ -1 & 0 & 0 \\ 0 & 1 & 0 \end{bmatrix}$	12.	$\begin{bmatrix} 0 & 0 & 1 \\ -1 & 0 & 0 \\ 0 & -1 & 0 \end{bmatrix}$
13.	$\begin{bmatrix} 0 & 0 & -1 \\ 0 & -1 & 0 \\ -1 & 0 & 0 \end{bmatrix}$	14.	$\begin{bmatrix} 0 & 0 & 1 \\ 0 & -1 & 0 \\ 1 & 0 & 0 \end{bmatrix}$	15.	$\begin{bmatrix} 0 & 0 & 1 \\ 0 & 1 & 0 \\ -1 & 0 & 0 \end{bmatrix}$	16.	$\begin{bmatrix} 0 & 0 & -1 \\ 0 & 1 & 0 \\ 1 & 0 & 0 \end{bmatrix}$
17.	$\begin{bmatrix} -1 & 0 & 0 \\ 0 & 0 & -1 \\ 0 & -1 & 0 \end{bmatrix}$	18.	$\begin{bmatrix} 1 & 0 & 0 \\ 0 & 0 & -1 \\ 0 & 1 & 0 \end{bmatrix}$	19.	$\begin{bmatrix} 1 & 0 & 0 \\ 0 & 0 & 1 \\ 0 & -1 & 0 \end{bmatrix}$	20.	$\begin{bmatrix} -1 & 0 & 0 \\ 0 & 0 & 1 \\ 0 & 1 & 0 \end{bmatrix}$
21.	$\begin{bmatrix} 0 & -1 & 0 \\ -1 & 0 & 0 \\ 0 & 0 & -1 \end{bmatrix}$	22.	$\begin{bmatrix} 0 & 1 & 0 \\ -1 & 0 & 0 \\ 0 & 0 & 1 \end{bmatrix}$	23.	$\begin{bmatrix} 0 & 1 & 0 \\ 1 & 0 & 0 \\ 0 & 0 & -1 \end{bmatrix}$	24.	$\begin{bmatrix} 0 & -1 & 0 \\ 1 & 0 & 0 \\ 0 & 0 & 1 \end{bmatrix}$

Table VII.3 The Four Symmetric Cases of a Rolled Polycrystalline Sheet

1.	$\begin{bmatrix} 1 & 0 & 0 \\ 0 & 1 & 0 \\ 0 & 0 & 1 \end{bmatrix}$	2.	$\begin{bmatrix} -1 & 0 & 0 \\ 0 & 1 & 0 \\ 0 & 0 & -1 \end{bmatrix}$	3.	$\begin{bmatrix} -1 & 0 & 0 \\ 0 & -1 & 0 \\ 0 & 0 & 1 \end{bmatrix}$	4.	$\begin{bmatrix} 1 & 0 & 0 \\ 0 & -1 & 0 \\ 0 & 0 & -1 \end{bmatrix}$

Now, the Euler angles of the resulting product orientation can be calculated from this last matrix, [SB]. As was shown in section II.2, the representation of an orientation in terms of Euler angles is given by the following matrix:

$$g(\varphi_1,\Phi,\varphi_2)=$$

$$\begin{bmatrix} \cos\varphi_1\cos\varphi_2-\sin\varphi_1\sin\varphi_2\cos\Phi & \sin\varphi_1\cos\varphi_2+\cos\varphi_1\sin\varphi_2\cos\Phi & \sin\varphi_2\sin\Phi \\ -\cos\varphi_1\sin\varphi_2-\sin\varphi_1\cos\varphi_2\cos\Phi & -\sin\varphi_1\sin\varphi_2+\cos\varphi_1\cos\varphi_2\cos\Phi & \cos\varphi_2\sin\Phi \\ \sin\varphi_1\sin\Phi & -\cos\varphi_1\sin\Phi & \cos\Phi \end{bmatrix}$$

(VII.8)

The three Euler angles $(\varphi_1,\Phi,\varphi_2)$ can be calculated from these last two expressions, VII.7 and VII.8. Only the points in the subspace H° are considered, in accordance with the symmetry criteria employed. In this subspace, all three Euler angles run from 0 to 90°. Furthermore, it contains three symmetrically equivalent subspaces, which results in the "multiplicity" of each orientation. All three equivalent sets of Euler angles are recorded.

The last step is the determination of the Miller indices of the product orientation. They are estimated directly from [RES], since the i^{th} column of this matrix contains the direction cosines of the sample axes with respect to the crystal axes. For completeness, all three axes are calculated, although the ones representing the directions [*h'k'l'*] and [*u'v'w'*] are those corresponding to columns 3 and 1, respectively (compare to matrix [SC]). The indices, however, are given as numbers between 0 and 100, and not as the smallest possible ones, due to the fact that they correspond to the position given by the Euler angles, which are exact. It is then

necessary to approximate the resulting product orientations if low integer Miller indices are to be used (as is commonly done in the literature). This operation is discussed in detail in section VII.4

The complete procedure for the calculation of a product orientation is summarized in the flow diagram shown in Figure VII.1.

VII.4 Problems Associated with the Use of Miller Indices

The calculation of product orientations after transformation is carried out using matrix representation. Even though the initial data, parent component and axis of rotation, are given as low integer Miller indices, the output is not necessarily an orientation which can be expressed in the same manner. The use of Euler angles gives the resulting orientation an exact position in Euler space; if a set of Miller indices is to be assigned to such a component, then some approximation is frequently necessary. This approximation should be clearly specified, since different criteria may result in widely different Miller indices for the same set of Euler angles.

The three different criteria used here when choosing the appropriate indices are the following:

1. limitation of each index to a maximum value of 3;
2. limitation of each index to a maximum value of 5;
3. orientation with the smallest square root of the sum of squares of the indices.

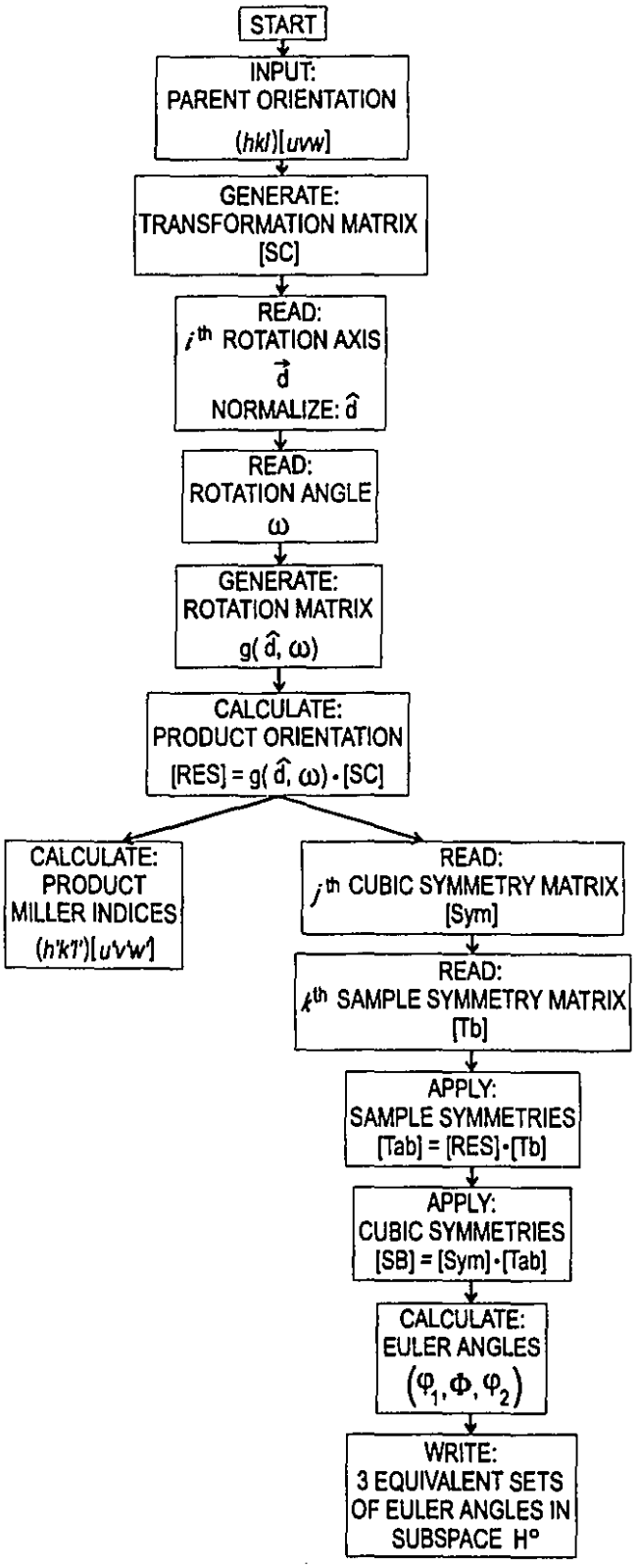

Figure VII.1 Flow diagram for the calculation of a product component.

The distance between the exact orientation (as given in terms of Euler angles) and the proposed approximate Miller indices was calculated. The indices selected were then the ones with the smallest distance (in Euler space) to the exact product component, for all the three cases mentioned above.

The transformation of the parent cube orientation, (100)[001], is described in detail to illustrate the problems associated with the designation of Miller indices for the 24 product components. Table VII.4 gives the exact Euler angles as well as the different possible Miller indices corresponding to each of the 24 variants of the Kurdjumov-Sachs relationship; this is done for the three criteria proposed, and the distances between the exact and approximate orientations are also listed.

Consider the results for variant numbers 1, 10, 14 and 24. The Miller indices corresponding to the exact position of these components, when using indices up to 100, are $\{8, 17, 100\}<100, 88, 22>$. With the first criterion, limiting the indices to an upper value of 3 results in the description of the orientation as $\{013\}<331>$, which is 10.7° away from the exact one. When the indices are allowed to be as high as 5, a closer approximation is found. For variant numbers 4, 7, 17 and 21, the same indices result in slightly smaller distances to the exact orientation. Similar arguments hold for the other 16 product components. However, neither of these two approximations leads to indices commonly used in the literature.

The third possibility is to select a neighbouring orientation whose square root of the sum of the squares of the Miller indices is the smallest possible value. This leads to orientations which are still further from the exact component, compared with the other

two criteria. For example, the first eight variants shown correspond to the well-known {001}<110> orientation, also known as the "rotated cube". Furthermore, the distance to the exact orientation (11.1°) is precisely the difference between the Kurdjumov-Sachs and Bain transformation relationships, as was shown in section III.1. It can also be noted from Table VII.4 that, when using the last criterion, the 24 product orientations of the cube component can be grouped as 3 distinct ones, with a frequency of 8 variants each. This is again in agreement with the relation between the two transformation relationships mentioned above, where 3 variants are expected from Bain, and 24 in the other case.

Table VII.4 Product Orientations after Transformation of the Cube ({100}<001>) Parent Component. Miller Indices Assigned According to Three Different Criteria

Exact Euler Angles			Variant No.†	Miller Indices up to 3		d ‡	Miller Indices up to 5		d ‡	Smallest $\sqrt{\Sigma(\text{Miller Indices})^2}$		d ‡
φ_1	Φ	φ_2		*hkl*	*uvw*		*hkl*	*uvw*		*hkl*	*uvw*	
[deg]	[deg]	[deg]				[deg]			[deg]			[deg]
41.2	80.4	4.4	1, 10, 14, 24	*013*	*331*	10.7	*015*	*551*	5.8	*001*	*110*	11.1
42.0	85.7	80.4	4, 7, 17, 21	*013*	*331*	9.9	*015*	*551*	5.2	*001*	*110*	11.1
85.6	80.4	48.8	2, 9, 13, 23	*133*	*310*	10.7	*155*	*510*	5.8	*011*	*100*	11.1
80.4	85.7	42.0	5, 12, 16, 20	*133*	*310*	9.9	*155*	*510*	5.2	*011*	*100*	11.1
4.4	80.4	41.2	3, 8, 18, 22	*133*	*011*	6.3	*144*	*011*	5.3	*011*	*011*	11.1
9.6	85.7	48.1	6, 11, 15, 19	*011*	*133*	6.3	*011*	*144*	5.3	*011*	*011*	11.1

† Numbers correspond with those given in Table VII.1.

‡ Distance in Euler space degrees between the exact orientation given in Euler angles and the approximate orientation defined with each Miller index criterion.

These results are entirely due to the fact that the cube orientation is one of the most highly symmetric. In the case of a more general parent orientation, the product components resulting after transformation via Kurdjumov-Sachs may very well all be different, even for the last criterion mentioned above. However, because of the considerations described above for the case of the cube component, the third criterion was selected for the assignment of Miller indices to the product orientations, and the distance of 11.1° was regarded as an upper bound in the approximation.

VII.5 Product Orientations

The results of the transformation calculations are presented in the following sections. They have been divided into recrystallization and deformation parent components. The product components are represented as a total of 35 orientations having Miller indices with a maximum value of 3. Four other orientations whose indices go up to 4 are included, since in some cases it was not possible to approximate an orientation within the distance of 11.1° selected as the maximum for indices of 3 or less. For comparison purposes, all 39 product components are shown in Tables VII.5 and VII.6 for the recrystallization and deformation parent orientations, even when they may belong only to one or the other case.

The numbers in the tables indicate the frequency of occurrence of every product component. A minimum frequency of 2 was adopted. A frequency of one out of the 24 variants was considered to be too weak to really influence the final texture, especially when it is the product of a minor parent orientation. Therefore, in some cases, the number of product variants will add up to 24, but in others it may be less.

VII.5.1 Recrystallization Product Components

The product components, expressed as Miller indices, of the selected recrystallization parent orientations are shown in Tables VII.5 a and b. It can be seen that the most important austenite recrystallization orientation, the cube $\{100\}<001>$, transforms into three components with a frequency of 8 out of 24 for each. For no other parent orientation is this frequency reached. In fact, only in three other cases does a frequency of 6 appear after transformation, and for all other cases it is even lower. As a result, the contribution to the final texture of the secondary parent orientations can be expected to be small.

Another point worth noting is that some components commonly regarded as being formed during the deformation of ferrite, like those belonging to the RD fibre ($\{hkl\}<110>$), may also be formed from recrystallization parent orientations.

The orientations in Table VII.5 that are shaded correspond to expected products of *deformation* parent components. They are included here so as to provide a complete list that can be compared with the deformation component table that follows. In the latter table, the shaded orientations correspond to expected products of *recrystallization* parent components that cannot be produced from deformation components.

Table VII.5a The bcc Product Components Formed from Recrystallization fcc Parent Orientations

PRODUCT COMPONENT	RECRYSTALLIZATION PARENT ORIENTATION					
	{100}<001>	{110}<111>	{100}<012>	{221}<212>	{113}<332>	{112}<534>
{100}<001>						
{001}<110>	8	4		2		
{100}<012>		4	4			
{100}<013>			4			
{110}<001>	8			2		
{110}<110>	8			2	2	
{110}<111>			4			
{110}<112>			4			
{110}<221>			4			3
{110}<113>			4			
{111}<110>		6				
{111}<112>						
{111}<123>						
{210}<120>					4	
{210}<121>						
{210}<122>				3	2	
{210}<123>				2		
{210}<124>						3
{112}<110>					6	5
{211}<120>		6				
{211}<113>						

Table VII.5b The bcc Product Components Formed from Recrystallization fcc Parent Orientations

PRODUCT COMPONENT	RECRYSTALLIZATION PARENT ORIENTATION					
	{100}<001>	{110}<111>	{100}<012>	{221}<212>	{113}<332>	{112}<534>
{211}<213>						
{221}<110>		2				
{221}<012>		2		3		
{221}<212>						
{221}<114>						
{310}<001>						
{310}<130>					2	
{310}<132>					2	
{113}<110>					2	3
{311}<112>						
{311}<114>						
{123}<210>				2	2	2
{123}<121>					2	
{123}<301>						
{114}<110>						
{421}<012>						
{421}<112>						
{421}<132>						

VII.5.2 Deformation Product Components

Tables VII.6 a and b list all the product components that originate from the deformation parent orientations selected. Here, only the Goss orientation transforms into variants with a frequency of 8; for all other fcc orientations, the products have frequencies of 6 down to 1 (but are reported here only down to 2). Two other important parent orientations, the copper and the brass, transform into at least one component with a frequency of 6. The S orientation, due to its lower symmetry, results in a larger number of low frequency product components, except for one: the $\{211\}<113>$, which also transforms from a number of other initial orientations, with fairly high frequencies. Two components which are produced after transformation of the cube, the main recrystallization orientation, may also be formed from deformation ones; they are the rotated cube ($\{001\}<110>$) and the rotated Goss ($\{110\}<110>$).

Table VII.6a The bcc Product Components Formed from Deformation fcc Parent Orientations

PRODUCT COMPONENT	DEFORMATION PARENT ORIENTATION										
	Copper: {112}<111>	Brass: {110}<112>	S: {123}<634>	Goss: {110}<001>	{123}<121>	{123}<412>	{123}<856>	{146}<211>	{332}<113>	{168}<211>	{135}<712>
{100}<001>				8						3	
{001}<110>		4									
{100}<012>		4									
{100}<013>											
{110}<001>											
{110}<110>	4								2		
{110}<111>											
{110}<112>									6		
{110}<221>											
{110}<113>									2		
{111}<110>				8							
{111}<112>		6								4	2
{111}<123>		2						2		3	
{210}<120>	4						2		4		
{210}<121>						3					2
{210}<122>			2								
{210}<123>					2				2		
{210}<124>											
{112}<110>	6			8			2				
{211}<120>		2			4	2					3
{211}<113>		6	5			4	5	5		5	2

Table VII.6b The bcc Product Components Formed from Deformation fcc Parent Orientations

PRODUCT COMPONENT	DEFORMATION PARENT ORIENTATION										
	Copper: {112}<111>	Brass: {110}<112>	S: {123}<634>	Goss: {110}<001>	{123}<121>	{123}<412>	{123}<856>	{146}<211>	{332}<113>	{168}<211>	{135}<712>
{211}<213>									2		
{221}<110>					3						
{221}<012>	2		2				3		2		2
{221}<212>											2
{221}<114>						2					
{310}<001>											2
{310}<130>									2		
{310}<132>										2	2
{113}<110>	2		2				2				
{311}<112>					4						
{311}<114>			2								
{123}<210>	4										
{123}<121>										2	
{123}<301>									2		
{114}<110>								2			
{421}<012>	2										
{421}<112>					2						
{421}<132>						2					

VII.6 Most Important Product Orientations

When analyzing experimental textures, it is important to be able to compare the observed bcc components rapidly and simply with those predicted using the Kurdjumov-Sachs relationship. In the case of recrystallized austenite, there are only three important product components: the rotated cube, Goss and rotated Goss. The product components formed from the four most important parent deformation orientations are listed in Table VII.7. These predictions are presented in Figure VII.2 on a $\varphi_2 = 45°$ section of Euler space. In this figure, the important bcc components are identified in terms of their Miller indices; the parent orientations which produce them are named, and the frequency of each product is given in brackets. Some simplifications were made; for instance, the $\{112\}<110>$ and $\{113\}<110>$ orientations produced from the copper are not distinguished; rather a frequency of 8 is assigned to the $\{112\}<110>$ product component.

Table VII.7 The Four Most Important Deformation Parent Components and their Corresponding Product Orientations

MAIN fcc DEFORMATION COMPONENTS							
COPPER {112}<111>		**BRASS {110}<112>**		**S {123}<634>**		**GOSS {110}<001>**	
Orientation	**f†**	**Orientation**	**f†**	**Orientation**	**f†**	**Orientation**	**f†**
{211}<011>	6	{111}<112>	6	{211}<113>	5	{100}<001>	8
{110}<110>	4	{211}<113>	6	{210}<122>	2	{111}<110>	8
{210}<120>	4	{001}<110>	4	{221}<012>	2	{112}<110>	8
{123}<210>	4	{100}<012>	4	{113}<110>	2		
{221}<012>	2	{111}<123>	2	{311}<114>	2		
{113}<110>	2	{211}<120>	2				
{421}<012>	2						

† Frequency of occurrence out of 24 variants.

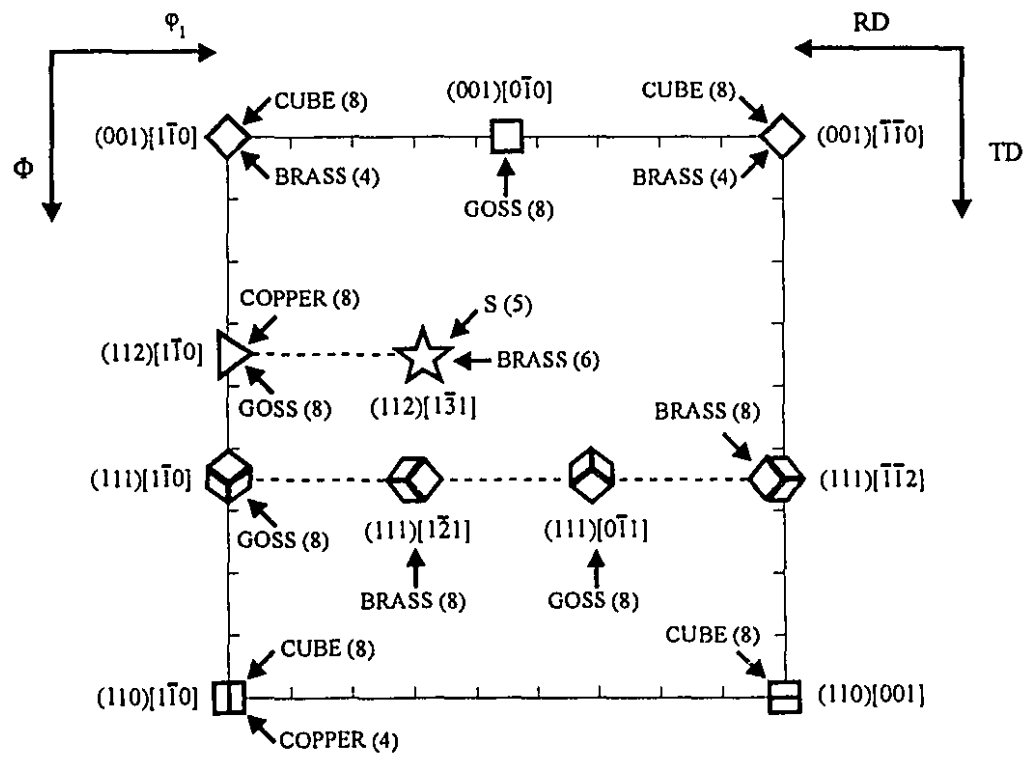

Figure VII.2 Selected bcc product orientations displayed on a $\varphi_2 = 45°$ section, showing the major fcc parent orientations from which they originate.

In experimental textures of steels, it is usual to find the RD and ND fibres. In order to investigate the possible origin of such continuous fibres in the austenite, three more parent orientations were transformed according to the Kurdjumov-Sachs relationship. These were the intermediate orientations Goss-brass, brass-S and S-copper. The results obtained are plotted in Figure VII.3, in a similar fashion to that employed for the previous figure. The frequencies are marked inside the symbols representing each parent orientation; those corresponding to components on the RD fibre are given as fractions so that the multiplicity that applies to this line in Euler space is respected. From this figure, it can be seen that the intermediate orientations analyzed do indeed strengthen some of the product components produced by the main parent orientations; however, they do so with quite low frequencies.

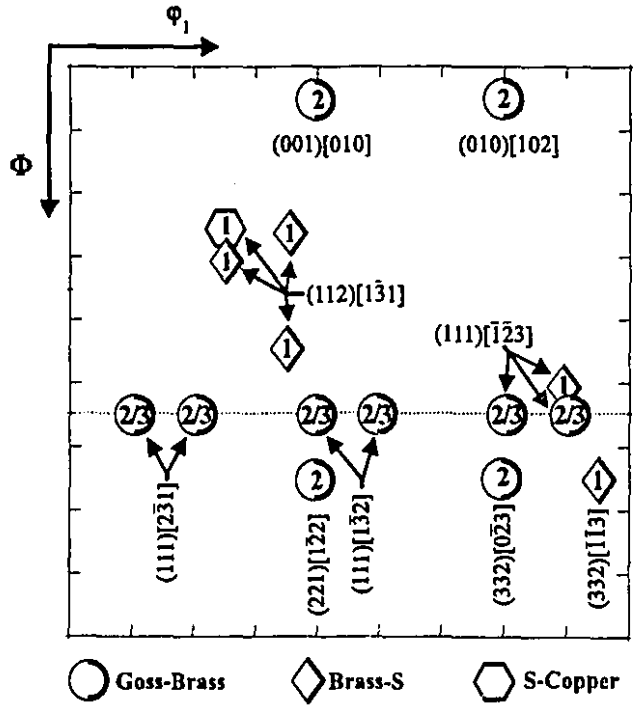

Figure VII.3 Selected bcc product orientations displayed on a $\varphi_2 = 45°$ section, showing the minor fcc parent orientations from which they originate.

The product components originating from the cube orientation, from the copper, brass and Goss, and from the Goss-brass, brass-S, S and S-copper are listed in Euler angle form in subspace I in the three tables that follow. In all the tables, the first column shows the number of *distinct* variants that forms from each of the parent orientations.

The six distinct variants of the transformed cube listed in Table VII.8 are reduced to three when approximate Miller indices are assigned to the exact orientations. Thus, the first and fourth variants in this table correspond to the rotated cube $\{001\}<110>$ in Figure VII.2, whereas the second and fifth on the one hand and third and sixth variant on the other correspond to the Goss $\{110\}<001>$ and rotated Goss $\{110\}<110>$, respectively. Similarly in Table VII.9, the six distinct variants of the transformed Goss may be grouped in pairs when the corresponding approximate Miller indices are used. Then, the first and third variants correspond to the transformed copper $\{113\}$-$\{112\}<110>$ in Figure VII.2, and the second and fifth on the one hand and the fourth and sixth variant on the other correspond to the cube $\{100\}<001>$ and the $\{111\}<110>$, respectively.

Table VII.8 The bcc Variants Produced from the Cube Component of Recrystallized Austenite

PARENT ORIENTATION: CUBE, (0°, 0°, 0°)			
Variant Number	EULER ANGLES OF PRODUCT COMPONENT [degrees]		
	φ_1	Φ	φ_2
1	65.8	10.5	65.8
2	6.4	42.1	75.6
3	83.6	42.1	14.4
4	24.2	10.5	24.2
5	14.4	42.1	83.6
6	75.6	42.1	6.4

Table VII.9 The bcc Variants Produced from Three of the Major Components in Unrecrystallized Austenite

Variant Number	DEFORMATION PARENT ORIENTATION								
	COPPER (90°, 35°, 45°)			BRASS (35°, 45°, 0°)			GOSS (0°, 45°, 0°)		
	EULER ANGLES OF PRODUCT COMPONENT [degrees]								
	φ_1	Φ	φ_2	φ_1	Φ	φ_2	φ_1	Φ	φ_2
1	3.9	40.1	28.1	49.8	41.6	37.8	14.6	41.6	37.8
2	81.4	25.7	4.1	76.0	10.3	72.8	68.7	10.3	17.2
3	14.5	36.6	27.2	27.9	35.6	54.1	7.4	35.6	35.9
4	7.2	20.1	52.2	42.7	35.6	35.9	5.3	54.7	45.0
5	10.4	28.6	55.4	33.5	10.3	17.2	54.7	5.3	45.0
6	4.6	40.1	8.8	20.7	41.6	52.2	12.6	50.0	33.1
7	20.2	25.7	32.8	30.0	54.7	45.0			
8	9.4	32.1	17.5	90.0	5.3	45.0			
9	71.6	32.8	18.7	22.7	50.0	56.9			
10	74.6	40.1	8.8	19.5	5.3	45.0			
11	0.0	24.7	45.0	47.8	50.0	33.1			
12	84.8	45.2	7.4	19.5	54.7	45.0			
13	0.0	35.3	45.0						

Table VII.10 The bcc Variants Produced from Four Other Texture Components in Unrecrystallized Austenite

Variant Number	DEFORMATION PARENT ORIENTATION											
	GOSS - BRASS (16°, 45°, 90°)			BRASS - S (47°, 41°, 77°)			S (59°, 37°, 63°)			S - COPPER (74°, 36°, 54°)		
	EULER ANGLES OF PRODUCT COMPONENT [degrees]											
	φ_1	Φ	φ_2	φ_1	Φ	φ_2	φ_1	Φ	φ_2	φ_1	Φ	φ_2
1	52.9	10.3	17.2	33.8	40.0	50.3	21.1	29.2	26.6	4.8	45.3	62.2
2	1.3	41.6	52.2	43.1	30.9	38.3	45.3	29.2	26.6	79.0	25.9	8.1
3	30.3	41.6	37.8	49.6	18.3	7.1	4.3	47.2	59.2	25.6	31.7	23.7
4	84.5	10.3	17.2	42.3	44.7	51.4	35.8	26.2	21.0	4.7	41.8	28.3
5	8.4	35.6	54.1	32.6	35.6	39.7	60.0	26.2	21.0	62.6	27.4	15.2
6	23.2	35.6	35.9	27.4	20.1	20.5	28.5	47.2	59.2	13.4	34.9	26.5
7	3.2	50.0	56.9	19.9	40.3	58.0	0.8	9.4	46.1	13.7	25.3	55.0
8	70.5	5.3	45.0	9.3	8.8	39.8	23.9	39.4	58.5	3.3	23.4	54.3
9	10.5	54.7	45.0	38.8	49.8	34.2	76.1	38.4	8.3	60.4	42.2	16.1
10	49.5	54.7	45.0	28.4	44.9	44.2	17.0	15.9	19.0	25.1	30.5	37.4
11	21.1	54.7	45.0	45.1	13.1	87.4	8.8	42.9	69.9	20.2	27.1	14.5
12	38.9	54.7	45.0	32.2	44.1	46.2	74.9	31.0	1.7	56.0	35.3	27.0
13	38.9	5.3	45.0	58.8	33.3	19.0	41.6	37.6	35.8	88.4	32.1	8.9
14	28.4	50.0	33.1	21.0	42.0	66.1	29.8	21.4	12.7	0.0	37.4	18.0
15	73.8	50.0	56.9	45.4	8.4	79.9	30.7	36.1	39.2	15.5	20.6	29.1
16	38.9	5.3	45.0	63.3	40.2	22.9	47.2	44.0	24.0	89.5	39.5	0.6
17				23.0	48.6	61.8	0.2	18.0	49.1	17.1	33.7	58.1
18				85.6	1.3	46.9	20.9	31.0	54.9	0.1	14.9	38.3
19				30.4	4.7	29.4	16.1	35.6	45.0	9.5	19.5	43.4
20				87.6	45.7	68.8	58.4	47.2	22.3	81.4	44.5	0.0
21				42.9	53.3	44.9	16.1	24.4	45.0	8.2	40.5	45.8
22				21.1	15.1	40.2	16.1	46.2	45.0	9.1	30.0	43.9
23				83.5	49.2	34.7	68.3	45.3	7.9	88.2	45.4	14.8
24				16.2	45.0	46.8	16.1	13.8	45.0	8.0	30.0	46.1

Chapter VIII

DISCUSSION

The influence of hot rolling parameters on the development of transformation textures is now becoming recognized. For instance, the occurrence of austenite recrystallization at the higher rolling temperatures is known to lead to the formation of the cube texture, which is weakened when the transformation to ferrite occurs. This is because, as indicated in Table VII.5 above, the cube component transforms into three product components, the $\{001\}<110>$, $\{110\}<001>$ and $\{110\}<110>$. Each one of these is predicted to be one third as intense as the parent orientation according to the Kurdjumov-Sachs relationship. Whether or not recrystallization takes place at a given temperature depends on the chemical composition of the material, which is thus one of the parameters that influences the final texture. The amount of reduction and the finish rolling temperature also affect the recrystallization kinetics, and even the initial grain size of the austenite plays a role.

The effect of these processing parameters on texture development will be considered in more detail here. The effect of finish rolling temperature is treated first.

The analysis is limited to the experimental observations corresponding to the higher austenitizing temperature and most severe reduction; nevertheless, as it extends to each of the materials studied, it includes the effect of chemical composition as well. The various finish rolling temperatures have been divided into two groups: rolling within the austenite range, both recrystallized and unrecrystallized, and finish rolling in the ferrite range. In the first case, a comparison is carried out between simulated and experimental transformation textures; this indicates the occurrence of variant selection and selective grain growth. Finally, changes in the texture produced by varying the austenitizing temperature (i.e., initial grain size) and the amount of rolling reduction are also examined.

VIII.1 Effect of Finish Rolling Temperature

The finish rolling temperature was varied for each material over a large range, from 1020°C down to 630°C (620°C in the case of the interstitial free steel). This includes the temperature ranges mentioned in Chapter IV, i.e., the recrystallized and unrecrystallized austenite regions, intercritical ($\gamma+\alpha$) region, and ferrite region. However, the particular conditions applicable to each steel varied slightly, due to their different chemical compositions. Thus, analysis of the microstructure and texture of the plain carbon steel samples finish rolled at 870°C indicated that some recrystallized austenite was still present, and that the high temperature phase was not unrecrystallized as expected. In the case of the IF steel, some rough estimates of the transformation temperature during the actual rolling trials indicated that some specimens were deformed in the intercritical range. Nevertheless, detailed studies of warm rolling in

this type of steel [77] show that the intercritical temperature range (the difference between the Ar_3 and Ar_1 temperatures) is as narrow as 30°C due to the low carbon level. Therefore, it seems reasonable to assume that, in the case of the interstitial free steel, rolling was carried out either above or below the intercritical range, i.e., either in the fully austenite or the fully ferrite region.

When rolling is finished before transformation starts, the ferrite simply inherits the texture developed in the parent austenite phase. Thus, it is possible to apply the Kurdjumov-Sachs relation to predict texture development. During rolling in the two phase region, however, the following processes occur concurrently and successively [45]: (1) crystal rotation of the parent phase, (2) transformation, and (3) crystal rotation of the product phase. The resultant texture is therefore more complex and is significantly influenced by the relative contributions of the three processes. The third process is of course still more important in the case of warm rolling.

VIII.1.1 Main fcc Deformation Texture Components

It has been shown [73] that the main texture components in deformed fcc metals are located within the so-called "α" and "β" fibres. The first consists of the orientations between $(101)[0\bar{1}0]$ (Goss) and $(101)[\bar{1}\bar{2}1]$ (brass), while the second runs from brass, through $(213)[\bar{3}\bar{6}4]$ (S), and finally ends at $(112)[\bar{1}\,\bar{1}\,1]$, the copper orientation.

The distribution of the texture along these fibres depends greatly on the amount of deformation:

- when low rolling reductions are employed, the fibres are relatively homogeneously populated;
- when higher reductions are applied, the "β" fibre is strengthened, and the Goss orientation decreases in intensity, leading in some cases to the almost complete elimination of the "α" fibre;
- when the deformation is very large, the "β" fibre continues to be strengthened, with the highest intensity located at the S component.

The detailed behaviour of these ideal orientations during deformation was studied recently using a rate-dependent crystal plasticity model [78, 79]. Different levels of strain were considered by using three kinds of boundary conditions: plane strain compression (full constraints) at low strains, and lath and pancake compression at intermediate and large strains, respectively (relaxed constraints). This analysis permitted assessment of the stabilities of the ideal orientations along the "α" and "β" fibres.

It was shown that, at low reductions, the orientations of fcc metals rotate towards the two fibres mentioned above. The flow velocities of the orientations in the vicinities of these two fibres increase with further deformation, while they are low for the orientations which have already reached the fibres. Eventually, the "α" fibre disappears, while the orientations in the "β" attain a stable end position near the copper orientation. This, however, requires an extremely large amount of deformation (strains of 5), prior to which the rolling texture extends along the entire length of the "β" fibre.

The orientation development along such fcc fibres is presented schematically in Figure VIII.1. Here, G represents the Goss, B the brass, C the copper, T the Taylor {4,4,11}<11,11,8> (which is close to the copper), and S'_1, S_3 and S'_3, the three variations of the S component corresponding to {124}<211> + 9° in φ_1, {123}<634> and {123}<634> + 6° in φ_1, respectively.

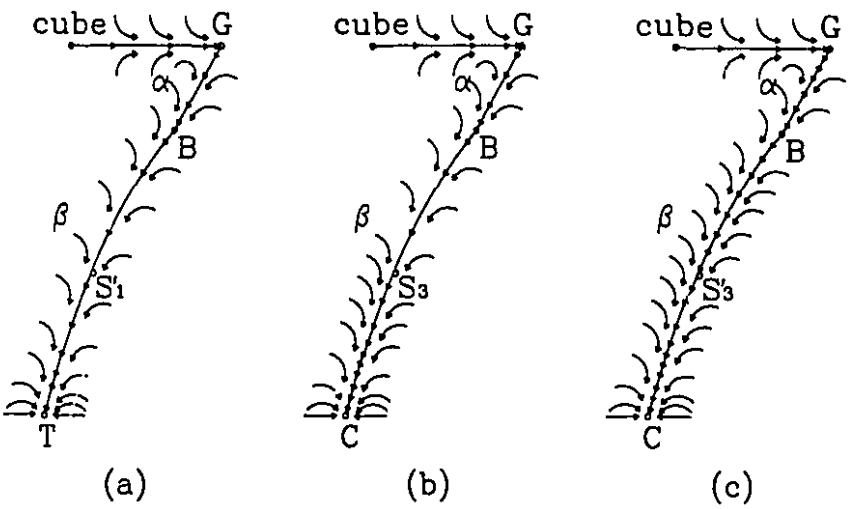

Figure VIII.1 Schematic models of orientation development during: (a) plane strain compression, (b) lath compression and (c) pancake compression. After [79].

The density distributions along the two fcc fibres depend not only on the shapes of the grains, but also on the orientation distribution present before rolling. For example, if the Goss component is initially strong, the deformed texture will have a sharp brass orientation, since the flow velocity of orientations along the "α" fibre is low even when large amounts of deformation are applied.

VIII.1.2 Finish Rolling in the Austenite Range

A finish rolling temperature of 1020°C corresponds to the recrystallized austenite region for all three steels. As already mentioned, the cube is the predominant fcc orientation under these conditions. According to Kurdjumov-Sachs, it is expected to transform with equal strength into the {001}<110>, {110}<110> and {110}<001> bcc components. From the experimental texture of the plain carbon steel (Figure VI.15), it can be seen that only the first two orientations are present, with comparable strengths, while the third one is completely missing. In the case of the other two materials (Figures VI.33 and VI.51), the rotated cube has the strongest intensity, followed by the rotated Goss with moderate strength; the transformed Goss orientation is also present, although at a lower intensity.

According to Tables VII.5a and VII.6a, four different γ components (including both recrystallization and deformation ones) can give rise to the bcc {001}<110> orientation. However, from the present experimental conditions, it seems reasonable to conclude that it has formed from the cube, {100}<001>. Thus, the differences in the intensities of the three cube transformation products described above indicate that variant selection in favour of the rotated cube is occurring during transformation.

Lowering the finish rolling temperature to 870°C results in no appreciable change in the texture of the plain carbon steel. The microstructure is also comparable to the one that corresponds to a finishing temperature of 1020°C, with only slight evidence of pancaking. Thus, it can be concluded that the ferrite in this material

transformed from a largely recrystallized austenite, and that this is responsible for the very weak texture.

The interstitial free steel, on the other hand, displays a gradually weaker rotated cube component, going from 1020°C to 920°C and then down to 870°C, and a smaller decrease in the intensity of the $\{110\}<110>$ orientation. Also, the microstructure becomes finer as the finishing temperature is decreased. These two observations, weaker texture and finer final grain size, can be explained if, in addition to variant selection during transformation, allowance is made for a selective growth mechanism. At high finishing temperatures, selective growth could enhance the importance of the $\{001\}<110>$ component at the expense of the two other orientations.

It has also been observed [80] that the ferrite grains nucleated at austenite boundaries can grow i) coherently into untransformed grains with which there is a Kurdjumov-Sachs relationship, or ii) incoherently into austenite grains with which there is no simple coincidence relationship. The extensive growth of such incoherent nuclei seems to occur at the higher temperatures of transformation, and is inhibited at low transformation temperatures, which are promoted by high cooling rates. Conversely, lowering the finish rolling temperature in the austenite range promotes pancaking, which in turn *raises* the transformation temperature. This thus encourages the growth of incoherent nuclei, reducing the strength of the rotated cube component, as well as refining the final microstructure.

In the case of the niobium microalloyed steel, lowering the finish rolling temperature to 870°C results in a pronounced change in texture. It can be seen from

Figure VI.33 that the {112}-{113}<110> components emerge with the highest intensities; these result from the transformation of the copper and Goss, and to a lesser extent the S, orientations in the deformed austenite, as already described (Table VII.7). The copper is also expected to produce some {110}<110>, although with only 4 variants instead of the 8 belonging to the {112}-{113}<110> partial fibre, see Table VII.7. As the {110}<110> is only a fifth as intense as the {112}-{113}<110> in Figure VI.33, it is clear that some form of variant selection is taking place. The intensity of the rotated cube component is still considerable, with an f(g) slightly above 4. However, in this case, it is the presence of the brass component in the pancaked austenite that can be considered responsible for the appearance of the {001}<110> orientation in the ferrite.

An important additional set of orientations are those in the vicinity of {554}<225>; these are illustrated in the TD fibre of Figure VI.33b. They are considered to form from the brass component in the deformed austenite, as indicated in Figure VI.11. Finally, the ND fibre is unevenly populated and displays relatively low intensities. It is in fact shifted towards the {211}<113> orientation, which is the main transformation product of the S component. (It is expected to occur at a frequency of 5 out of 24, see Table VII.7). This orientation does not belong to any of the fibres plotted here, but can be found in the φ_2=45° section of the ODF, as indicated in Figure VI.11. Although the {211}<113> orientation is not generally mentioned in the literature, there is evidence of its presence in the hot band after transformation, as can be seen in Figure VIII.2, taken from the work of Vanderschueren et al. [81].

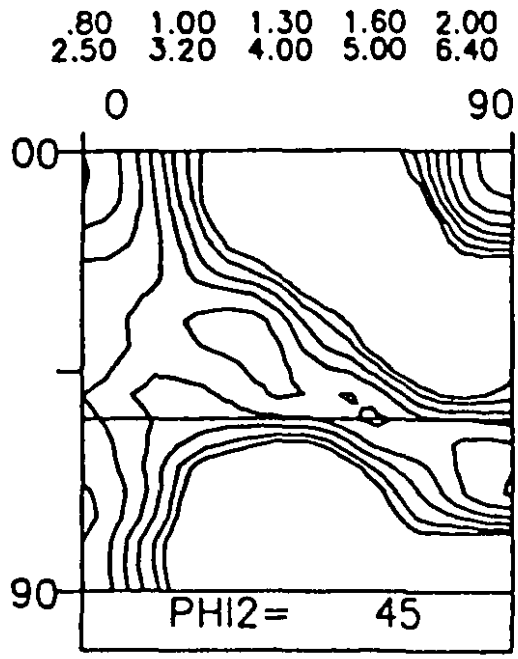

Figure VIII.2 Hot band texture for a steel with 0.012%C-0.067%Mn, finish rolled at 895°C. After [81].

In summary, when there is sufficient Nb present to produce austenite pancaking, lowering the finishing temperature leads to the intensification of the transformation products of the copper, brass, S and Goss fcc orientations. Such components will be inherited by the ferrite, although their proportions will be influenced by the occurrence of variant selection and selective growth. The factors that determine the *extent* (as opposed to the presence) of variant selection and selective growth are unfortunately little understood at this point and remain a subject for future investigation.

VIII.1.3 Comparison between Experimental and Simulated Textures

In a recent study carried out by co-workers in collaboration with the present author [82], some bcc transformation textures were derived analytically from the textures of annealed and cold rolled samples of an fcc Ni30Co alloy. These predictions were compared with the textures determined on the present Nb microalloyed steel finish rolled at 1020°C and 870°C. In this investigation, the experimental fcc recrystallization and rolling textures were expressed in terms of *continuous* ODF's as opposed to the *discrete* orientations employed here. The Kurdjumov-Sachs relationship was again assumed, together with the absence of variant selection.

The experimental ODF's of the recrystallized and deformed fcc model material are presented in Figures VIII.3 (a) and (b), respectively. Both textures appear quite sharp, with intensities of over 20 times random. The main texture component of the recrystallized material is the cube $\{100\}<001>$; also present are a peak close to the S component, the $\{348\}<433>$ (with an intensity of 7.1), and a minor $\{210\}<001>$ component with $f(g)=2.5$. The maximum intensity of the cold rolled Ni-30Co alloy, Figure VIII.3(b), is located at the S $\{123\}<634>$ orientation. Other important components are the copper $\{112\}<111>$ ($f(g)=17.4$) and brass $\{110\}<112>$ ($f(g)=15.6$), and some minor peaks corresponding to the Goss $\{110\}<001>$, Goss/brass $\{110\}<115>$, brass/S $\{146\}<211>$ and $\{103\}<001>$ orientations.

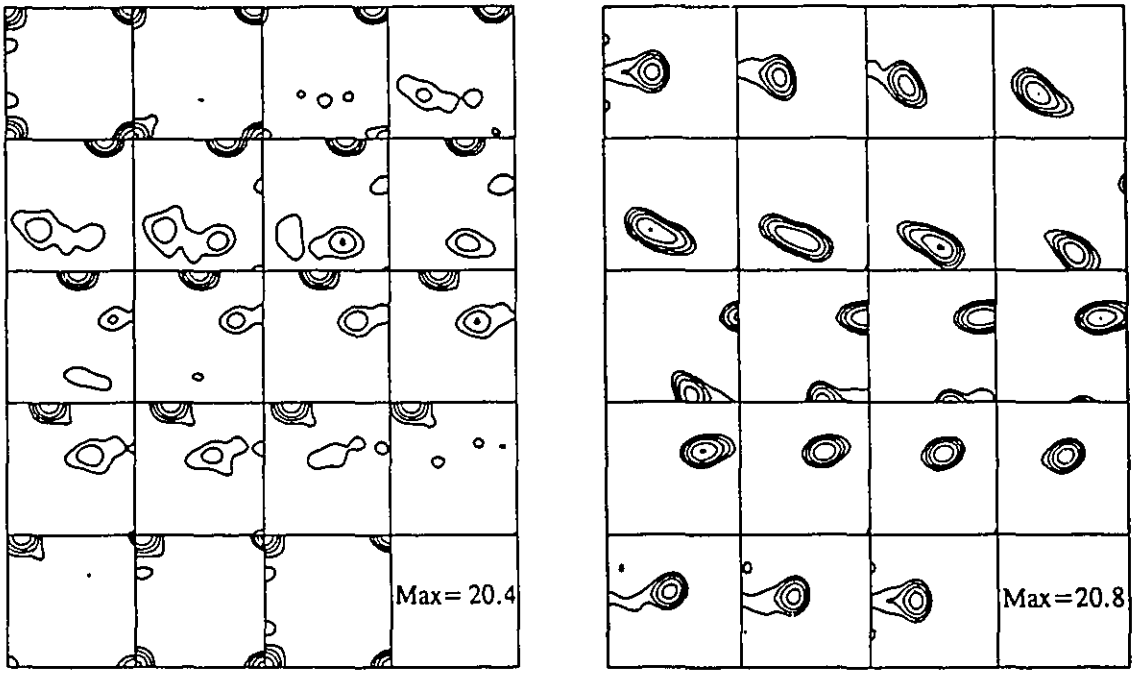

Figure VIII.3 Experimental ODF's (φ_2 sections 0°-90°, 5° intervals) of the Ni-30%Co alloy: (a) recrystallized and (b) cold rolled. Intensity levels: 2, 4, 7, 12, 20. After [82].

The bcc textures derived analytically from the fcc ODF's of the model material are shown in Figures VIII.4 (a) and (b); these correspond to the recrystallized and deformed cases, respectively. Both textures are much weaker than the initial ones, due to the transformation of each parent component into as many as 24 different product orientations, as required by Kurdjumov-Sachs. In the recrystallized and transformed condition, Figure VIII.4(a), the only two orientations of moderate strength are the {100}<011> and {110}<110>. In the deformed texture, the {113}-{112}<110> component is the sharpest, with an intensity of 4.5 times random; other moderately

strong components are the {332}<113>, {001}<110>, {110}<110> and {111}<112>.

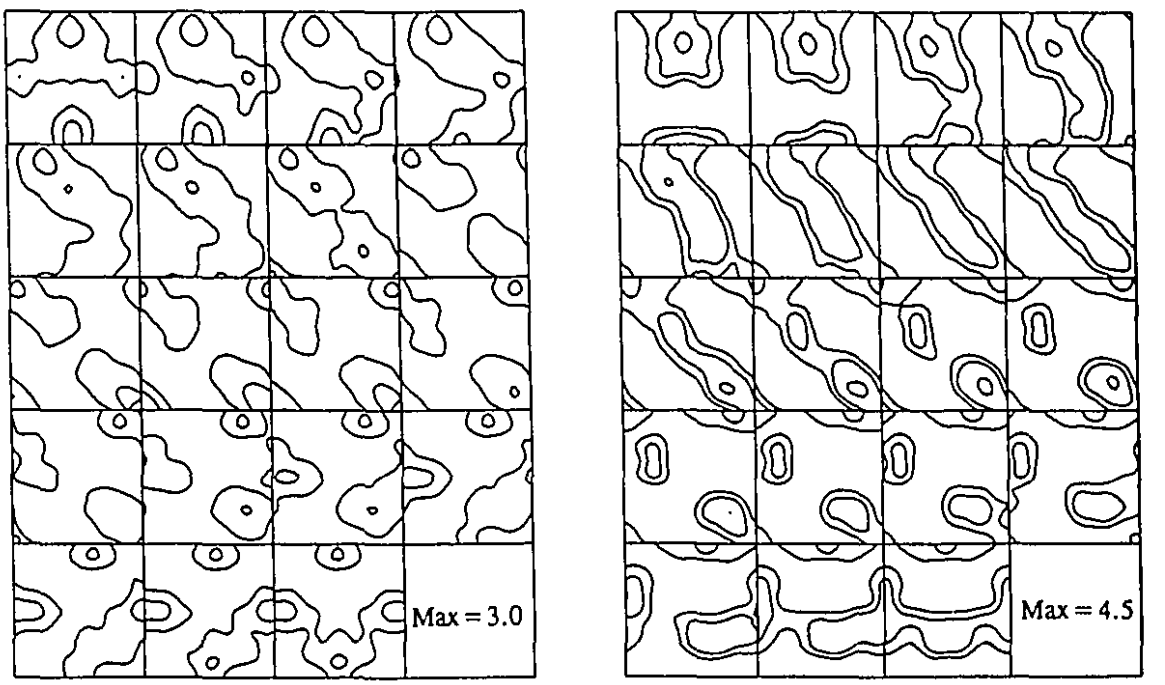

Figure VIII.4 Transformation ODF's (φ_1 sections 0°-90°, 5° intervals) of the (a) recrystallized and (b) cold rolled Ni-30%Co alloy derived using the Kurdjumov-Sachs relationship. Intensity levels: 1, 2, 4. After [82].

The *experimental* textures of the niobium microalloyed steel finish rolled at 1020°C and 870°C are shown in Figures VIII.5 (a) and (b), in φ_1 = constant sections. These correspond to samples N1 and N7 of Table V.2. In the sample finish rolled in the austenite recrystallization range (T_f = 1020°C), the two most important texture components are the {001}<110> and {110}<110>, with intensities of around 4× and 2× random. In the second case, when rolling was finished

within the γ no-recrystallization range (T_f = 870°C), the texture maximum was located near the {113}-{112}<110>, with an f(g) of about 8× random. Also, there is a reasonably strong {001}<110> component, and a moderate one at {332}<113>.

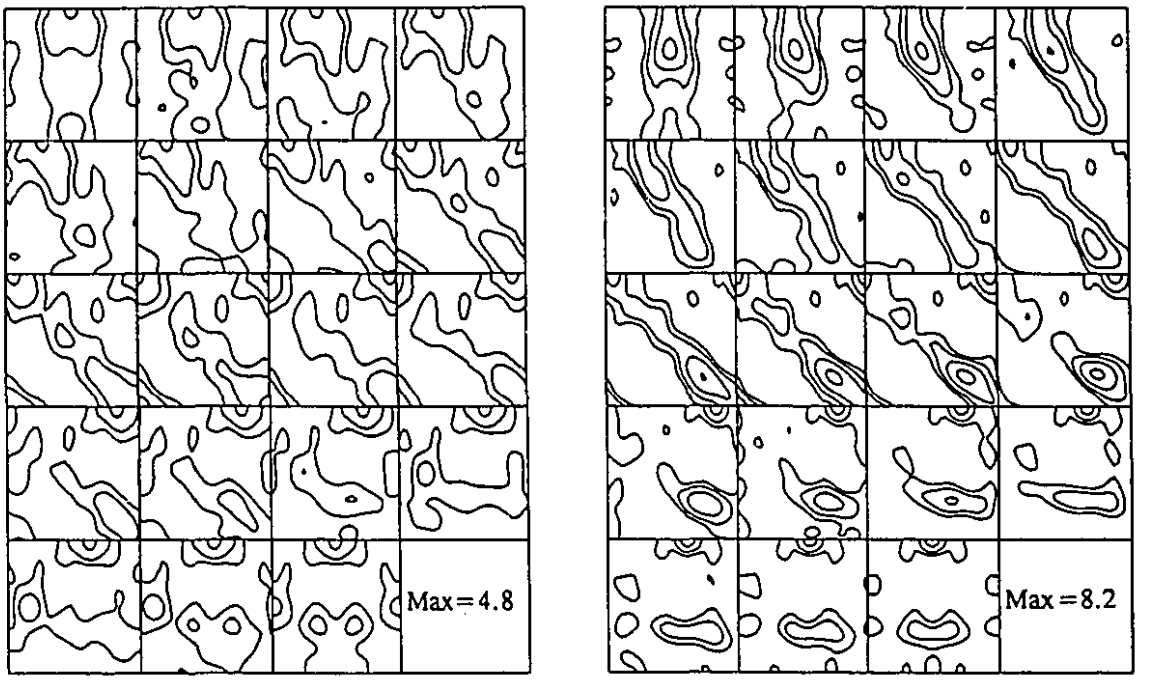

Figure VIII.5 Experimental ODF's (φ_1 sections 0°-90°, 5° intervals) of the Nb-steel hot rolled (a) in the recrystallization temperature range and (b) in the pancaking temperature range, both air cooled. Intensity levels: 1, 2, 4, 7. After [82].

It is evident from Figures VIII.4a and VIII.5a that the general features of the bcc texture derived analytically from the fcc texture of the recrystallized Ni-30Co alloy are in reasonably good correspondence with the texture of the niobium microalloyed steel finish rolled at 1020°C. The levels and locations of the intensity maxima are

comparable in the two cases, although the experimental texture is slightly sharper. By contrast, the experimental texture of the steel finish rolled in the austenite no-recrystallization range is considerable sharper (about 1.8 times) than the corresponding analytically derived one (Figures VIII.4b and VIII.5b, respectively), although the global characteristics are again similar.

A more visual illustration of the similarities and differences described above is provided in Figures VIII.6 (a) and (b), by means of "difference ODF's". Such diagrams were obtained by subtracting the ODF of Figure VIII.5a from that of Figure VIII.4a, and the ODF of Figure VIII.5b from the one of Figure VIII.4b. In Figure VIII.6, the regions where the intensities are higher in the experimental ODF are represented by the unshaded areas, and the regions where the intensities are higher in the predicted texture are shown shaded.

The following conclusions can be drawn from the data presented above:

(i) The fcc recrystallization range. The intensity of the {001}<110> component in the experimental ODF is more than twice as sharp as in the simulation. This could be explained by the occurrence of variant selection in favour of this component, assuming that it was formed from the cube parent component. In such an event, the {110}<110> and {110}<001> orientations would be expected to be *less sharp* than in the simulation, which was done without using any variant selection. Since the intensities of these two orientations are comparable in the experimental and simulated textures, it seems that the explanation for the observed textural differences must be provided by selective growth instead.

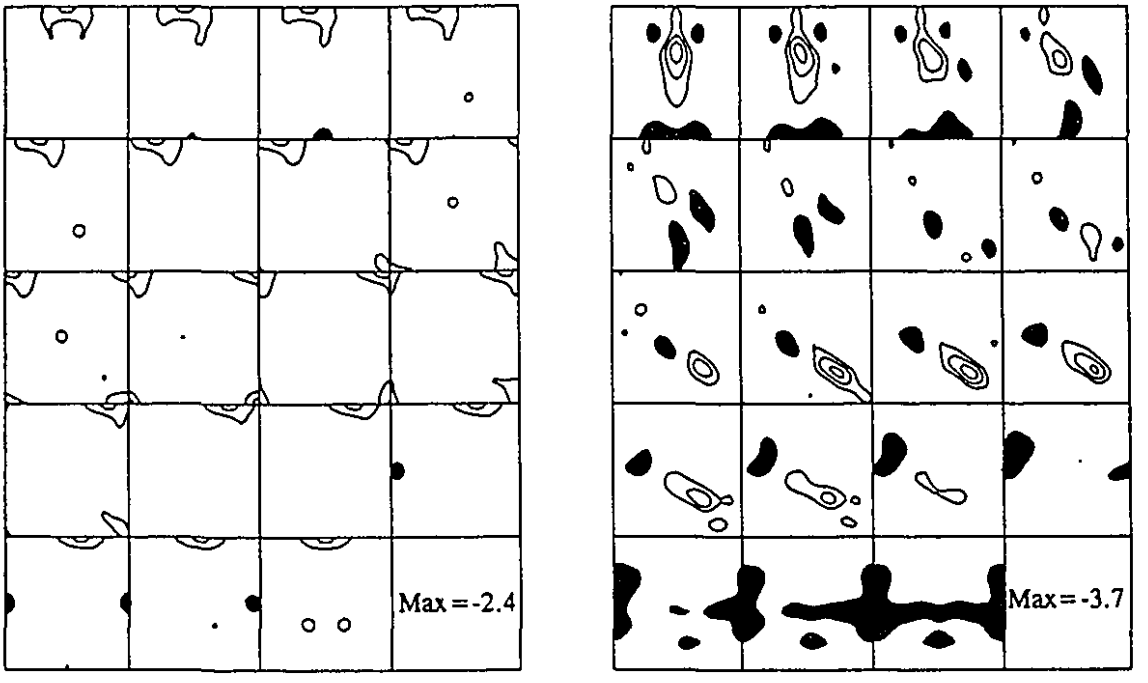

Figure VIII.6 Difference ODF's (φ_1 sections 0°-90°, 5° intervals) obtained by subtracting (a) the ODF of Figure VIII.5a from that of Figure VIII.4a and (b) the ODF of Figure VIII.5b from that of Figure VIII.4b. The regions where the intensities are higher in the experimental ODF are shown unshaded. The regions where the intensities are higher in the predicted ODF are illustrated by shaded areas. Intensity levels: -3, -2, -1, 1, 2, 3. After [82].

According to this view, the {001}<110> orientation grows selectively into the surrounding non-cube orientated γ matrix, as suggested in section VIII.1.2. Thus, the present results imply that when a cube orientated γ grain transforms into the {001}<110>, {110}<110> and {110}<001> α orientations, the {001}<110> component grows more rapidly than the other two orientations.

An alternative to the previous two mechanisms involves the presence of a mixed texture in the austenite prior to transformation, including other recrystallization as well as deformation fcc components. These could involve, for instance, the {110}<111>, {221}<212> and {113}<332> components, in addition to the brass and copper austenite components, as stated in Tables VII.5 and VII.6. Such additional austenite components could affect the relative strengths of the three products of the cube.

(ii) The fcc no-recrystallization range. In the case of the texture predicted from the *deformed* fcc alloy, both the {001}<110> and {110}<110> components have moderate intensities (f(g)≈3), but there is only a weak {110}<001>. This last orientation cannot be produced by the transformation, following the Kurdjumov-Sachs relationship, of any of the deformation components investigated here (Table VII.6a), but only from the cube. The origins of the first two components must lie in the fcc deformed texture, the rotated cube forming from the {110}<112> and the rotated Goss from the {112}<111>. In the experimental texture, the {001}<110> component is strong, while the {110}<110> is essentially absent. These observations can be explained in terms of the occurrence of variant selection in favour of the rotated cube component during transformation from the rolling texture orientations (mainly, the brass, as indicated in Figure VII.2). There may also be faster growth of the {001}<110> orientated regions into the γ matrix, as in the case of the steel finished in the austenite recrystallization range.

Another important difference between the simulated and experimental textures concerns the intensities of the {113}<110> and {332}<113> bcc components. These appear with nearly equal intensity in the simulations; however, in the

experimental textures, the {113}<110> is shifted towards the {112}<110> orientation and is about three times as intense as the {332}<113>. The bcc {113}-{112}<110> and {332}<113> (which is close to the {111}<112> component) are expected to be formed with similar intensities from the copper and brass components, respectively, of the deformed γ texture (as described in Table VII.7). Since it is assumed that the copper and brass in the austenite were present at similar intensities (for the deformation levels considered here and on the basis of the model fcc material results), once again the much sharper {113}-{112}<110> and weaker {332}<113> components can be explained by a combination of variant selection during the $\gamma \rightarrow \alpha$ transformation followed by selective growth.

Similar imbalances in the intensities of the {113}<110> and {332}<113> components were observed by Inagaki [83]; they were attributed to the presence of manganese (at a level of 2.48%), which is known to increase the stability of the austenite and consequently to decrease the transformation temperature. As the transformation temperature is lowered, grain growth is increasingly limited, and the relatively sharp "nucleation texture" is expected to be retained to an increasing degree. Through their effects on lowering the transformation temperature, higher cooling rates are expected to lead to results similar to those of higher Mn levels. In the present steel, with 1.35% Mn, a relatively high transformation temperature is involved. This should enhance the growth of specific α orientations (e.g. the {113}<110> and {001}<110>). Thus, the α texture produced during nucleation can be significantly altered via selective growth.

VIII.1.4 Effect of Variant Selection

The differences between the simulated and experimental textures described in the previous section have been explained by the occurrence of one or both of:

(i) variant selection during the $\gamma \rightarrow \alpha$ transformation, and

(ii) the selective growth of certain α orientations, a phenomenon affected by steel chemistry and cooling rate.

In order to investigate the effects of variant selection in the absence of perceptible growth, several plain carbon and niobium steel samples were quenched directly into water after controlled rolling, resulting in the formation of martensite. The texture results obtained were presented in Section VI.2.1.1, in Figures VI.24 to VI.29 for the plain carbon steel, and in Figures VI.42 to VI.47 for the niobium microalloyed steel. Two finish rolling temperatures were employed for each material, 1020°C and 870°C.

In the plain carbon steel, the higher cooling rate changed the relative strengths of the three products of the cube $\{100\}<001>$, as compared to the air cooled material. When the deformation is high enough (i.e. 90%) and for the finishing temperature of 1020°C, the $\{110\}<110>$ orientation becomes very strong, with an intensity even higher than that of the rotated cube. The latter remains unchanged as the reduction is increased, and the $\{110\}<001>$ component is very weak in most cases. It can therefore be concluded that variant selection occurs in the quenched samples, and that it favours the development of the $\{001\}<110>$ and $\{110\}<110>$ orientations.

When the samples are air cooled, the strengthening of the former at the expense of the latter can be explained as resulting from selective growth.

For the niobium microalloyed steel, the main difference in texture due to the increase in cooling rate concerns the samples transformed from unrecrystallized austenite. It consists of the strengthening of a peak at {111}<112> - {332}<113>, especially at a reduction of 90%, to nearly the same intensity as that displayed by the {113}-{112}<110> component.

To facilitate comparison of the simulated texture displayed in Figure VIII.4b with the corresponding texture of the quenched material (sample N10), the latter is replotted in terms of φ_1 sections in Figure VIII.7. Here the maximum orientation density is about 1.8 times higher than in the simulated texture, but in both cases the {332}<113> and {113}<110> orientations display nearly equal intensities. The latter observation can be interpreted as indicating either the absence of variant selection during quenching, or that the {113}<110> and {332}<113> components are equally favoured during transformation.

Thus, it appears that the final texture of the ferrite formed from recrystallized or deformed austenite is modified by both variant selection and selective growth, although the relative contributions of these two mechanisms may vary. The texture of the martensite obtained from unrecrystallized γ, on the other hand, is affected only, if at all, by variant selection.

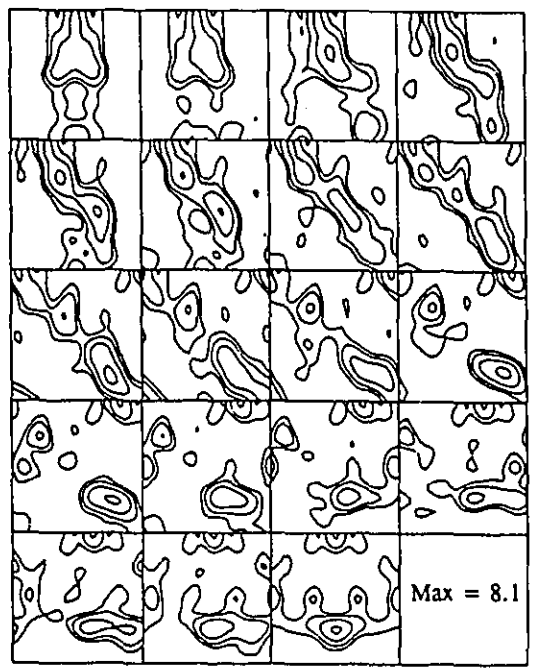

Figure VIII.7 Experimental ODF (φ_1 sections 0°-90°, 5° intervals) of the Nb steel water quenched after hot rolling in the pancaking temperature range (sample N10). Intensity levels: 1, 2, 4, 7.

The general intensity levels of the textures of the ferrite and martensite derived from unrecrystallized austenite are similar and about twice as sharp as the textures of the ferrite and martensite obtained from recrystallized austenite. In the pancaked cases, the parent austenite contains higher dislocation densities, before transformation, than the austenite in the recrystallized cases. Now, appreciable variant selection appears to take place during transformation from recrystallized austenite (for both ferrite and martensite), while apparently less variant selection occurs in the first and second cases.

Thus, the extent to which variant selection is involved seems to depend on the dislocation density of the parent austenite.

Since the Kurdjumov-Sachs relationship governs the γ-to-α as well as the γ-to-α' transformations, the preferred variants may be similar if such selection is independent of the cooling rate. This may be the reason why the general sharpnesses of the Nb steel textures, whether air cooled or quenched, are similar. The *differences* in the texture intensities in the two materials may then be explained as being due to selective α growth in the case of the ferrite, and the absence of selective growth in the case of the martensite.

VIII.1.5 Finish Rolling in the γ + α and α Regions

When rolling was finished in either the intercritical or the ferrite range, the texture was strengthened to various degrees in each of the steels studied here. Consider the samples austenitized at 1250°C and rolled to 90% reduction. The plots of the resulting RD, TD and ND fibres in Figures VI.15, VI.33 and VI.51 (for the plain carbon, Nb microalloyed and IF steel, respectively) clearly show the development of the texture as the finish rolling temperature is lowered.

In the plain carbon steel, finish rolling in the intercritical (α + γ) range did not produce any significant difference with respect to rolling in the austenitic region. When the temperature was lowered into the ferrite region and T_f's of 770°C and 730°C were employed, a very broad peak including the orientations between {114}<110>

and {223}<110> began to develop, but always with intensities lower than 4.0 times random. Also, the {554}<225> component was slightly enhanced. The lowest ferrite T_f of 630°C led to the sharpest texture, with a very strong {223}<110> component [f(g)=8] and a well defined peak at the {554}<225> orientation. The ND fibre was also enhanced, and reached an intensity of 4.0 times random. Thus, it is clear that the deformation of ferrite is essential in this material if a fairly strong texture is to be produced.

For the niobium microalloyed steel, the partial RD fibre (from the {001}<110> to the {111}<110> component) was already strong after deformation in the austenite no-recrystallization range. When rolling was finished within the intercritical temperature range, the texture displayed a similar profile, with only a slightly weaker {113}-{112}<110> orientation. The latter is produced by transformation from the copper and Goss fcc deformation components; it is also strengthened by ferrite rolling through rotation of the {113}<110> into the {112}<110> and finally into the {223}<110> position. Therefore, as the finishing temperature is decreased, the sharpness of the inherited texture decreases since the austenite receives less deformation, and it is deformation of the ferrite that increasingly contributes to the formation of the final texture. This is evident from the warm rolling texture, in which the {223}<110> component attains the highest intensity.

Thus it appears that the textures formed by warm rolling are only slightly influenced by the initial transformation texture inherited by the ferrite from the austenite. This is further supported by the observation that an almost perfect ND fibre of about the same strength is present in both the plain carbon and microalloyed steels

after ferrite rolling, although the intensities of the textures in the two steels differed widely at the beginning of α rolling.

For the interstitial free steel, it was assumed that the three lowest finishing temperatures all correspond to the ferrite region. Decreasing this temperature (which corresponds to increasing the amount of ferrite deformation) definitely produces the rotation of the orientations described in sections IV.4.3 and IV.4.4. Thus, from Figure VI.51a, it is clear that the RD fibre changes from having a broad peak that includes the {114}-{112}<110> orientations at T_f = 820°C and 720°C, to a definite overall maximum corresponding to the {223}<110> component at 620°C. Similarly, from the TD fibre in Figure VI.51, it can be seen that the {554}<225> component is moderately strengthened and shifted in the direction of the {111}<112>. Finally, the ND fibre displays an increase in intensity from an f(g) = 4 to an f(g) = 6 as the finish rolling temperature is reduced from 820°C to 620°C.

VIII.2 Effect of Austenitizing Temperature

The initial austenite grain size is a parameter which will affect the final texture of a controlled rolled material, since, for instance, it influences the process of recrystallization before transformation. It also determines the amount of shear banding and deformation banding that takes place, as their incidence increases with grain size. The austenite grain size is determined by the soaking or austenitizing temperature of the steel before deformation starts. It was shown for a 0.1%C-0.3%Si-1.6%Mn-0.04%Nb steel by Inagaki [37] that a sharper texture is obtained when the soaking temperature is

decreased from 1250°C to 1100°C, that is when the initial grain size is reduced. His results are reproduced here in Figure VIII.8, for a finish rolling temperature of 800°C (the only one investigated). The final microstructure he observed was also finer, and the spacing between pearlite bands was narrower.

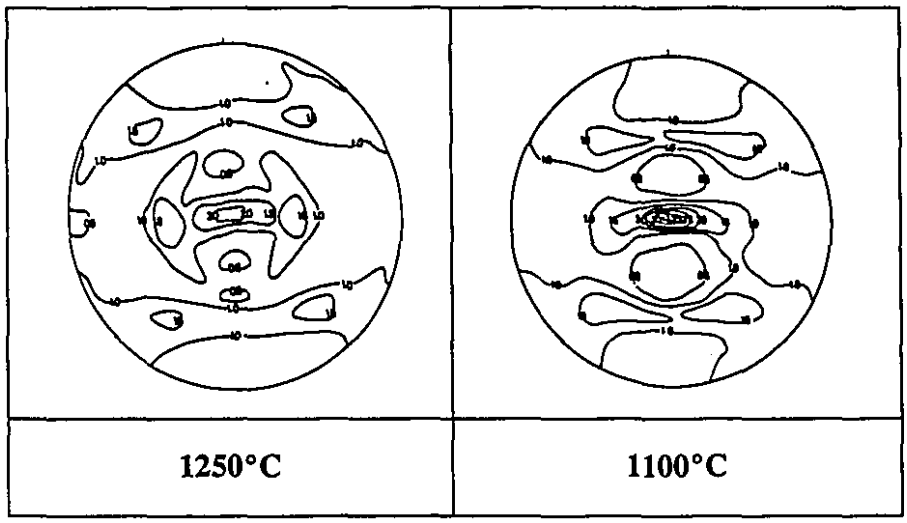

Figure VIII.8 Effect of soaking temperature on the texture of a 0.1%C-0.3%Si-1.6%Mn-0.04%Nb steel. (200) pole figures. After [37].

In this work, the effect of austenitizing temperature was investigated for all the finish rolling temperatures, and for all three steels. The results expressed in the form of (200) pole figures were presented in Figures VI.20, VI.38 and VI.56 for the plain carbon, Nb microalloyed and interstitial free steels, respectively. The corresponding $\varphi_2 = 45°$ sections were given in Figures VI.22, VI.40 and VI.58, and the RD, TD and ND fibres in Figures VI.23, VI.41 and VI.59. All these trials involved an austenitizing temperature of 1150°C and a total rolling reduction of 90%.

These results show that the analysis of (200) pole figures alone can be misleading. Thus, for the plain carbon steel, the pole figures indicate that the lower austenitizing temperature consistently results in a stronger texture. However, from the ODF's and fibres, it can be seen that the texture was strengthened only for finishing temperatures of 1020°C and 730°C; in the case of warm rolling, a finer initial grain size produced *weaker* fibres with broader maxima. Nevertheless, the {001}<110> and {110}<001> orientations display slight increases in intensity, pointing to the presence of a stronger cube component in the austenite when the material has a finer grain size.

For the Nb microalloyed steel, the samples finish rolled at the higher temperatures display comparable textures independently of the austenitizing temperature. When the T_f is reduced to 730°C and 630°C, a stronger RD fibre (shifted towards the {112}-{223}<110> component) and a stronger {554}<225> orientation are produced when the initial grain size is reduced, although the ND fibre remains stronger for the higher austenitizing temperature of 1250°C.

Finally, in the case of the interstitial free steel, the textures are comparable despite the decrease in the initial grain size, with only a slightly weaker and broader RD fibre for T_f = 820°C to 620°C. For this material, data corresponding to an austenitizing temperature of 1150°C with a reduction of 75% are also available, for finishing temperatures of 1020°C, 920°C, 820°C and 720°C; these fibres were presented in Figure VI.63 above. The corresponding fibres for the higher soaking temperature were shown in Figure VI.55, only for T_f's of 820°C and 720°C. The {001}<110> component, as well as the partial RD fibre running up to the

{111}<110> orientation, are strengthened when the finer initial grain size is employed. In the sample finish rolled at 820°C, the ND fibre and the {554}<225> component are also stronger for the lower soaking temperature, but the changes are not substantial.

The experimental results therefore indicate that the texture is not particularly sensitive to the austenitization temperature. Other processing parameters, such as the finish rolling temperature, appear to play a much larger role in the development of the texture. Nevertheless, the general trend observed is that lower reheating temperatures and finer initial grain sizes lead to textures that are somewhat more intense.

VIII.3 Effect of Amount of Reduction

The amount of deformation was studied for a soaking temperature of 1250°C in the case of the plain carbon and Nb microalloyed steels, and for both austenitizing temperatures of 1250°C and 1150°C for the interstitial free steel. Two levels of reduction were investigated, 75% and 90%. The details of the rolling schedules were presented in Tables V.3, V.5 and V.6.

In the plain carbon steel, a reduction of 75% produced very flat textures, as shown in Figure VI.19. In the samples finish rolled in the austenite range, the transformation products of the cube orientation prevail, but always with intensities below f(g) = 3. With lower finishing temperatures, some strengthening of the partial RD fibre between the {114}<110> and {223}<110> orientations was observed, as

well as a slight increase of the {554}<225> and {332}<113> components. However, such enhancements are minor and are regarded as unimportant. With respect to the microstructures, the lower reduction produced structures with quite large and equiaxed grains, as compared to the material deformed to 90%. Thus, for this material, a deformation of 75% is not enough to promote the development of a strong texture, even for the warm rolling condition.

Even for the niobium microalloyed steel, a rolling reduction of 75% was not enough to promote a strong texture, or a fine microstructure. It can be seen in Figure VI.37 that, although slightly stronger compared to the plain carbon steel, the fibres display intensities around or below 4 times random, for all the finishing temperatures. It is possible to recognize the transformation products of the cube for the samples rolled within the austenite range. When the lower T_f's were employed, the orientations which can be identified indeed correspond to the transformation products derived from the fcc deformation components, such as the {112}<110> (transformed from the copper) and the {111}<112> (transformed from the brass). However, their low intensities indicate that neither parent orientation was present at a high intensity level. It is of interest that the transformed components are not particularly strengthened by rotation of the bcc grains as a result of intercritical or warm rolling.

For the two IF steel samples austenitized at 1250°C and rolled to 75% reduction, again the textures are weaker than the corresponding ones produced by the higher deformation (with the exception of the orientations around {554}<225>, which are comparable). Otherwise, the partial RD fibre running from {001}<110> to {111}<110> is about 30% weaker, with an intensity maximum located between the

{223}<110> and {111}<110> components. On the other hand, when an austenitizing temperature of 1150°C was employed, the textures display similar characteristics at the two amounts of deformation. The most important difference is the location of the maximum for the RD fibre; it can be seen from Figures VI.59 and VI.63 that with increasing deformation, the {114}-{113}<110> orientations are rotated towards the {223}<110> component. Therefore, a finer grain size in this material promotes the development of a fairly sharp texture, and this is maintained even for the lower reduction. Nevertheless, the higher amount of deformation still results in the stronger texture.

VIII.4 Effect of Chemical Composition

The results discussed above clearly show the importance of the chemical composition on the nature and sharpness of the texture after controlled rolling. In the plain carbon steel, since the temperature of no-recrystallization is only slightly higher than the transformation temperature, the austenite is able to recrystallize prior to transformation to ferrite, resulting in a very weak texture. For this material, the only way to promote a sharp texture is by applying large reductions and finish rolling at low temperatures, within the ferrite range.

The recrystallization of austenite can be retarded by the addition of alloying elements (such as niobium) to the steel. This promotes the strengthening of fcc deformation components, and leads to the inheritance of a fairly strong texture in the

ferrite. The partial {114}-{223}<110> fibre is developed, and the rotated cube {001}<110> is also strong. However, the ND fibre, as well as the {554}<225> and surrounding orientations, are formed with a high intensity only after warm rolling.

The interstitial free steel developed the strongest overall texture after warm rolling. The ND fibre, as well as the orientations around {554}<225>, reached an intensity of 6 times random. However, the partial RD fibre is also very strong, including the rotated cube, which degrades the formability properties of this material.

Chapter IX

CONCLUSIONS

In this work, the effect of hot rolling parameters on the development of transformation textures was studied. Three materials were selected: a plain carbon, a niobium microalloyed and an interstitial free steel. The experimental processing variables investigated were the austenitizing temperature, amount of reduction, and finish rolling temperature. The resulting ferrite textures were measured. The latter were compared with the transformation textures predicted to form from recrystallized or cold rolled fcc parent orientations using the Kurdjumov-Sachs relationship. The results obtained led to the following conclusions.

1. When most of the reduction was applied in the austenite recrystallization range for the three materials, the cube texture appeared to form. This was converted on transformation into the rotated cube $\{001\}<110>$, the Goss $\{110\}<001>$ and the rotated Goss $\{110\}<110>$, with the first one being favoured over the other two.

2. When the austenite remained in the pancaked state, lowering the finishing temperature resulted in the intensification of the transformation products of the copper {112}<111>, brass {110}<112>, S {123}<634> and Goss {110}<001> fcc orientations.

3. The Kurdjumov Sachs calculations showed that: i) the copper is expected to transform into the {112}<110>, {110}<110>, {210}<120> and {123}<210> orientations; ii) the brass into the {111}<112>, {211}<113>, {001}<110> and {100}<012>; iii) the S into the {211}<113>; and iv) the Goss into the {100}<001>, {111}<110> and {112}<110>.

4. The experimental results indicate that the intensities of the transformation products do not exactly follow the pattern called for by the calculations. It appears instead that: i) during transformation from the copper, the {112}<110> is favoured over the {110}<110> and {210}<120>; ii) during transformation from the brass, the {001}<110> is favoured over the {111}<112> and {211}<113> (for orientations in the vicinity of the {111}<112>, the {554}<225> and {332}<113> are favoured over the {111}<123> and {111}<112> respectively); and iii) during transformation from the Goss, the {111}<110> is favoured over the {100}<001> and {112}<110>.

5. The calculations indicate that the final texture of the ferrite formed from recrystallized or deformed austenite is modified by both variant selection and selective growth, although the relative contributions of these two mechanisms may vary.

6. When rolling is continued after transformation has begun, it is the deformation of the ferrite that determines the final texture. As the finish rolling temperature is decreased, the RD fibre is strengthened, with the overall maximum located around the {223}<110> orientation. A strong {554}<225> component is formed, and the ND fibre displays higher intensities. However, the rotated cube is also present at a relatively high intensity, and if the material is further processed, this can be detrimental to its formability properties.

7. In general, lower reheating temperatures, and thus finer initial grain sizes, lead to more intense textures. However, this effect is not very pronounced and can easily be masked by the influence of other more important processing factors.

8. Larger deformations are necessary to promote the formation of stronger textures. The microstructure is refined as the amount of reduction is increased, and the rotations which lead to the development of important preferred orientations are also enhanced.

9. In the plain carbon steel, only warm rolling produced a strong texture. At austenite finish rolling temperatures, recrystallization occurs, and the texture inherited by the ferrite is rather weak. In the interstitial free steel, the strongest textures are again produced by warm rolling. In the niobium steel, since the recrystallization of austenite is retarded by the presence of the microalloying element, the fcc deformation components are strengthened. A fairly strong texture is then inherited by the ferrite, which can in turn be further enhanced by ferrite deformation after transformation.

STATEMENT OF ORIGINALITY AND CONTRIBUTION TO KNOWLEDGE

1. A detailed and systematic set of rolling experiments was carried out in which samples were finished in the following four temperature ranges: i) austenite recrystallization, ii) austenite pancaking, iii) intercritical rolling, and iv) warm (ferrite) rolling. The textures which resulted were carefully measured and are presented here in a very complete form, so that they can become a useful reference for the interpretation of industrial observations. The detailed effects of processing parameters on texture development were determined, and the most important texture components were identified in each experiment. Thus, the rotated cube $\{001\}<110>$, which is the main orientation produced by transformation from recrystallized austenite, was shown to also be present when deformation is applied in the pancaked austenite range, and after warm rolling. It was demonstrated here for the first time that this is because it can also originate from the fcc brass (deformation) component. The other main orientations produced by transformation from pancaked austenite correspond to the products of the copper, brass, S and Goss fcc components. The partial RD fibre, the ND fibre and orientations around the $\{554\}<225>$ were identified as resulting from the transformation of these orientations; the $\{211\}<113>$ component was also found to be an important transformation product. There is evidence of the existence of the latter in literature, but it had not been explicitly mentioned before, nor was its provenance deduced.

2. It was shown in this work that lower reheating temperatures and finer austenite grain sizes lead to more intense ferrite textures. However, this effect can be

masked by the influence of more important parameters, such as the finish rolling temperature or amount of reduction.

3. The transformation products that form from individual fcc recrystallization and deformation parent orientations were calculated using the Kurdjumov-Sachs relationship. The results include, not only the indices of the product components, but also the frequencies of their occurrence. Useful diagrams or maps (Figure VII.2 and its complementary Figure VII.3) were constructed from these results, in which the most significant bcc components are shown together with the parent orientation(s) from which they arise. Such diagrams, first introduced in this work, can be used to analyze bcc transformation textures in steels, and relate them to their origins in the austenite. These diagrams can also be employed to make processing changes that will increase or decrease the intensities of particular components.

4. Each product orientation was designated by selecting the representation whose square root of the sum of the squares of the Miller indices takes the smallest possible value within a distance of 11.5 degrees of the exact location. Alternative designations, closer to the exact Euler orientation, but with higher Miller indices, were also derived. This analysis made it clear that when a particular transformation component, defined in Euler coordinates, is converted into Miller index form, considerable variations can occur between authors, resulting from the extent to which low indices are sought. Several important product equivalences, which can again be useful in the interpretation of steel textures, were first derived in this investigation. Thus, the $\{001\}<110>$ orientation can also be represented by the indices $\{013\}<331>$ or $\{015\}<551>$, which are in fact closer to the exact orientation of the

transformation product of the cube when it is defined in terms of Euler angles. This aspect of transformation textures has not previously been discussed in the literature, particularly with respect to the Kurdjumov-Sachs relationship. Its importance resides in the fact that orientations such as the {332}<113> (frequently cited as the product of the brass {110}<112>) can also be designated as the {111}<112>, if the rules outlined above for the cube are followed.

5. It was shown here that both variant selection and selective growth take place during the transformation from austenite, either recrystallized or deformed, to ferrite. The occurrence of variant selection was deduced by comparing the predictions of the Kurdjumov-Sachs relationship with the experimental results. The presence of selective growth was detected in a similar way by comparing the textures produced by quenching (little growth) and air cooling (appreciable growth). Although not absolutely proved, such detailed inferences about the extent of variant selection and of selective growth during steel processing have not previously been put forward in the metallurgical literature.

REFERENCES

1. Van Melsen, Andrew G.: From Atomos to Atom, The History of the Concept Atom. Duquesne Studies, Philosophical Series 1, Duquesne University Press, Pittsburgh 19, Pa., 1952, pp. 99-109.

2. Wenk, Hans Rudolf: Preferred Orientations in Deformed Metals and Rocks: An Introduction to Modern Texture Analysis. Academic Press, Inc. Orlando, Florida, 1985.

3. Bunge, H. J.: "Texture Analysis in Materials Science", Butterworths, London, 1982.

4. Bunge, H. J.: "Texture and Directional Properties of Materials." Directional Properties of Materials, H. J. Bunge (ed.), Informationgesellschaft, Verlag (1988) 1-63.

5. Hansen, Jorn, Jan Pospiech and Kurt Lücke: "Tables for Texture Analysis of Cubic Crystals." Berlin; New York: Springer Verlag, 1978.

6. Hatherley, M. and W. B. Hutchinson: "An Introduction to Textures in Metals." Monograph No.5, The Institution of Metallurgists, London, 1979.

7. Bunge, H. J.: "Representation of Preferred Orientations." Preferred Orientation in Deformed Metals and Rocks: An Introduction to Modern Texture Analysis, Hans-Rudolf Wenk (ed.), Academic Press (1985) 73-108.

8. Williams, R. O.: Trans. Met. Soc. AIME, **242** (1968) 104-115.

9. Ruer, D. and R. Baro: Adv. X-ray Analy., **20** (1977) 187.

10. Roe, R. J.: J. Appl. Phys., **36** (1965) 2024-2031.

11. Bunge, H. J.: Z. Metallkunde, **56** (1965) 872-874.

12. Imhof, J.: Z. Metallkunde, **68** (1977 38-43.

13. Matthies, S. and W. G. Vinel: Phys. Stat. Sol. (b), **112** (1982) 111-120.

14. Matthies, S.: Phys. Stat. Sol., **92** (1979) 135-138.

15. Bain, Edgar C. "The Nature of Martensite." Trans. AIME, **70** (1924) 25-35.

16. Kurdjumov, Von G. and G. Sachs. "Über den Mechanismus der Stahlhärtung." Z. Physik, **64** (1930) 325-43.

17. Nishiyama, Zenji. "X-Ray Investigation of the Mechanism of the Transformation from Face- Centred Cubic Lattice to Body-Centred Cubic." Sci. Rep. Tohoku Imperial University, **23** (1934) 637-664.

18. Nishiyama, Zenji. "On the Transformation Gamma → Alpha of Stainless Invar Caused by Stress and the Mechanism of the Transformation." Sci. Rep. Tohoku Imperial University, **25** (1936) 94-103.

19. Wassermann, G. Archiv für das Eisenhüttenwesen, **6** (1933) 347.

20. Greninger, Alden B. and Alexander R. Troiano. Trans AIME, **180** (1940) 307.

21. Greninger, Alden B. and Alexander R. Troiano. "The Mechanism of Martensite Formation." Metals Trans., **185** (1949) 590-98.

22. Roberts, C.S. "Effect of Carbon on the Volume Fractions and Lattice Parameters of Retained Austenite and Martensite." Journal of Metals, **5** (1953) 203-204.

23. Taylor, A.: "X-ray Metallography", Wiley, New York, 1961.

24. Davies, Graeme John and Richard Marcus Bateman. "The Influence of Variant Selection in the Inheritance of Texture during Phase Transformations." Proceedings of the Sixth International Conference on Textures of Materials, edited by Shin-ichi Nagashima. The Iron and Steel Institute of Japan, Tokyo (1981) 132-48.

25. Kallend, J. S., P. P. Morris and G. J. Davies. "Texture Transformations - The Misorientation Distribution Function." Acta Metall., **24** (1976) 361-70.

26. Davies, G. J., J. S Kallend and P. P. Morris. "The Quantitative Prediction of Transformation Textures." Acta Metall., **24** (1976) 159-72.

27. Ray, R. K. and J. J. Jonas. "Transformation Textures in Steels." Int. Mater. Rev. **35.1** (1990) 1-36.

28. Humbert, M. "Inherited Texture in Phase Transformation." Directional Properties of Materials, H. J. Bunge (ed.), Informationgesellschaft, Verlag (1988) 223-38.

29. Furubayashi, Ei-ichi, Hirofumi Miyaji and Minoru Nobuki. "A Simple Model of Predicting the Transformation Textures in Thermomechanically Processed Steels." Transactions ISIJ, **27** (1987) 513-19.

30. Bokros, J. C. and E. F. Parker. Acta Metall., **11** (1963) 1291.

31. Senuma, Takehide and Hiroshi Yada: "Textures and Deep Drawability of Low and Ultra Low Carbon Steel Sheets Hot Rolled below A_{R_3} Temperatures." Proceedings of the International Conference on 'Physical Metallurgy of Thermomechanical Processing of Steels and Other Metals', Vol. 2, Tokyo, The Iron and Steel Institute of Japan, 1988, pp. 636-643.

32. Hashimoto, Shunichi, Terutoshi Yakushiji, Takahiro Kashima and Koji Hosomi: "Effects of Hot Rolling Conditions on R-Value of Hot Rolled and Annealed Extra Low Carbon Steels." Proceedings of the International Conference on 'Physical Metallurgy of Thermomechanical Processing of Steels and Other Metals', Vol. 2, Tokyo, The Iron and Steel Institute of Japan, 1988, pp. 652-659.

33. Saitoh, Hajime, Kohsaku Ushioda, Takehide Senuma, Takaaki Nakamura and Kazuyoshi Esaka: "Structural and Textural Evolution during Subsequent Annealing of Steel Sheet Hot Rolled in α Phase." Proceedings of the International Conference on 'Physical Metallurgy of Thermomechanical Processing of Steels and Other Metals', Vol. 2, Tokyo, The Iron and Steel Institute of Japan, 1988, pp. 628-635.

34. Nakamura, Takaaki and Kazuyoshi Esaka: "Development of Hot Rolled Steel Sheet with High $\bar{r}$-Value." Proceedings of the International Conference on 'Physical Metallurgy of Thermomechanical Processing of Steels and Other Metals', Vol. 2, Tokyo, The Iron and Steel Institute of Japan, 1988, pp. 644-651.

35. Meyer, L., F. Heisterkamp and W. Mueschenborn: Microalloying '75: proceedings of the International Symposium on HSLA Steels, New York, Union Carbide Corp., 1977, p. 153.

36. Krauss, G., D. O. Wilshynsky and D. K. Matlock: "Processing and Properties of Interstitial-Free Steels." Proceedings of the International Symposium on Interstitial Free Steel Sheet: Processing, Fabrication and Properties, edited by L. E. Collins and D. L. Baragar. The Metallurgical Society of the Canadian Institute of Mining and Metallurgy, Ottawa, Ontario, 1991, pp. 1-14.

37. Inagaki, Hirosuke. "Transformation Textures in Control-Rolled High Tensile Strength Steel." Proceedings of the Fifth International Conference on Textures of Materials, Vol. 2, edited by G. Gottstein and K. Lücke, Springer Verlag, Berlin, 1978, pp. 157-166.

38. Hibbard, W. R. and W. R. Tully: Trans. AIME, **221** (1961) 336.

39. King, A. D. and T. Bell: "Crystallography of Grain Boundary Proeutectoid Ferrite." Metall. Trans., **6A** (1975) 1419-29.

40. Oakwood, T. G., W. E. Heitmann and E. S. Madrzyk: in 'The Hot Deformation of Austenite', American Institute of Mining, Metallurgical and Petroleum Engineers, New York, 1977, p. 204.

41. Lamberights, M. and T. Greday: in 'The Hot Deformation of Austenite', American Institute of Mining, Metallurgical and Petroleum Engineers, New York, 1977, p. 286.

42. Takechi, Hiroshi: "Developments in High-Strength Hot- and Cold-Rolled Steels for Automotive Applications." Proceedings of the Symposium on Hot and Cold Rolled Sheet Steels, edited by R. Pradhan and G. Ludkovsky, The Metallurgical Society, Pennsylvania, 1988, pp. 117-138.

43. Senuma, Takehide, Hiroshi Yada, Ryo Shimizu and Jiro Harase. "Textures of Low Carbon and Titanium Bearing Extra Low Carbon Steel Sheets Hot Rolled Below A_{R3} Temperatures." Acta Metall. Mater., **38** (1990) 2673.

44. Senuma, Takehide and Kaoru Kawasaki: "Texture Formation in Ti-Bearing IF Steel Sheets throughout the Rolling and Annealing Processes in Terms of the Influence of Hot Rolling Conditions on Deep Drawability." ISIJ International, **34** No.1 (1994) 51-60.

45. Inagaki, Hirosuke. "Transformation Textures in Steels." Proceedings of the Sixth International Conference on Textures of Materials, Vol. 1, edited by S. Nagashima, The Iron and Steel Institute of Japan, Tokyo, 1981, pp. 149-163.

46. Inagaki, Hirosuke. "Effect of Finishing Temperature on the Texture Development in Control-Rolled Low Carbon Steel." Z. Metallkde, **74** (1983) 716-26.

47. Inagaki, Hirosuke. "Formation of Transformation Textures in Control-Rolled Low Carbon Steels." Z. Metallkde, **75** (1984) 510-16.

48. Inagaki, Hirosuke. "Effect of Crystallographic Texture on the Separation Behaviour of Control-Rolled Low Carbon Steel." Z. Metallkde, **76** (1985) 85-91.

49. Inagaki, Hirosuke. "Fractographic Study of the Formation of the Separation in a Control-Rolled Low Carbon Steel." Z. Metallkde, **79** (1988) 364-74.

50. McG. Tegart, W. J. and A. Gittins: in 'The Hot Deformation of Austenite', American Institute of Mining, Metallurgical and Petroleum Engineers, New York, 1977, p. 1.

51. Hu, Hsun and John S. Kallend: "Transformation Textures of Thermomechanically Processed 5Ni-Steel Plates." Proceedings of the Sixth International Conference on Textures of Materials, Vol. 1, edited by S. Nagashima, The Iron and Steel Institute of Japan, Tokyo, 1981, pp. 164-180.

52. Davies, G. J., J. S. Kallend and P. P. Morris: "The Influence of Hot Deformation of Austenite on the Properties of Ferrite Through the Development and Inheritance of Texture." in 'The Hot Deformation of Austenite', American Institute of Mining, Metallurgical and Petroleum Engineers, New York, 1977, pp. 599-627.

53. Jones, A. and B. Walker: "The Structural State of Austenite during Continuous Hot Strip Mill Rolling." Metal Science, **8** (1974) 397-406.

54. Lotter, Ulrich, Lutz Meyer and Rolf-Dietrich Knorr: "Texturen in Warmband aus Mikrolegierten Stählen." Arch. Eisenhüttenwes., **47** No.5 (1976) 289-294.

55. Lotter, Ulrich and Lutz Meyer: "Texture and Yield Strength Anisotropy of Microalloyed Thermomechanically Treated High-Strength Steels." Metals Technology, January (1977) 27-31.

56. Tanaka, Tomo, Nobuhisa Tabata, Taneo Hatomura and Chiaki Shiga: "Three Stages of the Controlled-Rolling Process." 'Microalloying '75', Union Carbide Corporation, New York, 1977, pp. 107-119.

57. Ouchi, C., T. Sanpei, T. Okita and I. Kozasu: in 'The Hot Deformation of Austenite', American Institute of Mining, Metallurgical and Petroleum Engineers, New York, 1977, p. 316.

58. Yutori, Tashiaki and Rikuo Ogawa. "Formation of Transformation Textures in Accelerateed-Cooled Steels after Controlled Rolling." Proceedings of the Sixth International Conference on Textures of Materials, Vol. 1, edited by S. Nagashima, The Iron and Steel Institute of Japan, Tokyo, 1981, pp. 669-679.

59. Tanaka, T.: Int. Met. Rev., 26, No. 4 (1981) 185.

60. Coleman, T., D. Dulieu and A. Gouch: "The Structure and Properties of Controlled Processed High Strength Ferrite-Pearlite Steels." in 'The Microstructure and Design of Alloys', The Metals Society, London, 1973, pp. 70-74.

61. Little, J. H., J. A. Chapman, W. B. Morrison and B. Mintz: "The Production of High Strength Plate Steels by Controlled Rolling." in 'The Microstructure and Design of Alloys', The Metals Society, London, 1973, pp. 80-84.

62. Vlad, Constantin M. and Hans J. Bunge. "On the Stability of the γ/α Transformation $\{112\}<110>$ Texture." Proceedings of the Sixth International Conference on Textures of Materials, Vol. 1, edited by S. Nagashima, The Iron and Steel Institute of Japan, Tokyo, 1981, pp. 639-648.

63. Bramfitt, B. L. and A. R. Marder: "The Influence of Microstructure and Crystallographic Texture on the Strength and Notch Toughness of a Low-Carbon Steel." in 'Processing and Properties of Low Carbon Steels', AIME, New York, U.S.A., 1973, pp. 191-224.

64. Hawkins, D. N.: "Cleavage Separations in Warm-Rolled Low-Carbon Steels." Metals Technology, September (1976) 417-421.

65. Tanaka, Tomoo and Tabata Nobuhisa: "Measurement of Austenite to Ferrite Transformation Temperatures in Niobium-Bearing Steels During Controlled Rolling." Tetsu-to-Hagané (J. Iron Steel Inst. Jpn.), **64** (1978) 1353.

66. Tóth, L. S., J. J. Jonas, D. Daniel and R. K. Ray. "Development of Ferrite Rolling Textures in Low and Extra Low Carbon Steels." Metallurgical Transactions A, **21A** (1990) 2985-3000.

67. Hashimoto, S., T. Yakushiji, T. Kashima and K. Hosomi. "Effects of Solute Carbon and Hot Rolling Temperature on Recrystallization Texture of Hot Rolled and Annealed Extra Low Carbon Sheet Steels." Proceedings of the Eighth International Conference on Textures of Materials, edited by J. S. Kallend and G. Gottstein, Warrendale, PA, The Metallurgical Society of AIME, 1988, pp. 673-678.

68. Barbosa, R., F. Boratto, S. Yue, and J. J. Jonas. Proc. Int. Symp. on Processing, Microstructure and Properties of HSLA Steels, Editor A. J. de Ardo Jr., TMS-AIME, Warrendale, PA, 1988, 51.

69. Gupta, I. and D. Bhattacharya: Metallurgy of Vacuum-Degassed Steel Products, TMS 1990, p. 55.

70. Chapellier, P., R. K. Ray and J. J. Jonas. "Prediction of Transformation Textures in Steels." Acta Metall.Mater., **38** (1990) 1475-90

71. Goodman S. R. and Hu Hsun. "Annealing Textures in an 18-8 Austenitic Stainless Steel." Trans. AIME, **233** (1965) 103-110.

72. Goodman S. R. and Hu Hsun. "Texture Transition in Austenitic Stainless Steels." Trans. AIME, **230** (1964) 1413-19.

73. Hirsch, J. and K. Lücke. "Overview No. 76: Mechanism of Deformation and Development of Rolling Textures in Polycrystalline fcc Metals - I. Description of Rolling Texture Development in Homogeneous CuZn Alloys." Acta Metall., **36.11** (1988) 2863-82.

74. Bateman, Richard Marcus and Graeme John Davies. "The Inheritance of Texture on Transformation from Austenite to Martensite in an Fe-30Ni Alloy." Proceedings of the 6th International Conference on Textures of Materials, Vol. 2, The Iron and Steel Institute of Japan, (1981) 690-702.

75. Pospiech, Jan. "Die Parameter der Drehung und die Orientierungs-verteilungsfunktion (OVF)." Kristall und Technik, 7 (1972) 1057-72.

76. Steurer, Walter. "Elements of Symmetry in Periodic Lattices, Quasicrystals." Materials Science and Technology: A Comprehensive Treatment. Vol. 1: Structure of Solids. Edited by R. W. Cahn, P. Haasen, E. J. Kramer. Weinheim, FDR; New York, NY: VCH, 1991.

77. Samuel, F.H., S. Yue, B.A. Zbinden and J. J. Jonas: "Recrystallization Characteristics of a Ti-Containing Interstitial-Free Steel During Hot Rolling," paper presented at the AIME Symposium on Metallurgy of Vacuum Degassed Carbon Steel Products (Indianapolis, IN), American Institute of Mining, Metallurgical, and Petroleum Engineers, Oct. 1989

78. Zhou, Y., K. W. Neale and L. S. Tóth: Acta metall. mater., 39 (1991) 2921.

79. Zhou, Y., L. S. Tóth and K. W. Neale: Acta metall. mater., 40 (1992) 3179.

80. A.D. King and T. Bell: Metall. Trans. 6A (1975) 1419.

81. Vanderschueren, D., P. Van Houtte, E. Aernoudt, J. Dilewijns and C. Standaert: "Hot Rolling Textures of Low Carbon Steel Sheets and Their Influence on the Texture After Continuous Annealing." Advances in Hot Deformation Textures and Microstructures, proceedings of a symposium sponsored by TMS and ASM Int. Edited by John J. Jonas, Thomas R. Bieler and Keith J. Bowman. The Minerals, Metals and Materials Society, 1994, pp. 95-106.

82. Savoie, J., R. K. Ray, M. P. Butrón-Guillén and J. J. Jonas: "Comparison between Simulated and Experimental Transformation Textures in a Nb Microalloyed Steel," Acta metall. mater., 42 No. 7 (1994) 2511-2523.

83. Inagaki, H.: Trans. Iron Steel Inst. Japan, 17 (1977) 166.

Appendix A

FORTRAN PROGRAM

The source code of the FORTRAN program employed in the calculation of product orientations from discrete parent components is presented here. The initial parent orientation must be supplied. The data file called "trans24.dat" contains the 9 elements of each of the 24 matrices of cubic symmetry given in Chapter VII.3 (Table VII.1). The results, consisting of the Miller indices (given as integers between 0 and 100) and the three sets of Euler angles (for all three equivalent positions of every orientation in reduced Euler space) of each of the 24 resulting variants are stored in the file called "hat.pat".

```
C  TO ROTATE AN ORIENTATION

C  © László S. Tóth, 22.04.1991. KUL Leuven
C  Adapted by Martha Patricia Butrón-Guillén
C  Rotation of 90° about <112>, considering all 24 symmetry elements

      implicit real*8 (a-h,o-z)
      integer*4 dir1,dir2,dir3
      character*1 grain,symm,rotat
      dimension g(3,3),sc(3,3),res(3,3),sb(3,3),ind(96),m(96)
      dimension dir1(3),dir2(3),dir3(3),f1(96),f(96),f2(96)
      dimension dd1(24),dd2(24),dd3(24)

C  The 24 axes of rotation, after Kurdjumov-Sachs:

      data dd1(1),dd1(2),dd1(3),dd1(4),dd1(5),dd1(6),dd1(7),dd1(8),dd1(9),dd1(10),
     *dd1(11),dd1(12),dd1(13),dd1(14)/-1.,1.,-1.,1.,2.,-2.,1.,-1.,1.,-1.,-2.,2.-1.,1./
      data dd1(15),dd1(16),dd1(17),dd1(18),dd1(19)/2.,-2.,-1.,1.,2./
      data dd1(20),dd1(21),dd1(22),dd1(23),dd1(24)/-2.,-1.,1.,-1.,1./

      data dd2(1),dd2(2),dd2(3),dd2(4),dd2(5),dd2(6),dd2(7),dd2(8),dd2(9),dd2(10),
     *dd2(11),dd2(12),dd2(13),dd2(14)/2.,-2.,-1.,1.,-1.,1.,-1.,1.,2.,-2.,-1.,1.,-2.,2./
      data dd2(15),dd2(16),dd2(17),dd2(18),dd2(19)/1.,-1.,1.,-1.,-1./
      data dd2(20),dd2(21),dd2(22),dd2(23),dd2(24)/1.,-1.,1.,2.,-2./

      data dd3(1),dd3(2),dd3(3),dd3(4),dd3(5),dd3(6),dd3(7),dd3(8),dd3(9),dd3(10),
     *dd3(11),dd3(12),dd3(13),dd3(14)/-1.,1.,2.,-2.,-1.,1.,2.,-2.,-1.,1.,-1.,1.,-1.,1./
      data dd3(15),dd3(16),dd3(17),dd3(18),dd3(19)/-1.,1.,2.,-2.,1./
      data dd3(20),dd3(21),dd3(22),dd3(23),dd3(24)/-1.,-2.,2.,1.,-1./

C  Open file to store results:

      open(1,file='hat.pat',status='unknown')

      pi=dacos(-1.d0)
      s2=dsqrt(2.d0)
      s3=dsqrt(3.d0)
      s6=dsqrt(6.d0)
      deg=180.d0/pi

      kat=0
      n=3
      m2=1
```

```
C  Asking for the Miller indices of the parent orientation:

      write(*,100) n
100   format(/'Enter the Miller indices of axis ',i1,'.. ' $)
      read(*,*) xn,yn,zn
      write(*,110) m2
110   format(/'Enter the Miller indices of axis ',i1,'.. ' $)
      read(*,*) xm,ym,zm

      ixn=xn
      iyn=yn
      izn=zn
      ixm=xm
      iym=ym
      izm=zm

      write (1,120) ixn,iyn,izn,ixm,iym,izm
120   format (i3,1x,i3,1x,i3,3x,i3,1x,i3,1x,i3///)

C  Get the transformation matrix of this parent orientation:

      call miller (n,m2,xn,yn,zn,xm,ym,zm,sc)

130   kat = kat+1
      isymm = 4

      d1 = dd1(kat)
      d2 = dd2(kat)
      d3 = dd3(kat)

      idk1 = dd1(kat)
      idk2 = dd2(kat)
      idk3 = dd3(kat)

      write (1,140) idk1,idk2,idk3
140   format (i2,1x,i2,1x,i2)

C  Normalization of the direction:

      sum=dsqrt(d1*d1+d2*d2+d3*d3)
      d1 = d1/sum
      d2 = d2/sum
      d3 = d3/sum
```

```
C  Definition of the angle of rotation:

      om = 90
      om = om/deg

C  Generation of the rotation matrix g:

      call rot (g,d1,d2,d3,om)

C  Multiplication of g and sc

      do 150 i = 1,3
      do 150 j = 1,3
      res(i,j) = 0.d0
      do 150 k = 1,3
150   res(i,j) = res(i,j)+g(i,k)*sc(k,j)

C  Obtain the new Euler angles:

      call angles (isymm,res,f1,f,f2,kk)

      write(*,160)
160   format (/' ******************************'/
     *' Equivalent orientations found:'//'    fi1    fi    fi2    multiplicity'/)

C  Multiplicity m(i):

      d = 1.d-6
      do 170 i = 1,kk
      ind(i) = 1
      m(i) = 0
      do 170 j = 1,kk
170   if (dabs(f1(i)-f1(j)).lt.d.and.dabs(f(i)-f(j)).lt.d.and.dabs(f2(i)-
     *f2(j)).lt.d) m(i)=m(i)+1

      do 190 i = 1,kk
      if (ind(i).eq.1) write(*,200) f1(i),f(i),f2(i),m(i)
      if (ind(i).eq.1) write(1,210) f1(i),f(i),f2(i)

      do 180 j = 1,kk
180   if (dabs(f1(i)-f1(j)).lt.d.and.dabs(f(i)-f(j)).lt.d.and.dabs(f2(i)-
     *f2(j)).lt.d) ind(j)=0
```

```
190   continue
      write(*,*)

200   format(3x,f6.2,2x,f5.2,2x,f5.2,8x,i2)
210   format(f6.2,1x,f5.2,1x,f5.2,)

C  Calculate Miller indices; the ith column of res(i,j) contains the direction
C  cosines of the sample axes with respect to the crystal axes:

      big1 = 0.d0
      big2 = 0.d0
      big3 = 0.d0

      do 220 j = 1,3
      if (dabs(res(j,1)).gt.big1) big1=dabs(res(j,1))
      if (dabs(res(j,2)).gt.big2) big2=dabs(res(j,2))
      if (dabs(res(j,3)).gt.big3) big3=dabs(res(j,3))
220   continue

      do 230 i = 1,3
      dir1(i) = dnint(res(i,1)*100.d0/big1)
      dir2(i)=dnint(res(i,2)*100.d0/big2)
230   dir3(i)=dnint(res(i,3)*100.d0/big3)

      write (*,250) (dir3(i),i=1,3),(dir1(i),i=1,3)
      write (1,240) (dir3(i),i=1,3),(dir1(i),i=1,3)

240   format (3i5/,3i5/,3i5//)
250   format (/
     *'Miller indices of sample axis 1: ',3i5/
     *'Miller indices of sample axis 2: ',3i5/
     *'Miller indices of sample axis 3: ',3i5//)

      if (kat.eq.24) then
      goto 260
      else
      goto 130
      end if

      close(1)
260   end

C  The rotation matrix around a given direction by a given angle:
```

```
      subroutine rot(g,d1,d2,d3,om)

      implicit real*8 (a-h,o-z)
      dimension g(3,3)
      cs=dcos(om)
      si=dsin(om)
      g(1,1)=(1.d0-d1*d1)*cs+d1*d1
      g(1,2)=d1*d2*(1.d0-cs)+d3*si
      g(1,3)=d1*d3*(1.d0-cs)-d2*si
      g(2,1)=d1*d2*(1.d0-cs)-d3*si
      g(2,2)=(1.d0-d2*d2)*cs+d2*d2
      g(2,3)=d2*d3*(1.d0-cs)+d1*si
      g(3,1)=d1*d3*(1.d0-cs)+d2*si
      g(3,2)=d2*d3*(1.d0-cs)-d1*si
      g(3,3)=(1.d0-d3*d3)*cs+d3*d3
      return
      end
```

C Eulerian transformation matrix:

```
      subroutine eul (sc,FI1,FI,FI2)

      implicit real*8 (a-h,o-z)
      dimension sc(3,3)
      cfi=  dcos(fi)
      sfi=  dsin(fi)
      cfi1= dcos(fi1)
      sfi1= dsin(fi1)
      cfi2= dcos(fi2)
      sfi2= dsin(fi2)
      sc(1,1)=cfi1*cfi2-sfi1*sfi2*cfi
      sc(1,2)=sfi1*cfi2+cfi1*sfi2*cfi
      sc(1,3)=sfi2*sfi
      sc(2,1)=-cfi1*sfi2-sfi1*cfi2*cfi
      sc(2,2)=-sfi1*sfi2+cfi1*cfi2*cfi
      sc(2,3)=cfi2*sfi
      sc(3,1)=sfi1*sfi
      sc(3,2)=-cfi1*sfi
      sc(3,3)=cfi
      return
      end
```

C Recalculation of the new Euler angles:

```
      subroutine angles(isymm,sc,f1,f,f2,kk)

      implicit real*8 (a-h,o-z)
      dimension sc(3,3),tb(4,3,3),sym(24,3,3),sb(3,3),tab(3,3)
      dimension f1(96),f(98),f2(96)

      kk=0
      pi=dacos(-1.d0)
      deg=180.d0/pi

C  Reading the 24 cubic symmetry matrices from data file:

      open(2,file='trans24.dat',status='old')
      do 270 i=1,24
      read(2,*) sym(i,1,1),sym(i,1,2),sym(i,1,3),sym(i,2,1),
     *sym(i,2,2),sym(i,2,3),sym(i,3,1),sym(i,3,2),sym(i,3,3)
270   continue
      close (2)

C  The sample symmetry matrices for orthorhombic symmetry:

      if(isymm.eq.4) then
      do 280 i=1,4
      do 280 j=1,3
      do 28 k=1,3
280   tb(i,j,k)=0.d0
      tb(1,1,1)=1.d0
      tb(1,2,2)=1.d0
      tb(1,3,3)=1.d0
      tb(2,1,1)=-1.d0
      tb(2,2,2)=1.d0
      tb(2,3,3)=-1.d0
      tb(3,1,1)=-1.d0
      tb(3,2,2)=-1.d0
      tb(3,3,3)=1.d0
      tb(4,1,1)=1.d0
      tb(4,2,2)=-1.d0
      tb(4,3,3)=-1.d0
      end if

C  Applying the sample symmetries:

      do 330 mk=1,isymm
```

```
      do 290 k=1,3
      do 290 j=1,3
      tab(k,j)=0.d0
      do 290 l=1,3
290   tab(k,j)=tab(k,j)+sc(k,l)*tb(mk,l,j)

C  Applying the cubic symmetries on tab:

      do 330 n=1,24
      do 300 k=1,3
      do 300 l=1,3
      sb(k,l)=0.d0
      do 300 m=1,3
300   sb(k,l)=sb(k,l)+sym(n,m,k)*tab(m,l)

C  Recalculation of the Euler angles:

      fiv=dacos(sb(3,3))
      sfi=dsin(fiv)
      ha=1.d0-1.d-8
      if(dabs(sb(3,3)).gt.ha) go to 310

C  fi different than zero:

      fi1v=datan2(sb(3,1)/sfi,-sb(3,2)/sfi)
      fi2v=datan2(sb(1,3)/sfi, sb(2,3)/sfi)
      go to 320

C  fi equal to zero:

310   fi2v=0.d0
      fi1v=datan2(-sb(2,1),sb(1,1))

320   continue

C  Check if the Euler angles obtained are within the right ranges (symmetry):

      fi1=fi1v*deg
      fi=fiv*deg
      fi2=fi2v*deg
      d=1.d-6
      if(dabs(dabs(fi1)-d).le.d) fi1=0.d0
      if(dabs(dabs(fi)-d).le.d) fi=0.d0
```

```
      if(dabs(dabs(fi2)-d).le.d) fi2=0.d0
      if(dabs(dabs(fi1)-90.d0).le.d) fi1=90.d0
      if(dabs(dabs(fi)-90.d0).le.d) fi=90.d0
      if(dabs(dabs(fi2)-90.d0).le.d) fi2=90.d0
      if(dabs(dabs(fi1)-180.d0).le.d) fi1=180.d0
      if(dabs(dabs(fi)-60.d0).le.d) fi=60.d0
      if(dabs(dabs(fi2)-180.d0).le.d) fi2=180.d0

      if(isymm.eq.4) then
      if(fi1.ge.0.d0.and.fi1.le.90.d0.and.fi.ge.0.d0.and.fi.le.90.d0.
     *and.fi2.ge.0.d0.and.fi2.le.90.d0) then
      kk=kk+1
      f1(kk)=fi1
      f(kk)=fi
      f2(kk)=fi2
      end if
      end if

330   continue

      return
      end

C  Determination of the transformation matrix from the Miller indices:

      subroutine miller(n,m,xn,yn,zn,xm,ym,zm,sc)
      implicit real*8 (a-h,o-z)
      dimension sc(3,3)
      pi=dacos(-1.d0)
      deg=pi/180.d0

C  Determination of the third axis:

      f((n*m).eq.2) k=3
      if((n*m).eq.3) k=2
      if((n*m).eq.6) k=1

C  Normalization:

      s=dsqrt(xn*xn+yn*yn+zn*zn)
      sc(1,n)=xn/s
      sc(2,n)=yn/s
      sc(3,n)=zn/s
```

```
      s=dsqrt(xm*xm+ym*ym+zm*zm)
      sc(1,m)=xm/s
      sc(2,m)=ym/s
      sc(3,m)=zm/s

C     Determination of the third column of SC by the vector product of
C     the two known columns:

      if(k.eq.2) then
      i=3
      j=1
      end if
      if(k.eq.1) then
      i=2
      j=3
      end if
      if(k.eq.3) then
      i=1
      j=2
      end if
      sc(1,k)=sc(2,i)*sc(3,j)-sc(2,j)*sc(3,i)
      sc(2,k)=sc(1,j)*sc(3,i)-sc(1,i)*sc(3,j)
      sc(3,k)=sc(1,i)*sc(2,j)-sc(1,j)*sc(2,i)

      return
      end
```